Doctoral theses at NTNU, 2021:336

Sondre Gjengedal

Groundwater heat pump systems

New insights on design and on fluid flow in unconsolidated aquifers

Doctoral thesis

NTNU
Norwegian University of Science and Technology
Thesis for the Degree of
Philosophiae Doctor
Faculty of Engineering
Department of Geoscience and Petroleum

NTNU
Norwegian University of
Science and Technology

Sondre Gjengedal

Groundwater heat pump systems

New insights on design and on fluid flow in unconsolidated aquifers

Thesis for the Degree of Philosophiae Doctor

Trondheim, November 2021

Norwegian University of Science and Technology
Faculty of Engineering
Department of Geoscience and Petroleum

NTNU
Norwegian University of
Science and Technology

NTNU
Norwegian University of Science and Technology

Thesis for the Degree of Philosophiae Doctor

Faculty of Engineering
Department of Geoscience and Petroleum

ISBN 978-82-326-5780-3 (printed ver.)
ISBN 978-82-326-5311-9 (electronic ver.)
ISSN 1503-8181 (printed ver.)
ISSN 2703-8084 (online ver.)

Doctoral theses at NTNU, 2021:336

Printed by NTNU Grafisk senter

Abstract

Groundwater heat pump (GWHP) systems utilize groundwater for heating and cooling applications in buildings. The main study site for this PhD project is in Melhus, Norway, where ten different GWHPs utilize an unconsolidated aquifer beneath the town center. This has provided a unique opportunity for field investigations, operational experience, and data acquisition from different GWHP systems. It is vitally important to understand how groundwater flows through both the aquifer and the GWHP system to ensure a reliable and sustainable utilization of the groundwater resource.

Both the design and the operational strategy employed by the GWHP system influence their long-term operations. All GWHP systems in Melhus are affected by clogging problems that disrupt the heating and cooling process. Clogging is a severe challenge for the successful long-term operation. One possible trigger event has been analyzed, which occurs when vacuum pressures develop in the pipes. Vacuum pressures affect the solubility of gases in water and can trigger exsolution of gas, which has the potential to catalyze precipitation reactions and cause clogging. Vacuum pressures should therefore be avoided in GWHP systems when the aquifer is sensitive to pressure variations and hydraulic stresses due to pumping.

In some cases, clogging caused the entire GWHP system to malfunction due to absence of surveillance and maintenance routines. Routine maintenance is important for GWHP systems. Surveillance equipment that measures the hydraulic and thermal performance of the GWHP system must be installed in order to detect where and when maintenance is needed. This also allow the step-test surveillance procedure to detect clogging in the system. A GWHP-specialist should follow up and interpret the performance data and schedule for the correct maintenance measures. Maintenance and operational control necessitate that the GWHP design and the groundwater pipe layout allow easy access for cleaning equipment to all parts of the groundwater system. The pipeline should not enter the building and the groundwater heat exchanger should therefore be installed in the production well manhole. A module-based design strategy is favorable where one production well and one injection well function as a well-pair. This will enable one pair to be cleaned while other well-pairs can ensure that the GWHP system is operational throughout the cleaning process.

When designing GWHP systems it is crucial that the GWHP-specialist is involved at an early stage in new projects and that pre-investigations are performed on-site in advance of system construction. It is recommended to utilize the full thermal potential of each liter of groundwater. The groundwater temperature should be lowered as much as possible, restricted to the lower limit of 2°C after heat exchange. The required pumping rate needed in the heat production process can then be minimized according to the local aquifer conditions and the available groundwater temperature, normally 3-8°C in Norway. This will minimize the hydraulic stresses enforced on the aquifer through pumping and reduce the risk of clogging.

The hydraulic stresses induced in a porous aquifer is governed by the permeability of the pores within the soil. This phenomenon was studied by means of a novel and innovative 3D technique. It is demonstrated that the permeability of a single pore can be described by the Stokes equation. The permeability is a function of the pore geometry, where the pore shape, the specific porosity, the specific surface area, and the contraction ratio of the pore channel, have governing roles. This knowledge is valuable when interpreting hydrogeological data, GWHP performance data, and for numerical modeling of groundwater flow.

Acknowledgements

It is now finally clear to me that a PhD is not just about the thesis itself, but mostly about the process of doing the work. The work has been an uphill struggle, but you might say that an uphill struggle elevates your mind and view upon the world. This is obvious for some people, but it must be experienced before realization finally dawns on you. In realizing this it is easier to appreciate the view of the land from the top of the hill, and it makes it easier to accept the fact that there is a new and even bigger hill conveniently hidden behind that huge boulder over there.

All of this was of course pointed out to me quite early in my Ph.D. career. Sometimes quite literally by people pointing me in the right direction. In the beginning, this was done by my main supervisor Professor Bjørge Brattli and by my co-supervisor Associate Professor Randi K. Ramstad. The pointing could in-fact have been incorporated into a relatively neat dancing routine (if they were into that sort of thing). I am immensely thankful for your help.

Due to the unforeseen retirement of Bjørge, Randi later became my main supervisor. Professor Bjørn Syvert Frengstad at NTNU and Dr. Bernt Olav Hilmo at Asplan Viak AS came to my aid as co-supervisors in May 2017. Thank you all for stepping in for Bjørge at such a crucial time in my thesis. On a professional level I have enjoyed your help and guidance, but on a personal level I have enjoyed your openness, directness and low-key approach for new ideas and views. You gave me great amounts of freedom to do as I pleased, and I think that this is one of the reasons why I finished at all. I now contemplate climbing that new hill in the future thanks to you.

I was lucky to be included in a large working group in the research project ORMEL. This allowed me to grow rapidly as a researcher thanks to the knowledge shearing guidance of the other experienced participants. Apart from my supervisors, I especially relied on Mari H. Riise and Henrik Holmberg at Asplan Viak AS, and Atle Dagestad, Guri Venvik, Øystein Jæger and Anna Seither at NGU in the preliminary parts of my PhD thesis. I especially enjoyed your company during the many hours of field work in Melhus and Elverum, conducting field measurements, drilling of groundwater wells, pumping tests in wells and a lot of other exiting stuff. Thank you all for your help.

Later on, Lars A. Stenvik joined our research group as a new Ph.D. candidate. Lars and I enjoyed many a discussion on groundwater and heat pump related issues. Our shearing of new ideas and, not the least, shearing of the workload on both the field work and on the article-writhing was warmly welcomed. Thank you for our close collaboration throughout the last years of my Ph.D. and I hope we can continue our collaboration in the future.

Some things in life are unforeseen and indeed quite random with respect to how I got involved with new colleagues at work. One such situation occurred when I met Associate Professor Pål-Tore S. Storli at the Department of Energy and Process Engineering. Pål-Tore happened to reply to one of my e-mails during a period of time where I was heavily immersed in field data acquisition in Melhus. I needed to test my idea of a concept regarding gas exsolution as a precipitation trigger and he turned out to be a great and willing sparring partner. We later enjoyed publishing together. Thank you Pål-Tore for your help and for taking time off your busy schedule.

Similarly, on the morning of September 9th 2016, I quite randomly happened to walk into the office of Vegard Brøtan, then a post-doctoral candidate at NTNU, asking for a person that could help med build some very small spherical particles in a 3D printer. Vegard quickly realized that I was not up to date with the limitations of 3D printing machinery at that time, but he offered to

hear my proposal for a research project. Luckily for me he liked the idea and with the help and knowledge of Olav Åsebø Berg at SINTEF AS we managed to construct some fantastic 3D samples, perfectly designed to fit with the laboratory equipment at the IGP reservoir laboratory. I am very thankful for Vegard`s and Olav's time, effort and help during the 2-year long testing period. Without your expertise on additive manufacturing the idea of constructing artificial 3D porous media would have remained an idea. I sincerely hope that we can continue our collaboration in the future.

In similar fashion I contacted Ole Tore Buset at the Department of Physics, whom I asked for help to conduct CT-imaging on these 3D samples. Ole said he could help me, but that this had to be done after working hours and in-between the other projects that he had to do. He allowed me to participate in the lab work as well, and we spent many an hour together in the computer laboratory with the image analysis software. With the additional help of Erik Larsen at the Department of Geoscience and Petroleum, we could finally perform the full image analysis of the 3D data (also done after working hours and in-between his other projects). Without your help I would never have had the luxury of such high-quality data. Thank you both for your help.

However, despite our best effort to customize the 3D printed samples to the specification of the laboratory equipment in the permeability lab, there were still encountered numerous unexpected challenges during the permeability tests. Professor Ole Torsæter then became a great sparring partner in the lab and we had many a fruitful discussion on the various topics that needed correcting, both of theoretical and of practical nature. Thankfully, the chief staff engineer in this laboratory was Roger Overå. Thank you both for all your help with customizing the equipment and providing all off those useful tips, e.g. on sealing oil leakages. Not the least, Noralf Vedvik and Steffen Wærnes Moen in the workshop also came to my aid in my times of trouble and helped with the customization of the laboratory equipment. Without their help, my lab measurements would indeed have been interesting, but probably very incorrect. I am of course thankful for your help, but most of all I am thankful for our many coffee breaks, small-talks and big-talks in-between all the work. For this I consider you my friends.

I have also been fortunate to receive aid from several senior scientists within various scientific fields in the final stages of the article writing and review processes. I hereby express my gratitude and a special thanks to Associate Professor Jørn Stene at the Department of Energy and Process Engineering (Paper IV), Professor Emeritus Stephen John Lippard at the Department of Geoscience and Petroleum (Paper V and thesis manuscript), Professor Håkon Tjelmeland at the Department of Mathematical Sciences (Paper VI) for the help you offered with pre-submission review and external review of the articles.

Finally, and most importantly, thank you Kristina Husevåg Lund for… everything. Especially for your patience and for refraining my frustration in the toughest periods of my PhD, the periods that only you were allowed to see. You make my life better in every way.

List of content

Section of original papers

Paper I:

Gjengedal, S.; Ramstad, R. K.; Hilmo, B. O.; Frengstad, B. S., (**2018**). *Video inspection of wells in open loop ground source heat pump systems in Norway.* Editor: Prof. Spitler, J. D. IGSHPA conference proceedings *2018.* International Ground Source Heat Pump Association, Oklahoma.

https://doi.org/10.22488/okstate.18.000025

Paper II:

Ramstad, R. K., Gjengedal, S., Frengstad, B. S., Hilmo, B. O.; Riise, M. H. & Holmberg, H., (**2020**). *Groundwater for Heating and Cooling in Melhus and Elverum in Norway – Highlights from the ORMEL-Project with Focus on Infiltration Wells.* Proceedings World Geothermal Congress 2020. Reykjavik. Iceland.

https://pangea.stanford.edu/ERE/db/WGC/Abstract.php?PaperID=6892

Paper III:

Gjengedal, S.; Stenvik, L. A.; Storli, P. T.; Ramstad, R. K.; Hilmo, B. O.; Frengstad, B. S., (**2019**). *Design of groundwater heat pump systems. Principles, tools and strategies for controlling gas and precipitation problems.* Energies. Vol. 12. Issue 19. pp. 3657.

https://doi.org/10.3390/en12193657

Paper IV:

Gjengedal, S.; Ramstad, R. K.; Hilmo, B. O.; Frengstad, B. S., (**2019**). *Fouling and clogging surveillance in open loop GSHP systems. A systematic procedure for fouling and clogging detection in the whole groundwater circuit*. Bulletin of Engineering Geology and the Environment. Springer Verlagen. Vol. 79. pp. 69-82.

https://doi.org/10.1007/s10064-019-01556-5

Paper V:

Gjengedal, S.; Stenvik, L. A.; Ramstad, R. K.; Ulfsnes, J. I.; Hilmo, B. O. & Frengstad, B. S., (**2020**). *Online remote-controlled and cost-effective fouling and clogging surveillance of a groundwater heat pump system.* Bulletin of Engineering Geology and the Environment. Springer Verlagen. Vol. 80. pp. 1063-1072.

https://doi.org/10.1007/s10064-020-01963-z

Paper VI:

Gjengedal, S.; Brøtan, V.; Buset, O. T.; Larsen, E.; Berg. O. Å.; Torsæter, O.; Ramstad, R. K.; Hilmo, B. O.; Frengstad, B. S., (**2020**). *Fluid flow through 3D printed particle beds. A new technique for understanding permeability and validating and improving predictability of empirical equations*. Transport in Porous Media. Netherlands. Springer Verlagen. Vol 134-1. pp. 1-40.

https://doi.org/10.1007/s11242-020-01432-x

1 Introduction

The challenge of this century is to tackle the ongoing climate changes due to man-made CO_2 emissions and pollution. We see an increased attention globally on the use of renewable energy to reduce the global greenhouse gas emissions. Buildings are estimated to expend 40% of all the energy that is utilized in EU, making buildings the largest single energy consumer in Europe (European Commission, 2021). Heating and cooling of buildings and infrastructure currently amount to an annual energy load of 72,5 TWh in Norway (Oslo Economics / Asplan Viak, 2020). To improve the energy efficiency of buildings is therefore considered an important measure in order to reach the national decarbonization goals of 50 percent reduction of CO_2 equivalent emissions by 2030 compared to the 1990 levels (Oslo Economics / Asplan Viak, 2020).

In European context the decarbonization goals for the building sector aims to replace the fossil fuel-based energy sources, e.g. from oil, gas, and coal industries. These are replaced by electricity generated from renewable and environmentally friendly energy sources e.g. from solar, wind and hydro power (Spilde, et al., 2019). However, the Norwegian energy market is different and rather unique due the highly developed hydro power industry. In 2019 the hydro-power industry produced 93,4 % of the 135 TWh annual electric energy production in Norway and covers 100 % of the national onshore electric energy demand in a normal year (Statistisk sentralbyrå, 2021). This already makes Norway's power production nearly emission free in terms of CO_2 equivalent emissions.

With regard to heating and cooling of buildings it is estimated that 48 TWh are provided by an electric power source, covering approximately 67 % of the annual 72,5 TWh heating and cooling load (Oslo Economics / Asplan Viak, 2020). Electric resistance panels, electric boilers, and heat pumps are typical heating applications. Electricity covers 80 % of the total energy load in the household sector. The goal is therefore to reduce the electric energy required for space heating, so that electric energy can be made available for the industry sector, the export industries, and for the transportations sector (Olje- og energidepartementet, 2016). It is estimated that the nationwide demand for electrical energy will increase towards 2040, predicted to be 159 TWh per year in 2040 (Spilde, et al., 2019). This growth is projected in the industry and transportation sector, while the building sector is predicted to decrease its electrical demand in the future (figure 1-1).

Shallow ground source heat pump (GSHP) systems are one of the key technologies and one of the best energy alternatives for achieving our energy goals within the building sector (Oslo Economics / Asplan Viak, 2020). Ground source heat pump systems produce thermal energy (heat) from the ground beneath the building itself. This is beneficial for space heating in buildings because GSHP applications allow buildings to acquire their thermal energy from a local energy source.

Local thermal energy production is beneficial because it reduces the demand for bought electrical energy and the heating costs for the building owner. A typical heat pump system reduces the electrical energy costs by 60–80%, or even more in the case of free cooling. Secondly, local energy production reduces the burden on the electric power grid (Stene, 1997; Banks, 2012). There is currently a strong focus in Norway to strengthen the supply capacity and supply safety of the electric power grid (Olje- og energidepartementet, 2016). This makes GSHP systems advantageous in view of a nationwide energy perspective.

Ramstad (2011) estimates that the national demand for thermal energy can be covered by GSHP technology. Compared to Sweden we see that this is a viable statement. Sweden has a more mature GSHP industry, particularly in the household sector where the development of GSHP utilization has been ongoing since the 1970's (Gehlin, et al., 2020).

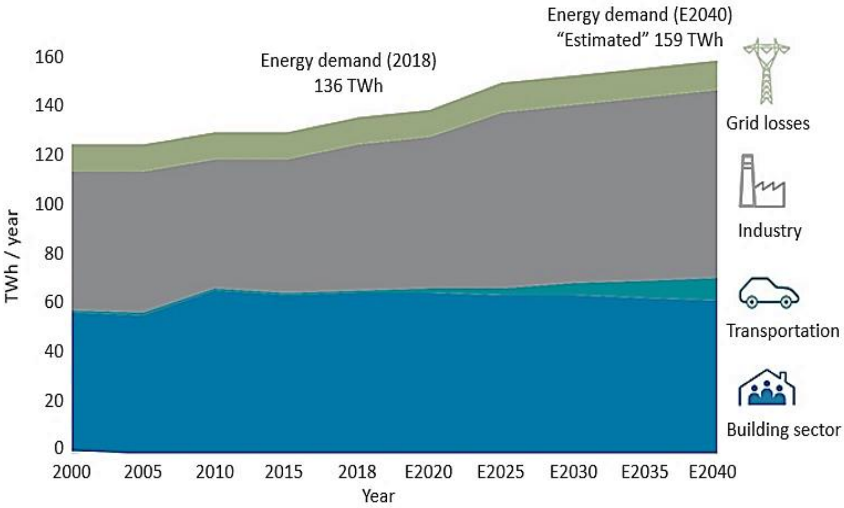

Figure 1-1 *Projected demand for electrical energy in Norway towards the year 2040 (Spilde, et al., 2019).*

Before the 1970's Sweden relied heavily on oil as the thermal energy source in buildings. Following the oil price crises in the 1970's, this reliance on oil triggered a nationwide effort to achieve an oil-independent energy system. Heat pump technology was then promoted and funded by the government through the Swedish Council for Building Research (Gehlin, et al., 2020). Today Sweden has more than 590.000 GSHP systems installed and an average of 12.000 – 14.500 new GSHP units are being installed per year (Gehlin, et al., 2020). Norway has 60.000 installed GSHP installations today (Midttømme, et al., 2020) and has historically seen annual sales of 2500 – 3450 new GSHP units (Midttømme, et al., 2020; Norsk Varmepumpeforening, 2021). The potential for further development and utilization of GSHP technology in Norway is thus apparent.

GSHP technology is competitive, both economically and technologically, for large-scale thermal applications (Midttømme, et al., 2020; Midttømme, et al., 2016). Between 2010 and 2015 the Norwegian GSHP industry experienced a market development trending towards larger GSHP installations. Similar trends are now seen in Sweden since the market for single-family buildings are becoming saturated (Gehlin, et al., 2020).

Low electricity prizes are one of the reasons why GSHP technology is less utilized in the Norwegian energy market compared to other European countries. The Norwegian sales figures of 2019 now show a decreasing trend in number of new GWHP installations, with less than 1500 new installed units (Norsk Varmepumpeforening, 2021). One factor for this trend might be the relatively low price on electricity during the recent years (Statistisk sentralbyrå, 2021). However, Midttømme et al. (2020) suggest that this trend is rather due to the recent reduction of subsidies provided by the government.

1.2 General background

A number of different solutions and technologies exists among low-temperature ground source heating and cooling applications. These various technologies are designed and developed for different geological settings and the main differences of design are primarily seen in the type of equipment installed in the ground (Banks, 2012; Stene, 1997; Rees, 2016; Laloui & Rotta Loria, 2019)

There are two main categories of system design for GSHP systems: the *direct* solution and the *in-direct* solution. The most common type in Norway is the in-direct solutions, typically labelled "*closed loop"* systems. Closed loop systems acquire thermal energy from a geological source by circulating a fluid in a closed piping system (figure 1-2). The fluid undergoes a minor temperature change and a change in thermal energy throughout the process of circulation. These pipes are typically installed vertically in boreholes that are about two to four hundred meters deep. More than 90 % of all GSHP systems in Norway are energy-well systems in crystalline bedrock (Midttømme, et al., 2016).

Another closed loop system design is where the pipes are installed horizontally in dug ditches in the ground, typically 1-2 meters below the terrain surface (figure 1-2). Horizontal closed loop systems are relatively rare in Norway but are common in other European countries, e.g. Sweden where more than 140.000 horizontal loop GSHP systems are registered (Gehlin, et al., 2020).

Figure 1-2 *Common types of ground coupled heat pump systems. (**left**) Energy wells in bedrock (in-direct closed loop system). (**middle**) Horizontal pipes in dug ditches. (**right**) Groundwater systems that pump groundwater from aquifers (direct system). Modified after Normann Etek AS (source unknown).*

The heat pump system considered in this PhD thesis is the groundwater heat pump (GWHP) system (figure 1-2). GWHP systems extract heat from *groundwater* and belong to the direct solution category, typically labeled "*open loop*" systems. The groundwater is physically extracted from the ground and pumped into the building and through a heat exchanger. The heat is thus acquired *directly* from the source by bringing the source into the building. GWHP systems must be located close to an *aquifer* and their efficiency relies on the local hydrogeological conditions within this aquifer. Some aquifers are used for seasonal storage of thermal energy and these GWHP systems are labeled aquifer thermal energy storage (ATES) systems (Abesser, 2010; Abuasbeh & Acuña, 2018; Andersson, et al., 2013).

An aquifer refers to a saturated region of the subsurface that can produce an economically feasible quantity of water to a well (Fetter, 2001). Suitable aquifers are relatively rare in Norway (Frengstad & Dagestad, 2008), and GWHP systems currently account for a small fraction of the total number of GSHP systems. Midttømme, et al. (2020) report on approximately 30 known aquifer heat pump systems at present. Sweden has more than 10.000 GWHP, ATES installations and surface water installations installed to date, most of which were installed in the 1980's (Gehlin, et al., 2020).

Today Sweden sees 5–10 new large groundwater systems (>100 kW power capacity) being installed annually and Gehlin & Andersson (2019) report that approximately 300 medium and large GWHP systems (>50 kW power capacity) and 180 medium and large ATES systems are active today, providing approximately 185 MW of thermal power capacity.

Another large GWHP and ATES nation in Europe is the Netherlands. Almost 95 % of all GSHP systems in the Netherlands are GWHP or ATES systems. Bakema (2016) estimated that there would be about 2600 GWHP and ATES installations in the Netherlands by 2018. These systems provide up to 2600 MW of thermal power capacity and produce 2 TWh each year. The number of new installations has typically seen a 10 % growth each year, where GWHP technology typically replaces gas as the predominant heat source in the domestic sector. However, Bakema (2016) foresees that the growth of new GWHP systems will be slowing down in the future, partly due the economic situation in the Netherlands and the relatively low cost of gas, but also due to new governmental legislations.

Legislation in the Netherlands requires GWHP owners to conduct an environmental risk assessment, where the influence of the GWHP activity on the local environment and on neighboring properties has to be evaluated and documented. Similar legislations are enforced in many other European countries e.g. Denmark, Germany, and England (Hähnlein, et al., 2010). Norwegian legislation does not currently enforce such requirements directly, but ongoing research activities focus on this topic. Solli`s (2020) PhD thesis has produced the first extensive legal analysis of the Norwegian legislation and The Norwegian Ministry of Petroleum and Energy (OED) now evaluates whether new legislations should be enforced. The obligation to conduct an environmental risk assessment might therefore become a requirement also in Norway in the future.

To evaluate a GWHP system is a multidisciplinary task and involves the disciplines of thermodynamics, fluid mechanics, hydrogeology, geology, water chemistry, environmental legislations, climatic concerns, heat pump technology, automation, finance, and practical engineering tasks. Each of these disciplines are individual topics of scientific importance, but they inevitably rely on each other when viewed from a GWHP design perspective.

1.3 PhD thesis background

This PhD thesis focuses on the Melhus aquifer in Trøndelag, Mid-Norway. The town of Melhus has utilized GWHP technology since 1999 which makes it a pioneer in Norwegian GWHP context. The Melhus aquifer was one of the main study sites for the research project Optimal Resource Utilization of Groundwater for Heating and Cooling in Melhus and Elverum, the ORMEL-project. This Ph.D. project was initiated as an integrated part of the ORMEL-project.

The ORMEL-project was conducted between 2015-2019 and was initiated by the Norwegian University of Science and Technology (NTNU, project leader) and Melhus municipality (project owner) to improve their management of the groundwater resource in Melhus. The ORMEL-project comprised of a working group of participants from the municipalities of Melhus and Elverum, researchers from The Geological Survey of Norway (NGU), NTNU, and the consulting company Asplan Viak AS. The project had a budget of 8 million NOK where six million NOK was funded by the Regional Research Fund Mid Norway (RFFMN grant number: 239074) and two million NOK was funded by the project partners. In addition, the Faculty of Engineering at NTNU provided the full funding for this Ph.D.

Several of the GWHP systems in Melhus faced operational problems in the years prior to the ORMEL-project (Rolf Aune, pers. comm.; Riise, 2015). These problems typically affected the parts of the systems that are in contact with circulating groundwater. Clogging tended to occur within these important components and rendered these GWHP systems unable to produce sufficient groundwater. This made these systems seem unreliable. Failure and critical malfunction of key components happened to some of these installations (Riise, 2015). During the ORMEL-project it became clear that the different GWHP owners in Melhus were satisfied with the financial benefit of their systems, but they often highlighted their concerns for these seemingly unpredictable clogging issues.

Riise (2015) highlights some possible causes to the operational problems observed prior to the ORMEL project. Clogging problems are linked to an inappropriate system design. It was concluded that a lack of knowledge of the local hydrogeological-conditions, poor as-built documentation and a lack of systems surveillance were a part of the problem (Riise, 2015). The local geological conditions were rarely considered sufficiently before construction of the systems, and hydrogeological expertise was rarely consulted.

The need for a design strategy that ensures a reliable, predictable, and sustainable form of utilization of the groundwater resource became apparent from Riise`s (2015) studies. This is also stressed as key success factors in the GWHP literature (Andersson, et al., 2013; Banks, 2012; Rees, 2016; Midttømme, et al., 2017). The work presented in this doctoral thesis is a result of the expressed needs from the industry for a better understanding of the dynamic behavior of aquifers and of groundwater heat pump systems.

1.4 Research objectives

A major goal for a GWHP system is to ensure a reliable and sustainable flow of groundwater through the system so that it can produce thermal energy for the building. The fluid mechanical properties that control the flow of water through each part of the system are central to this goal. The hydraulic performance of each individual component in the system layout will therefore have implications for the design. Four hypotheses are formulated and tested to investigate how a GWHP system functions and how clogging of key components can influence the performance of a GWHP system:

I. Clogging is triggered by the design and operation of GWHP systems.

II. Monitoring of the GWHP system performance with a hydraulic step-test surveillance procedure will improve the reliability of the GWHP systems and provides a means for early detection of clogging in distinct parts of the system.

III. Fluid flow in unconsolidated aquifers is similar to fluid flow in pipes. The Hagen-Poiseuille-relations of pipe flow therefore applies to unconsolidated aquifers.

IV. The permeability of unconsolidated sediments is directly related to the diameter of the particles that constitute the soil.

By testing these four hypotheses, conclusions can be drawn that lead to a better understanding of the design conditions and limitations of GWHP systems. This can contribute to improve the basis from which the appropriate GWHP design can be evaluated and determined.

1.5 Thesis structure.

The thesis is presented as a compilation of four journal articles and two conference papers, proceeded by a summarizing part. The articles focus on specific and individual aspects of a GWHP system. The intention of the summarizing section is to supplement the articles and present an overview of the work. The summarizing section consists of an introduction to the research field, the thesis project, and the study site. The main findings are discussed, and a design strategy is presented.

2 Theory

This chapter provides a brief overview of the state-of-the-art of the GWHP technology and Norwegian unconsolidated aquifers.

2.1 Groundwater heat pump systems – State-of-the-art

There are two main categories of GWHP systems employed in Norway and worldwide today, the *exploitation* scheme and the *re-injection* scheme (figure 2-1) (Bakema, 2001; Stene, 1997; Abesser, 2010; Banks, 2012; Abuasbeh & Acuña, 2018; Andersson, et al., 2003; García-Gil, et al., 2016). The goal of the designs is to provide the building with thermal energy by pumping groundwater from a production well through a groundwater heat exchanger. Thermal energy in the groundwater is extracted by the heat exchanger, and the water temperature is decreased in heating mode or increased in cooling mode. In figure 2-1 this is exemplified by the groundwater having a $\Delta T \approx 3K$ lower temperature after heat exchange.

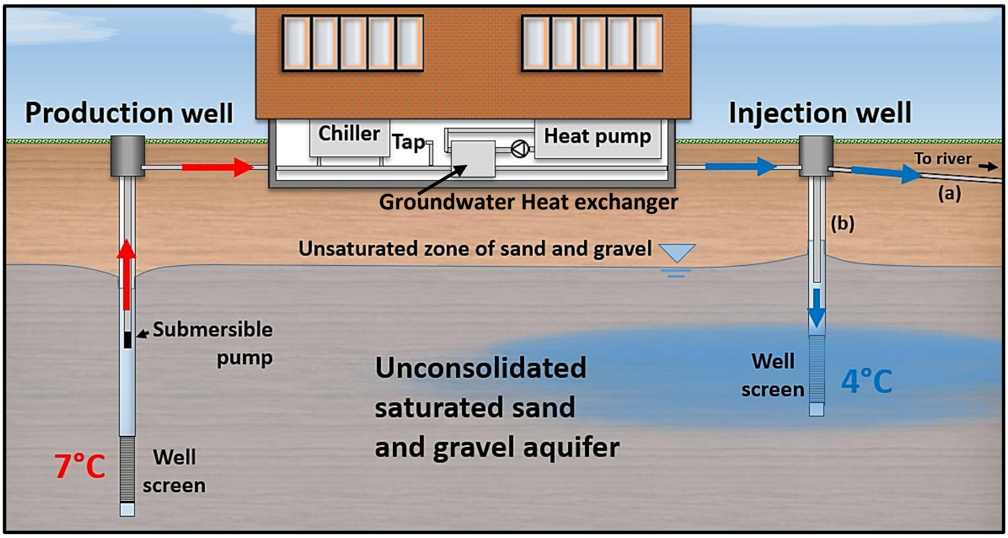

Figure 2-1 *Sketch of two typical GWHP system configurations. Groundwater is extracted from an aquifer through a production well and utilized as a heat source by a heat pump system or as a heat sink by a chiller. The water is either* (***a***) *disposed of to a nearby discharge site (river), or* (***b***) *re-injected into the aquifer.*

The two designs differ in the way they dispose of the groundwater. The exploitation scheme physically disposes of the groundwater away from the premises, e.g. by discarding the water into the local storm drain system that leads the water towards a river (figure 2-1a). This is termed an exploitation scheme because the water is permanently withdrawn from the aquifer (Abesser, 2010; Banks, 2012). This is an early type of design and is not common in Norway today because exploitation of groundwater is regulated by the water authorities. Contractors have to apply for extraction permits if the GWHP requires more than 100 m^3 of groundwater per day (§ 45 of LOV-2000-11-24-82 (Olje- og energidepartementet, 2000)). Another reason is that aquifers might not receive sufficient groundwater recharge to accommodate the pumping capacity required by the exploitation scheme. The re-injection scheme ensures that the GWHP system can maintain a reliable groundwater level throughout the whole year (figure 2-1b). Additionally, the contractors do not have to apply for extraction permits when constructing a re-injection GWHP system.

The thermal power supplied by the water is directly proportional to the quantity of water that is pumped through the groundwater heat exchanger. This is shown in the heat rate equation (2.1) which states that the thermal power from the groundwater P (kW) is proportional to the temperature alteration ΔT (K) of the groundwater. Each liter of water has a volumetric heat capacity $\rho C_P \approx 4{,}2$ kJ/l·K. This water is provided to the building at a steady rate Q (l/s) by the groundwater pump.

$$\boldsymbol{P = Q \cdot \Delta T \cdot \rho C_p} \qquad \text{Eq. 2.1}$$

Equation 2.1 is typically used to determine the pumping rate required from the groundwater wells. A single production well in an ideal unconsolidated aquifer might yield more than 20 l/s of groundwater. This enables GWHP systems to be highly cost effective because even large buildings only need one set of wells (>100 kW thermal power capacity) (as seen in figure 2-1). This differs from the more common GSHP systems with closed loop energy-wells in bedrock where >100 kW thermal power capacity will require multiple energy-wells.

Still, very large buildings might require several groundwater wells. Norway’s largest groundwater heat pump system is the Oslo Airport Gardermoen ATES system, which utilizes 9 production wells and 9 injection wells to accommodate the thermal energy demand of the airport buildings. Each of the wells provides approximately 8.3 l/s of groundwater to the heat exchangers, yielding a total of ~75.0 l/s pumping capacity (Eggen & Vangsnes, 2005).

Groundwater wells in unconsolidated soils are drilled with a steel welded casing (figure 2-2) preventing the soil particles from collapsing into the well bore. The most important aspect of the well design is linked to the well screens. The well screens are perforated sections of the well where water is allowed to enter the well bore, while still retaining the soil outside of the well. This is achieved by customizing the size of the screen slot openings with respect to the soil particle grain size distribution (Fetter, 2001; Driscoll, 1986). A common design in sorted soils is to utilize a filter pack with properly graded sand or gravel that will retain the aquifer material (Gustafson, 1983). The preferred design method in Norway is a methodology where the screen slots are customized to the *in-situ* soil conditions. This type of well is often termed *naturally developed wells* in the literature (Driscoll, 1986; Houben & Treskatis, 2007).

The hydraulic properties of the nearby sediments are then improved through well conditioning methods. This involves periodic pressure shocking and flushing methods, so called airlifting (Driscoll, 1986). Figure 2-3 shows airlifting of a well in Melhus. The well conditioning is vitally important because it removes fine particles from the vicinity of the well, while the coarser particles remain and constitute a “*natural formation filter*” in the near well region (figure 2-2). This method of design is often successful in glaciofluvial soils, because they are well graded and consist of a mixture of different soil particle sizes (Gustafson, 1983).

The methodology utilized for sizing the GWHP wells is equivalent to the conventional design of drinking water wells. The groundwater wells are typically designed to have a flow entrance velocity less than 3.0 cm/s in all parts of the screen, and this is a traditional well dimensioning approach in many countries (Driscoll, 1986; Banks, 2012; Houben & Treskatis, 2007; Fetter, 2001; Van Beek, 2010). The specific dimensions of the well screens are always specified to the soil particle grain sizes. The length of the well screen and the screen slot openings are designed so that the entrance velocity criterion is met. The injection well screen is often longer than the production well screen.

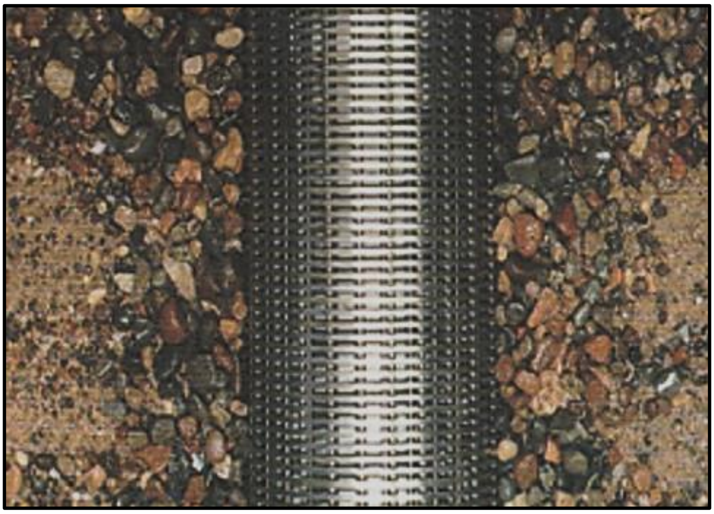

Figure 2-2 *A typical con-slot well screen utilized in Norwegian groundwater wells. The well conditioning removes the fine particles in the vicinity of the well screen and the remaining soil material function as a naturally developed filter (Driscoll, 1986).*

Figure 2-3 *Periodic airlifting, shocking and flushing, of the groundwater well is crucial for developing a proper naturally developed well filters (Photo: Randi Kalskin Ramstad).*

The diameter of the groundwater wells is determined by the size requirements of the groundwater pump (figure 2-4). The re-injection well does not have a pump and the diameter is therefore often smaller than for most production wells.

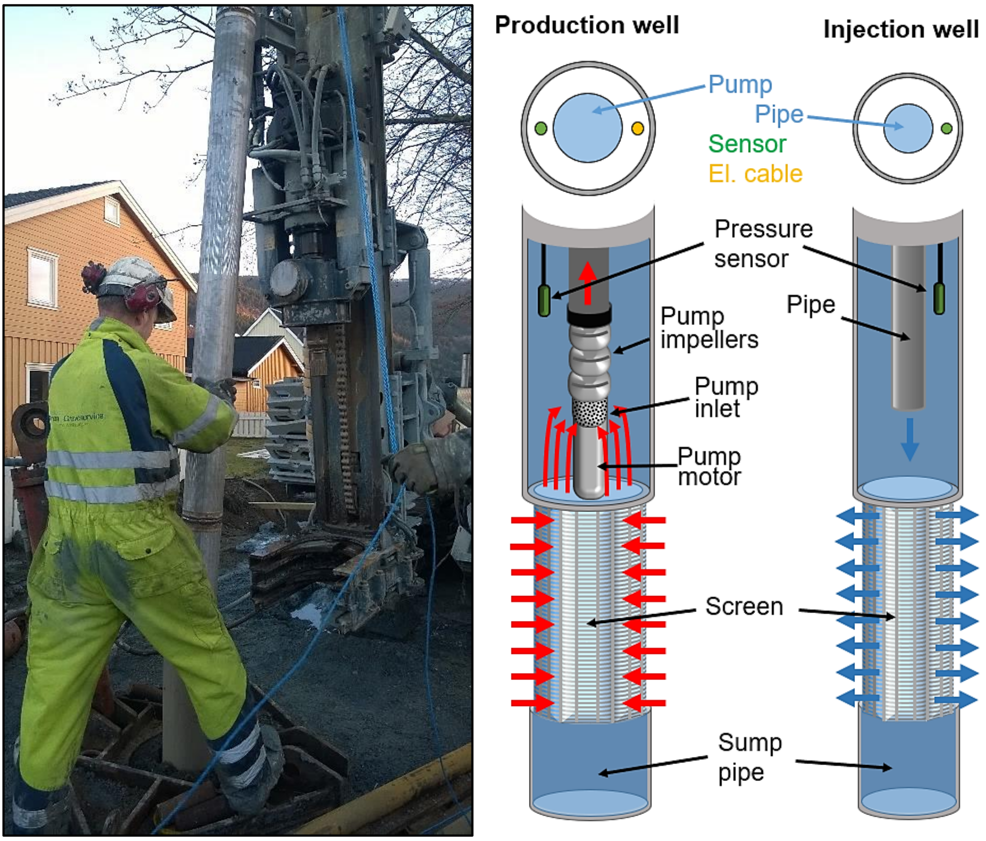

Figure 2-4 *Groundwater wells in Norway. (**left**) Installation of the well screen within the well bore. (**right)** Sketch of the typical GWHP well design with components. The length of the screened section varies depending on the required flow rate. The diameter of the well varies depending on the size of the submersible pump or injection pipe. The injection well screen is often longer than the production well screen.*

2.2 Hydraulic properties of GWHP systems

A GWHP system connects to the aquifer through five major components (figure 2-1): the production well, the submersible pump, the injection well, the groundwater heat exchanger, and the connecting piping system. The specific layout and design of these five components determine the functionality and the pumping capacity and thereby they control the thermal power capacity of the system (ref. equation 2.1).

The submersible pump converts electrical energy into mechanical energy and induces a flow of water through the piping system. The size of the submersible pump motor determines the pumping capacity of the system and the size of the pump must be selected in accordance with the hydraulic resistance of the system. Equation 2.2 states that the electric power required to run the submersible pump W_{pump} (kW) is proportional to the hydraulic resistance h (m) of the system, the rate of flow Q (l/s) and the weight of the water $\rho_w g$ (N). The efficiency of the pump η_{pump} is typically 50 % or less for most submersible pumps and demonstrates that a significant amount of the energy is converted to heat in the pumping process (Grundfos AS, 2021).

$$\boldsymbol{W_{pump}} = \frac{\boldsymbol{\rho_w \cdot g \cdot Q \cdot h}}{\boldsymbol{\eta_{pump}}} \qquad \text{Eq. 2.2}$$

The total hydraulic resistance (*h*) is a sum of the static and the dynamic heads of the entire system layout (equation 2.3). The static head h_{static} (m) is the elevation difference from the water table to the discharge site (figure 2-5). The dynamic head $h_{dynamic}$ (m) are frictional resistances and inertial resistances enforced by the motion of the water through the aquifer and the piping system. The magnitude of the resistances is unique for any GWHP system and is a function of the components utilized in the design.

$$\boldsymbol{h = h_{static\ head} + h_{dynamic\ head}} \qquad \text{Eq. 2.3}$$

As an example, we can evaluate the two simplified hydraulic systems illustrated in figure 2-5, one exploitation system (red) and one re-injection system (blue). Assume that both systems are constructed with the same type of pump and pipe components, but the length of pipeline and the distance to the discharge site are different between the two designs. In the exploitation system the groundwater is pumped to a local storm drain channel and requires only 50 meters of pipe. However, there is a 10-meter static elevation head to the manhole.

In the re-injection system, the groundwater is reinjected to the aquifer and since the water is injected below the water table the static elevation head is saved. The injection well is placed a fair distance away and the piping system is 200 meters long. The hydraulic resistance of these two designs can be estimated through the *energy equation* (described in detail in Paper III). The final form of the equation is shown in equation 2.4 to demonstrate the effect of the example design layouts in figure 2-5.

$$\boldsymbol{h = a + b \cdot Q + c \cdot Q^2} \qquad \text{Eq. 2.4}$$

The *a*-factor (m) corresponds to the static head, the *b*-factor (s) is associated with the frictional resistance that occurs in the aquifer and in the piping system. The *c*-factor ($s^2 \cdot m^{-1}$) is associated with the inertial resistances in the piping system, but some inertial resistance can originate from the aquifer if the groundwater flow velocity is relatively high (e.g. more than the 3.0 cm/s guideline) (Driscoll, 1986).

Combined with equation 2.2 this shows that the work required by the pump is subjected to hydraulic resistances of the first, the second and the third power of the pumping rate (Eq. 2.5). The *b*- and *c*-factors are directly associated with the length and diameter of the piping system and it is here that the system design can be modified to reduce the hydraulic resistance of the piping layout. The aquifer resistances are a function of the in-situ soil conditions. These soil conditions will be equal for both the exploitation system and the re-injection system design.

$$\boldsymbol{W_{pump}} = \frac{\boldsymbol{\rho_w \cdot g \cdot (a \cdot Q + b \cdot Q^2 + c \cdot Q^3)}}{\boldsymbol{\eta_{pump}}} \qquad \text{Eq. 2.5}$$

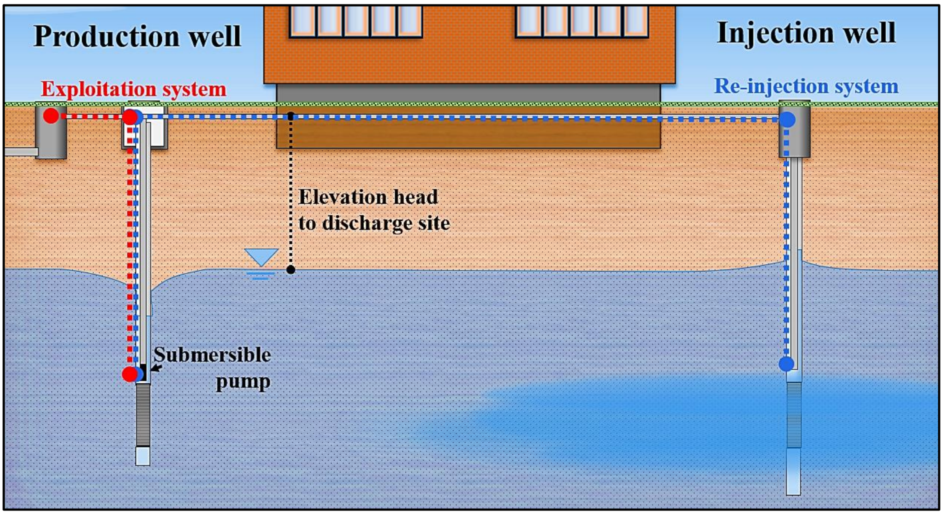

Figure 2-5 *Principle sketch of two GWHP piping systems that utilize an aquifer found 10 meters below the surface (not to scale).* ***A****) The exploitation system where water is pumped 50 meters to a manhole.* ***B****) The re-injection system where water is pumped 200 meters to an injection well.*

The main difference in the pump performance is seen in figure 2-6, where a typical set of pump performance curves for a 5.8 kW submersible pump is drawn with respect to the pumping rate. The performance of a pump depends on the motor speed (60%, 80 % and 100%). The operating point of the system is located where the performance curves (black lines) intersect the hydraulic resistance curves of the exploitation system (red dashed line) and the re-injection system (blue dashed line), respectively.

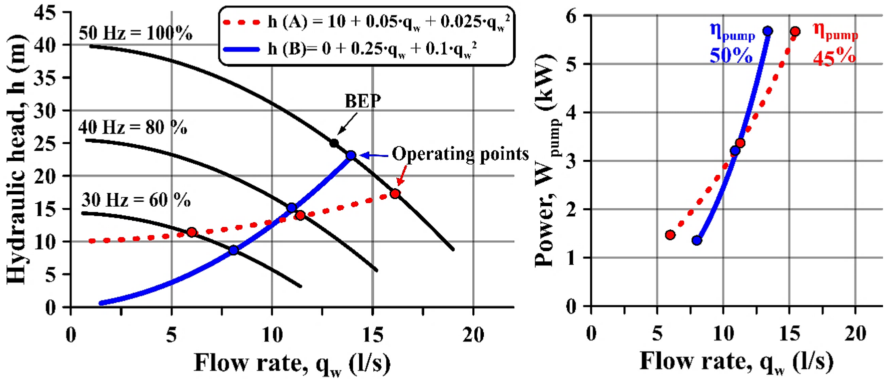

Figure 2-6 *Principle performance curves of hydraulic head, h (m), (****left****) and power requirement,* W_{pump} *(kW), (****right****) for the groundwater pump in figure 2.5. The pump operates at three different pump speeds (60%, 80% and 100%). The head is calculated from the energy equation, where the final equation is seen in the legend. The* W_{pump} *is calculated from equation 2.5 with* $\rho = 998$ *kg/m*^{3}*,* $\mu = 1.0$ *mPa·s,* $g = 9{,}81$ *m/s*^{2} *and pipe internal diameter is 3" in both cases. Constant pump efficiency is assumed for each speed and the efficiency of system B is slightly higher because it operates closer to the "best efficiency point" (BEP) of the 5.8 kW pump.*

At the 30 Hz speed this intersection occurs at Q = 6 l/s flow rate for the exploitation system and at Q = 8 l/s flow rate for re-injection system. The elevation head of the exploitation system causes the hydraulic system curve (red) to start at 10 m, while the re-injection system (blue) starts at 0 m because the reinjection pipeline is installed below the water table. This causes the re-injection system to perform better than the exploitation system at low motor speeds and enables the pump to produce higher rates of flow at the same workload W_{pump}.

However, there is a flow rate threshold (at Q > 11.0 l/s) where the long piping layout of the re-injection system requires more power for groundwater circulation than the exploitation system. This occurs because the magnitude of friction and inertial resistance in the pipes increase proportionally with the flow rate and with the length of the pipe. The friction head and inertial head within the pipes will eventually surpass the elevation head of the system when the pump operates beyond a given rate of flow. This can cause the re-injection system to perform worse than the exploitation system at higher rates of flow and the maximum capacity of the pump is lower. The exploitation system can produce 6 l/s < Q < 17 l/s, while the same pump will have a narrower range of flow rates between 8 l/s < Q < 13 l/s in the re-injection system.

This shows that the piping layout can have important implications for the hydraulic performance of the GWHP system. In this particular example, the exploitation system is more flexible due to the lower dynamic head of the system which allows the pump to produce a relatively larger range of flow rates at the same range of motor speeds 30 – 50 Hz. The piping layout will therefore determine the capability of the system to provide variable rates of groundwater flow. This is an important topic because the hydraulic performance of the system will indirectly determine the range of thermal power capacity available for the GWHP system (ref. equation 2.1).

2.3 Hydraulic properties of aquifers

The hydraulic properties of the aquifer govern how groundwater flows through the soil formation and towards a groundwater well. These properties therefore govern the aquifer's potential as a thermal heat source. The most important hydraulic properties of unconsolidated aquifers are the hydraulic conductivity K (m/s) of the soil and the porosity of the soil (n).

The hydraulic conductivity is a proportionality coefficient in Darcy`s law (2.6) and describes the ease with which water can move through the soil (D'arcy, 1856). The response of the hydraulic gradient δh (m) is linear with respect to the average superficial flow velocity u_s (m/s) of the water as it flows through a soil section of length L *(m)*. This is visualized in figure 2-7 where water flows through a cylinder filled with sand. The flow path of the fluid leads the water past the sand particles, and this will induce viscous strain that reduces the hydraulic head in the direction of the groundwater flow.

$$\boldsymbol{\delta h = \frac{1}{K} \cdot u_s \cdot L} \qquad \text{Eq. 2.6}$$

The superficial flow velocity (u_s) demonstrates that the Darcy equation considers the average behavior of the whole section of the soil filled cylinder. The movement of water is impeded by the soil particles and the flow of water has to "zigzag" around the soil particles (figure 2-7). This causes the actual flow velocities within each of the pores to be higher than the average velocity of the whole section of soil. The size and shape of the soil particles also affect the pore channel shape. It is typical for the hydraulic conductivity to have large spatial variations in natural soils and in aquifers where the soil composition often varies.

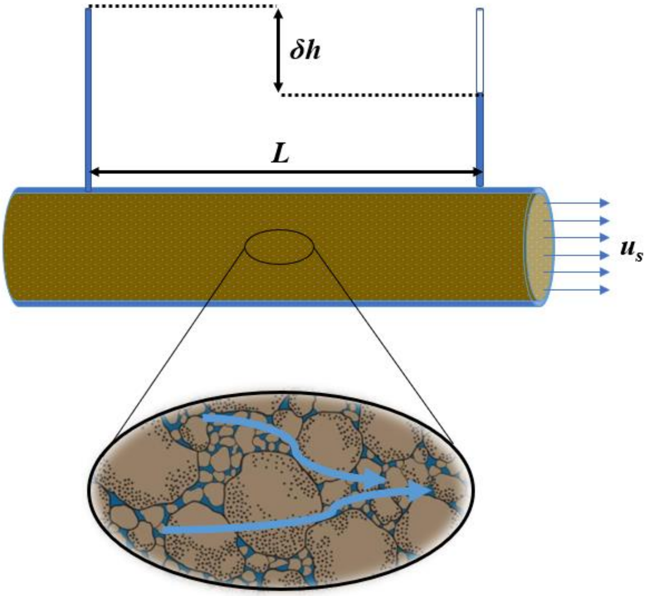

Figure 2-7 *The principle of Darcy's law. The flow of water through a soil specimen induces a reduction of the hydraulic gradient (δh) in the direction of flow. The magnitude of reduction is proportional to the velocity of the flow (u_S) and the length (L) of the specimen and inversely proportional to the hydraulic conductivity (K) of the soil, seen in equation 2.6.*

The porosity n (-) of the sediment is particularly important in GWHP applications because this represents the ratio of water per unit volume of soil. Water has a higher volumetric heat capacity ($\rho C_P \approx 4.2$ kJ/l·K at 20 °C) than rocks and minerals (e.g. $\rho C_P \approx 1.9$-2.0 kJ/ l·K at 20 °C for quartz). A high porosity is beneficial because this provides more heat per unit volume of aquifer. Relevant ranges for soil porosities and hydraulic conductivities for typical unconsolidated soils are provided in table 2-1.

Table 2-1 *Typical ranges for various hydraulic properties in unconsolidated soils (Fetter, 2001; Johnson, 1967; Domenico & Schwartz, 1990).*

Dominant sediment type	**Porosity, *n* (%)**	**Specific yield, *S* (%) (typical ranges)**	**Dominant particle diameter size, *d* (mm)**	**Hydraulic conductivity, m/s**
Clay	30 – 60	0 – 12	d < 0.002	10^{-12}-10^{-8}
Silt	35 – 50	3 – 19	0.002 – 0.063	10^{-9}-10^{-5}
Sand	25 – 51	10 – 35	0.063 – 2.0	10^{-7}-10^{-3}
Gravel	20 – 40	21 – 26	d > 2.0	10^{-4}-10^{-1}

When the in-situ properties of an aquifer are determined in the field, e.g. during pumping tests, the hydraulic properties of the whole geological unit affect the outcome of the test. The properties often vary because the size and the shape of the soil particles might be different in various parts of the aquifer. The *Transmissivity*, T (m^2/s) of the aquifer (Theis, 1935; Thiem, 1887) is therefore considered. The transmissivity is a function of the thickness of the aquifer times the average hydraulic conductivity of the soil and describes the aquifer’s over-all ability to transmit groundwater flow towards a well (equation 2.7).

$$\boldsymbol{T = K_{avg} \cdot saturated\ aquifer\ thickness} \qquad \text{Eq. 2.7}$$

Similarly, the in-situ porosity of the soil is not determined in the field. It is the storativity of the aquifer that is measured from field testing with pumping tests (Driscoll, 1986; Fetter, 2001; Johnson, 1967). The storativity *S* (-) of the aquifer is a dimensionless property that describes the aquifer’s capacity to release water from storage during pumping. The theoretical maximum amount of water that can be released from storage corresponds to the porosity of the soil. However, water molecules readily cling to the surface of soil particles during drainage, and the actual water volume available for release is less than the porosity (equation 2.8).

$$\boldsymbol{S < n} \qquad \text{Eq. 2.8}$$

Soils dominated by smaller particle grains will release less water because small grains have a relatively larger amount of surface area per unit volume. This phenomenon effectively reduces the storativity of the fine sediments, which is evident by comparing the typical porosity values and storativity values of soils in Table 2-1. Aquifers utilized for GWHP purposes are typically dominated by sand and gravel soils, where the both the hydraulic conductivity and the storativity are favorable. Table 2-1 demonstrates the potential for large variations in natural soils and it is therefore important to conduct field investigations to determine the local hydraulic properties of aquifers.

2.4 Aquifers as heat sources – In Norway

Aquifers can be categorized into unconsolidated aquifers and bedrock aquifers. Bedrock aquifer GWHP systems are rare in Norway because the greater part of the Norwegian bedrock consists of impermeable crystalline rocks. Groundwater flow occurs along fracture systems in bedrock aquifers. Fracture systems in crystalline rocks seldom produce sufficient quantities of groundwater for waterworks (Frengstad & Dagestad, 2008). There are a few examples of Norwegian GWHP systems in bedrock aquifers, e.g. the Asker Panorama installation in Asker, the Økern Portal installation in Oslo and installations in Tønsberg (NGU, 2014).

The majority of GWHP system in Norway utilize groundwater from unconsolidated aquifers. To locate such aquifers within the subsurface is an early goal for a new GWHP project. The Geological Survey of Norway (NGU) has conducted pre-investigative studies across Norway to determine the potential for GWHP technology (e.g. Hansen, et al., 2005; Hilmo, et al., 2000; Larsen, et al., 2016; Dagestad, et al., 2005; Midttømme, et al., 2000; Solberg, et al., 2014; Ramstad & Hilmo, 1999). Many of these locations now utilize the aquifers for GWHP heating and cooling applications and are listed in the NGU database (NGU, 2014). There are active GWHP systems in almost all parts of the country, i.a. Troms, Rana, Melhus (Storrø, 2000), Elverum (Elverum kommune, 2018), Luster, Kvinesdal, Seljord (Dyrud, 2008), Sande, Lier, Drammen, Gausdal, Oppdal, Voss, Alvdal and Gardermoen (Eggen & Vangsnes, 2005).

Aquifers have a potential for large spatial variations, both in regards of the in-situ hydraulic properties and in view of the size and spatial extent of the formation. It is therefore important to conduct sufficient field investigations when evaluating the potential utilization of GWHP technology in new projects. The most important hydrogeological conditions that must be quantified are visualized in figure 2-8. These hydrogeological and hydrological conditions influence an aquifer`s capacity to provide groundwater flow towards a well in a reliable and consistent manner, and will govern the design of the GWHP system (Abesser, 2010; Andersson, et al., 2003; Banks, 2012; Schomburgk, et al., 2005; Snijders & Drijver, 2016).

The depth to the water table determines the static head required by the groundwater pump. Large depths are unfavorable because the electric power required for pumping will be correspondingly large. Too shallow depths are also unfavorable because this limits the possibility to re-inject the water with sufficient over-pressure (Banks, 2012). Shallow depth is also unfavorable in Norway due to the cold ambient air temperatures during the winter, which pose a certain risk of freezing the upper soil crust. The preferred extraction depth in Norway is therefore at a depth of 15-25 meters below the surface. Local geological and climatic conditions always play a role and site-specific field investigations are always required.

One important consideration is the amount of groundwater that is available for the GWHP system. This is controlled by the thickness of the saturated deposit and the spatial extent of the aquifer. Some authors provide "rule of thumb" guidelines for this, but the size requirement of the aquifer is essentially a function of the amount of heat required by the building.

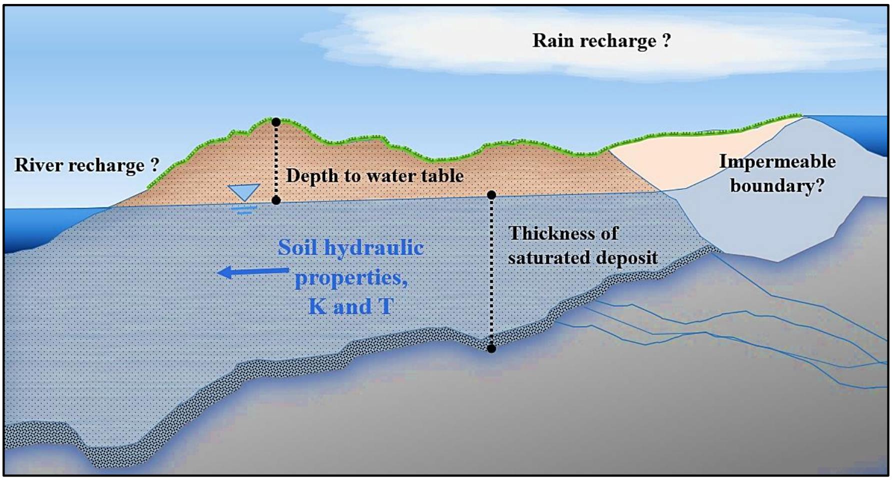

Figure 2-8 *A typical permeable soil formation that can be utilized by GWHP systems. The depth to the water table, the thickness of the deposit and the hydraulic properties of the soil govern the flow of water through the formation.*

The thickness of the saturated deposit limits the length of the production well screen and the injection well screen in the GWHP design. Together with the hydraulic conductivity of the soil K (m/s), the aquifer thickness governs the over-all flow properties of the aquifer, as shown in equation 2.7. An ideal aquifer refers to a thick gravel aquifer, which has $T > 10^{-2}$ m^2/s (Snijders & Drijver, 2016; Schomburgk, et al., 2005). Transmissivities in the range $10^{-3} < T < 10^{-2}$ m^2/s are still reasonable for GWHP systems and infer a thin gravel aquifer or a thick sand aquifer. Transmissivities of less than 10^{-3} m^2/s refer to thinner sand aquifers or soils dominated by fine sand and silt sediments, which can be challenging to utilize for GWHP purposes.

An aquifer that is hydraulicly connected to a nearby river or lake is ideal for exploitation systems. However, the contractors must apply for a permit if the production rate exceeds 100 m^3 per day (Oljeog energidepartementet, 2000). If the aquifer receives insufficient recharge, e.g. through limited local rain and snow (precipitation), the re-injection system is more appropriate. This also applies if recharge to the aquifer is hindered by impermeable boundaries. Impermeable boundaries limit or hamper groundwater flow and unconsolidated aquifers are often bound by the impermeable crystalline bedrock below the aquifer or might be surrounded by unconsolidated soils of silts and clays with low permeability.

An important limiting factor for utilization of groundwater for *heating* purposes is the freezing point of water at approximately 0°C. During heating mode, the temperature of the groundwater is reduced (figure 2-1) and the heat pump systems must avoid freezing of the groundwater to avoid damage to the piping system and disrupt the flow of water. The groundwater temperature is typically kept above 2°C after heat exchange (Jørn Stene, pers. comm.). Typical GWHP systems are designed to extract ΔT=2-4°C from the water. The natural groundwater temperature in Norwegian aquifers should therefore ideally be 4-5°C or more if utilized for heating purposes. This is similar to the guideline limits for utilization of freshwater found in lakes or rivers (Smebye, et al., 2011).

The groundwater temperature is basically governed by the local annual average surface air temperature which is progressively colder further to the north of Norway (figure 2-9). The steady groundwater temperature is typically highest along the coastal regions of Norway, and gradually decreases further inland and towards higher elevations.

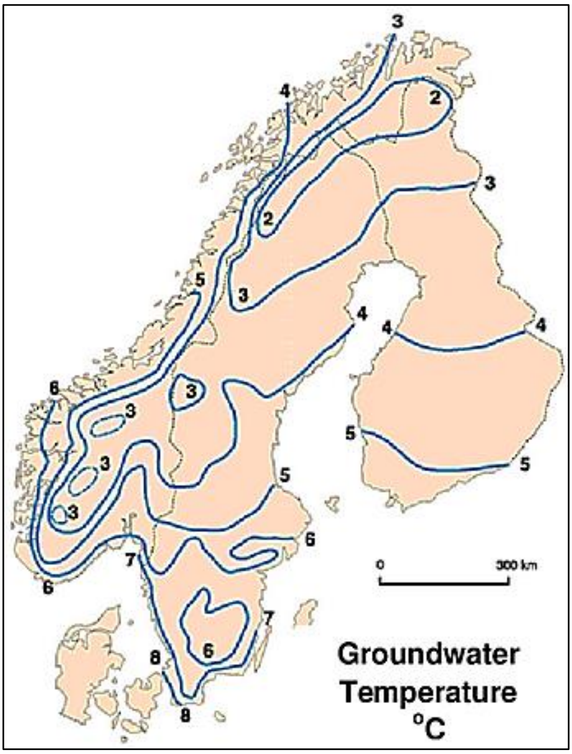

Figure 2-9 *Groundwater temperature map for Norway, Sweden, and Finland (Modified from (Stene, et al., 2008), constructed from original data found in (Kirkhusmo & Sønsterud, 1988).*

Along the northern coast of Finnmark the average annual groundwater temperature is typically 2–3°C (Sand, 1989; Hårstad, 1988). While along the southern coast of Norway the temperature is typically 7-8 °C (Kirkhusmo & Sønsterud, 1988; Blaker, et al., 2019; Gundersen, et al., 2019) In Mid-Norway the temperatures are typically 5-6 °C (Kirkhusmo & Sønsterud, 1988; L'Heureux, et al., 2019; Quinteros, et al., 2019). Local variations occur, and the Melhus aquifer in Mid-Norway has stable annual average groundwater temperatures of 6–9°C or higher depending on the depth and location of the wells in the aquifer. Groundwater located close to the terrain surface tends to display a seasonal variation in temperature, while groundwaters located deeper than 10-15 meters below the terrain often display a constant groundwater temperature all year round (Kirkhusmo & Sønsterud, 1988).

The constant groundwater temperature at > 10 meters depth is often higher than the annual average surface air temperature. The slightly higher temperature of the ground can have many local causes, e.g. due to urbanization and industry, but in northern countries this is typically a function of the amount and duration of snow cover during the winter. The snow provides additional insulation from the coldest winter temperatures and the ground temperature is often up to ~1.5°C higher than the local annual average surface air temperature (Kjellsson, 2009).

2.5 The Melhus aquifer – a brief description

The Melhus aquifer is the main study site of this PhD thesis. The town of Melhus is located in the Gauldal valley in Mid-Norway, approximately 20 km south of the city of Trondheim (figure 2-10). The town center is situated on a floodplain on the Gauldal valley floor, separated into a western and eastern part by the river Gaula. Immediately to the north of the populated area, the town scenery is dominated by Melhusryggen, an 80 to 110 meter high forested ridge that stretches halfway across the valley from the mountain of Vassfjellet to the river Gaula.

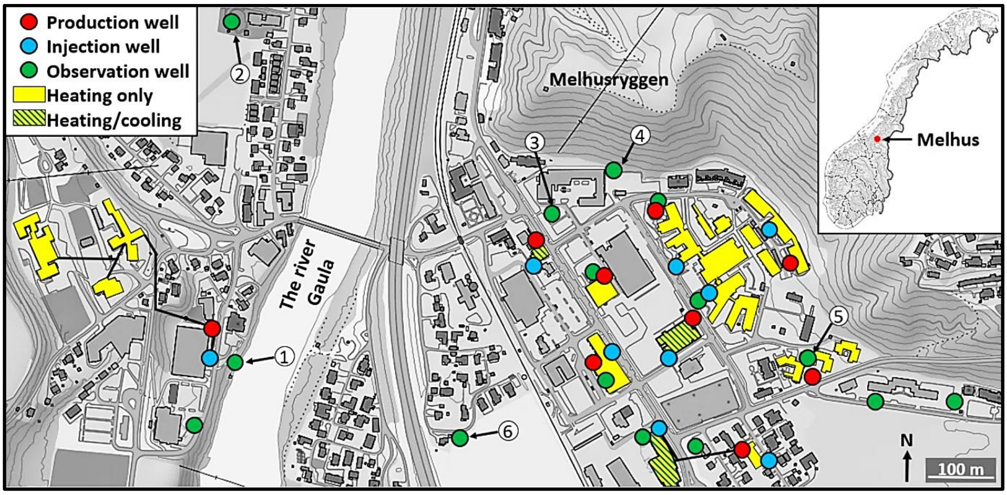

Figure 2-10 *Overview of the town center of Melhus with the ten GWHP installations (yellow buildings) and the corresponding groundwater wells indicated. The ORMEL-project has monitored several observation wells since 2015. Well numbers 1-6 are highlighted because they are mentioned in the text (original map source: www.kartverket.no).*

Melhusryggen marks the upper part of the Quaternary deposit known as the Melhus aquifer, an aquifer that in part extends beneath the town center to the south of the ridge. The river Gaula represents a hydraulic source of groundwater recharge and drainage, which divides the Melhus aquifer into a western and eastern part that fluctuate in response to the river water level.

Today this aquifer supplies ten building complexes with heat, and three of them with cooling (figure 2-10). Two are exploitation systems where the exploited groundwater is returned to the river Gaula through the local storm drain system. The rest are re-injection systems that re-inject the groundwater locally within their property. The size of the installations ranges from 50 – 600 kW installed heat production capacity, with most installations within the range of 100 – 200 kW (Riise, 2015). The GWHP systems broadly follow the design principles presented in chapter 2.1. All of the systems utilize a single production well for their operation and rely on a single re-injection well, except one which has two re-injection wells. The main difference among the ten installations is the depth and size of the groundwater wells. The aquifer soil is not uniformly distributed along the valley and this causes the well depths to vary depending on their location.

The Melhusryggen ridge is a glaciofluvial landform created in the last phase of the former ice age (figure 2-11). The origin of the aquifer is related to the glacial fluctuations in this region during the ice age in the Younger Dryas era, approximately 10 800-9 700 years BP. Multiple glacial advances and recessions during this time period resulted in several large glaciofluvial depositional landforms along the Gauldal valley, so-called sub-marine terminal moraines (Reite, 1983; Reite, 1985; Reite, et al., 1999).

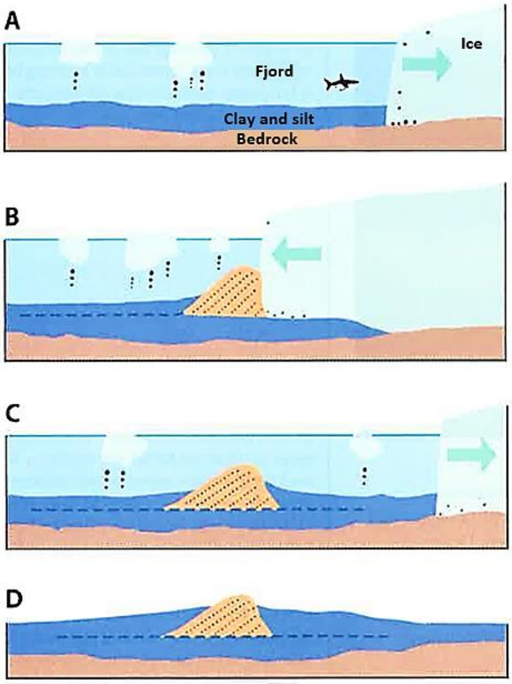

Figure 2-11 *Schematic sketch of a sequence of depositional events which might have created the Melhusryggen ridge* (Reite, et al., 1999). ***A****) A glacial retreat allows marine sediments to settle in the valley.* ***B****) The glacier readvances and halts for a period at the location of today's ridge.* ***C****) A subsequent retreat allows for more marine sediments to cover the ridge.* ***D****) The post glacial rebound has elevated the land above sea level into the present-day situation.*

Melhusryggen is a terminal moraine and consists of glaciofluvial sand and gravel covered by marine silt and clay sediments. The local marine limit is located 170 meters above the current sea level. These sediments therefore indicate that the Melhus aquifer was originally deposited below the sea water surface. The aquifer is covered by progressively more clay and silt further away from the crest, and the depth to the glaciofluvial sediments increases further southwards from the foot of the ridge (figure 2-12). The GWHP systems situated close to the ridge need only drill the groundwater wells to 20 – 30 meters depth to access the aquifer, while the GWHP systems located further away from the ridge need to drill 60 – 80 meters or more. This has inevitably led to some slight variations in well design among the various installations, mainly with regards to the well depths, diameters and installed location of the submersible pump in the wells.

The Melhus aquifer has been investigated in the ORMEL-project. Several deep wells were drilled for scientific mapping purposes in 2015–2016 (green color in figure 2-10). The deepest observation well was drilled to 94 meters depth (no. 6), without encountering bedrock. Only the wells on the western side of the river encountered bedrock. One of these wells is highlighted in figure 2-10 (no. 1) where bedrock was encountered at 27.5 m depth below the surface. The drilling log-data of well no. 1 shows a five-meter-thick layer of clay sediments covering the bedrock floor (Hellestveit, 2018). This clay layer provides an impermeable barrier beneath the sand and gravel aquifer.

Førde (2015) and Hellestveit (2018) have compiled all the available geological data and the new ORMEL-data into 3D-models of the aquifer (figure 2-12). The wells in figure 2-10 are seen in the model and indicate that the thickness of the clay deposits (blue color in the columns) gradually increases to the south of the ridge. A wide range of geophysical methods have been applied to locate the bedrock floor throughout the valley, i.a. reflection seismic (Sindre, 1980), refraction seismic (Mauring , 1992), 2D receptivity measurements (Solberg, et al., 2014), and gravimetry (Tassis, et al., 2016). The depth to bedrock is considered to be more than 200–300 meters below the terrain level in the town center area east of Gaula.

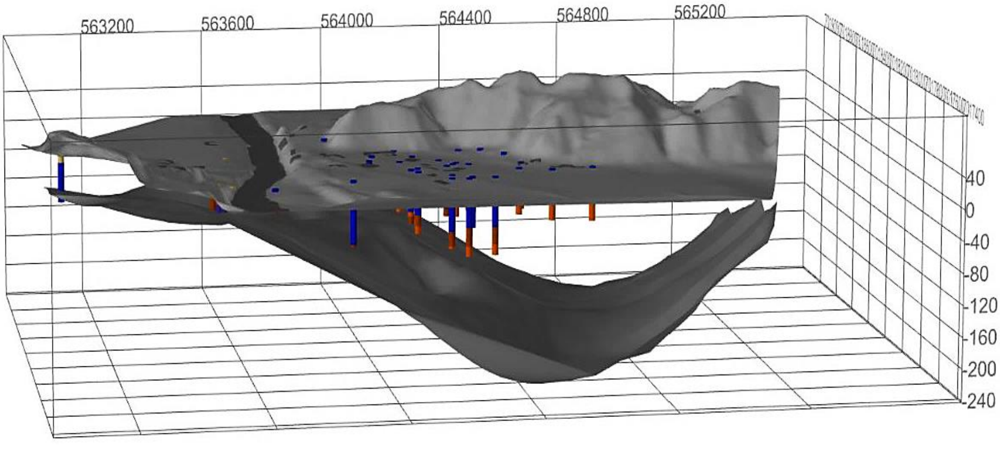

Figure 2-12 *3D-model overview of the Melhus aquifer (Hellestveit, 2018). The Z-axis elevations refer to the sea level elevation (NN2000). The terrain surface and the bedrock surface are shown as grey sheets. The groundwater wells are shown as vertical cylinders with marine sediments (blue) and glaciofluvial sediments (orange).*

Hydrogeological data from observation wells have been collected since 2015 and is presented in detail by Riise (2015), Førde (2015), Brøste (2017) and Hellestveit (2018). The river is considered to be the primary source of groundwater recharge to the aquifer. The data show that the aquifer water table is controlled by the water level in the river Gaula and varies between 1-5 meters above sea level. The water level displays seasonal variations and trends that mimic the flooding events in the river throughout the year.

Three GWHP systems extract about 35 l/s in total from the aquifer and discharge the water to the river Gaula down-stream of the town. The amount of groundwater recharge supplied from the river is sufficient to maintain the current level of exploitation and the aquifer water level does not currently show any signs of over-exploitation and permanent lowering of the water table. Relatively large local differences in water temperatures and chemical signatures are reported by Hellestveit (2018) and Brøste (2017), but no field data or field observations currently suggest that the limit for the thermal exploitation is reached.

3 Summary of articles

This section presents the motivation and background for the work leading to the scientific articles. Some additional information that was not included in the original papers is also provided. Figure 3.1 shows the overall topic of focus in the articles and gives an overview of the hypotheses that are addressed.

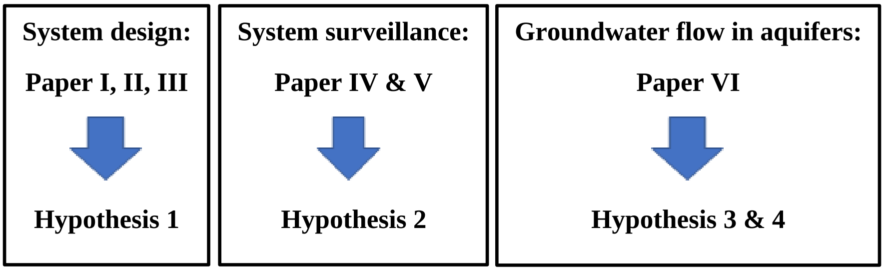

Figure 3-1 *Structure of the doctoral thesis articles.*

The articles are attached after the synthesis section and the proper introduction to the topics, the data analysis, and the scientific methods are provided in the articles.

3.1 Papers I & II:

Paper I: Gjengedal, S., Ramstad, R. K., Hilmo, B. O. & Frengstad, B. S., **2018**. *Video inspection of wells in open loop ground source heat pump systems in Norway.* Editor: Prof. Jeffrey D. Spitler. International Ground Source Heat Pump Association, Oklahoma. In *IGSHPA conference proceedings 2018*.

Paper II: Ramstad, R. K., Gjengedal, S., Frengstad, B. S., Hilmo, B. O.; Riise, M. H. & Holmberg, H., **2020**. *Groundwater for Heating and Cooling in Melhus and Elverum in Norway – Highlights from the ORMEL-Project with Focus on Infiltration Wells.* Proceedings World Geothermal Congress 2020. Reykjavik. Iceland.

Background

Inspection of the GWHP systems in Melhus revealed that the systems were poorly outfitted with sensory equipment. This made it difficult to evaluate or predict whether the systems required maintenance. Routine maintenance was rarely performed, and several critical clogging faults were often detected at late stages in their development when critical malfunctions became apparent.

The ORMEL project therefore conducted systematic video inspections of the GWHP wells in Melhus (figure 3-2). Most wells were usually found to be affected by some type of clogging, particularly the re-injection wells. A variety of different cleaning methods were tested on these wells, e.g. a high-pressure jet, airlifting methods, and sequential pumping methods. The Lena Terrace GWHP is presented as a case study in Paper II that exemplifies the complexity of the clogging problems and the effects of the different cleaning techniques.

Results

Video inspection is a very useful tool for inspection of wells and pipes. The cause and severity of clogging problems can be assessed, and detailed images allow experienced observers to distinguish between different clogging types based on the clogging texture, color, and growth in the well. Clogging due to sediment particles, precipitation compounds or bacterial slimes were found in the different wells in Melhus and Elverum.

Video inspections were useful to evaluate the effectiveness of cleaning methods. The cleaning technique that combines the use of water steaming and sectional screen pumping was the best cleaning method for removal of iron incrustations and sediments from groundwater wells in Melhus. The rehabilitation of the Lena Terrace GWHP system shows that the development of clogging can vary with time. Routine surveillance is therefore proven essential for avoiding critical malfunctions, especially because the removal of material from the well screen and sump pipe can be challenging if the cleaning is performed at a late stage in the clogging development. The ORMEL-project concluded that video inspections should be a standardized documentation and surveillance method for GWHP systems.

Figure 3-2 *Video inspection of wells. (**Left**) The Supervision*^{TM} *SVR 140/SVC100 pan and tilt video camera (Gjøvaag AS). (**Middle**) The camera is remotely controlled from the inspection vehicle (Gjøvaag AS). (**Right**) In this Melhus installation the pipe is 24 meters long and a large crane and several people had to help in order to lift it out of the well bore (Picture by Mari Helen Riise).*

The main drawbacks with the video inspection of wells involve the cost of preparing the wells for assessment. The conventional well design is compact and does not have enough space for a camera in the well. This requires the pipe and groundwater pump to be lifted out of the well before inspection (figure 3-2). The GWHP system is shut-off during the inspection.

It can be challenging and costly to dismantle deep wells in an urban environment, e.g. damage to the cars parked in a nearby parking lot must be avoided (figure 3-2). An alternative groundwater well design that enables video inspection with ease during operation is suggested. The new design is essentially a well bore with a slightly larger diameter than is required by the pump alone. This will allow for a camera and cleaning equipment to fit along the pipe (figure 3-3).

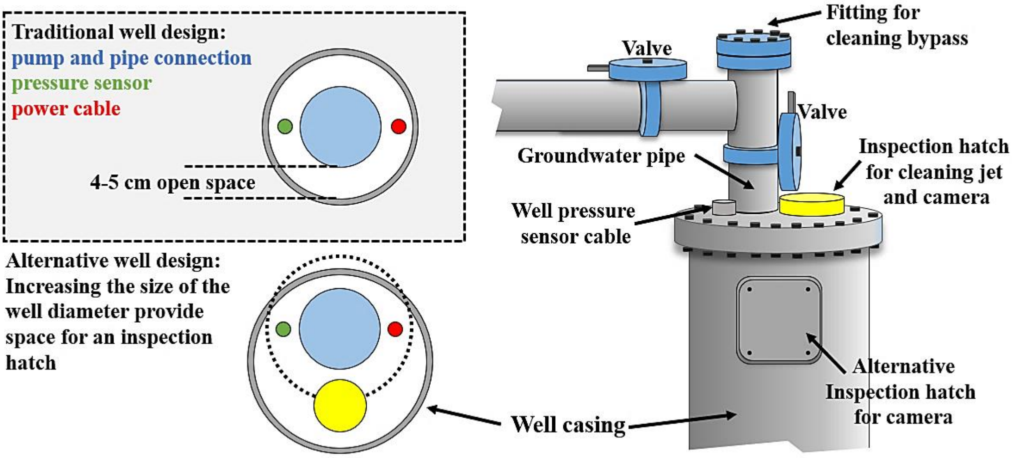

Figure 3-3 *Principle sketch of the suggested GWHP well design. Increasing the diameter of the well provides space for an inspection hatch. An alternative hatch on the casing is possible.*

3.2 Paper III:

Gjengedal, S., Stenvik, L. A., Storli, P. T., Ramstad, R. K., Hilmo, B. O. & Frengstad, B. S., **2019**. *Design of groundwater heat pump systems. Principles, tools, and strategies for controlling gas and precipitation problems*. *Energies*.12. 3657.

Background

Clogging problems in GWHP systems are typically linked to precipitation reactions that produce various iron compounds. Redox reactions are an important mechanism that produce these compounds and may occur if the groundwater is mixed with oxygen from the air, or by mixing of water bodies with different chemical qualities and redox potentials.

Clogging problems in Melhus have therefore been viewed as an issue that is caused by oxygenation of the groundwater. Investigations in Melhus revealed that the re-injection systems had vacuum pressures in the pipeline-loop. This was identified as a potential problem because some of the piping-systems were not air-tight. Air entered the piping-systems and mixed with the water before re-entry to the aquifer. This allowed air to oxygenate the water and facilitate precipitation reactions.

Other GWHP systems had no observable leakages of air into the system, but they still had problems with iron precipitation, even with low dissolved oxygen levels. A question arose whether other parts of the design could cause alteration to the groundwater chemistry and trigger precipitation reactions. Gas bubbles were later observed in the groundwater during water sampling in some installations and observation wells (Brøste, 2017). The odor of the water (e.g. rotten eggs) indicated the presence of non-atmospheric gases in the water. The ability of the GWHP systems to prevent gas exsolution and alterations to the groundwater chemistry was therefore questioned.

A new hypothesis was developed: that vacuum pressures could trigger precipitation reactions in water when e.g. carbon dioxide (CO_2) was allowed to de-gas temporarily in a pipeline (figure 3-4). The time needed for the water quality to recover could possibly allow precipitation reactions to occur within a limited timeframe of chemical imbalance, even though the pressure should be restored at a later stage in the GWHP system.

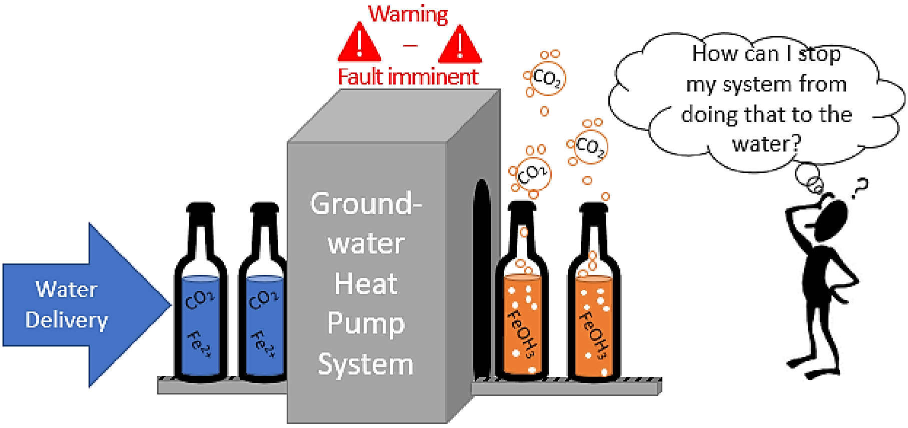

Figure 3-4 *The graphical abstract of Paper III is presented in the on-line version of the paper (https://doi.org/10.3390/en12193657)*

Results

The paper demonstrates a hydraulic grade line analysis that shows how pressure and temperature change in the groundwater as it travels along the piping system of a fictional GWHP system. Pressure and temperature variations influence the solubility of gases in the water and the gas will form a separate phase as bubbles if the saturation limit is breached. This is visualized for the solubility of CO_2 with a solubility grade line (SGL). The analysis show that the saturation limit can be breached at specific locations in the system design. This typically occurs due to vacuum pressures in the reinjection pipeline.

It is shown that key components have an influence on the pressure of the system, dependent on their specific location in the design layout. To avoid gas exsolution within the system one must select the proper location for the submersible pump, the groundwater heat exchanger, and the injection pipeline within the injection well. Vacuum pressures can only be entirely avoided if the induced suction pressure in the injection well pipe is kept above the atmospheric pressure. This will typically require some type of flow controlling devise to be installed in the injection well, for example a backpressure valve or turbine installed at the reinjection pipeline exit.

3.3 Papers IV & V:

Paper IV: Gjengedal, S., Ramstad, R. K., Hilmo, B. O. & Frengstad, B. S., **2019**. *Fouling and clogging surveillance in open loop GSHP systems. A systematic procedure for fouling and clogging detection in the whole groundwater circuit*. Bulletin of Engineering Geology and the Environment. Springer Berlin Heidelberg.

Paper V: Gjengedal, S.; Stenvik, L. A.; Ramstad, R. K.; Ulfsnes, J. I.; Hilmo, B. O. & Frengstad, B. S., **2020**. *Online remote-controlled and cost-effective fouling and clogging surveillance of a groundwater heat pump system.* Bulletin of Engineering Geology and the Environment. Springer Verlagen.

Background

Operational data were important for the ORMEL-project as a means of evaluating the influence of GWHP activity on the aquifer. However, none of the GWHP systems had installed sufficient sensory equipment to monitor this in their system. Current Norwegian legislations do not require GWHP systems to monitor their system nor to document their impact on the local environment.

The clogging issues shown in Papers I, II and III demonstrate that GWHP systems require tools that can evaluate and predict the need for maintenance. This motivated for the development of a surveillance procedure that enable measurements of operational data to serve a practical surveillance function. This is beneficial because operational data also can be used to document the potential impact of the GWHP system on the local environment.

Results

The effects of clogging and fouling on the system performance are exemplified and the theoretical foundation for a surveillance procedure based on performance data is presented. The performance of GWHP systems can be monitored with four temperature sensors and two pressure sensors when a step-test performance test is conducted.

The Lena Terrace tests were applied routinely over a period of seven weeks to assess the performance of the GWHP system through the autumn of 2019. The performance data revealed that clogging problems could be detected in the production well, injection well, and within the groundwater heat exchanger. Maintenance of the groundwater heat exchanger was then performed before the problem became too severe. The effect of this cleaning was measured by a step-test afterwards. The two articles demonstrate that the step-test surveillance procedure can be conducted within a 1-hour test period without shutting off the heat pump. The step-test procedure is thus proven to be a cost-effective and accurate monitoring method for GWHP systems.

3.4 Paper VI:

Gjengedal, S.; Brøtan, V.; Buset, O. T.; Larsen, E.; Berg. O. Å.; Torsæter, O.; Ramstad, R. K.; Hilmo, B. O.; Frengstad, B. S., **2020**. *Fluid flow through 3D printed particle beds. A new technique for understanding permeability and validating and improving predictability of empirical equations*. Transport in Porous Media. Vol 134-1. pp. 1-40. Netherlands. Springer Verlagen.

Background

It is important to evaluate the hydraulic properties of an aquifer when conducting site investigations for GWHP systems. The best method for determining the hydraulic properties is through pumping tests, but this is time consuming and costly. It is therefore common to perform simple empirical correlations at an early stage in new GWHP projects.

A frequently applied method in Norway is the grain size correlation method. This empirical approach estimates the hydraulic conductivity K (m/s) of a soil sample from a grain size distribution analysis. This analysis gives a sieving curve (figure 3-5) which shows the weight percentage of the different intervals of soil particle diameters in the sample. Numerous soil scientists have correlated these diameter sizes to hydraulic conductivity measurements and these empirical correlations are often used for prediction purposes (Chapuis, 2012).

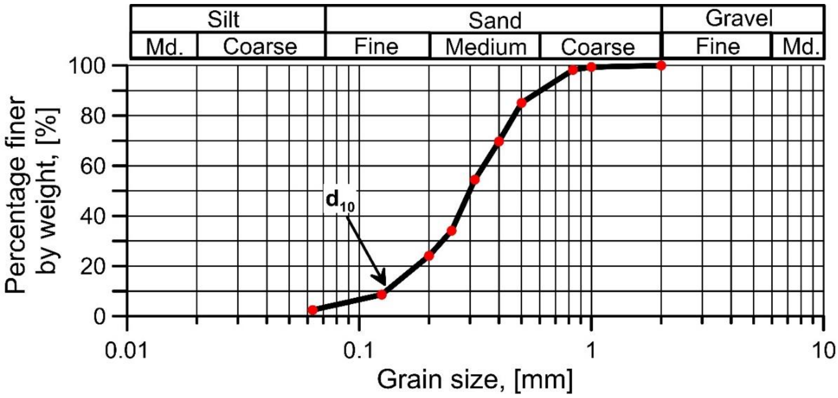

Figure 3-5 *The size of the particles that intersect the 10% weight line of the grain size distribution curve represents the characteristic length dimension of the sediment in the empirical Hazen method. Data from (Tømmerdal, 2017).*

A common empirical correlation is the Hazen-equation (3.1) (described in Fetter, 2001), where the d_{10} particle diameter size (cm) from the sieving curves is selected to represent the characteristic length dimension of the sediment (figure 3-5). The geometry coefficient C (-) is a function of the sorting and packing arrangement of the sediments.

$$\boldsymbol{K = C \cdot d_{10}{}^2} \qquad \text{Eq. 3.1}$$

In the preliminary phase of the PhD work, equation 3.1 was rigorously tested through conventional permeability tests with the permeability apparatus at the IGP laboratory. Soil samples were collected from the drilling spoils from the ORMEL-wells in Melhus and Elverum. Haugen (2016) and Tømmerdal (2017) conducted a total of 21 and 12 tests on these soil samples, respectively.

Haugen (2016) and Tømmerdal (2017) concluded that the Hazen-equation and many other empirical equations give poor and inaccurate correlations. Tømmerdal (2017) also concluded that the Kozney–Carman equation was the best alternative among all of the empirical correlations, in good agreement with the recommendations of Chapuis (2012). This motivated for the work presented in Paper VI.

Results

Paper VI approached this topic through constructing artificial samples of porous media with 3D printing. The development and fabrication of the 3D geometries was a challenge. The sample design had to fit with numerous other laboratory equipment, while still preserving the integrity and the geometrical properties intended with the design. Most of the laboratory equipment and the testing procedures had to be customized to produce reliable measurements. A 2-year long trial period of testing with different additive manufacturing (AM) techniques, materials and building strategies finally gave acceptable results (figure 3-6), owing to the expertise of Dr. Vegard Brøtan and Olav Å. Berg at SINTEF Manufacturing AS.

Figure 3-6 *Additive manufacturing facilities at the NTNU AM laboratory in Trondheim and at SINTEF Manufacturing AS. (**Left**) Cleaning of the samples after fabrication. Health and safety measures are important because the microscopic Marlok C1650 powder particles are very fine. (**Top Right**) Vegard Brøtan is preparing the Concept Laser M2 PBF-LB machine with the four CAD models. The building chamber is within the grey machine to the right. (**Bottom right**) A failed test specimen of Samples A-D shows the first 1 cm of fabrication. The machine can fabricate all 24 samples simultaneously. This required one full week of continuous fabrication.*

Another 6 months of testing was needed in the permeability laboratory at the Department of Geoscience and Petroleum at NTNU. Numerous permeability tests were performed with oil, water, and air. Different problems were encountered with each fluid type. One problem with the air-permeability equipment was the inaccurate pressure recordings due to the high permeability of the samples. The main problem with the distilled water tests was the corrosion of the samples. The water permeability would typically change during the test and could not be reproduced. Oil was therefore the best fluid for these tests.

The tests also showed that adjustments had to be made to the standard Hassler flow cell configuration (figure 3-7). Two enlarged feeding nodes were needed to reduce the parasitic hydraulic losses through the cell. Highly accurate pressure sensors and recording equipment were essential to produce reliable measurements. The combination of one 260D Teledyne ISCO pump and two VP-12K Vindum Pumps were used to obtain the pressure response from the Darcy flow regime and the Forchheimer flow regime for all four sample types. Finally, a predefined testing procedure was developed to ensure proper propagation of the test and to reduce uncertainties in the least square regressions of the data.

The major findings and results presented in Paper VI concluded with a new semi-analytical equation based on the Navier–Stokes equation of fluid mechanics. This analogy represents a new equational form that describes the Darcy-equation in a new way.

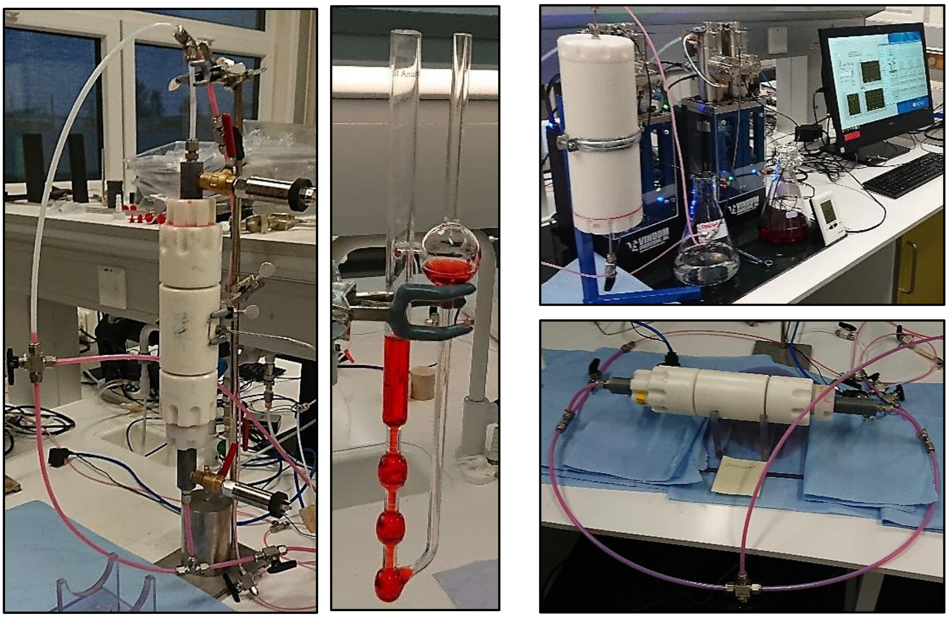

Figure 3-7 *Permeability laboratory and facilities at the Department of Geoscience and Petroleum at NTNU. (**Left**) The Hassler flow cell during sample saturation. Air is evacuated from the cell through the top fitting. (**Middle**) The SI Analytics Capillary Viscometer D50 with the EXXSOL D60 oil. **(Top right)** The two VP-12K Vindum Pumps and fluid reservoirs. The control panels were integrated in the computer (**Bottom right**) The horizontally oriented Hassler flow cell during test start-up.*

4 Discussion

In this section the results of the doctoral thesis work are discussed with respect to the underlying hypotheses. It is recommended that the papers are read beforehand.

4.1 Hypothesis I

Clogging is triggered by the design and operational strategy of GWHP systems.

Clogging is a phenomenon where a blockage disrupts the fluid flow. There are several types of clogging that affect GWHP systems and groundwater wells (e.g. (Driscoll, 1986; Fetter, 2001; Van Beek, 2010; Bakema, 2001; Banks, 2012; Snijders & Drijver, 2016; García-Gil, et al., 2016; Andersson, 1999; Houben & Treskatis, 2007; Houben, 2006) (Houben & Weihe, 2010). The most common problems are:

- Sediment particles – Suffusion mechanisms
- Gas – pressure/temperature/solubility mechanisms
- Chemical clogging - precipitation mechanisms or corrosion mechanisms
- Biofouling – bacterial slimes.

It is common to distinguish between mechanical clogging and chemical clogging depending on the origin of the clogging material. Mechanical clogging is typically associated with suffusion of soil particles through the well screen during pumping or entrainment of gas in pores. Chemical clogging is associated with precipitation reactions in the water. These reactions might be catalyzed by biological processes.

The subject of clogging is intricate, and several clogging mechanisms are often at work simultaneously in the GWHP systems. In Melhus it was typically found that chemical clogging affected the groundwater heat exchanger, while suffusion mechanisms clogged the re-injection well, or a combination of both occurred in the entire system. Mechanical clogging by soil particles typically develops due to an incorrect production well design (Rafferty, 2001). Inappropriate production well performance in terms of sand and silt content inevitably means that this material will be deposited in the injection well. Injection systems require particle free groundwater circulation and special care must be devoted to the well design when designing a re-injection GWHP system. Alternatively, some systems should employ a surface removal system for extra precaution (Rafferty, 2001).

The literature states that the pumping rate has a governing role for most problems found to occur in groundwater wells, both in terms of chemically and mechanically induced problems (Driscoll, 1986; Fetter, 2001; Houben & Treskatis, 2007; Van Beek, 2010; Roscoe Moss Company, 1990; Vikovic & Soro, 1992; Bieske, et al., 1998). Reduction of the pumping rates from a given well will directly reduce the problems and the risks associated with:

- Dynamic head losses
- Suffusion of fine particles from the aquifer into the well and piping system
- Exsolution of dissolved gases
- Mixing of incompatible waters (precipitation reactions)
- Corrosion of system components, e.g. valves, pumps, and pipes.
- Alteration of the natural groundwater flow regime and water level

Minimized pumping rates should therefore be emphasized in the design (Rafferty, 2001). This entails that a relatively large portion of the heat production in GWHP systems should be provided through extended temperature alterations (ΔT) rather than high pumping rates (Q).

The chemical clogging problems are often complex. The chemical equilibrium of aqueous solutions relies on a variety of chemical, thermodynamical, and mechanical properties. The most important properties are listed below (Stumm & Morgan, 1996).

- pH of the groundwater
- Eh of the groundwater and available oxidants in solution
- In-situ temperature and pressure of the groundwater
- Types and amounts of dissolved gases and the corresponding gas/water equilibrium
- Types of dissolved ions and their speciation determine the possibility for:
    - Precipitation reactions (i.a. Iron, Manganese, Carbonates)
    - Corrosion (i.a. Sulphates, Nitrates, Chlorine)

The ideal intention behind the GWHP design is to avoid alterations of the chemical equilibrium of the groundwater. This implies that all of the above-mentioned properties must remain unchanged throughout the entire GWHP operation. This is not possible because the temperature and the pressure conditions of the groundwater are always altered by a GWHP system. The main concern for GWHP designers should therefore be to minimize the risks and consequences of chemical alterations. This requires the designer to know how the system design can influence the chemical equilibrium of the groundwater.

A major challenge for GWHP systems, compared to e.g. domestic water wells, is the re-injection design where the water is returned to the aquifer in a different location. This location in the aquifer might have different chemical compositions than the extraction site, which by itself can facilitate an imbalance in the groundwater mixture. Alteration of the groundwater temperature and pressure before re-injection can also facilitate other side-effects, e.g. lower the gas solubility in the water and trigger pH alterations. It is therefore clear that a GWHP system in itself has the potential to alter the chemical equilibrium of the groundwater in numerous ways.

Some design rules are described in the literature for avoiding chemical precipitation issues. The most important rule is to prevent mixing of groundwater with air. Mixing will enable oxygenation of the water, and CO_2 can exsolve from the water. Both situations will subsequently trigger precipitation reactions (Bakema, 2001; Banks, 2012; García-Gil, et al., 2016; Rafferty, 2001). Mixing dissimilar groundwater qualities should be avoided for the same reason. In practice this means that the designer must install the wells in the appropriate geological stratum and control the stresses enforced on the aquifer during pumping.

In Paper III the influence of the GWHP design is investigated on two other types of mixing, namely pressure mixing and temperature mixing. Clogging due to gas bubbles and chemical precipitation can occur due to pressure or temperature alterations (Bakema, 2001; Sniegocki & Reed, 1963). It is often stated that the changes in pressure and temperature must be large for this to affect the chemical equilibrium directly (Garcia-Gil et al., 2016), but this is not the case if the pressure change can facilitate pH alterations (e.g. exsolution of CO_2). Even small pH alterations can trigger precipitation reactions in aqueous solutions if the water is saturated with dissolved ions and result in e.g. calcium carbonate scaling or ferric iron precipitation (Stumm & Morgan, 1996).

The occurrence of vacuum pressures can potentially trigger gas exsolution. Whether gas exsolution is a primary cause for precipitation clogging in Melhus is not clear and further studies on this topic are necessary. The presented studies show that vacuum pressures should be avoided in GWHP systems.

One important reason for this is that vacuum pressures allow air to enter into the piping system if the pipes are not fully airtight. This can trigger oxygenation of the water and should be avoided.

The theoretical calculations in Paper III show that a back-pressure device should be installed at the injection well pipe exit to fully avoid vacuum pressures in the piping system. This device should ideally be a turbine because this will recover some of the energy used by the submersible pump. There are no known GWHP systems that employ turbines for pressure control. Other back-pressure devices are applicable, but it is not clear how they will function in practice. Further studies on this topic are necessary and a systematic testing scheme should be employed to investigate how the backpressure can be maintained in GWHP systems without causing harm to the other components.

Experience shows that it is difficult to avoid clogging problems altogether. Regular maintenance of GWHP systems must therefore be scheduled. The pipeline and the wells should have easy access for the most common cleaning methods. Typical on-site cleaning methods employed in Norway today are:

- **Cleaning of the pipeline**:
    - High pressure jets and flushing techniques similar to the methods employed for cleaning of sewer systems.
- **Cleaning of the groundwater heat exchanger**:
    - Acid treatment methods are used if the clogging consists of chemical incrustations.
    - Back-flushing is sometimes sufficient if the clogging consists of particles and sediments.
    - Dismantling before cleaning is often needed in severe clogging and fouling cases.
- **Cleaning of the wells:**
    - Reversed flushing and airlifting are common techniques for removal of soil particles.
    - Steaming methods if the clogging consists of chemical incrustations.
    - Acid treatment methods can be used but are rarely used in wells.
    - Disinfectants (chlorine) are used in wells affected by bacterial slimes.

Easy access for these methods should be quite straightforward by incorporating fittings and fixtures along the pipeworks. However, this is not easy for groundwater wells in Norway today because the wells are not constructed with this in mind. The most common airlifting and reversed flushing methods will typically require dismantling of these wells before cleaning. This increases the total costs of the maintenance operation and necessitate that the GWHP is shut-off during the cleaning process.

It is recommended to have larger diameter wells that enable cleaning equipment and inspection equipment to be employed without having to dismantle the well. A temporary surface disposal system might also come in handy as a means of diverting the water flow in the event that the injection well must be removed from service. This will allow continued operation of the system during routine maintenance.

In summary, the presented work demonstrates that the design and operation of GWHP systems can trigger clogging. Many design solutions can be applied to limit the consequence of clogging and this must therefore be given high priority when designing GWHP systems.

4.2 Hypothesis II

Monitoring of the GWHP system performance with a step-test surveillance procedure will improve the reliability of the GWHP systems and provides a means for early detection of clogging in distinct parts of the system.

It is recognized that GWHP systems must be associated with a certain degree of operational risk. GWHP systems are prone to clogging and the survey of Bakema (2001) concludes that clogging problems were encountered in at least 25–30% of new ATES systems in Europe during the 1980-1990s. Andersson et al. (2003) report of similar problems in 40% of ATES systems in Sweden. The Gardermoen ATES system in Norway has similar problems (Eggen and Vangsnes, 2005) and the ORMEL-project found that clogging problems affect all of the GWHP systems in Melhus.

Clogging and fouling should be treated at an early stage in their development. The incrustation of sediments and precipitates becomes harder to clean with time and this reduces the effusiveness of cleaning (Andersson, 1999; Bakema, 2001; Houben & Treskatis, 2007; Mansuy, 1998; Kerner, 2011). Groundwater wells will deteriorate more rapidly if the wells have been severely clogged in advance, because the clogging material might have been able to penetrate deep into the aquifer and cannot be sufficiently removed (Van Beek, 2010; Houben & Treskatis, 2007). Similarly, if the groundwater heat exchanger is severely clogged, cleaning methods are ineffective because the clogging deposits in-between the heat exchanger plates cannot be accessed by cleaning fluids.

The risks of clogging should be dealt with in the GWHP design and implanted in the operational strategy of the system. A typical strategy can be seen in the Gardermoen ATES system where they schedule for regular cleaning of the groundwater heat exchanger every other year and the wells at a few years' intervals. The annual maintenance costs amount to approximately 2% of the initial investment costs (Eggen and Vangsnes, 2005). This level of maintenance is typical for many large-scale heat pump applications (Stene, 2001).

Similar maintenance strategies should be adopted by the Melhus systems. However, the challenge for the Melhus GWHP systems is that these GWHP systems are much smaller than the Gardermoen ATES system. The annual costs for maintenance can therefore be comparatively higher. Yet, the consequences of critical malfunctions can be relatively larger for small GWHP systems, since small systems usually rely on only one well-pair for their heating system. Critical malfunctions might force the heat pump system to be shut off. The back-up boiler must then supply the whole heat load at a much higher cost. The importance of performing regular maintenance even in small GWHP systems should therefore be apparent.

Deciding the optimal timeframe of maintenance intervals for the various cleaning methods can be challenging (Kerner, 2011). A common maintenance strategy in the district heating industry is to perform cleaning when it is profitable (Gudmundsson, et al., 2016; Kerner, 2011). This strategy should be well understood by the GWHP owners because the cost of allowing the system to operate at lower levels of efficiency will be higher than the cost of cleaning. Systematic surveillance of the GWHP performance allow the interval for cleaning to be prescribed according to the performance enhancing benefits of the cleaning.

Paper IV describes how the surveillance of the whole heat source system can be performed with pressure and temperature sensors. This type of performance monitoring is ideal for GWHP systems because all system components can be assessed simultaneously by conducting a "*step-test*" during regular operation of the GWHP system. In Paper V it is shown how the Lena Terrace GWHP system was tested via remote control.

A revised version of sensor configurations is shown in figure 4-1, modified to include the experience gained from recent testing at Lena Terrace in Melhus. The sensor configuration suggested in Paper IV was initially developed with the minimum number of sensors required for the test. The new configuration in figure 4-1 is easier to work with in practice.

A flow meter (FL) is added, in addition to two more pressure sensors (p2 and p3) on each side of the groundwater heat exchanger. These sensors are added because the temperature sensors at Lena Terrace were not properly calibrated and would not produce reliable results. If the flow meter and the p2 and p3 sensors are added, the test can be conducted without relying on the temperature sensors.

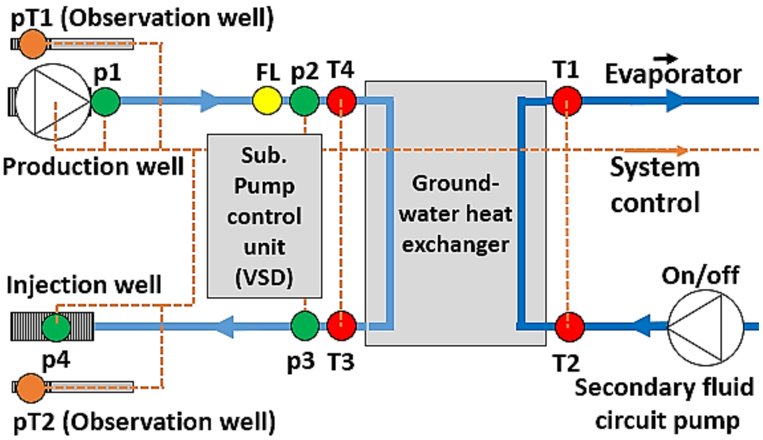

Figure 4-1 *Revised principle sketch of the typical open loop GSHP system surveillance scheme with temperature sensors (red dots, T1-T4), pressure sensors (green dots, p1-p4), pressure & temperature sensors (orange dots, pT1-pT2) and flowmeter (yellow dot).*

The accuracy of the surveillance method relies on the individual sensors used in the instrumentation. If the sensors are not properly calibrated the test will produce erroneous results. This also occurs if the sensors have too poor accuracy, or too large measuring ranges compared to the measuring intervals that are relevant for each component. The sensors must be installed at the correct location in the piping system and have sufficiently sampling frequency. Data logging at least every minute when performing a step-test is recommended to provide an adequate overview of the situation.

The pressure sensors in the production well and the injection well should ideally have ± 1.0 mbar accuracy (equivalent to ± 1.0 cm water column height). This accuracy provides proper data resolution in a groundwater well in gravel and sandy soils. Similarly, the temperature sensors should have a high quality, e.g. accuracy of ± 0.1 °C or less. The temperature response in T1-T4 will be delayed due to the relatively slow reaction time and the interpretation of the transient time temperature data can be challenging (Gudmundsson et al., 2016).

For maximum cost-benefit it is important for the surveillance procedure to discover the location of the clogging in the systems at an early stage. Correct data interpretation is therefore important, and personnel with hydrogeology and heat pump knowledge is needed for data interpretation. It is also recommended to have “un-clogged” reference data from the first start-up of the GWHP system. Sensory equipment must therefore be an integrated part of the GWHP design in the planning stage of projects.

Monitoring and surveillance alone do not make a GWHP system reliable. The consumer will still suffer if the systems are not designed with easy access for effective cleaning methods. The design of the GWHP systems should not only focus on detecting clogging problems, but also to reduce the consequences of these faults. It is crucial that the GWHP designer and hydrogeological consultant are involved at an early stage in new building projects and that site-specific testing and pre-investigations are performed in advance. Only then will the full potential of the surveillance system be realized.

In summary, surveillance and monitoring of the system performance can improve the reliability of GWHP systems because clogging can be detected in an early stage and critical faults can be avoided.

4.3 Hypothesis III:

Fluid flow in unconsolidated aquifers is similar to fluid flow in pipes. The Hagen-Poiseuille-relations of pipe flow therefore applies to unconsolidated aquifers.

The Hagen–Poiseuille-equation of fluid flow in pipes is a steady linear flow equation that describes the proportionality of pressure drop (ΔP) versus the average fluid velocity (Q/A) of an incompressible Newtonian fluid (μ) flowing through a length of pipe (L) of uniform internal circular cross section (D_{Pipe}) (equation 4.1).

$$\boldsymbol{\Delta P = \frac{32}{D_{Pipe}^2} \cdot \mu \cdot \frac{Q \cdot L}{A}} \qquad \text{Eq. 4.1}$$

The equation describes how a fluid in motion interacts with the pipe wall. The flow induces viscous friction along the pipe wall surface and results in a loss of pressure within the fluid. The Hagen–Poiseuille-equation describes exactly how the pressure reduction occurs in a perfectly uniform circular pipe. The circular geometry produces a proportionality factor of $32/D^2_{Pipe}$.

The Hagen–Poiseuille-equation is often referred to in traditional porous media flow studies as an analogy for how fluid flow through a pore channel might behave (e.g. (Kozney, 1927; Carman, 1937; Eurgon & Orning, 1949). When one visually compares the Hagen–Poiseuille-equation to the empirical Darcy-equation (4.2) the analogy seems fitting. The Darcy-equation is also a steady linear flow equation that describes the proportionality of pressure drop (ΔP) versus the average superficial fluid velocity (u_s=Q/A) of an incompressible Newtonian fluid (μ) flowing in a porous media of length (L).

$$\boldsymbol{\Delta P = \frac{1}{k} \cdot \mu \cdot \frac{Q \cdot L}{A}} \qquad \text{Eq. 4.2}$$

The resemblance of the two equations is apparent and the analogy to the Hagen–Poiseuille-equation appears to be appropriate. By comparing the two equations one observes that the permeability of the porous media (k) should be analog to the diameter of a pipe. Even Kozney (1927) viewed each pore channel as though it represents a small pipe. The whole porous media was then viewed as a bundle of multiple pipes oriented along the flow axis through the media.

It is therefore tempting to assume that the permeability of the Darcy-equation is also related to some form of representative diameter size. This is often assumed in soil sciences where the diameter of a particle is used in empirical correlations, e.g. the Hazen-equation (3.1) (Chapuis. 2012). This assumption is falsified by Paper VI. The four different samples that were tested show that none of their permeabilities are comparable to a bundle of straight and circular pore channels.

A new analog to the Stokes flow approximation was therefore proposed. The differences between the Stokes analogy and the Hagen–Poiseuille analogy might not seem substantial, but the theoretical implications are significant and have consequences for how the behavior of fluid flow in porous media should be perceived. The major difference of the Stokes analogy versus the Hagen–Poiseuille analogy is how the velocity distribution of the fluid flow is described. In Hagen–Poiseuille flow the velocity distribution is viewed to be consistent throughout the pipe, because the geometry of the pipe never changes. The fluid velocity will therefore never change along the pipe length. This analogy is correct for uniform straight channels, but pore channels in unconsolidated soils are not straight nor uniform.

In this respect the Stokes flow approximation is distinctively different because the velocity distribution in the flow field will continuously change along the pore channel due to a variation in the channel geometry. This causes the fluid to consistently accelerate and decelerate from one pore to the next. This acceleration has a profound effect on the flow dynamics and probably explains why the Stokes flow approximation is found to better describe the data in Paper VI.

The influence of acceleration explains why porous media flows generally exhibit larger losses of mechanical energy than due to the viscous shear alone. This can be justified through the conservational laws, the conservation of mass, of momentum, and of energy. Mass balance requires that the fluid mass that flows through the pore body also flows through the pore throat. Since the channel opening of the pore throat is smaller than the pore body, the velocity of the fluid must increase as it approaches the pore throat (and vice versa). This change of velocity through the channel induces a redistribution of energy forms, from static energy to dynamic energy. These energy forms are associated with different forces that act on the fluid and balance each other, in accordance with the energy equation. As a fluid flows from one pore body to the next, the energy needed to accelerate the fluid flow and the force and energy needed to overcome the friction render the pressure unable to fully recover upon deceleration in the next pore. This energy is converted to heat (Çengel & Cimbala, 2014).

Figure 4-2 visualizes the distribution of friction forces and pressure forces acting on a solid surface along a non-uniform pore channel. The pressure forces are induced normal to the solid surface and the pressure forces are largest in areas of the pore where the velocity is low, corresponding to the pore body region of the pore. Fluid motion parallel to the solid surface induces frictional shear forces and is largest in the pore throat region where the velocity is high. The force of convective acceleration is exerted on the whole fluid mass in motion and the acceleration force is largest where the change of the velocity is greatest. This corresponds to the areas where the channel geometry changes the most.

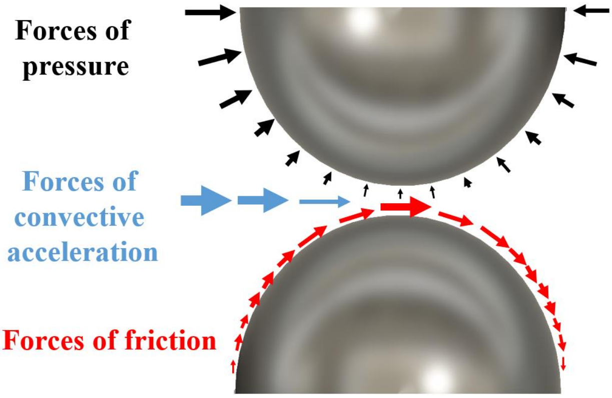

Figure 4-2 *Sketch of forces exerted by fluid flow through a non-uniform pore channel (not to scale). The velocity of the flow increases as the channel contracts. The frictional shear forces (**red arrows**) on the particle act parallel to the solid surfaces and increase as the velocity increases. The pressure forces (**black arrows**) act normal to the solid surfaces and decrease as the velocity increase. The convective acceleration is largest in areas where the channel geometry changes the most (**blue arrows**). The size of the arrows indicates the relative change of magnitude of the forces along the channel.*

The implications of the Stokes flow analogy might not be easy to distinguish from the Hagen–Poiseuille analogy in practice, because it is always the average superficial velocity that is actually measured in experiments. The superficial velocity of the flow is often averaged over the length of the porous media sample and the velocity of the flow is seemingly constant to the observer. Consider then the following simile to fluid flow in porous media:

> *Envision that a single pore channel through a soil sample is comparable to a winding road from point A to point B. A fluid flowing in this pore channel is comparable to a car driving on that road. In practical experiments the velocity of interest is the speed with which the car can drive from point A to B on the road. The Hagen–Poiseuille analogy views the speed of the car to be constant from A to B and the expected amount of fuel (energy) spent by the car is reflected in this assumption. The Stokes flow analogy states that the speed of the car is consistently accelerating and decelerating on the winding road. The Stokes flow car is able to achieve the same average velocity as the Hagen–Poiseuille car and arrives at point B at the same time, but this is achieved by expending much more fuel and energy than the Hagen–Poiseuille car.*

This simile illustrates the behavioral difference of the two analogies. In fluid mechanics this difference implies that the Hagen–Poiseuille equation is only applicable in steady state conditions, both with respect to *time & space*, while the Stokes flow equation only relies on steady state conditions with respect to *time*.

The influence of convective acceleration explains why porous media flows deviate from linearity. It is not possible to explain this phenomenon by the Hagen–Poiseuille analogy. The effects of acceleration influence the flow progressively more at higher velocities, where the inertial properties of the fluid gradually start to dominate the flow resistance. This occurs due to the non-uniformity of the pore channel which causes the flow to bend and curve along the pore surfaces. Chengle & Chimbala (2014) portray the following simile to the influence of inertia on the fluid flow:

> "*When driving on country roads, it is a common safety measure to slow down at sharp turns in order to avoid being thrown off the road. Many drivers have learned the hard way that a car refuses to comply when forced to turn curves at excessive speeds. We can view this phenomenon as "the separation of cars" from roads…. A fluid acts much the same way when forced to flow over a curved surface at high velocities… At sufficiently high velocities, the fluid stream detaches itself from the surface of the body. This is called flow separation".*

Envision that two fluids are two differently sized vehicles, for example a small car and a large bus, both driving along the same curved stretch of "*road*" at high speed. Because of its greater weight, the bus would have to drive at lower speeds than the car if not to be thrown off the road. The same phenomenon explains why water has a lower velocity threshold than oil, because water has a higher density than oil. Data from Paper VI (Figure 14) show that the divergence from linearity is observed at lower velocities for water (0.29 cm/s) than for oil (0.47 cm/s) for Sample A3, but these velocities still correspond to the same Reynold number ($Re_{C3\text{-}oil}$=0.28 and $Re_{C3\text{-}water}$=0.28). Non-linear pressure responses develop earlier for dense fluids because the force of acceleration increases proportionally with the fluid density (force = mass · acceleration).

The Hagen–Poiseuille equation is essentially an explicit solution of the Stokes equation in the special case of a circular geometry. In equation 4.3 all the relevant components of the Stokes flow equation are given mathematically, as described in Paper VI.

$$\boldsymbol{F_{viscous\ strain}} = \boldsymbol{C} \cdot \boldsymbol{\mu} \cdot \boldsymbol{V} \cdot \boldsymbol{L} \qquad \text{Eq. 4.3}$$

where	C (-)	represents the dissipating coefficient of viscous strain
	μ (Pa·s)	is the dynamic viscosity of the fluid (temperature dependent)
	V (m/s)	is the reference velocity of the fluid within the pore
	L (m)	is the length of the pore channel

The mathematical implications of the Stokes flow approximation are here seen in the dissipating coefficient $\boldsymbol{C}$ (-). This coefficient accounts for the spatial variations of the viscous stresses that is induced along the channel. The viscous stresses vary along the pore channel because the fluid velocity varies along the pore channel (figure 4-2). A reference velocity V must therefore be chosen, from which the distribution of viscous stress is evaluated. A unique dissipating coefficient C will then result depending on the choice of reference velocity V.

In Paper VI it is suggested that the reference velocity should be the average fluid velocity in the pore body. It is argued that this choice give rise to the Stokes sphere constant (C=3π) as a representative approximate value for the constant C. The results of the presented experiments in Paper VI support this assumption.

However, this is only appropriate as long as the pore channels induce convective acceleration to the flow velocity. If the channel geometry is straight and uniform the fluid velocity will not accelerate, and the 3π constant is therefore not appropriate. In the case of a uniform pore channel, similar to that of a pipe, no convective acceleration occurs (figure 4-3). The forces of viscous stress along the whole pore channel can therefore be associated with the same velocity vector along the entire length of the channel. Consequently, there are no spatial variations of the viscous stresses along the pore channel and the dissipating coefficient C = 1.

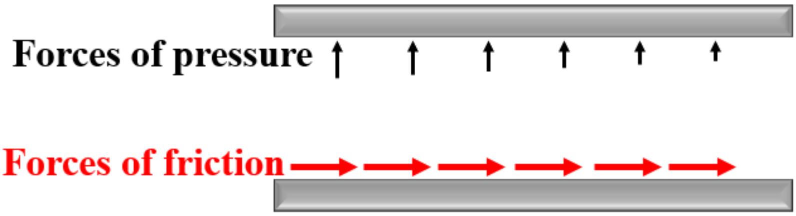

Figure 4-3 *Schematic sketch of forces exerted by fluid flow through a straight and uniform pore channel (not to scale). The frictional shear forces (**red arrows**) on the particle act parallel with the solid surfaces and are constant along the entire length. The pressure forces (**black arrows**) act normal to the solid surfaces. The size of the arrows indicates the relative change of magnitude of the forces along the channel.*

The Stokes flow equation (equation 4.3) is then simplified to equation 4.4 (note that the dissipating coefficient ***C*** seemingly does not occur in the Hagen–Poiseuille-equation).

$$\boldsymbol{F_{viscous\ shear} = \mu \cdot V \cdot L} \qquad \text{Eq. 4.4}$$

The reference velocity *V* is then representative for the entire pore channel and the maximum velocity of the flow is usually selected for this purpose. In fluid mechanics of pipes this force is normally expressed in terms of the fluid pressure (Chengle and Chimbala, 2014). Rearranging equation 4.4 into a pressure relation provides equation 4.5.

$$\boldsymbol{\Delta P = \frac{1}{m^2} \cdot \mu \cdot V \cdot L} \qquad \text{Eq. 4.5}$$

where the characteristic length unit *m* (m) expressed in equation 4.6 is the classic description of the characteristic geometry of the pipe. The characteristic length unit describes how the pressure forces and the friction forces of the fluid motion interact with the channel geometry (Schiller, 1923). For a circular pore this simplifies to an expression described by the pore diameter (D_{pore}).

$$\boldsymbol{m = \frac{volume\ of\ fluid\ in\ pore}{pore\ internal\ surface\ area} = \frac{\pi \cdot r_{pore}^2 \cdot L}{2 \cdot \pi \cdot r_{pore} \cdot L} = \frac{D_{pore}}{4}} \qquad \text{Eq. 4.6}$$

The Stokes flow equation can then be expressed in terms of the pore channel diameter since the diameter is a representative length unit for the entire pore channel length.

$$\boldsymbol{\Delta P = \frac{16}{D^2{}_{pore}} \cdot \mu \cdot V \cdot L} \qquad \text{Eq. 4.7}$$

Finally, the reference velocity *V* as the maximum velocity of the flow is rarely convenient in practice. A correction to the average velocity V_{avg} is therefore typically performed in practical experiments. For a circular channel this is half the maximum velocity (Geometry factor $\boldsymbol{k_0}$ = 2.0, (Çengel & Cimbala, 2014)). The Stokes flow equation then becomes identical to the Hagen–Poiseuille-equation if the geometry of the pore is identical to a circular pipe (equation 4.1 = equation 4.8).

$$\Delta \boldsymbol{P} = \frac{\mathbf{32}}{\boldsymbol{D^2}_{\boldsymbol{pore}}} \cdot \boldsymbol{\mu} \cdot \boldsymbol{V_{avg}} \cdot \boldsymbol{L} \qquad \text{Eq. 4.8}$$

If the channel shape is different from a circle, the Stokes flow equation will change accordingly. In Figure 4-4 the corresponding equation for a uniform pore channel shaped like a square, an infinite rectangle (two plates), and an equilateral triangle are developed by the same procedure. These turn out identical to the ones found in the literature of fluid mechanics (e.g. (Çengel & Cimbala, 2014)). This demonstrates that the Hagen–Poiseuille analogy can only be correct for porous media in the special case where the pore channel geometry is identical to a uniform circular channel, where no convective acceleration occurs in the flow.

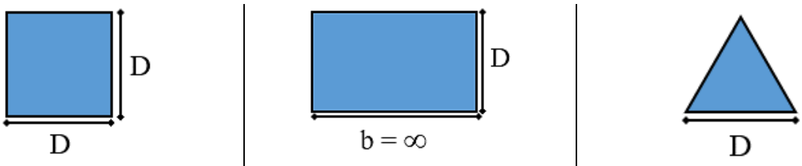

Volume: D·D·L Surface area: 4D·L Geometry factor $\boldsymbol{k_0}$ = 1.78 **m** = D/4	Volume: D·b·L Surface area: (2D + 2b) · L Geometry factor $\boldsymbol{k_0}$ = 3.0 **m** = D·b/ 2(D+b) ≈ D/2	Volume: D·D·1/2·L Surface area: 3D·L Geometry factor $\boldsymbol{k_0}$ = 1.67 **m** = D/6
$\Delta \boldsymbol{P} = \frac{\mathbf{16 \cdot 1.78}}{\boldsymbol{D^2}} \cdot \boldsymbol{\mu} \cdot \boldsymbol{V_{avg}} \cdot \boldsymbol{L}$	$\Delta \boldsymbol{P} = \frac{\mathbf{4 \cdot 3.0}}{\boldsymbol{D^2}} \cdot \boldsymbol{\mu} \cdot \boldsymbol{V_{avg}} \cdot \boldsymbol{L}$	$\Delta \boldsymbol{P} = \frac{\mathbf{36 \cdot 1.67}}{\boldsymbol{D^2}} \cdot \boldsymbol{\mu} \cdot \boldsymbol{V_{avg}} \cdot \boldsymbol{L}$

Figure 4-4 *The influence of the channel shape on the Stokes flow equation for uniform pore/pipe channels. The direction of flow is towards the reader*

In summary, the presented work demonstrates that the Hagen-Poiseuille-equation only applies to fluid flow in unconsolidated aquifers in the special case when the pore channel geometries within the aquifer are identical to uniform circular pipes. This is obviously never the case in nature because individual soil particles cannot be arranged so that they produce a pipe geometry.

4.4 Hypothesis IV:

The permeability of unconsolidated sediments is directly related to the diameter of the particles that constitute the soil.

Within hydrogeology and soil engineering it is common to estimate the hydraulic conductivity of a soil sample indirectly via a grain size correlation. Typically the d_{10} size from the sieving curve is selected, as in the Hazen-equation (3.1) (Fetter, 2001; Chapuis, 2012). However, the properties that should be investigated is the actual pore-space properties of the soil (Chapuis, 2012). In 1880 Seelheim (described in Chapuis (2012)) argued that the hydraulic conductivity of the soil should be compared to some representative pore diameter of the soil, not a particle diameter.

Paper VI reveals that neither the size of the particles nor the size of the pore diameter influence the permeability in the direct sense. It is the ratio of pore volume to pore surface area m (m) that defines the permeability. This is also the case for pipes, as the discussion in chapter 4.3 shows. But since a pipe has a uniform shape along the whole pipe length, the geometry of the pipe volume and pipe internal surface area can be fully described by the pipe diameter (equation 4.6).

This is not true for soils. The pores of unconsolidated soils are not uniform or consistently shaped channels, but a collection of different pores of various shapes and sizes. Even the geometry of a single pore requires multiple geometrical variables to properly describe the permeability of the pore. This is observed in equation 4.9 from Paper VI.

$$\boldsymbol{k = \frac{k_0 \cdot n^3}{3 \cdot \pi \cdot \tau^2 \cdot S^2}} \qquad \text{Eq. 4.9}$$

where the permeability k (m^2) includes the geometrical parameters:

n (-) is the specific porosity of the pore

S (m^{-1}) is the specific surface of the pore

τ (-) is the tortuosity of the pore channel

k_0 (-) is the shape of the pore channel at the pore body cross sectional area

C (-) is the dissipating coefficient of viscous stress, here equal to 3π

For this equation to be correctly expressed by means of the particle diameter of the particles that surround the pore, the equation must be modified e.g. in equation 4.10 (Carman, 1937).

$$\boldsymbol{S = \frac{Area\ of\ sphere}{Volume\ of\ sphere} \cdot Volume\ ratio\ of\ solids\ in\ the\ porous\ media = \frac{6 \cdot (1-n)}{\varphi \cdot d}} \qquad \text{Eq. 4.10}$$

where the particle dimeter, d (m), the porosity of the bed (n) and a surface factor that accounts for particle roughness and shape, φ (-), are needed to describe the specific surface area, S. Incorporating this into equation 4.9 provides equation 4.11.

$$\boldsymbol{k = \frac{k_0 \cdot \varphi^2 \cdot d^2 \cdot n^3}{108 \cdot \pi \cdot \tau^2 \cdot\ (1-n)^2}} \qquad \text{Eq. 4.11}$$

Equation 4.11 shows that the soil particle diameter is only one of many geometrical parameters that are needed to describe the permeability of a pore. This can be observed for the Sample B type in Paper VI which consists of 1.0 mm octahedrons (figure 4-5). Six copies of sample B were tested, and each sample had a unique permeability within the range $7.79 \cdot 10^{-10}$ – $1.00 \cdot 10^{-9}$ m^2. CT imaging and image analysis of the B3 and B6 samples showed that the specific porosity and specific surface of the samples were slightly different, but the diagonal diameter of the particles was always 1.0 mm for all samples.

This demonstrates that the permeability cannot be described correctly by a single diameter alone. It is therefore evident that traditional empirical correlations that rely on measurements of the soil particle diameter cannot account for the large variability in geometrical properties in soils. The predictability of the Hazen-equation (3.1) and similar empirical equations will therefore always contain a large degree of uncertainty.

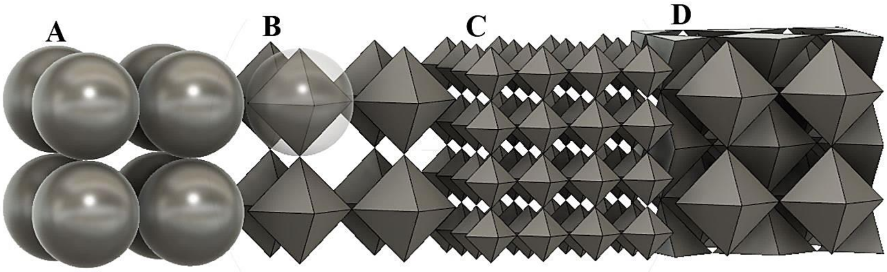

Figure 4-5 *Schematic sketch of the porous media geometries tested in Paper VI. The A type consists of 1.0 mm spheres and has a permeability of* $6.38 \cdot 10^{-11}$ – $7.28 \cdot 10^{-11}$ *m*^{2}*. The B and D types consist of 1.0 mm octahedrons and have a permeability of* $7.79 \cdot 10^{-10}$ – $1.00 \cdot 10^{-9}$ *m*^{2} *and* $4.35 \cdot 10^{-11}$ – $6.22 \cdot 10^{-11}$ *m*^{2}*, respectively. The C type consists of 0.5 mm octahedrons and has a permeability of* $7.45 \cdot 10^{-11}$ – $9.10 \cdot 10^{-11}$ *m*^{2}*.*

The main reason for continuous use of the simple empirical equations in engineering is the relatively low cost of acquiring the data and performing the analysis. A detailed description of the pore space of a given soil sample is a scientific challenge and requires comprehensive laboratory work. This is rarely included in the budget of most engineering projects. Simple grain size distribution curves are more routinely available in engineering projects because they often serve several purposes. The continuous use of empirical equations should therefore rely on the best empirical equations available.

The predictability of empirical equations has been extensively investigated by Chapuis (2012). Chapuis (2012) concluded that the best empirical equations rely on information of both the porosity and the specific surface area within the sample. For high quality data the Kozney-Carman-equation predicts the hydraulic conductivity value between one-third and three times that of the correct hydraulic conductivity measured in the laboratory (Chapuis & Abertin, 2003). A similar range is found in the results of the experiments in Paper VI where the Kozney-Carman-equation predicts the permeability value between 0.78 and 1.52 times the correct permeability. It is therefore recommended that an evaluation of the sample porosity and specific surface area should be included in the empirical analysis in engineering projects. A detailed step-by-step procedure is described in Chapuis (2012) and this should be implemented in engineering tasks when evaluating the hydraulic conductivity of soils.

Acquiring higher precision in the prediction of hydraulic conductivity than that of Chapuis and Aubertin (2003) with the Kozney-Carman-equation is not easy without comprehensive laboratory studies. Equation 4-9 suggests that the remaining discrepancies with the Kozney-Carman-equation are due to the shape of the pore (k_0) and the tortuous pathway (τ) of the pore channel. To quantify these parameters requires a detailed internal inspection of the pore-space. This is challenging for in-situ unconsolidated soils. It is therefore doubtful that equation 4-9 or equation 4-11 are applicable in practical engineering tasks in their current form without data from comprehensive laboratory studies.

Equation 4-9 can provide much information to engineers that need to interpret permeability data or determine input data for numerical modelling. Unlike the Kozney-Carman-equation, equation 4-9 states that the direction of flow through a pore network has an influence on fluid flow. This is shown in the homogeneous cubical packing of uniform spheres in figure 4-6. The flow is uniform in any of the main axis directions (X, Y or Z) and the flow characteristics will be equal because the geometry and the tortuosity of the pore channels are identical in these directions of flow.

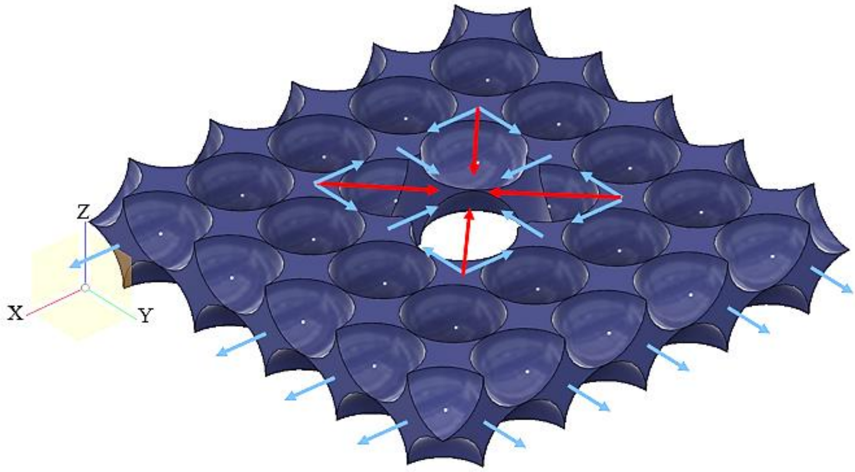

Figure 4-6 *Sketch of the pore matrix derived from a homogeneous porous media of uniform spheres stacked in a cubic array. The flow can be viewed as isentropic in the direction of the main axis (X, Y, Z) of the beds only (blue arrows). For radial flow towards a well it is impossible for the fluid to follow a straight flow path in all directions (e.g. red arrows). The permeability of the bed is thus affected by the direction of the flow with respect to the pore matrix orientation.*

However, if the flow is radial towards a point the most direct radial flow-path is obstructed by particles. The flow must "zigzag" around the particles and the tortuosity is not unity in all directions other than the main axis directions. The ratio of the highest to the lowest permeability would be 2/1 for the k_{max}/k_{min} in this case and is attributed to the variations in tortuosity only. The k_{max}/k_{min} ratio in most soils is often less than 4/1 (Chapuis & Gill, 1989). Hughes (1951) argues that anisotropic hydraulic conductivities are caused by directional and orientational properties of *non-spherical* particles in the soil. Equation 4-9 states that the anisotropic behavior also applies to uniform spherical particles and that the direction of flow has a governing role. Consulting equation 4-9 to evaluate the geometry of the pore space in numerical models might therefore be useful from an interpretational point of view.

In summary, the presented work demonstrates that the particle diameter sizes cannot be said to influence the permeability of a sediment directly. It is the pore shape, the ratio of pore volume to pore surface area and the direction of flow through the sediment that control the permeability of a soil.

4.5 The recommended GWHP design strategy

A design strategy is presented in figure 4-7 as an alternative to the *state-of-the art* in figure 2-1. The GWHP design should be module-based, and each module consists of one production well and one re-injection well. This well-pair is connected to an individual groundwater heat exchanger. For most small to medium scale GWHP systems (e.g. <200 kW or less) the operation will usually require only one set of wells and the module-based strategy will not differ much from the state-of-the art design. However, for large GWHP systems this module-based strategy will prevent mixing of water from different wells and enables one well-pair to be cleaned while others can maintain their function and ensure that the GWHP system is operational through the cleaning process. This is relevant both for exploitation systems and re-injection systems.

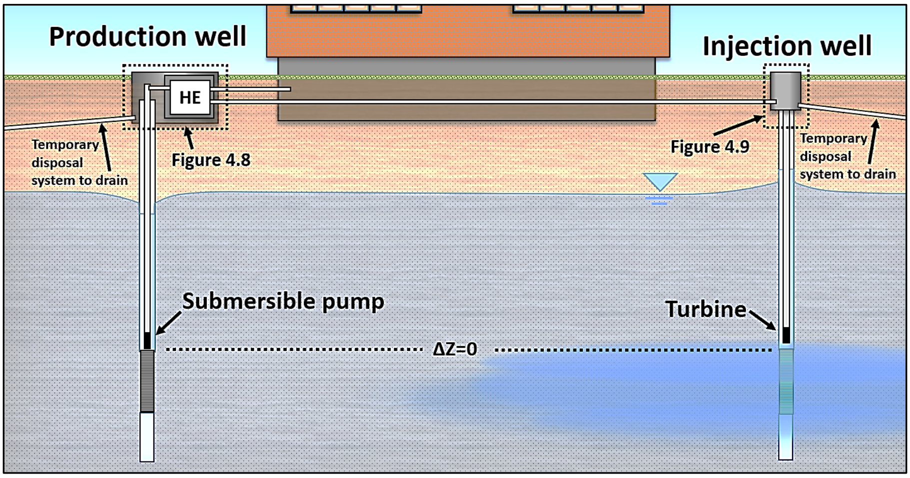

Figure 4-7 *Principle sketch of the recommended module based GWHP design.*

The operational strategy for a GWHP system should minimize the quantity of groundwater needed in the heat production process. A relatively large portion of the extracted heat should originate from the ΔT rather than from the quantity of groundwater (Q). This strategy reduces the risks of clogging and fouling in the groundwater system. A similar strategy is promoted by Rafferty (2001) and Snijders & Drijver (2016), but the Norwegian climate and aquifer conditions are colder than many European countries and provide different limitations for the design. For Norwegian conditions it is suggested that the return temperature after heat exchange should be lowered down to 2°C and that the required groundwater pumping rate (Q) is reduced to accommodate this criterion. This lower temperature limit is set to avoid freezing risks in the groundwater system.

The native groundwater temperature of Norwegian aquifers varies from 3-8°C (figure 2-9). The specific proportion of Q versus ΔT will therefore depend on the geographical location of the system. GWHP systems in northern Norway might have a ΔT=1-3°C, while systems in southern Norway might have ΔT=5-6°C. It will thus be easier to utilize aquifers in southern Norway because these GWHP systems will require less pumping capacity to achieve the same thermal power capacity (equation 2.1). However, to achieve this goal it is crucial that the GWHP designer and hydrogeological consultant is involved at an early stage in the building project and hydrogeological pre-investigations are performed in advance on the site. It is only then that the GWHP design can be customized to the aquifer conditions.

A principle sketch of the module is presented in figure 4-8 for an exploitation system, which is connected directly to figure 4-9 for a re-injection system. A number of components are included in figures 4-8 and 4-9 to ensure access for cleaning equipment. These components are explained in the following list. The design layout of GWHP systems and thereby the costs are more variable than for other heating and cooling alternatives. The relevance of cost is thus only mentioned in relative terms where it is appropriate.

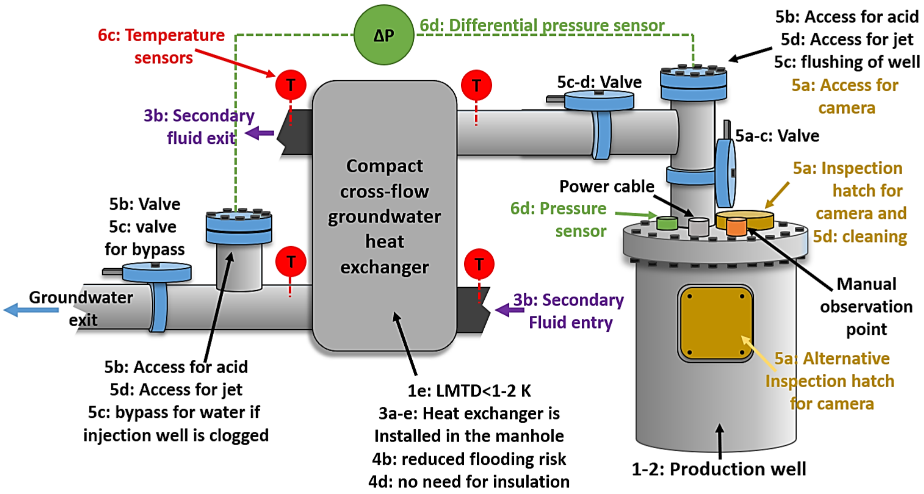

Figure 4-8 *Principle sketch of the suggested GWHP production/exploitation well design. The whole installation can fit within the well manhole. The individual parts are numbered according to the listed points in the text.*

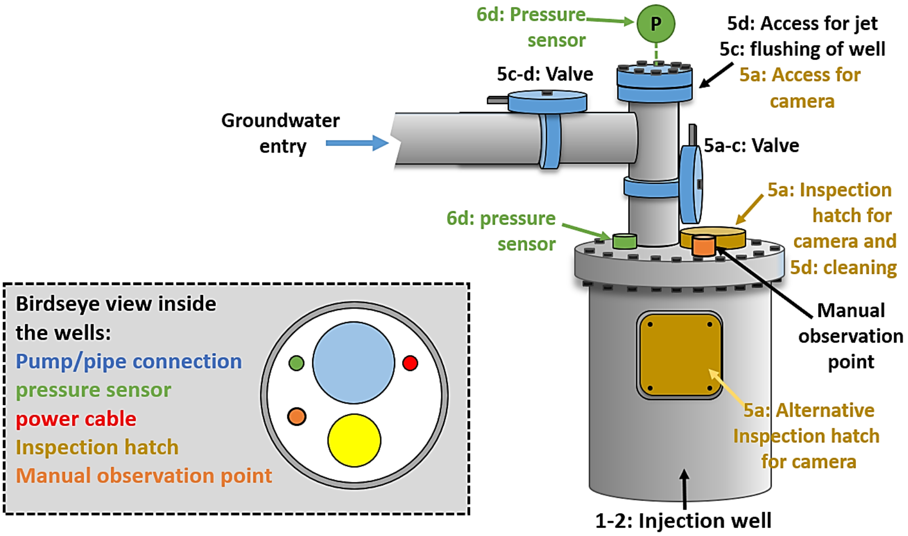

Figure 4-9 *Principle sketch of the suggested GWHP injection well design. A single injection well is connected to a single production well in the well-pair module. The individual parts are numbered according to the listed points in the text.*

The design strategy and the practical implications for the design are explained in the following list:

1. **Minimize the pumping rate (Q) needed in the heat production process**:
    a) **A higher success rate.** It is easier to produce less water from an aquifer. More aquifers might also become available for GWHP technology because the required aquifer thickness might be smaller, or the required hydraulic conductivity of the soil can be lower when less water is needed by the system.

    b) **Reduced the risk of thermal feed-back in re-injection systems**. The wells must typically be situated within the building's property, which limits the available distance between wells. The travel-time of the water in-between the wells is controlled by the spacing, the pumping rate and the local hydraulic gradient. A lower flow velocity through the aquifer will increase the travel-time and provide a larger buffer for thermal break-through. The travel-time is increased further if the injection well is located "down-stream" of the production well.

    c) **Smaller well pump – lower capital costs.** The size requirements for the submersible pump and the sizes and length of the well screens are proportional to the pumping rate required by the system. To minimize the required pumping rate can reduce the size of the submersible pump. This will allow the driller to reduce the diameter of the well and the drilling cost.

    d) **Use frequency converters that allow for variable pumping rates**. The GWHP system must be able to adjust the speed of the pump motor so that the pumping rate can be adjusted depending on the heat demand in the building. **The return temperature of the groundwater should be kept at 2°C**. It must be possible to adjust the pumping rate so that the ΔT can achieve this goal in the heat production process.

    e) **The logarithmic mean temperature difference (LMTD) of the groundwater heat exchanger should be within 1-2°C**. The temperature of the secondary fluid should be as close as possible to the outlet temperature of the groundwater to maximize the evaporation temperature in the heat pump (small approach temperature). A compact crossflow plate heat exchanger is usually preferable due to their small size.

    f) **Smaller pipe diameters – lower capital costs.** Lower pumping rate reduces the diameter requirements of the pipeline. The pipe size must be large enough to allow the pump to function over a wide range of flow velocities. Stene (1997) argues that the minimum flow velocity within the pipeline should be higher than 0.3 m/s to reduce clogging. This can function as a criterion for the pipeline dimensioning at the lowest pumping speed (30 Hz).

2. **Avoid altering the chemical composition of the groundwater**:
    a) **Wells are only connected to other wells that have similar chemical signatures**. If an installation requires more than one well-pair, these well-pairs should not be interconnected with each other. Each well-pair should have an individual groundwater heat exchanger instead of a large shared heat exchanger. Water quality analysis is required to determine which wells that have similar chemical compositions and that should be grouped into well-pairs. Pre-investigations and water quality sampling must therefore be performed in advance.

    b) **The submersible pump** should be installed close to the screened area of the production well. The pump will typically be installed just above the well screen, but other locations should be evaluated in some situations. The best hydraulic performance is achieved if the pump is installed within the screened area of the well. The pump should be installed below the well screen if the groundwater is saturated with gas.

    c) **The injection well screen** should be installed at the same depth, or deeper than the production well screen to reduce the risk of gas exsolution in the well screen area.

   d) **The return pipe in the injection well** should be installed close to the screened area of the well. The pipe should be installed below the screen if the groundwater is saturated with gas.

   e) **A back-pressure device should be installed** at the return pipe exit to control the pressure level in the groundwater pipeline. This hinders vacuum pressures in the piping system. The backpressure device should ideally be a turbine because this will allow for regeneration of electrical energy and improve the COP of the system.

3. **Minimize the required length of the groundwater pipeline.** This does not entail that the distance between the production well and the injection well should be short, but that the pipeline should be as short as possible between the two wells:

   a) **Smaller well pump – lower capital costs**. Minimal pipeline length reduces the hydraulic resistance in the groundwater pipeline. The size requirements of the submersible pump will be reduced, which in turn reduce the size requirements of the production well. The driller can reduce the diameter of the well and the drilling cost.

   b) **Increased energy efficiency for the GWHP system.** The efficiency of a submersible pump (η_{pump} 50%) is typically less than the efficiency of a high-quality circulatory pump used in the secondary fluid loop (e.g. η_{pump} 60-80%). The secondary fluid pipeline has no static head and no risk of clogging, so it is easier to select the best efficiency pump for this loop versus the groundwater loop. To reduce the length of groundwater loop by increasing the length of the secondary loop ensures less waste of energy and lowers the operational costs of the system.

   c) **Lowers investment cost on high-quality pipe components**. A short groundwater pipeline ensures that fewer parts come into contact with the groundwater. A shorter pipeline therefore requires fewer parts of high-quality materials (e.g. corrosion proof pipes).

   d) **Lower maintenance cost**. The number of components and over-all length of pipeline that needs regular clogging maintenance is reduced.

   e) **Reduces the timeframe for the groundwater outside of the aquifer.** The time spent by the water outside of the aquifer is minimized and can possibly reduce the timeframe of chemical imbalance and chemical reactions.

4. **Do not allow groundwater into the building**. The design of the groundwater pipeline is simplified if the pipeline never enters the building and fewer valves, bends and pipefittings (etc.) will be needed in the pipework. The groundwater heat exchanger should not be located in the basement of the building, but in the production well manhole:

   a) **Less space required by the GWHP system in the basement installation.** If the groundwater pipeline and the groundwater heat exchanger is removed from the basement the heat pump will require a smaller machinery room.

   b) **Reduces the flooding risks**. The groundwater pipeline might rupture due to corrosion or general deterioration. If the groundwater pipeline and the groundwater heat exchanger is removed from the basement the risk of flooding is eliminated.

   c) **Easier to control the pressure in the groundwater pipeline.** It is easier to control the pressure and avoid vacuum in the pipeline if the pipework is straightforward. The pipeline layout should be kept short and simple between the production well and the re-injection well with as few bends, constrictions, and valves as possible.

   d) **No need to insulate components – easy leakage detection.** The groundwater pipeline and the groundwater heat exchanger do not need insulation if they are located in the production well manhole. The temperature in the manhole will be similar to the water temperature and this eliminates the problems of condensation. It will be easier to discover corrosion problems and leakages from the heat exchanger and the pipeline.

5. **Easy access for maintenance equipment**. Regular maintenance requires easy access for cleaning equipment to the groundwater heat exchanger, piping system, injection well and production well. The same access points can be used for inspections and for cleaning. The cleaning methods that should be accounted for are:

    a) **Well access hatch for camera and cleaning equipment.** Allows the wells to be inspected during operation and the performance of the system will be easier to understand. This will require a larger well diameter than what the pump requires alone. If the size of the submersible pump is designed according to point 1c) and 3a) the new required well size should ideally be reduced compared to the state-of-the art design. In this case the state-of-the art well size can still be drilled, and the well will have additional room along the side of the pump, especially by installing the pump slightly off-center in the well, which makes room for the yellow circle in figure 4-9. Cleaning equipment can then be inserted into the well without having to dismantle the submersible pump. Otherwise, this will require a larger well diameter than the normal well design.

    b) **Acid treatment of the groundwater heat exchanger**. Pipe fittings and valves that allow for easy shut-off and cleaning of the heat exchanger are recommended and should be standardized for GWHP systems.

    c) **Reverse pumping and flushing of the well screens**. The wells should be reversed flushed before the start of each heating season. The water from the flushing contain particles that must be removed from the system and this requires a bypass in the pipeline via a temporary disposal to the surface drain.

    d) **Jet cleaning** of pipes and wells is recommended as an affordable routine cleaning strategy. This can be done in conjunction with flushing and pumping maintenance.

6. **Recommended surveillance equipment.** The sensory equipment must be able to document the performance of the system and its influence on the environment. The recommended level of surveillance can be achieved by installing:

    a) **Data storage.** Record the surveillance data. Clogging and other problems can be detected more easily if there exists a record of past performance data. All sensors should have digital memory or be connected to a storage unit.

    b) **Calibration.** The sensors and recording systems must be properly calibrated to ensure that the recorded data is correct. The sensor accuracies should be routinely checked.

    c) **Four temperature sensors** (per heat exchanger). The proper range for these temperature sensors will be -5 – 20°C. Limiting the range of the sensors will improve the accuracy. The sensors should have an accuracy of ± 0.1 °C (Pt100A or Pt1000A resistance thermometers).

    d) **Pressure sensors**. The minimum requirement is the water level measurements of the injection well and the production well. Pressure drop across the groundwater heat exchanger is also recommended. More sensors can be fitted along the groundwater pipeline on demand. The proper range for these sensors will vary depending on the hydraulic resistance in the pipeline and their accuracy might therefore vary. The pipeline sensors must be able to measure vacuum pressures. The water level sensors in the wells should have ± 1.0 mbar accuracy.

    e) **Volume flow meter in the groundwater pipeline.** The accuracy of the flow meter is typically limited within a certain range of pumping rates. The flow meter type must therefore be selected according to the pumping rates required by the operation. It must be able to follow the whole pump capacity range from 30-50 Hz motor speed.

5 Conclusions

The conclusions of the four hypotheses are summarized. Additionally, there are some supplementary findings regarding the GWHP design that are summarized after the hypotheses' section.

Hypothesis I:

Clogging is triggered by the design and operation of GWHP systems.

During the course of the ORMEL project and this PhD it was found that clogging problems affect all of the GWHP systems in Melhus. These problems involve clogging due to sediment suffusion or due to chemical precipitation and deposition of reaction compounds. These problems are typical for GWHP systems (i.a. Bakema, 2001; Banks, 2012; Snijders & Drijver, 2016). The GWHP literature, the ORMEL study, and this thesis show how an inappropriate well design can trigger sediment suffusion or how the piping layout can affect the groundwater chemistry. Clogging must be taken seriously because it causes system malfunctions. Chemically induced clogging is particularly challenging because numerous events can alter the chemical equilibrium of aqueous solutions. Typical examples are precipitation due to mixing of dissimilar groundwater qualities with each other or intermixing of air into the groundwater during pumping.

The influence of the GWHP design on the groundwater pressure and temperature during operation has been shown to affect the solubility of gases in the water. It is demonstrated that GWHP re-injection systems used in Norway cause vacuum pressures in the piping system. The groundwater temperature is also altered relative to the *in-situ* groundwater temperature. Both these events have the potential to trigger gas exsolution. The gas solubility in water depends on the hydrostatic pressure, the temperature, and the concentration of gas in the water. Some gases (e.g. CO_2) regulate the pH of the water and if these gases exsolve from the water they can catalyze precipitation reactions. One should therefore not allow gas exsolution in GWHP systems.

The magnitude of temperature alteration (ΔT), the hydrostatic pressure in the piping system, and the pumping rate (Q) are determined by the design and the operational strategy of the GWHP system. This demonstrates that both the design and the operational strategy of a GWHP system influence the solubility of gases in the water, which in turn has the potential to catalyze precipitation reactions. The presented work, along with those published by others, therefore verifies hypothesis I.

Hypothesis II:

Monitoring of the GWHP system performance with a hydraulic step-test surveillance procedure will improve the reliability of the GWHP systems and provides a means for early detection of clogging in distinct parts of the system.

The Melhus GWHP systems lack maintenance routines in the long-term operation. The presented work confirms that GWHP systems must schedule for regular maintenance in order to improve the reliability of the systems, as is frequently highlighted in the GWHP literature (i.a. Bakema, 2001, Andersson et al., 2003). In this respect "*regular*" is a relative term and can be defined uniquely for each individual GWHP system. A means to improve the reliability of the system is therefore to determine the appropriate timeframe for maintenance. Key parameters that describe the performance of the GWHP system should be monitored routinely with a surveillance procedure. This will help determine the proper timeframe for maintenance intervals.

The theoretical foundation for a surveillance procedure has been presented and shows that the hydraulic and the thermal performance of the system can be used to schedule maintenance intervals. Both performances fluctuate during normal operations and this requires a fixed point of reference for the surveillance procedure. The fixed reference point is the so-called *step-test procedure* which can detect if, when, and where a reduction of the hydraulic and the thermal performance has occurred.

The presented work therefore verifies hypothesis II. Routine surveillance and maintenance require the GWHP operation to have a competent operator/consultant that can follow up and interpret the performance data and schedule for the correct maintenance measures.

Hypothesis III:

Fluid flow in unconsolidated aquifers is similar to fluid flow in pipes. The Hagen-Poiseuille-relations of pipe flow therefore applies to unconsolidated aquifers.

The pore channels in unconsolidated aquifers have non-uniform shapes. A channel will have a wide pore body region and a narrow pore throat region along its length. The laboratory work presented in Paper VI demonstrates that these geometrical properties have a significant influence on the fluid flow. The non-uniformity of the pore channel induces a spatially dependent acceleration of the fluid velocity along the expanding and shrinking pore channel. The Hagen-Poiseuille equation does not account for this effect. The over-all effect of non-uniformity is that the loss of mechanical energy is relatively larger for fluid flow in unconsolidated aquifers than in pipes. Fluid flow in unconsolidated aquifers is therefore not similar to fluid flow in pipes and hypothesis III is falsified.

Hypothesis IV:

The permeability of unconsolidated sediments is directly related to the diameter of the particles that constitute the soil.

The permeability of a pore describes how the pore shape and size affects the fluid flow and is independent of the fluid properties and the temperature. The hydrogeological literature commonly relates the permeability to the diameter of the particles that constitute the soil. However, the diameter of the particles that surrounds the pore does not describe the shape of the pore nor its size, and the diameter of the particles is therefore not directly related to the permeability.

Paper VI states that other geometrical properties are needed to describe the permeability of a pore; the specific porosity, the specific surface, the shape of the pore channel and the contraction ratio of the pore channel. The orientation of the pore channel with respect to the flow direction (the tortuosity) also has an important role. These properties are unique for a pore. It is shown that the particle diameter cannot describe the permeability of a single pore. Therefore, an average particle diameter is not able to describe the average permeability of a soil either. Hypothesis IV is not verified.

Supplementary findings important for the design of GWHP systems.

It is important to utilize the full thermal potential of each liter of groundwater because this will reduce the hydraulic stresses enforced on the aquifer through pumping. For Norwegian aquifer conditions the groundwater temperatures are relatively cold (3-8 °C). The strategy then implies that the groundwater temperature should be lowered as much as possible, restricted to the lower limit of 2°C after heat exchange. To achieve this goal, it is crucial that the GWHP designer and hydrogeological consultant is involved at an early stage in the building project and that site investigations are performed beforehand. The required pumping rate (Q) needed in the heat production process can then be minimized according to the local aquifer conditions and the available groundwater temperature (ΔT).

Schedule for regular maintenance to avoid clogging in the long-term operations of GWHP systems. A module-based design where a production well and an injection well function as a well-pair is favorable and reduces the consequence of clogging. Maintenance is made easier because one well-pair can be cleaned while others can keep their function and ensure that the GWHP system is operational throughout the cleaning process. A best practice GWHP system should also have:

- Surveillance sensors that measure the hydraulic and the thermal performance of the system.
- Easy access for cleaning equipment to all parts of the groundwater system.
- Customized well design, piping layout, and a pumping strategy adapted to the *in-situ* pressure and temperature conditions of the aquifer.
- Groundwater pipeline length reduced to a minimum.
- The groundwater pipeline kept outside of GWHP building.
- The groundwater heat exchanger installed in the production well manhole.

References

Abesser, C., 2010, *Open-loop ground source heat pumps and the groundwater systems: A literature review of current applications, regulations, and problems,* London, British Geological Survay Open Report OR/10/045, Keyworth, Nottingham, UK, 24 pp.

Abuasbeh, M. & Acuña, J., 2018, *ATES system monitoring project, first measurements and performance evaluation: case study in Sweden,* Stockholm, Proceedings of the International Ground Source Heat Pump Association (IGSHPA) reasearch track conferance, September 18th-20th, Sweden, 10 pp.

Andersson, O., 1999. *Chemical treatment procedures and experiments in Sweden.* Apenzell, International Energy Agency, ECES expert meeting Annex 13.

Andersson, O., Ekestubbe, J. & Ekdahl, A., 2013, *UTES Underground Thermal Energy Storage – Applications and Market Development in Sweden*. Journal og Energy and Power Engineering, Issue 7, pp. 669-678.

Andersson, O., Hellström, G. & Nordell, B., 2003, *Heating and Cooling with UTES in Sweden - Current Situation and Potential Market Development*, Warsaw, Proceedings of the Futurstock conferance, September 1st-4th, Poland, 7 pp.

Bakema, G., 2001. *Well and borehole failures in UTESS. State of the art 2000,* Arnheim, IF Tecnology bv company report 2/9805/GW, second draft, The Netherlands, 48 pp.

Bakema, G., 2016, *Geothermal energy use, country update for the Netherlands*, Strasbourg, Proceedings of the European Geothermal Congress, September 19th – 24th, France, 7 pp.

Banks, D., 2012, *An introduction to thermogeology: ground source heating and cooling*, 2nd ed., New York: Wiley-Blackwell, ISBN:9780470670347.

Bieske, E., Rubbert, W. & Treskatis, C., 1998, *Bohrbrunnen.* 8th ed., Münichen: Oldenbuorg Verlag, Wien, 450 pp.

Blake, F. C., 1922, *The resistance of packing to fluid flow*, Transactions of the American Institute of Chemical Engineers, Vol. 14, Issue 3, pp. 415-421.

Blaker, Ø., Carroll, R., Paniagua, P., DeGroot, D. J. & L'Heureux, J-S., 2019, *Halden research site: geotechnical characterization of a post glacial silt*. American Institute of Mathematical Sciences (AIMS) Geosciences, Vol. 5, Issue 2, pp. 184-234.

Brøste, H. M., 2017, *Vannkvalitet knyttet til grunnvannsbaserte grunnvarmeanlegg i Melhus og Elverum.* Trondheim: NTNU, Master Thesis (In Norwegian [English translation: *Water quality assessment of groundwater from groundwater heat pump systems in Melhus and Elverum*]), 133 pp., Available from: http://hdl.handle.net/11250/2453843

Carman, P. C., 1937, *Fluid flow through granular beds*. Transactions of the Institute of Chemical Engineers, Volume 15, pp. 150-166.

Çengel, Y. A. & Cimbala, J. M., 2014, *Fluid mechanics: fundamentals and applications.* 3rd ed. in SI units, Boston: McGraw-Hill Education. 986 pp.

Chapuis, R. P., 2012, *Predicting the saturated hydraulic conductivity of soil: a review*. Bulletin of Engineering Geology and the Envionment, Vol. 71, pp. 401-434.

Chapuis, R. P. & Abertin, M., 2003, *On the use of the Kozeny–Carman equation to predict the hydraulic conductivity of soils*. Canadian Geotechnical Journal, Vol. 40, Issue 3, pp. 616-628.

Chapuis, R. P. & Gill, D. E., 1989, *Hydraulic anisotropy of homogeneous soils and rocks: influence of the densification process*. Bulletin of Engineering Geology and the Environment, Vol. 39, pp. 75-86.

D'arcy, H. P. G., 1856. *Les Fontaines Publiques de la Ville de Dijon.* Paris: Victor Dalmont, France.

Dagestad, A., Dalsegg, E., Heidenstrøm, B. & Colleuille, H., 2005, *Kartlegging av grunnvarmepotensialet fra løsmasser i Otta, Sel kommune,* Trondheim: Norges geologiske undersøkelse, NGU report 2005.048, pp. 67.

Domenico, A. A. & Schwartz, F. W., 1990, *Physical and Chemical Hydrogeology.* 1st ed., New York: Wiley, 824 pp., ISBN : 047150744X.

Driscoll, F. G., 1986, *Groundwater and Wells.* 2nd ed., St Paul, Minn: Johnson Division. 1089 pp., ISBN : 0961645601

Dyrud, I. F., 2008, *Kartlegging av grunnvarmepotensial i Seljord.* Bø: Høgskolen i Telemark, Master Thesis (In Norwegian [English translation: *Hydrogeological mapping of the geothermal potential of groundwater in Seljord*]. 111 pp., Available from: http://hdl.handle.net/11250/2438895

Eggen, G. & Vangsnes, G., 2005, *Heat pump for district cooling and heating of Oslo Airport Gardermoen.* Las Vegas, Proceedings of the 8th International Energy Agency (IEA) Heat Pump Conference. 7 pp.

Elverum kommune, 2018, *Årsmelding* , Elverum: Elverum kommune, Norway. 85 pp, Available from: http://planer.elverum.no/arsrapport2018/ [retrieved: 22.04.2021]

Ergon, S. & Orning, A. A., 1949, *Fluid flow through randomly packed columns and fluidized beds*. Industrial & Engineering Chemistry Research, Vol. 41, Issue 6, pp. 1179-1184.

European Commission, 2021, [Online source] Available from: https://ec.europa.eu/info/sites/info/files/energy_climate_change_environment/events/documents/in_focus_energy_efficiency_in_buildings_en.pdf [retrieved: 22.04.2021]

Fetter, C. W., 2001, *Applied Hydrogeology.* 4th ed., Upper Saddle River, N.J.: Prentice-Hall, 598 pp.

Frengstad, B. S. & Dagestad, A., 2008, *Groundwater in Norway – A question of looking under the stream for water*. pp. 136-143: Part of book: T. Slagstad & R. Dahl, eds., *Geology for society for 150 years – the legacy after Kjerulf.* Trondheim: Gråsteinen 12, 166 pp.

Førde, M. J., 2015, *Numerisk 3D-modellering av kvartærgeologi og hydrogeologi i Melhus sentrum - En vurdering av uttakskapasitet, optimal utnyttelse og forvaltning til energiformål*. Trondheim: NTNU, Master Thesis (in Norwegian [English translation: *Numerical 3D modelling of quarternary geology and hydrogeology underneath Melhus town center*]), 154 pp., Available from: http://hdl.handle.net/11250/2350392

García-Gil, A., Epting, J., Ayora, C., Garrido, E., Vazquez-Sune, E., Huggenberger, P. & Gimenez, C., 2016, *Reactive transport model for the quantification of risks induced by groundwater heat pump systems in urban aquifers*. Journal of Hydrology, Vol. 542, Issue 1, pp. 719-730.

Gehlin, S. & Andersson, O., 2019, *Geothermal energy use, country update for Sweden*. Den Haag, Proceedings of the European Geothermal Congress, June 11th – 14th, The Netherlands, 10 pp.

Gehlin, S., Andersson, O. & Rosberg, J.-E., 2020. *Country update for Sweden 2020.* Reykjavik, Proceedings of the World Geothermal Congress, April 26th – May 2nd, Iceland, 9 pp.

Grundfos AS, 2021. [Online source] Available at: https://product-selection.grundfos.com/no/sizing-result-page?qcid=1223117421 [Accessed 15.20.2021].

Gudmundsson, O., Palsson, H. & Lalot, S., 2016. *Online fouling detection of domestic hot water heat exchangers*. Heat Transfer Engineering, Vol. 37, Issue 15, pp. 1231-1241.

Gundersen, A., Hansen, R. C., Lunne, T., L'Heureux, J-S. & Strandvik, S.O., 2019, *Characterization and engineering properties of the NGTS Onsøy soft clay site*. American Institute of Mathematical Sciences (AIMS) Geosciences, Vol 5, Issue 3, pp. 665-703.

Gustafson, G., 1983, *Brunnsystem för värmelagring och värmeutvinning i akviferer.,* Stokcholm: Statens räd for byggnadsforskning, Report 39, 28 pp. (in Swedish).

Hansen, L., Rohr-Torp, E., Tønnesen, J. F. & Mauring, E., 2005, *Grunnvann og grunnvarme fra dype dalfyllinger langs Glåma,* Trondheim: Norges geologiske undersøkelse, NGU report 2002.082, pp. 47.

Haugen, T., 2016, *Estimering og sammenligning av hydraulisk ledningsevne ved hjelp av kornfordelingsanalyser, permeametertester og feltmåling.* Trondheim: NTNU, Master Thesis (in Norwegian [English translation: *Predicting the hydraulic conductivity through grain size distribution analysis, permeameter tests and field measurements*]), 150 pp., Available from: http://hdl.handle.net/11250/2404065

Hellestveit, M. S., 2018, *3D-modellering av grunnvannstrømning og varmetransport i akviferen i Melhus sentrum - En kvartær- og hydrogeologisk tolkning, med vurdering av uttakskapasitet.* Trondheim: NTNU, Master Thesis (in Norwegian [English translation: *3D modeling of groundwater flow and heat transport in an aquifer in Melhus*]), 173 pp., Available from: http://hdl.handle.net/11250/2502904

Hilmo, B. O., Ramstad, R. K. & Midttømme, K., 2000, *Grunnvarme som energikilde - innspill til fylkesdelplan for Hedemark med tema energi,* Trondheim: Norges geologiske undersøkelse. NGU report 2000.093, pp. 11.

Houben, G., 2006, *The influence of well hydraulics on the spatial distribution of well incrustation*. Groundwater, Vol. 44, Issue 5, pp. 668-675.

Houben, G. & Treskatis, C., 2007, *Water well Rehabilitation and reconstruction.* 1st ed., Michigan: Mc. Graw Hill Education. 391 pp.

Houben, G. & Weihe, U., 2010, *Spatial distribution of incrustations around a water well after 38 years of use*. Groundwater, Vol. 48, Issue 1, pp. 53-58.

Hughes, R. V., 1951, *Directional permeability trends in oil sand*, Den Haag, Proceedings of the 3rd International Congress of Petroleum, May 28th – June 6th, The Netherlands, 9 pp.

Hähnlein, S., Bayer, P. & Blum, P., 2010, *Review on the International legal status for the thermal use of groundwater*. Bali, Proceedings of the World Geothermal Congress. April 25th – 29th, Indonesia, 2 pp.

Hårstad, K., 1988, *Grunnvannstemperaturen i Norge.* Trondheim: SINTEF report STF36 F88001.

Johnson, A. I., 1967, *Spesific yield - Compilation of spesific yield for various materials,* Denver: U.S. Geological Survay – Report: Water supply paper 1662-D, 80 pp.

Kerner, J., 2011, *Compact, high-efficiency heat exchangers: Understanding fouling*. Chemical Engineering, Volume 118, Issue 6, 35 pp.

Kirkhusmo, L. A. & Sønsterud, R., 1988, *Overvåkning av grunnvann - Landsomfattende grunnvannsnett (LGN),* Trondheim: Norges geologiske undersøkelse. NGU report 88.046, pp. 17.

Kjellsson, E., 2009, *Solar Collectors Combined with Ground-Source Heat Pump in Dwellings - Analysis of System Performance,* Lund, Lund Teksniska Högskola – Byggnadsfysikk. Report TVBH-1018. Doctoral Thesis. 168 pp.

Kozeny, J., 1927, *Über kapillare leitung des wasser im boden*. Akademie die Wissenchaften, Vol. 136, Issue 2a, pp. 271-306.

Kruseman, G. P., Ridder, N. A. & Verweij, J. M., 1990, *Analysis and evaluation of pumping test data.* 2nd ed. (completely reviewed),Wageningen: International Institute for Land Reclamation and Improvement. Vol. 47, 377 pp.

L'Heureux, J-S., Lindgård, A. & Emdal , A., 2019, *The Tiller-Flotten research site: Geotechnical characterization of a very sensitive clay deposit*. American Institute of Mathematical Sciences (AIMS) Geosciences, Vol. 5, Issue 4, pp. 831-867.

Laloui, L. & Rotta Loria, A., 2019, *Analysis and Design of Energy Geostructures, Theoretical Essentials and Practical Application.* 1st ed. Academic Press. 1096 pp., ISBN: 9780128162231

Larsen, B. E., Ganerød, G. V. & Høgaas, F., 2016, *Bakkegeofysiske undersøkelser ved Ydalir og Elverum sentrum, Elverum kommune, Hedemark,* Trondheim: Norges geologiske undersøkelse. NGU report 2016.020, pp. 27.

Mauring , E., 1992, *Refraksjonsseismiske målinger på Melhus, Melhus kommune, Sør-Trøndelag,* Trondheim: Norges geologiske undersøkelse. NGU report 92.176, pp. 17.

Midttømme, K., Alonso, M. J., Krafft, C. G. & Kvalsvik, K., 2020, *Geothermal energy use in Norway, country update for 2015-2019.* Reykjavik, Proceedings of the World Geothermal Congress, Iceland, 9 pp.

Midttømme, K., Henne, I., Kochbach, J. & Ramstad, R. K., 2016. *Geothermal enegy use, country update for Norway.* Strasbourg, Proceedings of the World Geothermal Congress, September 19th – 24th, France, 10 pp.

Midttømme, K., Hilmo, B. O. & Ramstad, R. K., 2000, *Kartlegging av grunnvarmepotensialet i løsmasser og berggrunn i Alvdal,* Trondheim: Norges geologiske undersøkelse. NGU report 2000.063, pp. 33.

Midttømme, K., Kocbach, J., Ramstad, R. K. & Henne, I., 2017, *Aquifer thermal energy storage (ATES).* Technika Poszukiwan Geologicznych, Vol. 56, Issue 2, pp. 203-214.

Mansuy, N., 1998, *Well water rehabilitation, a practical guide to understand well problems and solutions.* St ed., Boca Raton: CRC Press, 192 pp.

NGU, 2014, [Online source] Available at: www.ngu.no/Grunnvarmeanlegg_092014
[Accessed 16 02 2021].

Norsk Varmepumpeforening, 2021, [Online source] Available from: https://www.novap.no/artikler/varmepumpesalget-11-ned-fra-rekordaret-2019 [Accessed 15.20.2021]

Olje- og energidepartementet, 2000, [Online source] Available from: https://lovdata.no/dokument/NL/lov/2000-11-24-82 [Accessed 15 02 2021].

Olje- og energidepartementet, 2016, *Kraft til endring - Energipolitikken mot 2030,* Oslo: Det kongelige olje- og energidepartement, 230 pp. Available from: https://www.regjeringen.no/no/dokumenter/meld.-st.-25-20152016/id2482952/?ch=1 [Accessed 15 02 2021].

Oslo Economics / Asplan Viak, 2020, *Kartlegging og vurdering av potensial for effektivisering av oppvarming og kjøling i Norge,* Oslo: Norges vassdrags- og energidirektorat. External report No. 8/2020, 69 pp.

Quinteros, S., Gundersen, A., L'Heureux, J-S., Carraro, A. H. & Jardine R., 2019, *Øysand research site: Geotechnical characterisation of deltaic sandy-silty soils.* American Institute of Mathematical Sciences (AIMS) Geosciences, Vol. 5, Issue 4, pp. 750-783.

Rafferty, K., 2001, *Design Aspects of Commercial Open-loop Heat Pump Systems,* Klamath Falls: Geo-Heat Center company report. 15 pp.

Ramstad, R. K., 2011, *Grunnvarme i Norge - kartlegging av økonomisk potensial,* Oslo: Norges vassdrags- og energidirektorat. Report 5/2011, 88 pp.

Ramstad, R. K. & Hilmo, B. O., 1999, *Kartlegging av potensialet for grunnvarmeuttak fra løsmasser i Elverum,* Trondheim: Norges geologiske undersøkelse. NGU report 99.008, pp. 63.

Rees, S., 2016, *Advances in ground-source heat pump systems.* 1st ed. Amsterdam: Woodhead Publishing: Elsevier Science & Technology number 100, 453 pp., ISBN: 9780081003114.

Reite, A. J., 1983. *Trondheim - Beskrivelse til kvartærgeologisk kart 1621 IV - M 1:50 000,* Trondheim: Norges geologiske undersøkelse.

Reite, A. J., 1985. *Støren - Beskrivelse av kvartærgeologisk kart 621 III - M 1:50 000,* Trondheim: Norges geologiske undersøkelse.

Reite, A. J., Sveian, H. & Erichsen, E., 1999. *Gråstein 5 - Trondheim fra istid til nåtid - landskapshistorie og løsmasser,* Trondheim: Norges geologiske undersøkelse.

Riise, M. H., 2015, *Praktisk guide for grunnvarmeanlegg basert på oppumpet grunnvann - Hydrogeologiske forundersøkelser, etablering, drift og oppfølging med utgangspunkt i erfaringer fra etablerte anlegg i Melhus sentrum.* Trondheim: NTNU, Master Thesis (in Norwegian [English translation: *Practicle guide to groundwater* *heat pump systems – hydrogeological pre investigations, constction, operations and know-how from existing installations in Melhus*]), 164 pp., Available from: http://hdl.handle.net/11250/2350389

Roscoe Moss Company, 1990, *Handbook of groundwater development.* 1st ed. New York: Wiley & Co., 512 pp. ISBN: 978047185611-5.

Sand, K., 1989, *Grunnvannstemperaturer i løsmasser langs Finnmarkskysten,* Trondheim: Norges geologiske undersøkelse. NGU report 89.093, pp. 11.

Schiller, L., 1923, *Über den Strömungwiderstand von Rohren verschiedenen Querschnitts und auhigkeitsgrades*. Zeitschrift für angewandte Mathematik und Mechanik, Vol. 3, Issue 2, pp. 2-13.

Schomburgk, S., Goyeneche, O., Gateau, C., Vernoux, J. & Denis, L., 2005, *Guide d'aide a La Decision pour L'installation de Pompes a Chaleur sur Nappe Aquifere en Region Ile-De-France: partie1, atlas hydrogeologique,* Orleans: BRGM/RP-53306-FR

Sindre, A., 1980, *Seismiske målinger 1972- 1977 i Gauldalen,* Trondheim: Norges geologiske undersøkelse. NGU report 1641, pp. 6.

Smeby, H., Midttømme, K. & Stene, J., 2011, *Kartlegging av energipotensialet for flatevann ved utnyttelse av varmepumper,* Oslo: Stiftelsen Norges Geotekniske Institutt, report no. 9/2011, 116 pp.

Sniegocki, R. T. & Reed, J. E., 1963, *Prinsiples of siphons with respect to the artificial-recharge studies in the Grand Prairie Region Arkansas,* Washington: U.S. Geological Survay – Water supply paper 1615, 19 pp.

Snijders , A. L. & Drijver, B. C., 2016, *Open-loop heat pump and thermal energy storage systems*. pp. 247-268. Part of book: Rees, S., 2016, *Advances in ground-source heat pump systems.* 1st ed. Amsterdam: Woodhead Publishing: Elsevier Science & Technology number 100, 453 pp., ISBN: 9780081003114.

Solberg, I.-L., Dagestad, A. & Dalsegg, E., 2014, *2D resistivitetsmålinger ved Brubakken, Melhus Sentrum og Skjerdingstad i Melhus kommune, Sør-Trøndelag, Data og tolkninger,* Trondheim: Norges geologiske undersøkelse, NGU report 2014.022, pp. 44.

Solli, G. S., 2020, *Ute av syne, ute av sinn - om rettigheter til og forvaltning av grunnvann i norsk rett.* Oslo: UiO, Universitetet i Oslo Det juridiske fakultet. Doctoral Thesis.

Spilde, D., Hodge, L. E., Magnussen, I. H., Hole, J., Buvik, M. & Horne, H, 2019, *Strømforbruk mot 2040,* Oslo: Norges vassdrags- og energidirektorat. Report no. 22/2019, 24 pp.

Statistisk sentralbyrå, 2021, [Online source] Available at: https://www.ssb.no/energi-og-industri/statistikker/elektrisitet [Accessed 15.02.2021].

Stene, J., 1997, *Varmepumper: grunnleggende varmepumpeteknikk*. 4th ed., Trondheim: SINTEF Energi, Report STF84A97302, ISBN : 8214003970.

Stene, J., Midttømme, K., Skarphagen , H. & Borgnes , B. G., 2008, *Design and operation of groundsource heat pump systems for heating and cooling of non-residentail buildings.* Zurich , Proceedings of the International IEA heat pump conference, May 20th – 22th, Switzerland, 12 pp.

Storrø, G., 2000, *Grunnvannsundersøkelser i tilknyttning til planlagte energibrønner i Lena-området, Melhus Sentrum,* Trondheim: Norges geologiske undersøkelse, NGU report 2000.069, pp. 44.

Stumm, W. & Morgan, J. J., 1996. *Aquatic chemistry: chemical equilibria and rates in natural waters.* 3rd ed. New York: Wiley, 1022 pp.

Tassis, G., Gellein, J. & Rønning, J. S., 2016. *Depth to bedrock and bedrock morphology from gravity measurements at Melhus, Melhus Municipality, Sør-Trøndelag,* Trondheim: Norges geologiske undersøkelse. NGU report 2016.011, pp. 43.

Theis, C. V., 1935, *The relation between the lowering of the piezometric surface and the rate and duration of discharge of a well using ground-water storage*. Transactions of the American Geophysical Union, Vol. 16, Issue 2, pp. 519-524.

Thiem, A., 1887, *Verfahress fur Natürlicher Grundwassergeschwindegkiten*. Polytechnisches Notizblatt, Vol. 42, p. 229.

Tømmerdal, H. M., 2017. *En evaluering av empiriske formler som relaterer kornfordeling til hydraulisk konduktivitet og deres egentehet til bruk i fluviale og glasifluviale sedimenter.* Trondheim: NTNU, Master Thesis (in Norwegian [English translation: *An evaluation of the empirical equations that relate the grain size distribution analysis to the hydraulic conductivity of soil and their uses*]), 159 pp., Available from: http://hdl.handle.net/11250/2452117

Van Beek, C. G. E. M., 2010. *Cause and prevention of clogging of wells abstracting groundwater from unconsolidated aquifers.* Amsterdam: Vrije University. Doctoral Thesis.

Vikovic, M. & Soro, A., 1992. *Hydraulics of wells - Theory and applications.* 1st ed. Littleton Colorado: Water resource publications, 354 pp., ISBN-10: 0918334764

Paper I

IGSHPA Research Track
Stockholm September 18-20, 2018

Video inspection of wells in open loop ground source heat pump systems in Norway.

Sondre Gjengedal, Randi K. Ramstad, Bernt Olav Hilmo, Bjørn Frengstad

ABSTRACT

This paper presents results from video inspections of groundwater wells in Melhus and Elverum, in Norway. The method has identified iron hydroxides, bacterial growth and sand production as causes of clogging in different wells. Video inspection has proven itself a reliable, inexpensive and quick method for such investigations. The videos supply documentation for the building owner about the well condition. A video inspection should be incorporated as a standard part of the tender document and an integrated part of the maintenance routine. Finally, open loop GSHP and ATES system wells should be designed and manufactured with integrated video inspection options. This will ease the fault detection process and reduce maintenance costs of the system through the lifetime of the wells.

INTRODUCTION

Ground source heat is a renewable energy source that has a potential for increased use in Norway. Through the ORMEL project, the municipalities of Melhus and Elverum are evaluating their potential for further development, specifically with the open loop ground source heat pump systems (open loop GSHP systems). Melhus has utilized ground water for heating and cooling purposes since 1999, with good results, while Elverum is currently investing in such systems. Aquifer thermal energy storage systems (ATES systems) are vulnerable towards many of the same problems as GSHP systems, but will not be described further in this paper.

The typical open loop GSHP systems in Melhus and Elverum utilize an unconsolidated Quaternary sand and gravel aquifer as a heat source. The production well and injection well connect to the aquifer through customized screens, which withholds the sediments, while groundwater is allowed to flow freely into the wells. A submersible pump in the production well pumps groundwater through a secondary heat exchanger in the building, where a secondary fluid extracts heat. After heat extraction, the groundwater is re-injected to the aquifer in the injection well. Elverum currently has one such open loop GSHP system in operation. Melhus has nine such open loop systems, which utilize groundwater from the same aquifer. Of the nine systems, seven have injection wells, while the remaining two utilize the local drainage system for disposal of the return water.

Unlike domestic water works, there are no requirements regarding water quality in open loop GSHP system in Norway. Specified water quality guidelines do not exist and water quality issues are often disregarded or insufficiently emphasized during the planning and design phase of new projects. Lack of specialist input from a hydrogeologist often leads to insufficient aquifer investigation. The production wells or injection wells are seldom sufficiently tested before or after the construction phase. Insufficient instrumentation and lack of monitoring of the systems during operation also contribute to late discovery of fouling and other water quality issues. All of these factors are likely contributors to increased risks of problems caused by faulty design or inappropriate operational strategies. Similar findings are reported by Bakema (2001) and Banks (2012) who emphasize that most open loop problems are best dealt with through correct system design.

Sondre Gjengedal: Ph.D. at Norwegian University of Science and Technology (sondre.gjengedal@ntnu.no).
Randi Kalskin Ramstad: Associate Professor at Norwegian University of Science and Technology (randi.kalskin.ramstad@ntnu.no).
Bernt Olav Hilmo (Ph.D.): Consultant at Asplan Viak AS (BerntOlav.Hilmo@Asplanviak.no).
Bjørn Frengstad: Professor at Norwegian University of Science and Technology (bjorn.frengstad@ntnu.no).

Since 1999, a wide range of problems has occurred with the systems in Melhus. These problems often involve clogging of the well screens, either the production wells or the injection wells (Riise, 2015). Typically, the injection wells are more prone to clogging than the production wells. All of the seven injection wells in Melhus have had clogging issues. In comparison, clogging have been detected in two out of nine production wells. In Elverum, one planned open loop GSHP system was terminated because three of the four production wells showed severe clogging issues during the pre-investigation phase of the project. The active open loop GSHP system in Elverum has experienced clogging issues in one out of its two production wells. Common for the problems found in Melhus is a lack of monitoring of the wells during normal system operation. Only three of the systems monitor groundwater flow rates and only one system monitor pressure levels in the production well. None of the injection wells is monitored. As a result, the faults are seldom detected before the clogging have had time to develop and have become a sever problem.

Clogging problems can originate from a wide range of sources that yield similar symptoms, such as reduced groundwater flow rates through the system and increased pressure drops in the groundwater flow through the affected components (Bakema, 2001, Banks, 2012, Andersson et al., 1984). It is common to distinguish between mechanical, chemical or microbial causes. Mechanical clogging involves incrustations of sand, silt and other suspended particles, which fill the pore space in the soil and clog system components. Chemical clogging involves precipitation of particles, which in turn incrusts on system components. Microbial clogging, or biofouling, is caused by bacteria, which grow on system components. All of these complications require different cleaning or corrective approaches (Andersson et al., 1984) and there exists a need to distinguish between them. Flow rate and pressure monitoring is not capable of such distinctions. Consequently, such problems often call for investigations by means of water quality analysis or visual inspection of the affected area to identify the problem cause.

EXAMPLES OF SUCCESSFUL VIDEO INSPECTIONS IN MELHUS AND ELVERUM

Video inspection offers a familiar, hands-on, versatile and reliable approach. The method is common in domestic waterworks in Norway, England (Banks, 1992), the Netherlands (van Beek et al., 2017), USA (Jansen and LoCoco, 2007, Gorder, 1963) and most likely other countries. Similar methods are common in other industries such as buildings and constructions, roads and sewage systems where video inspection is a standardized part of any project. Today`s high-resolution color imaging cameras are capable of forward-looking and sideways-looking views with 360 degrees rotation and variable depth of focus. During the inspection, the video is shown in real-time on a monitor with a depth display. Some cameras, like the *Supervision™ SVR 140/SVC100 pan and tilt camera* utilized in this study, are equipped with laser measuring tools, which for example enables measurement of screen slot openings in the well.

In groundwater wells, the usefulness of the method relies on the clarity of the water. Performing a flushing of the well and allowing particles to settle is in some cases recommended before the inspection, especially when inspecting new wells. Figure 1A shows a new well that had been pumped for 14 days and where the pumping ended one week before the video inspection. The 1 mm screen slot openings were measured to confirm that the well was constructed in accordance to the specifications given in the tender document. The lodged sand grains and the clarity of the water indicate that the well was constructed in good agreement with the local soil conditions.

The clarity of the water might be a good indication of a well's current condition and an inspection without pre-flushing might be useful in itself. Figure 1B shows a production well in Elverum where the well screen is clogged by a biofilm of iron bacteria. This particular production well is less than 1 year old and had not yet been connected to the heat pump system. It was not flushed before the inspection. In this case the bacterial growth seems to favor specific parts of the screen and builds on the screen surface in a foam-like structure, effectively clogging some of the openings. These observations might not have been possible if the well was flushed before the inspection. Disinfection with chlorine and cleaning were necessary before the well could be connected to the system.

Precipitated iron and manganese hydroxides is a common problem in Norwegian open loop systems (Riise, 2015). Often these particles accumulate in the injection well, after a journey through the rest of the system. But some examples of hydroxide precipitation is also found in production wells in Melhus. The production well screen in figure 1C is incrusted with precipitated iron hydroxides at the location of the pump inlet. The drawdown in the well was not monitored during operation and the water table was lowered below the suction inlet section of the pump. Mixture of air into the screen area allowed the chemical reaction to occur. Unlike the iron bacteria in figure 1B the precipitated hydroxides seem to evenly cover the screen slots. This well had functioned for 15 years before the problem was discovered and the well had to be abandoned because of faulty design.

The injection well in figure 1D is clogged by fine silt and clay particles. The particles originate from the sedimentary formation around the production well, where they are carried through the production well screen by the flow of water. The particles are unable to infiltrate back through the injection well screen and effectively clog the slots. Before the inspection the well was taken out of service and the suspended particles were allowed to settle. The picture shows some small particles of black manganese hydroxides still settling in the well. The problem was discovered 1.5-2 years after the plant was set in operation. The problem was solved by installing a filter on a part of the pipe section in the machinery room before reinjection of the groundwater back into the aquifer. The filter is regularly cleaned.

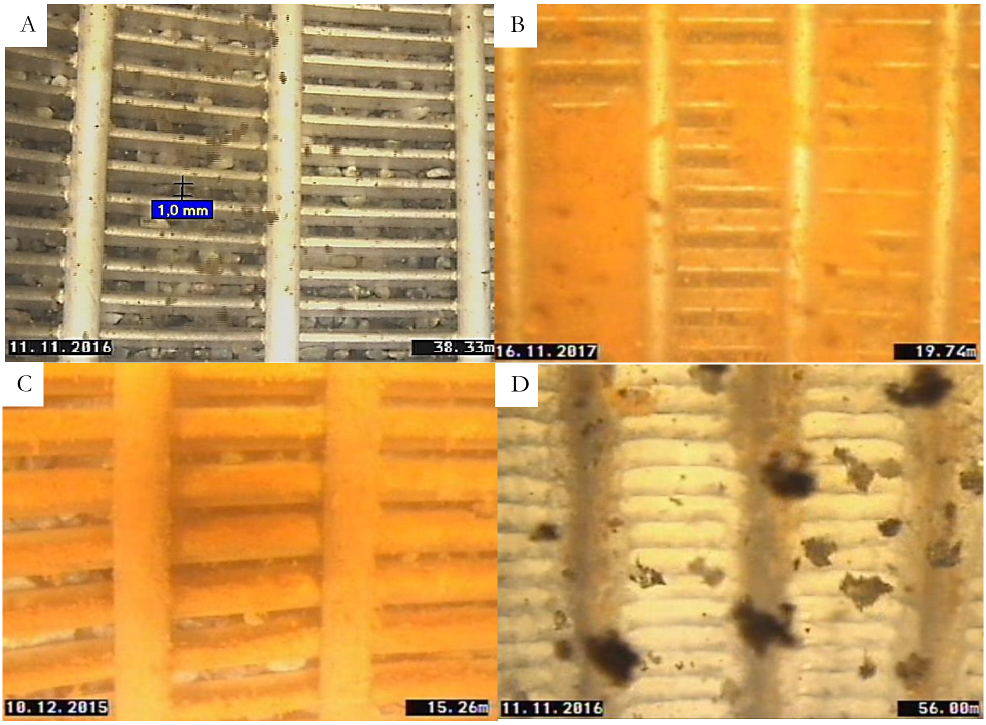

Figure 1 Video inspections of well screens. A: a newly constructed well in Melhus. The 1 mm slots were measured with a built-in laser tool. B: iron bacteria have infected this production well in Elverum. C: precipitated iron hydroxide incrustations on a production well screen in Melhus. D: sand and silt clogging an injection well screen in Melhus. Photos: Gjøvaag AS (part of the ORMEL project).

BENEFITS, COST AND DRAWBACKS

The presented video photos demonstrate the applicability of the method in open loop GSHP system wells. The investigation of newly constructed wells confirms that proper placement of screen, pump and pressure sensors are ensured and that the wells are constructed in agreement with the soil

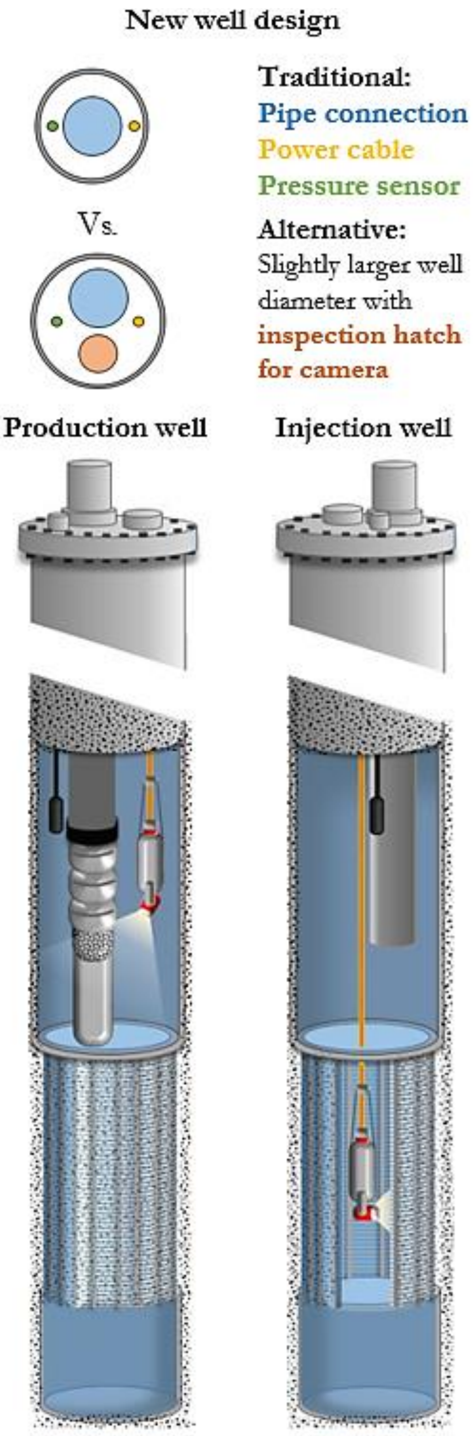

Figure 2 The traditional well design does not have space for a video camera. An alternative design that allows for real-time video inspection can reduce the over-all cost of fault detection.

conditions and the tender documents. The method can identify location and type of debris, scale and biofilm deposits in clogged wells. New vs. old well conditions can be compared and such information supply vital knowledge to the system operator and allow planning of appropriate maintenance and corrective measures. The method has also been applied in real-time to direct rehabilitation operations in the well or to identify sand-production zones in the well while pumping is in progress (Jansen and LoCoco, 2007).

The cost of a video inspection is a function of the actual inspection time and transportation cost to the site. The actual inspection time required for a single well depends mainly on the well depth and clarity of the water. For example, the depth of the wells shown in figure 1A-1D are 40 (A), 22 (B), 24 (C) and 58 (D) meters, respectively. The time needed for the inspections ranged from 15 (A), 15 (B), 23 (C) and 30 (D) minutes, respectively. The total cost of the individual video inspections ranged from 5000-5700 NOK (≈520-590 €) per well. By comparison, similar numbers have been reported by Banks (1992), where an average cost of 2500-6000 NOK (≈260-620 €) was registered in 1991.

A hydrogeologist can interpret the video during the inspection of the well or in the office afterwards. A digital copy of the video can also be sent to an expert (e.g. a microbiologist) for further evaluation.

The main drawbacks of the method involve the cost of preparing the wells for inspection. In Norway, the current open loop GSHP well designs generally follow the more traditional well designs applied for domestic drinking water purposes. Most of these wells are designed around the space required by the submersible pump, with minimum space available for other equipment. The camera utilized in this investigation required 90 mm diameter free space. Normally, the pump or injection pipe have to be dismantled and lifted out of the well for the camera to fit. The heat pump system must shut down during the video inspection, adding additional cost to the investigation.

If the well designs include enough space for a video camera while the pump and pipes are operating, the time needed and the over-all cost of the inspection is greatly reduced. A possible alternative would be to increase the well diameter sufficiently to give space for a camera along the side of the pump or injection pipe. An inspection “hatch” next to the pipe connections is a potential technique. By installing the pump and injection pipe slightly off-center, the additional well diameter needed for the camera might be minimized (figure 2). The video inspection can then be conducted during normal system operations and the actual well behaviors are observed live on the monitor while groundwater flows through the system. The increased installation cost due to a larger well diameter will be more than outweighed by the benefits of regular monitoring of the well conditions during the lifetime of the wells. In addition, a larger screen diameter would in most cases improve the well characteristics.

It might be argued that clogging problems also can be detected by measuring the specific flow or the pumping capacity. Although a reduction of the specific flow is easily understood by a hydrogeologist, a video presentation of the conditions in the well is a much stronger tool when trying to convince the well owner that a costly well rehabilitation is needed. If there is any doubt whether the well is installed according to order, a video inspection of the well can settle the dispute.

A record of routine video inspections from the wells were installed and onwards, will together with data on the performance of the open loop GSHP, be a strong tool for monitoring and documentation of the plant.

CONCLUSION

Video inspection of wells have proven to be a reliable, efficient and relatively low cost method for investigation of production wells and injection wells. A video inspection of the wells should be a standard part of the tender document in new open loop system and an integrated part of the maintenance routines. Open loop GSHP wells should be designed and manufactured with integrated video inspection options. This will ease the fault detection process and reduce maintenance costs of the system through the lifetime of the wells.

ACKNOWLEDGMENTS

The research project *Optimal Utilization of groundwater for heating and cooling in Melhus and Elverum*, the ORMEL project, is a cooperation between the municipalities of Melhus and Elverum, the Norwegian University of Science and Technology, Asplan Viak AS and the Geological Survey of Norway and with funding from the Norwegian Research Council. Erlend Skorstad at Gjøvaag AS performed the video inspection. We would like to thank all the involved institutions and persons for cooperation and financial contributions.

REFERENCES

Journal papers:

Gorder, Z. A. 1963. *Television Inspection of a Gravel Pack Well.* Journal - American Water Works Association, 55, 31-34.

Van Beek, C., Hubeek, A., De La Loma Gonzalez, B. & Stuyfzand, P. 2017. *Chemical and mechanical clogging of groundwater abstraction wells at well field Heel, the Netherlands.* Hydrogeology Journal, 25, 67-78.

Book:

Banks, D. 2012. *An introduction to thermogeology : ground source heating and cooling,* Chichester, Wiley-Blackwell.

Book section:

Jansen, J. & LoCoco, J. J. 2007. *Borehole Geophysics.* In: Sterret, R. J. (ed.) *Groundwater and Wells.* 3 ed. New Brighton: JohnsonscreensTM.

State of the art reports:

Andersson, A.-C., Andersson, O. & Gustafson, G. 1984. *Brunnar : undersökning, dimensionering, borrning, drift,* Stockholm.

Bakema, G. 2001. *Well and borehole failures in UTESS*. State of the art 2000. 2 ed. IF Technology bv.

Banks, D. 1992. *Grunnvannsbrønner : kontroll, vedlikehold, rehabilitering,* Trondheim, Norges geologiske undersøkelse.

Thesis:

Riise, M. H. 2015. *Praktisk guide for grunnvarmeanlegg basert på oppumpet grunnvann - Hydrogeologiske forundersøkelser, etablering, drift og oppfølging med utgangspunkt i erfaringer fra etablerte anlegg i Melhus sentrum*. NTNU.

Paper II

Proceedings World Geothermal Congress 2020+1
Reykjavik, Iceland, April - October 2021

Groundwater for Heating and Cooling in Melhus and Elverum in Norway – Highlights from the ORMEL-Project with Focus on Infiltration Wells

Randi Kalskin Ramstad, Sondre Gjengedal, Bjørn Syvert Frengstad, Bernt Olav Hilmo, Mari Helen Riise and Henrik Holmberg

S.P. Andersens veg 15A, 7431 Trondheim

Randi.Kalskin.Ramstad@ntnu.no

Keywords: Hydrogeology, open system ground water heat pump (GWHP), aquifer, groundwater wells, well rehabilitation

ABSTRACT

The main objective in the research project called *Optimal Utilization of Groundwater for Heating and Cooling in Melhus and Elverum* (2015-2018) in Norway has been to provide a sufficient and sustainable base of knowledge for optimized utilization and management of the aquifer in the two town centers. Many open system GWHP in the center of Melhus have challenges with clogging of the injection wells due to iron and manganese precipitations, and/or filling of the wells with particles of sand and silt pumped with groundwater. Precipitation of iron and manganese reduce the capacity of wells and affects pumps, pipes and heat exchangers. The infiltration capacity is gradually reduced by the filling of the well screen part of the infiltration well. Therefore, the screened groundwater wells in sand and gravel aquifers, and especially the infiltration wells have gained special attention in this article. Re-infiltration of heat exchanged groundwater to the aquifer seems to be more challenging than pumping groundwater from a production well. Another important point is that the experience with the use of screened infiltration wells at least in Norway, is scarce and almost limited to the open ground source heat pump installations where the first ones were established around 20 years ago. Before the ORMEL-projects including the sequel ORMEL2, there has been little systematic studies on the use of groundwater for energy purposes in Norway.

The experience from rehabilitation of an infiltration well in an open system GWHP installation at Melhus, namely Lena Terrace, has been used to illustrate the complexity of the problem to be addressed and the need for a systematic approach with the topic. Here a mix of both precipitation of iron oxides and sedimentations seems to occur. Theoretically and in general, we cannot exclude the possibility that some pumping wells also continuously produces suspended solids with the groundwater. The best rehabilitation results of the infiltration well at Lena Terrace seems to be the steaming and the sectional mammoth pumping. Rehabilitation of drinking water wells also often obtain good results with this method. However, the method is not widely used maybe due to limited availability by the industry and knowledge. Compared to production wells, the need of rehabilitation of infiltration wells seems to be more present with respect to both sediments and precipitation of e.g. iron and manganese oxides. Therefore, it is time to develop the steaming and mammoth pumping procedure further so that this well cleaning method is easily available, effective and can be used on a regular basis and before the infiltration rate in the infiltration well is critically low. Two more important issues are also addressed in the Lena Terrace case, namely the usefulness of the video inspection and the need for good surveillance of the operation of the open system GWHP. Video inspections document, and give a cost effective well condition analysis, and should be used before and after well rehabilitations in addition to hydraulic tests. The need of a central control and monitoring system is essential. With the new central control system available at Lena Terrace this winter, the last rehabilitation in July 2019 was initiated with basis in the monitoring of the water level in the infiltration well and done as a preventive measure before the situation got critical.

This broad perspective and approach concerning the use of groundwater to energy purposes should continue taking into account the ongoing plans for establishing a large-scale system in Melhus. This involves further work with design, to understand precipitation mechanisms and conditions, to achieve effective operating strategies with routinely and cost-effective maintenance and targeted well rehabilitation procedures.

1. INTRODUCTION

The main objective in ORMEL has been to provide a professional and sustainable basis for an optimal use and management of the groundwater resources in the town centers of Melhus and Elverum in Norway. The groundwater resources consist of sand and gravel aquifers. A comprehensive program of investigations has been performed within the project (2015-2018), e.g. drilling of investigations- and production wells, well testing, well rehabilitation and modelling. Previously, mapping of the groundwater resources has been lacking, and different levels of experience and competence by the use of groundwater to energy purposes has been limiting factors for the use of this renewable energy source.

The aquifer in Melhus is large and should be utilized on a commercial and large scale. The potential for heat extraction from the groundwater in the center of Melhus is estimated to be in the range from 5-10 MW and 15-30 GWh/year depending on how the systems are operated (Ramstad et al. 2018). The potential for cooling is in the same order of magnitude or more. These numbers are larger than the demand for heating and cooling in the center of Melhus. There are also areas in Elverum where large quantities of groundwater can be used locally. ORMEL2 (2018-2021) is a sequel to ORMEL focusing on iron and manganese issues in groundwater, and a hydrogeological design and operational basis for a large scale utilization of the groundwater resource for energy purposes in the center of Melhus.

The use of groundwater for energy purposes

The use of groundwater for energy purposes has a relatively short history in Norway. The ATES system at Oslo airport Gardermoen build in 1998 is among the first systems in Norway (Eggen and Vangsnes 2005), together with the first in Melhus in

1999 (Riise 2015). Traditionally, groundwater in sand and gravel aquifers in Norway has been used for drinking water purposes. When starting to utilize groundwater for energy purposes, the heating industry was introduced for hydrogeology. Unfortunately, the hydrogeological knowledge and experience already gained by the drinking water industry regarding groundwater wells in sand and gravel aquifers, has to a little extent been taken advantage of by the heating industry. Thus, some mistakes experienced and overcome within the drinking water industry, have therefore been redone within the heating industry when starting using groundwater for energy purposes. The ORMEL-project has contributed to bridge this gap in every level of the value chain so that there is enough system knowledge to design, operate and maintain profitable open system ground source heat pump systems (GWHP) in a systematic way. The complexity of these kind of systems requires multidisciplinary skills spanning from knowledge on extraction of groundwater from sand and gravel deposits, heat pump technology, automation/monitoring and operation and maintenance. Extensive cooperation between the disciplines and a sufficient level of system knowledge are necessary to ensure the integrity of the system as a whole.

Figure 1 shows the principles for the use of groundwater for heating purposes. In heating mode the groundwater is pumped from a production well. The energy is extracted by lowering the temperature of the groundwater in a separate heat exchanger prior to the heat pump. Finally, the groundwater is re-infiltrated into the aquifer by an infiltration well. Both the production and infiltration well are typically made by continuous and slotted (con-slot) screens as seen to the left in Figure 2. In cooling mode, e.g. the system can be switched.

An important difference between the use of groundwater for drinking and energy purposes, is the need for an infiltration well for re-infiltration of heat exchanged groundwater to the aquifer. Due to the re-infiltration there is no net extraction of groundwater from the aquifer, only a net extraction of energy either by lowering or elevating the temperature of the re-infiltrated groundwater. Except for a few drinking water plants with artificial infiltration of water in vertical groundwater wells, the experience with infiltration wells in Norway is limited.

Many open system GWHP in the center of Melhus have challenges with clogging of the injection wells due to iron and manganese precipitations, and/or filling of the wells with particles of sand and silt pumped with groundwater. Precipitation of iron and manganese reduce the well capacity and the life-time of pumps, pipes and heat exchangers. The infiltration capacity is gradually reduced by the filling of well screen part of the infiltration well. The solution to many of these problems are better maintenance and system design ensuring simple and routinely maintenance. This paper presents the highlights from the ORMEL-project with special focus on rehabilitation of infiltration wells with reduced infiltration capacity due to sedimentation and precipitated iron oxides, illustrated by an example from one of the plants in Melhus called Lena Terrace. These results have a wide application and transfer value within hydrogeology and screened water wells.

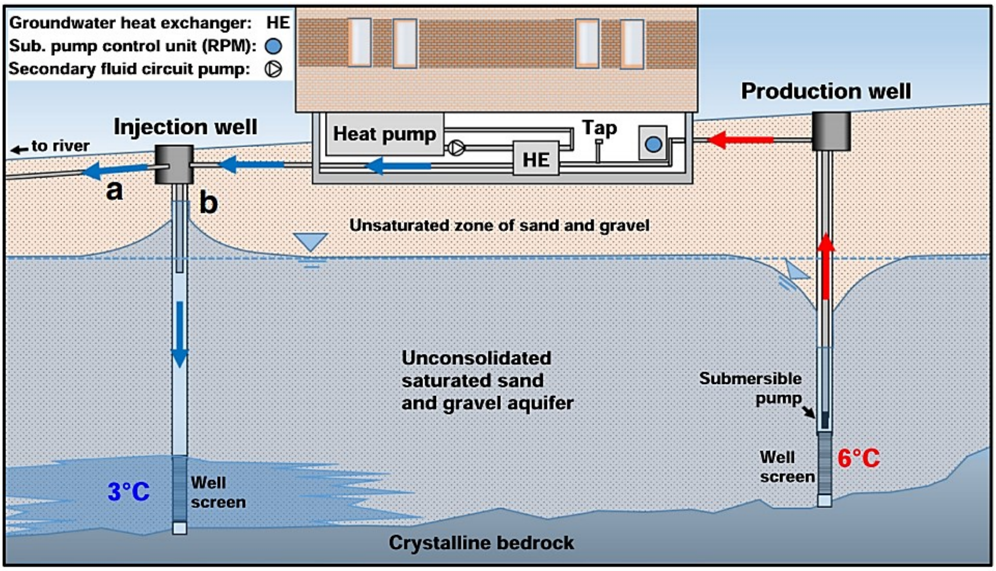

Figure 1: Principle drawing of the use of groundwater for heating purposes. Groundwater is pumped from a production well, the groundwater is heat exchanged in a separate heat exchanger prior to the heat pump. Groundwater with a few degrees lower temperature is re-infiltrated into the aquifer by an infiltration well (Gjengedal et al., 2019). Both the production and infiltration well are typically made by continuous and slotted (con-slot) screens as seen to the left in Figure 2.

A typical groundwater well in Norway

A typical groundwater well in Norway consists of con-slot well screens in a sand and/or gravel aquifer of glacial or fluvial origin. Figure 2 shows a con-slot well screen seen from the outside. A natural filter of coarser sand and gravel near the screen is made by washing out the finer particles which can be seen further out in the formation. Washing of the well screen after installation is an important step in establishing the groundwater well. The procedure consists of pulses with pumping air into the formation after the installation of the well screen. The groundwater is pushed back in the formation and when the air pressure releases, the hydraulic pressure creates a flow back which can be seen as a "blow out" of water from the well (to the right in Figure 2). Many repetitions and sectionalized washing ensure a well-functioning natural filter with high permeability around the well screen as seen in the left picture.

Commonly a groundwater well is between 10 and 40 meters deep and produces10-30 liters/second, but sometimes more. The groundwater has a stable temperature all year around. In the most northern and in mountain areas of Norway, the groundwater temperature can be too cold to utilize for heating purposes. The content of iron and manganese solved as ions in the groundwater can sometimes be challenging with respect to precipitation of oxides.

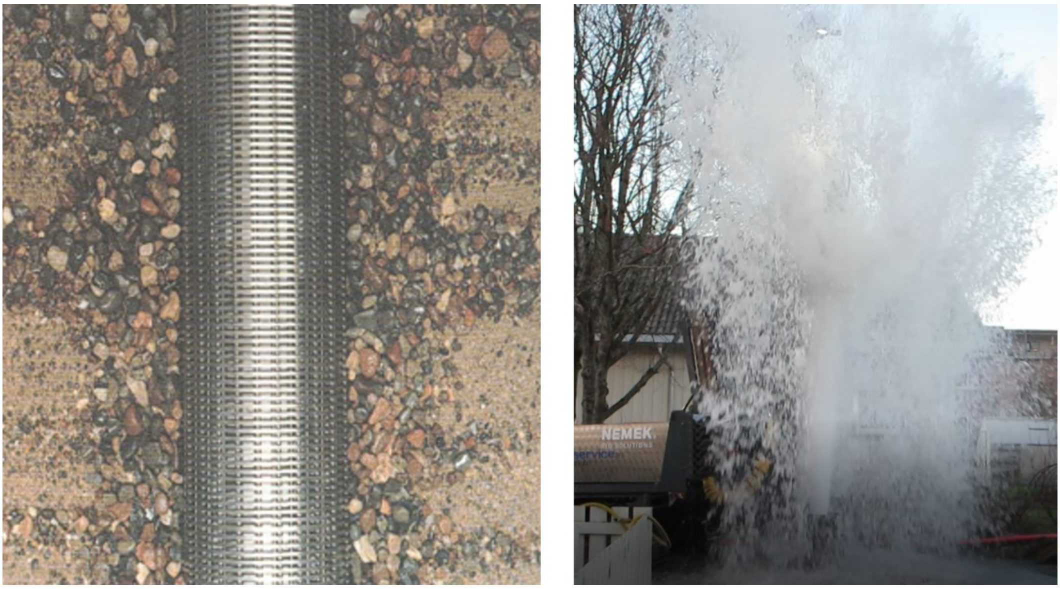

Figure 2: The left picture (from Driscoll) shows a con-slot well screen seen from the outside. A natural filter of coarser sand and gravel near the screen is made by washing (picture at the right) out the finer particles which can be seen further out in the formation. Washing of the well screen after installation can be seen of the picture to the right. Pulses of pumping air into the formation after the installation of the well screen, creates a "blow out" of water from the well. Many repetitions and sectionalized washing, ensures a well-functioning natural filter with high permeability around the well screen as seen in the picture to the left.

2. METHODOLOGY

The methodology is divided into two parts. First the sedimentation potential of suspended solids in infiltration wells is estimated, and secondly, the method for rehabilitation the infiltration well at open system GWHP plant at Lena Terrace in Melhus is described.

The main objective of the calculation of the sedimentation potential is to highlight how small concentration of suspended solids that is needed to fill up the screened part of an infiltration well with a normal diameter and a given time. Some general assumptions are the basis for the calculations, e.g. the amount of suspended solid in the groundwater is set to 0.1 mg/liter. The groundwater containing this amount of suspended solids is produced by the production well, pumped through the heat exchanger and deposited within the well, or in the well formation outside the well screen. In this study and for simplicity, all the suspended particles are assumed to be deposited in the bottom of the infiltration well. The density of the suspended solid is assumed to be 1800 kg/m^3, which is an average of the rock density (2600 kg/m^3) and water (1000 kg/m^3).

The GWHP plant at Lena Terrace was first established in 2003 and rebuilt due to several technical problems both with the groundwater system and the heat pump in 2015. Before the rebuilding, the infiltration well was used as the production well. The well screen has a diameter of 161 mm, is 10-meter-long and placed 23.5-33.5 meters below the wellhead. The specific pumping capacity of the infiltration well before the plant was put into operation in the fall of 2015 was 12 liters/second per meter cone of depression. A normal pumping rate of the plant is 16-17 liters/second supplying a heat pump of 340 kW. The infiltration capacity was too low both in February and October 2018, and a rehabilitation method by suction, jet flushing and pumping was attempted. In February the infiltration well was flowing over the wellhead with a pumping rate around 10 liters/second, and approximately 0.6 meters of the bottom of the well was filled with sediments. Several steps with jet flushing, video inspection, pumping and infiltration tests were performed. In October 2018, the groundwater level was critically high with reduced pumping rate, and suction and jet flushing were repeated in order to get the infiltration capacity high enough to secure the operation of the plant during the following heating season.

A new rehabilitation was necessary summer 2019, but now a steaming and washing method with mammoth pumping was used. The steaming means that the infiltration well is continuously filled with boiling water 12-16 hours prior to the start of the mammoth pumping. The well screen washing / mammoth pumping was done in sections of 0.5 meter which ensures a thorough and systematic cleaning of the well screen. The rubber packers sealing the section are adjusted to the well diameter. The air supply between the packers are done by an air hose around 3 meters above the section. The function of the mammoth pumping is quite similar to the washing procedure which is carried out immediately after the screen installation to obtain a natural formation filter (Figure 2).

The different rehabilitation methods used in the infiltration well at Lena Terrace will be compared with respect to removal of sediments and improvement of hydraulic properties. The different stages of well rehabilitation are documented by video filming of the well.

3. RESULTS

Sediment production, rehabilitation of the infiltration well and documentation

Assuming a very modest content of suspended solids of 0.1 mg/liter in the groundwater, the left diagram in Figure 3 shows the pumping rate versus the amount of suspended solids in the groundwater produced per day. With a constant pumping rate of 15 liters/second the amount of suspended solids following the groundwater is about 130 grams per day. These numbers correspond to a sedimentation height in the infiltration well of 1.5 meter per year if the diameter of the well is 161 mm (the right diagram in Figure 3).

Figure 4 (left picture) shows a section of the well screen before rehabilitation in February 2018 when the water was flowing over. Pictures from the video inspection of the well screen after jet flushing can be seen in the middle and to the right. The two pictures are within 10 centimeters, and large parts of the screen is still clogged with precipitated iron oxides (picture in the middle) as prior to the jet flushing (left picture), while the natural filter of sand and gravel can be seen in some parts (right picture). Some areas where the formation behind the well screen is tight and cemented were also observed. After jet flushing and simultaneously pumping, the specific capacity of the well was 7 liter/second per meter cone of depression of the groundwater.

The infiltration well at Lena Terrace has a total depth of 36.5 meter below the wellhead. In the cleaning performed in February 2018, the sediment column within the well increased from 0.6 to around 1 meter of the 3 meter long catcher pipe in the bottom of the infiltration well due to the remains from the high pressure jet flushing. Only minor sediments was removed in the cleaning in October 2018, and the infiltration well was filled with sediments up to around 32 meters below the wellhead (Figure 5 to the left– the camera stopped at 31.92 meters as the deepest) after the rehabilitation, i.e. a total of 4.5 meters with sediments. This includes 3 meters in the catcher pipe below the well screen and 1.5 meters into the well screen. This also means, that the sediment filling in the infiltration well increased by 3.5 meters in a period of approximately eight months, from February to October 2018. After the rehabilitation in July 2019 with steaming and mammoth pumping in sections of 0.5 meters, the sediments were completely removed from the infiltration well (Figure 5 and the pictures to the right). The color of the muddy water and the content of mud from the mammoth pumping varied between the sections, but was mainly brown and reddish (the pictures to the left in Figure 6). Some of the removed sediments from the well can be seen in the picture to the right of Figure 6.

Figure 7 shows the groundwater part of the monitoring display for the open system GWHP at Lena Terrace around one month before (left) and 3 weeks after (right) the rehabilitation of the infiltration well ("returbrønn), respectively. The water level in the infiltration well is only 3 meter below the wellhead with a pumping rate of 9.9 liter/second before rehabilitation, and is 17.8 m meter below the wellhead with a slightly higher pumping rate of 11.6 liter/second after the rehabilitation. The groundwater level in the infiltration well is approximately 14.5 meter lower than prior to the rehabilitation, taken into account a dry period with little precipitation. The monitoring display was established during winter 2019 and is still under development and testing.

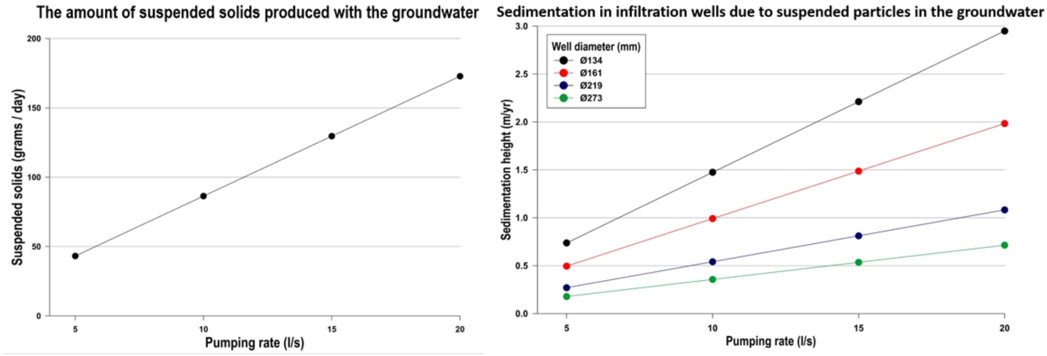

Figure 3: Pumping rate versus the amount of suspended solids and the sedimentation height in an infiltration well with different diameter can be seen on the diagram at the left and right, respectively.

Figure 4: Picture at left: The well screen is tight before rehabilitation in February 2018 when the water was flowing over. The blurry picture is caused by a thin film on the camera lens. Picture in the middle and at the right: Video inspection of the well screen after jet flushing with mixed results. The pictures are within 10 centimeters, and large parts of the screen is still clogged with precipitated iron oxides (middle), while the natural filter of sand and gravel can be seen in some parts (right picture)

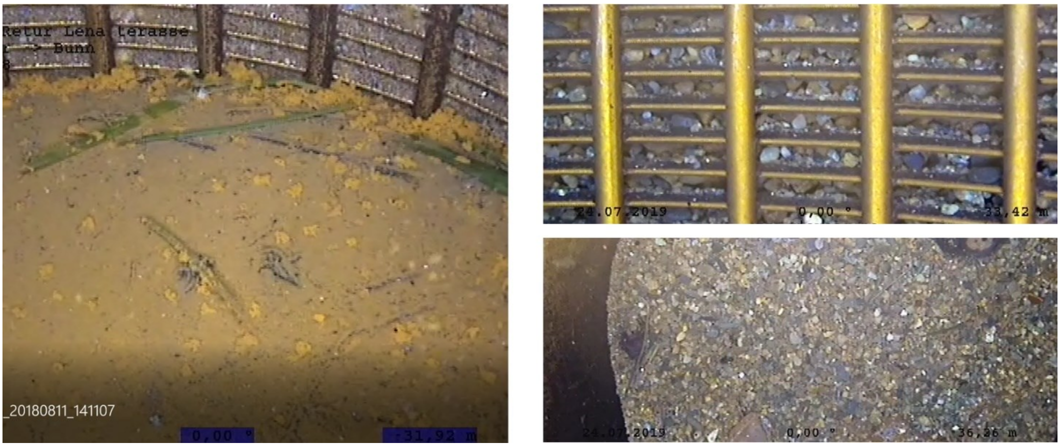

Figure 5: The left picture from the video inspection shows the infiltration well after the rehabilitation in October 2018 when sediments still fills up parts of the well screen (up to approximately 32 meters below the wellhead). The pictures at the right shows the infiltration well after rehabilitation in July 2019. The well is cleaned all the way, including 3 meters below the well screen. The upper picture is from the bottom of the well screen which was filled with sediments prior to the rehabilitation (left picture). The sand grains can clearly be seen behind the slots. The lower picture shows the sediments in the bottom of the well at around 36.5 meter below the wellhead.

Figure 6: The pictures at the left shows the mammoth pumping in the upper and lower screen section, respectively. The upper picture is muddy water cleaning the aquifer formation outside the screen (inside the formation), while the lower picture shows very muddy water from removing the sediments in the lower part of the well. The picture to the right shows some of the removed material from the well. Note the reddish color.

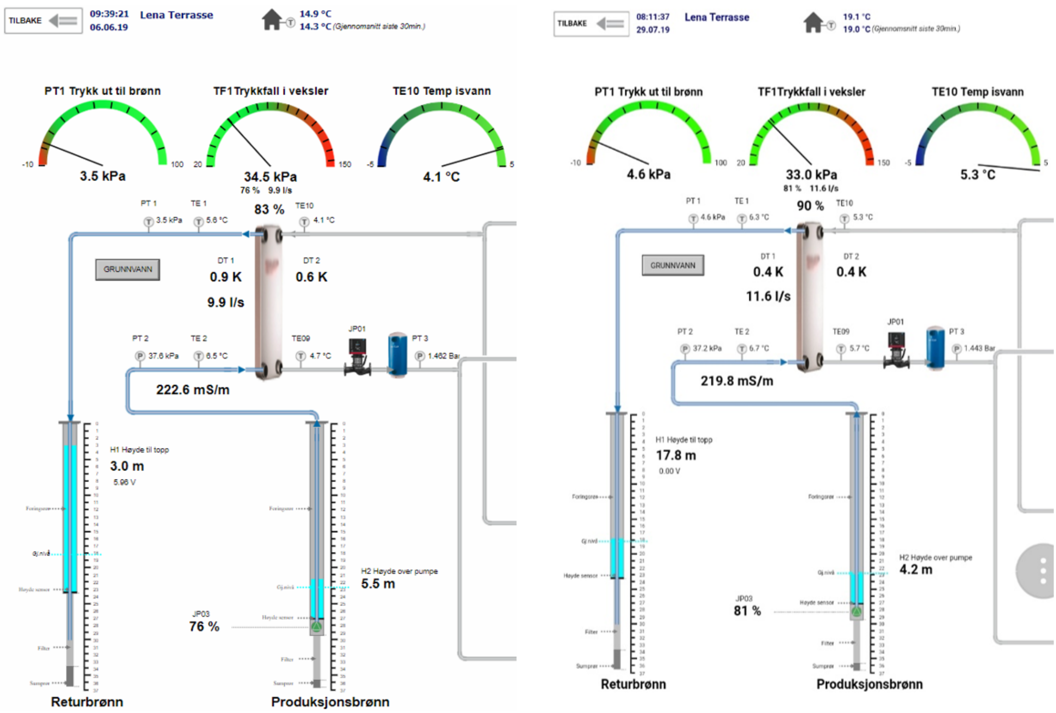

Figure 7: The groundwater part of the monitoring display for the open system GSHP at Lena Terrace around one month before and 3 weeks after the rehabilitation of the infiltration well ("returbrønn), respectively can be seen to the left and right. The water level in the infiltration well is only 3 meter below the wellhead with a pumping rate of 9.9 liter/second before rehabilitation, and is 17.8 m meter below the wellhead with a slightly higher pumping rate of 11.6 liter/second after the rehabilitation.

4. CONCLUSION AND DISCUSSION

The research project ORMEL (2015-2018) and the sequel ORMEL2 focus on the use of groundwater for energy purposes. The screened groundwater wells in sand and gravel aquifers, and especially the infiltration well has gained special attention in this article. Returning heat exchanged groundwater to the aquifer by means of an infiltration well seems to be more challenging than extracting groundwater from a production well. Another important point is that the experience with the use of screened infiltration wells at least in Norway is scarce and nearly limited to the open system GWHP installations. Before the ORMEL-projects, there has been little systematic studies on the use of groundwater for energy purposes in Norway. The key is to include the entire value chain in the research and to imply the new knowledge at the operating level in the business.

The experience from rehabilitation of an infiltration well in an open system GWHP installation at Melhus, namely Lena Terrace, has been used to illustrate the complexity of the problem and the need for a systematic approach to the topic. Here both precipitation of iron oxides and sedimentations seem to occur. The cause of the problem is not yet fully understood as well as the best rehabilitation practice for the each, and a mix of the phenomena. A calculation of the sedimentation potential where the groundwater contains a modest concentration of suspended solids was included to show that we cannot exclude the possibility that some production wells of groundwater also continuously produces suspended solids with the groundwater. For instance, a content of suspended solids of 0.1 mg/l and a continuous pumping of 15 liters/second will cause a filling of 1.5 meter per year in a 161 mm diameter infiltration well.

The sedimentation production at Lena Terrace cannot be fully explained by now, but the sedimentation filling the first 2.5 years of operation was approximately 0.6 meter, while the filling during the 8 months period from February to October 2018 was around 3.5 meters. A possible explanation of the considerable filling of sediments in that short period of time, is that the remaining residuals from the rehabilitation in February 2018 (jet flushing and simultaneously pumping) settled when the pumping was finished. The filling of 0.6 meters the first 2.5 years corresponds to only 0.016 mg/l of suspended solids with the groundwater.

The best rehabilitation results of the infiltration well at Lena Terrace seems to be the steaming and the sectional mammoth pumping. Rehabilitation of drinking water wells also often obtain good results with this method. However, the method is not widely used and offered by the industry. Compared to production wells, the need of rehabilitation of infiltration wells seems to be more present with respect to both sediments and precipitation of e.g. iron and manganese oxides (Gjengedal et al. 2019). Therefore, it is time to develop the steaming and mammoth pumping procedure further so that this well cleaning method is easily available, effective and can be used on a regular basis and before the infiltration rate in the infiltration well is critically low. In addition to the trial and error approach with jet flushing, pumping and suction, as well as the steaming / mammoth pumping, the Lena Terrace example illustrates two more important issues, namely the usefulness of the video inspection and the need for good surveillance of the operation of the open system GWHP. Video inspections document, and gives a cost effective well condition analysis, and should be used before and after well rehabilitations in addition to hydraulic tests (Gjengedal et al., 2018). The need of a central control and monitoring system is essential (Gjengedal et al. 2019). As shown for Lena Terrace which got their central control system this winter, the last rehabilitation was performed with basis of the monitoring of the water level in the infiltration well and could then be done in advance and before the situation was critical. The central control also shows the results of the rehabilitation instantly and for long periods by saving all the monitored data for eventually deeper analysis.

This broad perspective and approach concerning the use of groundwater to energy purposes should continue taking into account the ongoing plans for establishing a large-scale system in Melhus. This involves further work with design, to understand precipitation mechanisms and conditions, to achieve effective operating strategies with routinely and cost effective maintenance and targeted well rehabilitation procedures.

5. ACKNOWLEDGEMENTS

The investigations presented here are part of the research project Optimal Utilization of Groundwater for Heating and Cooling in Melhus and Elverum (ORMEL). This is a cooperation between Melhus and Elverum municipality, the Norwegian University of Science and Technology, Asplan Viak AS, the Geological Survey of Norway, receiving funding from the Regional Research Funds in Mid Norway. A huge thanks to Gjøvaag AS by Erlend Skorstad and Hallingdal Brønn og Graveservice by Rune Gurigard for the cooperation with the well rehabilitation, as well as Lena Terrace by Jan Fallmyr. Also thanks to Jan Ivar Ulfsnes at Optiview AS for the nice cooperation with the central control and monitoring system.

6. REFERENCES

Driscoll F.G.: *Groundwater and wells – second edition*. Utah water resources laboratory, ISBN 09-616-45601 (1986).

Eggen G. and Vangsnes G.: *Heat pump for district cooling and heating of Oslo Airport Gardermoen*. Proceedings of the 8th IEA Heat Pump Conference, (2005), 7 pp.

Gjengedal S, Ramstad R.K., Hilmo B.O. and Frengstad B.S.: *Video inspection of wells in open loop ground source heat pump systems in Norway*. IGSHPA conference proceedings. Stockholm. Sweden. 18-20 September. Doi: 10.22488/okstate.18.000025. (2018)

Gjengedal, S., Ramstad, R.K., Hilmo, B.O., Frengstad, B.S.: Fouling and clogging surveillance in open system GWHP systems, *Bull Eng Geol Env*. Doi: 10.1007/s10064-019-01556-5, (2019), 1-14.

Ramstad R.K., Gjengedal S., Frengstad B.S., Hilmo B.O., Dagestad A., Riise M.H., Holmberg H., Venvik G., Eikevik T., Børseth M. and Skari H.E.: *ORMEL – Optimal ressursutnyttelse av grunnvann til varme og kjøling i Melhus og Elverum*. Popular science article as the final summary of the research project (2018).

Riise, M.H.: *Praktisk guide for grunnvarmeanlegg basert på oppumpet grunnvann : Hydrogeologiske forundersøkelser, etablering, drift og oppfølging med utgangspunkt i erfaringer fra etablerte anlegg i Melhus sentrum* (Master thesis). NTNU, Trondheim (2015).

Paper III

energies

MDPI

Article

Design of Groundwater Heat Pump Systems. Principles, Tools, and Strategies for Controlling Gas and Precipitation Problems

Sondre Gjengedal [1,*], Lars A. Stenvik [1], Pål-Tore S. Storli [2], Randi K. Ramstad [1], Bernt O. Hilmo [3] and Bjørn S. Frengstad [1]

[1] Department of Geoscience and Petroleum, Norwegian University of Science and Technology, 7034 Trondheim, Norway; lars.a.stenvik@ntnu.no (L.A.S.); randi.kalskin.ramstad@ntnu.no (R.K.R.); bjorn.frengstad@ntnu.no (B.S.F.)
[2] Department of Energy and Process Engineering, Norwegian University of Science and Technology, 7034 Trondheim, Norway; pal-tore.storli@ntnu.no
[3] Asplan Viak AS, 7030 Trondheim, Norway; berntolav.hilmo@asplanviak.no
* Correspondence: sondre.gjengedal@ntnu.no

Received: 30 July 2019; Accepted: 23 September 2019; Published: 25 September 2019

Abstract: The utilization of groundwater heat pump systems is increasing in Norway, which are currently widely employed for heating and cooling applications in the town center of Melhus. The investigations of the Melhus installations are detecting gas exsolution as a possible trigger for precipitation reaction that causes incrustation of iron and manganese compounds in the systems. This paper discusses risks associated with gas exsolution and considers gas exsolution triggers in a typical Norwegian groundwater heat pump (GWHP) system configuration. The concept of the solubility grade line (SGL) is developed and suggested as a tool for optimizing the design. Based on SGL analysis and the intention of avoiding gas exsolution during heat production, an alternative system design in the same aquifer is presented and compared. The analyses show that the traditional system design is predisposed to gas clogging risks and prone to vacuum pressures in parts of the system. The alternative design mediates the risks by adjusting the well and piping configuration and by applying a backpressure technique. The results demonstrate how the groundwater heat pump system design can be customized according to local aquifer conditions to avoid gas exsolution during operation. It is recommended that the presented method of analysis should be utilized in dimensioning of systems and included in the monitoring scheme of the systems.

Keywords: groundwater; groundwater heat pump (GWHP) systems; aquifer; design and control principles; dissolved gases; temperature; pressure; hydraulic grade line; solubility grade line

---

1. Introduction

Ground source heat pump (GSHP) systems have become increasingly popular in Norway during the recent decades. Similar trends are also seen worldwide, and recent studies indicate a large potential for the technology [1]. Among a wide range of GSHP concepts, groundwater heat pump (GWHP) systems, also known as open loop GSHP systems, are unique because they extract thermal energy directly from groundwater rather than via heat collectors in soil or bedrock formations. These systems are less common than closed loop GSHP systems, but GWHP systems provide an efficient and cost-effective alternative in areas where the local hydrogeological conditions are favorable, especially for medium to large facilities (>100 kW heating capacity systems) and for facilities with large annual cooling demands.

These systems extract groundwater from an aquifer. In Norway, GWHP technology is typically applied in areas with large Quaternary deposits of saturated sand and gravel material. Many aspects of system performance are governed by the local and the over-all aquifer conditions. An aquifer formation beneath the town center of Melhus (Norway) is currently utilized as a heat source by nine individual GWHP systems. The first installation started production in 1999 and is still in operation today. A range of clogging and fouling problems has occurred in the different systems over the years, leading to the recent investigations [2–5].

The problems typically distinguish into three main categories: (1) Suspension and deposition of sediments in the system, (2) bacterial growth in the groundwater—biofouling, (3) chemical fouling, typically by iron and/or manganese compounds. These problems are identical to problems reported in many similar GWHP systems [6–13]. However, these references also emphasis several clogging issues caused by or catalyzed by a fourth problem category: (4) Exsolution of gases dissolved in groundwater. The exsolution and escape of specific gases, e.g., CO_2, can facilitate chemical imbalances in the groundwater and cause precipitation reactions. Nordell et al. [12] describe findings of iron precipitation caused by exsolution of CO_2 in borehole bedrock wells in the Emmaboda borehole thermal energy storage system. Gas exsolution also represents a direct risk of clogging by gas bubbles in, e.g., the well screen upon re-injection, which is a reported problem by many others e.g., [6,9,10]. Observations and investigations in Melhus by Brøste [3] have revealed gas bubbles in the groundwater during groundwater sampling, similar to some of the observations of Yon-Gyung et al. [14] in a CO_2 storage site in Korea. This arguably points towards gas exsolution as a possible cause for some of the clogging and fouling problems found in Melhus. This is currently being investigated.

This paper deals with the topic of GWHP design solutions and their influence on pressure- and temperature-induced gas exsolution within the systems. The traditional Norwegian design does not consider in-situ pressures and temperatures as key design parameters to avoid clogging problems, and the design thus enforces alterations to the in-situ groundwater conditions during operation. As examples of a typical gas exsolution triggers, pressure and temperature changes within a typical Norwegian GWHP system configuration are analyzed and presented. The analysis shows how the design affects the gas solubility in groundwater. An alternative design strategy introduces the solubility grade line (SGL) as a design tool for optimizing the system configuration. The new strategy provides an alternative approach to the traditional Norwegian GWHP design methodology and focuses on preventing or limiting the risk of gas exsolution.

1.1. Current Investigations in Melhus

There are two typical GWHP system design concepts employed in Melhus, i.e., with or without reinjection of groundwater to the aquifer (Figure 1). The heat pump system connects to the aquifer through a production well with slotted screens. Groundwater is pumped from the production well through a groundwater heat exchanger (HE), where thermal energy is extracted from or injected into the water. The water temperature is typically reduced or increased by 3–4 °C, respectively. The Melhus aquifer receives sufficient groundwater recharge and the systems can discharge the heat-exchanged groundwater through the local drainage system (Figure 1a). However, the more common system solution is designed to re-inject the heat-exchanged groundwater back into the aquifer in an injection well (Figure 1b). Re-injection is deemed favorable because it helps maintain the water level in the aquifer and the contractors do not have to apply for extraction permits from the regulating authorities. Groundwater from different depths are extracted depending on the location of the different installations. The shallowest installation utilizes water from a depth of 5–20 m and the deepest installation utilizes water from a depth of 60–70 m with respect to the water table.

The nine GSHP systems are cost-effective, but all of them have experienced a variety of different clogging and fouling issues. The major issues are related to clogging of the injection wells and the surrounding aquifer formation. All of the seven re-injection systems have experienced clogging of the injection well screen [5]. The clogging material is often a mixture of sediments and precipitated hydroxides [3,4]. Inspections of the systems have shown that re-injection of groundwater is done without a backpressure technique, and vacuum pressures have been observed in the re-injection pipeline in several installations. Banks [10] (p.226) discusses this issue and suggests that >0.5 bar over-pressure should be achieved everywhere within the groundwater circuit to mediate this problem. Similarly, gas-related problems in deep Australian groundwater systems (>500 m depth) have led their industrial standard to recommend fully pressurized GWHP systems, typically with 1–4 bar over-pressure [11].

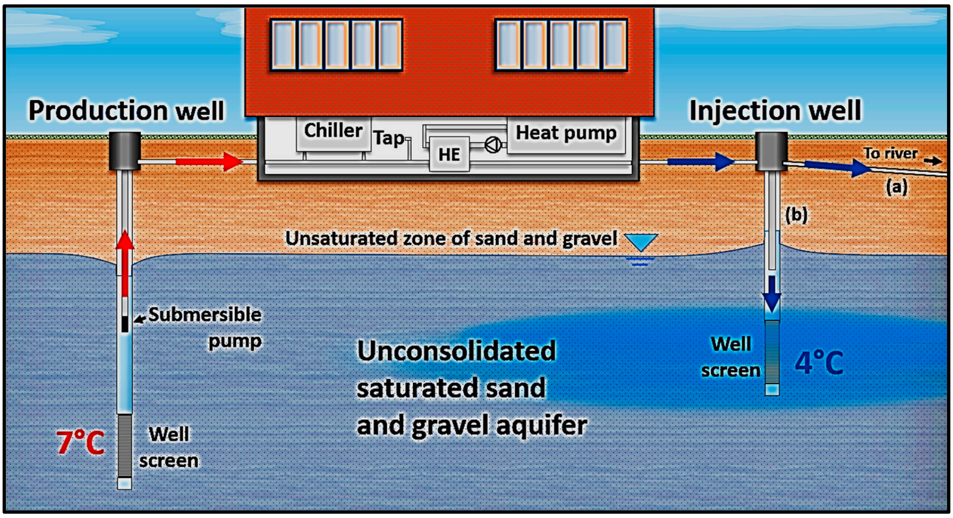

Figure 1. Types of groundwater heat pump (GWHP) systems in Melhus. (**a**) Design solution with run-off to nearby river through the local drainage system. (**b**) Most common design with re-injection of groundwater. A tap in the machinery room allows for water quality sampling.

Vacuum pressures have also been observed in the pipeline leading into the basement of the building on several occasions, sometimes as far back as the groundwater heat exchanger. Seven of the Melhus systems have experienced fouling of the groundwater heat exchanger (Figure 2a), but whether this is triggered by vacuum pressures or not is unclear. Mixing of different groundwater qualities in the system, or alteration of the groundwater temperature, are typically emphasized to explain why such fouling has occurred [6,9,10,15]. Water quality sampling of the aquifer [2,3], in different installations and observation wells, has revealed large spatial variations in both ion concentrations and dissolved oxygen levels in the aquifer. For instance, dissolved iron and manganese ions were found to vary from 0.05–5.78 mg/L and 0.01–0.68 mg/L respectively, depending on the location and depth of the different wells in the aquifer formation. The issue of chemical precipitation is thus a complex matter, probably with multiple triggering factors. In Melhus, the loss of in-situ pressure in the pipeline is now perceived to be a part of the problem.

Inspection of a particular production well in 2017 suggests that loss of pressure might be relevant for the observed fouling problems. The production wells in Melhus are seldom affected by clogging issues [4], but in this particular well, the pump was installed in the screened section of the well (Figure 2b). During a routine maintenance check of the 15-m-long screen, a video-inspection of the well revealed a minor issue where precipitated iron hydroxides were found highly localized in the screen area at the location of the suction inlet section of the submersible pump, 10–11 m below the water table. Houben [15] reports that similar observations are typical for water wells in general, and emphasizes that the rate of fouling deposition is enhanced in areas of high flow velocities. He states that this is likely caused by the mixing of different groundwater qualities, but this explanation seems insufficient considering the small area of affected screen (20 cm in diameter) after eight years of continuous operation. The suction inlet section of the pump is often associated with high entrance velocities that cause relatively large losses of hydrostatic pressure around the pump entrance. If these pressure losses contribute to exsolution of dissolved gases that in turn affect the chemical balance of the groundwater, it might provide an explanation for the observed fouling. In this case, the problem can be easily avoided by correcting the system design. The physical–chemical relations concerning gas solubility and chemical precipitation are thus relevant for GWHP designers.

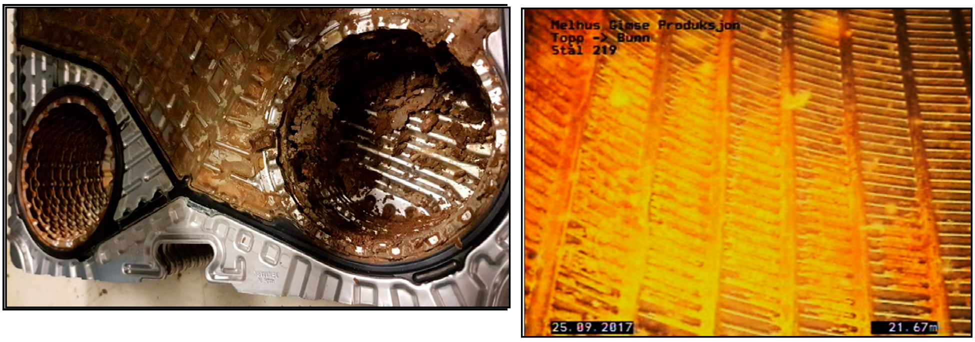

(**a**) (**b**)

Figure 2. Clogging issues in Melhus. (**a**) Iron compounds and sediment inside a groundwater plate heat exchanger. (**b**) Local iron precipitation in the well screen surrounding the water inlet of a submersible pump in a production well. Affected area is approximately 20 cm in diameter and is probably caused by loss of hydrostatic pressure and gas exsolution during production.

1.2. Relevance of Gas Solubility and Chemical Precipitation in GWHP Design

To broaden the relevance of gas solubility in GWHP systems, it is appropriate to recount the relations of some gases to that of chemical precipitation. Numerous physical-chemical relations concern the topic of dissolved gases and their possible influence on precipitation reactions. Oxygen (O_2) and carbon dioxide (CO_2) are often considered the most relevant gases because they affect the chemical equilibrium of many compounds [16]. Most of the clogging problems in Melhus are connected to precipitation of iron and manganese compounds specifically. The following section therefore focuses on these two elements in relation to oxygen (O_2) and carbon dioxide (CO_2) gases. Some possible gas-related precipitation triggers are highlighted. Microbial activity that catalyzes precipitation reactions is not within the scope of this paper.

The dissolution and precipitation of iron and manganese is governed by the solvent's redox potential (Eh) and pH [16,17]. Assuming chemical equilibria, the stability fields of various iron species can be visualized in Eh–pH diagrams. Higher Eh and pH levels in groundwater would, for most elements, tend to favor insoluble species. In the case of iron and manganese (Figure 3), it is evident that the soluble species of Fe^{2+} and Mn^{2+} are favored below $pH \approx 6$ with decreasing solubility with higher Eh levels, conditions that are commonly found in many aquifer formations. However, numerous factors control Eh and pH, thus making the dissolution–precipitation process more complex.

Eh is controlled by the oxidant availability. High Eh values indicate a large abundance of oxidants, leading to higher oxidation states of the reductants, i.e., electron donors. Oxygen (O_2) is the thermodynamically preferred oxidant. Oxygen depletion, so called anoxic conditions, make nitrate (NO_3^-), manganese (Mn^{4+}), iron (Fe^{3+}), sulphate (SO_4^{2-}), and carbon dioxide (CO_2) in sequence the thermodynamically preferred oxidants [18]. Anoxic conditions are usually found in deeper parts of water bodies, as oxygen supply is lower there [16]. Mixing anoxic groundwater with oxygen-rich groundwater, or mixing with oxygen in the air, are typical precipitation triggers because this alters the preferred iron or manganese species from soluble species, e.g., Fe^{2+}, to insoluble species that are unable to stay in solution, e.g., Fe_2O_3 (Figure 3). Groundwater quality mixing and leakages of air into the system should thus be avoided. This forms the basis for much of the prevailing emphasis on groundwater quality issues within the GWHP design [10].

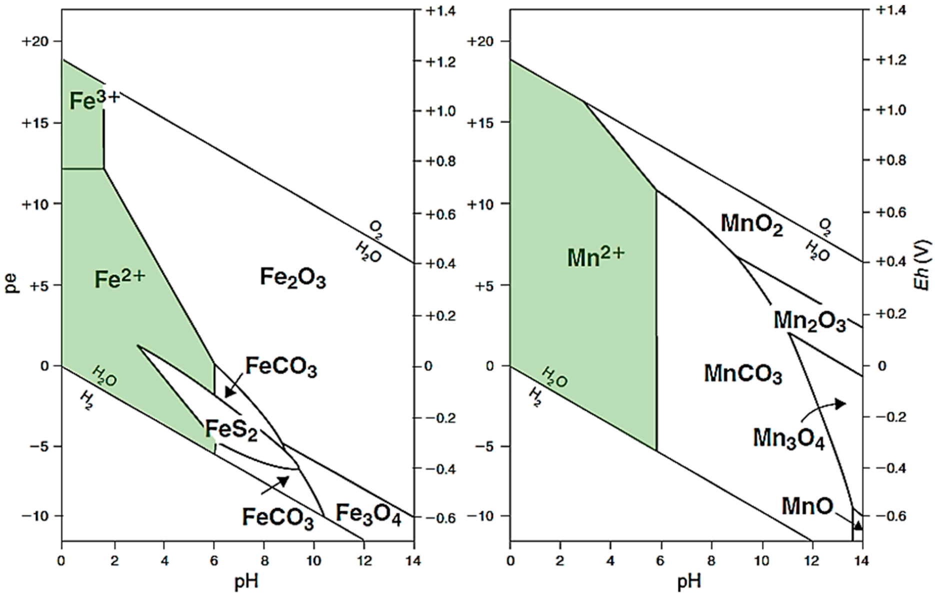

Figure 3. Relations for iron and manganese at 25 °C and 1.0 bar total pressure. Solubility contours are plotted at activities = 10^{-6}. Total dissolved sulfur = 10^{-6} mol/l. Total dissolved inorganic carbon activity = 10^{0} mol/l. Soluble species are highlighted in green, while insoluble species are shown in white (modified after [18] and [19]).

The Eh–pH diagram represents an equilibrium approach and characterizes a steady state situation where the reactions have had sufficient time to stabilize. Aquifers in general, and especially aquifers utilized in GWHP systems, never achieve equilibrium, making kinetic considerations necessary for evaluating chemical relations. The reactions involved in iron and manganese dissolution and precipitation display various rates and rate controlling factors. For the oxidation of ferrous iron, the following rate equation is relevant and exemplifies some interesting relations [20]:

$$-\frac{d\left[Fe^{2+}\right]}{dt} = k\cdot\left[Fe^{2+}\right]\cdot p_{O_2}\cdot[OH^-]^2 \tag{1}$$

where k is a temperature-dependent rate constant, $[Fe^{2+}]$ is the ferrous iron concentration, $p(O_2)$ is the partial pressure of oxygen, and $[OH^-]$ is the hydroxide concentration. Catalytic effects of other ions in solution and complex formation affects the reaction rate, which often makes the practical utilization of Equation (1) difficult. Even in ideal conditions, Equation (1) is only rate controlling up to pH ≈ 7. When pH > 8, the pH component of Equation (1) is so large that the amount of available O_2 and the diffusion of O_2 becomes rate controlling in practice [20]. Temperature effects have a minor and often negligible influence on the rate reaction constant (k). This is because the magnitude of temperature change is often small in GWHP systems, as discussed by, e.g., [21]. Without emphasizing the practical usefulness of Equation (1), the equation shows how the kinetics are more sensitive to alterations of pH than to Eh if pH > 5, due to the second order term of $[OH^-]$ and the single order term of $p(O_2)$, respectively. The works of, e.g., [15,22,23] demonstrate that the severity of precipitation problems in groundwater wells often cannot be explained by oxygenation ($p(O_2)$) or large concentration of dissolved iron ions alone ($[Fe^{2+}]$), and pH alteration mechanisms have been identified as major contributors to the problems. Accounting for pH controlling physical–chemical relations in the GWHP system design is thus relevant.

Carbon dioxide is the major pH-controlling component in groundwater [18]. This is due to the dissolution and chemical reactions CO_2 undergoes in contact with water. A relatively small proportion of the total dissolved CO_2 hydrates, forming carbonic acid (H_2CO_3). This diprotic acid affects the pH level of the groundwater and lowers the pH if the water does not have sufficient buffering capacity. The magnitude of pH change depends on the water quality in question and the amount of alteration of dissolved carbon dioxide in the water [16]. Other gases are also relevant, e.g., the sulfur system may contribute to the acidity of natural waters [24,25], but this will not be elaborated upon here.

Physical properties that control the amount of dissolved carbon dioxide in the groundwater can have an indirect influence on the pH level of the water. Gas solubility (in water) is dependent on pressure, concentration, and temperature, as stated in Henry's law [26]. Figure 4 shows data provided by Colt [27] and exemplifies the relations of Henry's law in a water body supplied with CO_2 from an atmosphere with 0.039% atm $p(CO_2)$. The figure shows that higher partial pressures and lower water temperatures facilitate more gas dissolution. For groundwater with a given chemical signature, this implies that CO_2 is more soluble at low water temperatures and higher partial pressures of $p(CO_2)$, corresponding to greater aquifer depths.

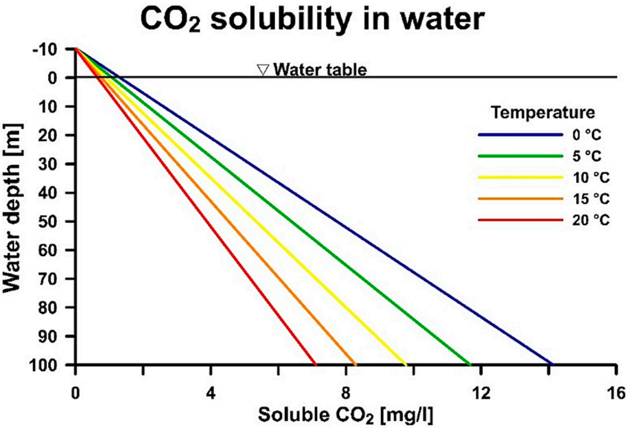

Figure 4. CO_2 solubility as a function of water depth (m) and temperature (°C). Derived from a fixed concentration of CO_2 gas of 0.039% atm $p(CO_2)$. Based on data from [27–29], found in [27].

This has practical relevance for GWHP systems, because extracting water from a water body at a given depth below the water table triggers a loss of pressure, leading to CO_2 oversaturation. The exsolution of CO_2 triggers a chemical imbalance in the groundwater. This results in a rise of pH, and subsequently causes precipitation reactions [16,18]. This phenomenon is stressed by Garcia-Gil et al. [23], who demonstrate a direct risk for precipitation in groundwater systems in Zaragoza (Spain) if the water is allowed to interact with the atmosphere before re-injection. This is both because oxygen can dissolve into the water, and also because carbon dioxide can escape the system.

The water might also be oversaturated with gas if the temperature is increased. In this way, even though the temperature effects are often negligible, e.g., on the rate reaction of Equation (1) directly (k), the temperature can have an indirect influence on the pH. Accordingly, temperature indirectly poses an important role in the kinetics. The utilization of groundwater for cooling purposes in a GWHP system is thus more at risk than a system that utilizes groundwater for heating applications.

The concentration of ions and gases in the groundwater is defined by the local geological conditions in an aquifer system, and there is typically no intension for the GWHP system to alter the chemical composition of the groundwater during production [10]. However, altering the pressure and temperature conditions of the groundwater do enforce changes to the in-situ groundwater conditions. To evaluate the pressure and temperature conditions in the whole GWHP system is necessary to properly assess the risks of gas clogging caused by gas exsolution and its possible relevance for other fouling issues.

2. Method of Analysis

To properly assess the risks of gas exsolution in a system, one must investigate the influence of the system design on the groundwater pressure and temperature during operation. GWHP systems and aquifer thermal energy storage (ATES) systems are highly fluctuating pressure and temperature systems. Pressure changes through a system can be visualized in diagrams via the hydraulic grade line (HGL); a method frequently applied in fluid mechanics [30]. The HGL describes the magnitude of hydrostatic pressure head and elevation head at any given location through the entire length of a system. The method requires a detailed description of each system component. Effects caused by size, length, and roughness of the piping system need to be considered, in addition to their elevation with respect to a common reference datum. Energy losses caused by flow through the aquifer, pump, heat exchanger, pipes, and pipefittings (valves, bends, filters, etc.) must also be considered. All these effects are dependent on the groundwater flow rate. These effects are expressed in terms of hydraulic heads (m) in the form of the steady-flow energy equation (rearranged after equation 5.77 in [30]:

$$\frac{p_2}{\rho g} = \frac{p_1}{\rho g} + \alpha_1 \frac{V_1^2}{2g} - \alpha_2 \frac{V_2^2}{2g} + (z_1 - z_2) + h_{pump} - h_{losses} - h_{turbine} \tag{2}$$

where p denotes the hydrostatic pressure (Pa), V the mean groundwater flow velocity (m/s), g the acceleration due to gravity (m/s^2), $\rho$the density of groundwater (kg/m^3), z the elevation (m) in relation to a reference plane, and $\alpha$is a correction factor for turbulence in pipes, usually α= 1.05 [30]. The subscripts 1 and 2 denote two arbitrary locations in the system. The terms $p/\rho g$are the pressure heads (m), $V^2/2g$ are the velocity heads (m), and z are the elevation heads (m) for the two point along the system. Hydraulic head supplied by the submersible pump is included in the term h_{pump} (m). The sum of all frictional and inertial losses is included in the term h_{losses} (m). The term $h_{turbine}$ (m) is usually not relevant, but signifies that regeneration of energy is possible in some system. The reader is encouraged to read [30] for more information on this topic and for examples on how to estimate these parameters in piping systems. For estimation of aquifer pressure losses, the reader is encouraged to read [31].

Equation (2) states that parts of the hydrostatic pressure are converted to kinetic energy, especially in regions of high flow velocities, e.g., at the pump entrance or through narrow channels, e.g., within a plate heat exchanger. Pressure is also converted into potential energy if the water is relocated to a point of higher elevation relative to the reference elevation. When considering their effects on gas solubility, alterations of energy forms must be considered as losses of pressure, in a similar fashion as to that of the frictional pressure losses induced by fluid flow through the system. For this reason, Equation (2) is rearranged in this paper for pressure head to give a modified form of the HGL, termed the gauge pressure head grade line (GPHGL). The assumption made is: Point 1 can be chosen to be at the water table in the aquifer and at a sufficient distance away from the inlet of the pump. The velocity squared of the water at this point is thus negligible. The reference elevation is said to be at this elevation, thereby $z_1 = 0$. The pressure here is, by definition, the atmospheric pressure, and substituting into Equation (2) the gauge pressure at an arbitrary point can be calculated by Equation (3):

$$\frac{p_{gauge}}{\rho g} = h_{pump} - z_2 - h_{losses} - h_{turbine} - \alpha \frac{Q^2}{2gA^2} \tag{3}$$

The term h_{pump} and h_{losses} are the heads corresponding to energy added by the pump and lost to friction, respectively, to the flow up to a given point. Inside the pipe, the mean velocity is conveniently calculated as Q/A, where Q is the flow (m^3/s) and A is the cross-sectional area of the pipe (m^2). The pump being a component at a fixed location means that, for a point in front of the pump, h_{pump} should not be present in Equation (3). The sum of all the head losses are met by the submersible pump, which must supply an amount of hydraulic head equal to the losses to maintain the balance of Equation (3) at the designed rate of flow. The argument for this is understood if the arbitrary point is at the water table a significant distance away from the injection well; here, the elevation is zero, the velocity squared is negligible, the gauge pressure is zero—making h_{pump} and h_{losses} equal. The equation thus also describes the power needed, P (W), to circulate the groundwater:

$$P = \frac{\rho \cdot g \cdot Q \cdot h_{pump}}{\eta} \tag{4}$$

where η is the coefficient of mechanical and hydraulic efficiency of the pump, typically ranging from 0.5–0.75 or less for submersible pumps depending on pump size and motor speed [32]. In this sense, the GPHGL also visualizes the energy needed for groundwater circulation at the specific mode of operation.

The GPHGL analysis is constructed by Equation (3) along a line (A–I) that describes the pressure exerted on the water traveling along the line through the system during operation. Along the line, the water is assigned properties with respect to the water table and the flow velocity at each point along the line. The GPHGL is a visualization of the bulk pressure exerted on the water at different segments in the GWHP system. This pressure directly controls gas solubility in the water. As the pressure varies through the system, the solubility of gases is altered according to Henry's law. The GPHGL therefore describes the general risk of gas exsolution in the system.

However, alterations of temperature in the groundwater heat exchanger renders the GPHGL and Equation (3) unable to adequately describe the system's influence on gas solubility. Combining Equation (3) with the temperature solubility relations for, e.g., CO_2 in water, the GPHGL is modified further to provide a solubility grade line (SGL) for the system in relation to CO_2 specifically. In this study, this is done for water with 0.039% atm. $p(CO_2)$, corresponding to atmospheric concentrations. This data is readily available for a wide range of temperatures and pressures in Colt [27]. The behavioral trends are seen in Figure 4, and the variable pressure and temperature components result in different solubilities for the water along the line (A–I). The reader is referred to [27] for the specific details regarding the solubility relations that constitute Figure 4. Solubility of other gases are not considered in the SGL.

For simplicity, the SGL analysis in this paper does not consider the thermal energy provided by cooling of the submersible pump motor or the thermal energy provided by frictional losses through the system, as these thermal contributions are estimated to be small in relation to the heat exchanged in the groundwater heat exchanger. Considering the GWHP system presented in Figure 1, it is apparent that several components can cause considerable alterations to the gas solubility as the groundwater travels through the system. The application of the GPHGL and the SGL will be presented in the following section for two different fictional GWHP systems with 0.039% atm. $p(CO_2)$-saturated groundwater conditions.

3. Example of Gas Exsolution Triggers and Application of the SGL

The examples presented in the following sections are theoretical and are not actual systems in Melhus. The first example presents a design that follows the traditional Norwegian GWHP concept. Numerous risk areas of this design are presented. The second example is a new design approach that eliminates all of the risk areas by relocating the system components in the aquifer. The components are otherwise identical in both examples. These two systems demonstrate that the design and location of the wells and piping system can have a profound effect on gas solubility during groundwater circulation.

For simplicity, the example cases assume that the groundwater is saturated with CO_2 at the location of the production well screen and injection well screen depths, corresponding to the solubility relations provided by Colt [27]. This situation would resemble an unconfined aquifer with limited or no organic material in the soil formation. This situation serves as an example of how gas clogging risks in an aquifer can be managed through design and system control.

The water table is, per definition, the location of the atmospheric pressure in the aquifer. The GPHGL analysis in the presented examples refers to the water table as the reference datum for gauge pressure calculations, $Z_{water\ table} = 0$. It should be noted that the water table might have seasonal fluctuations in natural groundwater systems and that the presented examples must be viewed as steady state situations. Only the aquifer, piping (3″ ID), and heat exchanger pressure losses are included in the analysis and the components are equal for the two cases, with the exception of the piping length and well depths. The cases are thus simplified versions of actual systems, but they are intended to demonstrate the concepts, not to present a specific system in Melhus.

3.1. The Traditional Norwegian GWHP Design Concept

The traditional Norwegian open loop well design follows the same dimensioning principles utilized in wells constructed for drinking water purposes. The main purpose of the design is to provide the GWHP system with sufficient groundwater circulation (Q (m^3/s)) and, thus, thermal energy. In practice, these principles involve minimizing the investment cost by limiting the well size and depth (z (m)) and, thus, reduce the drilling costs. In a homogeneous and isotropic aquifer, where impermeable sediments in the aquifer are not an issue, this principle can typically lead to the GWHP system configuration in Figure 5. Here, the injection well screen (H) is located at a shallow depth ($\Delta z > 0$ (m)) compared to the production well screen (B).

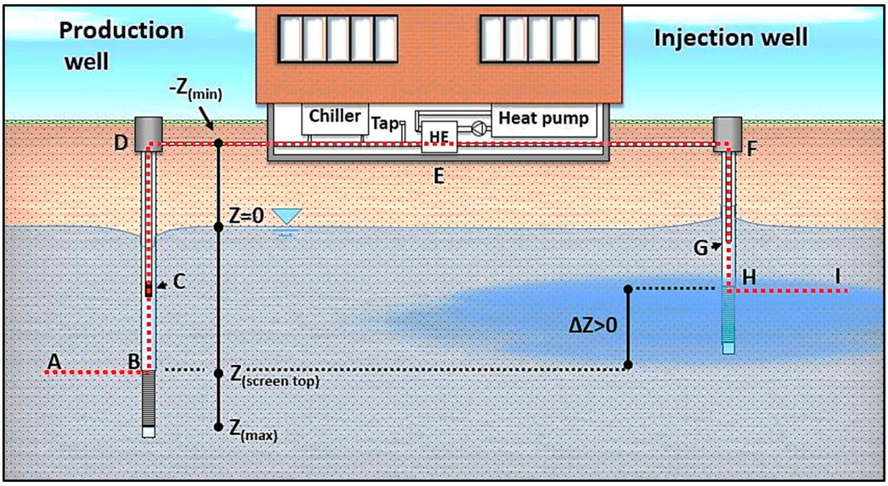

Figure 5. Traditional Norwegian GWHP design methodology can typically result in this system configuration. Different key components (A–I) are installed at various depths (z) in relation to the water level of the aquifer, $Z_{\text{water table}} = 0$ m.

The exact placement of the submersible pump in the production well (C) and the outlet pipe in the injection well (G) are selected based on evaluations of operational risks. The submersible pump must be installed sufficiently deep to prevent excessive drawdown of the well water level at the designed maximum flow rate. This often leads to a pump placement directly above the well screen, consequently maximizing the available drawdown potential of the well. However, if the well is sufficiently deep and the risks of excessive drawdown are small, the pump can typically be located as seen in Figure 5 to save costs on raiser pipe length and electrical cable. Similarly, the injection pipe outlet (G) must be submerged below the water table to limit the risk of mixing with the air in the well bore before injection. The injection pipe is rarely located deeper than a few meters below the well water table.

Before injection, the thermal energy is extracted in the groundwater heat exchanger in the basement of the building, which is located a certain elevation above the water table in the aquifer ($-Z_{\text{min}}$ (m)). The location of the heat exchanger is often close to the heat pump unit, contributing to an as short as possible indirect loop of secondary fluid, yielding lower costs associated with the indirect loop and the circulation of secondary fluid. This might be convenient in many installations, but if the distance from the wells to the building is great, the length of the groundwater loop can sometimes be several hundred meters more than the shortest distance between the wells themselves.

The system design presented in Figure 5 imposes a number of pressure changes to the groundwater as it travels through the system. As a simplified example, we can consider the following situation where the production well screen is installed at B = 20–25 m depth and the injection well screen at H = 10–15 m depth. The submersible pump is installed at C = 10 m depth and the injection pipe exit at G = 3 m depth. Figure 6 presents these key design components in view of their effects on CO_2 solubility in groundwater. In addition, the groundwater temperature is altered depending on the energy demand in the building. If there exists a cooling demand, the groundwater temperature is re-injected into the aquifer with a higher temperature than the original temperature, e.g., an increase from 5–10 °C.

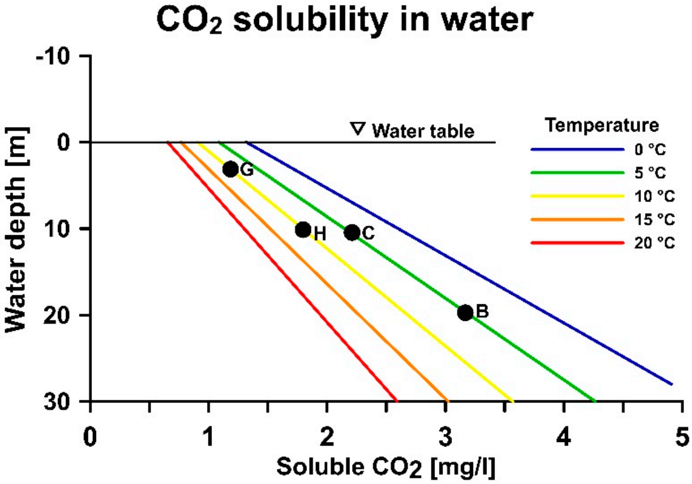

Figure 6. Degassing of CO_2 in the production well and the injection well associated with the traditional Norwegian GWHP design. The location of the screens (**B**,**H**), pump (**C**), and injection pipe (**G**) are plotted in the solubility regions for CO_2, ref. Figure 4. Here, the GWHP system operates in a 5 °C cooling mode.

The location of the pump at 10 m above the production well screen triggers a pressure drop of 1.0 bar and the solubility of CO_2 decreases (Figure 6B,C). The initial groundwater is saturated with CO_2, the gas is exsolved out of the water phase, and chemical reactions are triggered. These reactions increase the pH level of the water, which in turn can trigger precipitation reactions.

The shallow placement of the injection pipe (G) in the injection well, combined with the increased temperature caused by the cooling of the building, further decreases the solubility of gases and increases the gas exsolution (Figure 6C vs. Figure 6G). The groundwater is further depleted with CO_2 and the chemical reactions are accelerated and allowed to continue. The shallow injection screen depth prevents the CO_2 bubbles from dissolving, and the bubbles effectively clog the well screen and aquifer formation near the well (Figure 6G,H).

The GPHGL analysis of the pressure reveals the dynamic pressure changes through the piping system. The GPHGL analysis along the dotted line A–I in Figure 5 shows that the traditional system configuration is predisposed to losses of pressure after the groundwater has entered through the production well screen (Figure 7). Frictional losses in this aquifer only cause minor drawdown losses before entry through the screen (A–B). This is typical for highly permeable aquifers. The length of the well screen allows for mixing of groundwater from 20–25 m depth before the entry to the pump. The groundwater entering at the bottom of the screen is thus subjected to larger losses of pressure and corresponding changes in gas solubility.

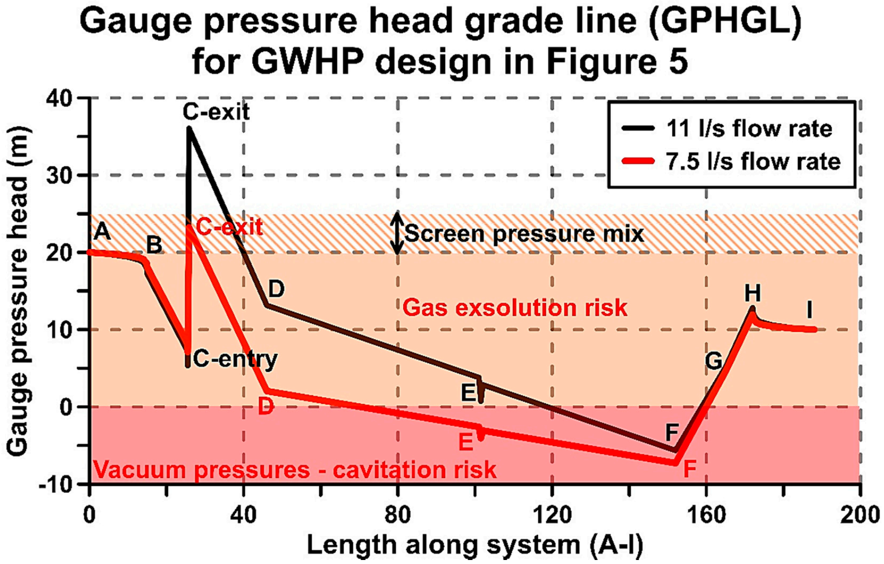

Figure 7. Pressure grade line (GPHGL) for the groundwater flow line A–I in Figure 5. The GPHGL is estimated based on Equation (3). The groundwater is saturated with gas at the depth of the well screens. The gas exsolution risk area is relevant for all types of gases, and these gases form bubbles in the highlighted area.

In addition to the 1.0 bar pressure loss before the pump (B–C), the actual pressure loss at the pump entry can be higher because of the relatively high speed of the water when entering into the pump impellers (7.5 l/s vs. 11 l/s of C-entry in Figure 7). The abrupt pressure increase displayed at C represents the additional pressure, h_{pump}, that is supplied by the submersible pump. The input power is equal to the frictional and elevation losses in the system. The input power and the supplied pressure is thus smaller for the 7.5 l/s vs. 11 l/s mode of operation. After pump exit (C-exit), the additional pressure supplied by the pump is quickly dissipated by the elevation rise towards the top well fitting (C-exit towards D).

The length D–F represents the pipe length from the production well to the injection well which, in this case, is 105 m. Since the heat exchanger is located in the basement of the building, the distance D–F is often unnecessarily long and filled with bends, valves, and filters. These components are not included in this analysis, but can contribute to local low-pressure zones along the D–F line that might enter the vacuum region of the GPHGL diagram. This is exemplified by the slight dip within the heat exchanger (E). The risk associated with vacuum is, e.g., severe gas exsolution caused by significant loss of gas solubility (Figure 4). In the worst case, the water starts to boil, and the onset of cavitation might occur. The severity of the vacuum and size of the vacuum region depends on the flow rate and the specific location of different components in the system. For this system, the heat exchanger (E) enters the vacuum region if the flow rate is reduced from 11 to 7.5 l/s (Figure 7).

The injection pipe (G) is submerged beneath the water table and the risk of entering the vacuum region is largely controlled by the elevation difference from water table within the well and the injection well top fitting (F). The elevation difference from F to the well water table causes a suction within the pipe, and the magnitude of suction is proportional to the elevation distance of F above the well water table. The re-injection of groundwater into the aquifer (I) requires an increase in the hydraulic gradient (H–I). This leads to an artificially high water level within the injection well. The magnitude of suction in the system is thus a function of the injection well characteristics and the mode of operation. For instance, the suction is larger at lower rates of flow, as seen in Figure 7.

The GPHGL analysis shows that the location of the injection well screen at a shallower depth causes a permanent loss of pressure (I vs. A). The traditional system design is unable to avoid gas clogging issues if the groundwater is saturated with gas.

3.2. New Design Principle and Proposed Alternative Design Concept

The new design alternative incorporates considerations of pressure and temperature, in addition to the traditional design principles. The design should provide the building with sufficient thermal energy without allowing gas exsolution to occur. This can be avoided by imposing a consistent rise in pressure within the system, instead of allowing pressure to drop. This means that the whole system must be designed in relation to the location of the production well screen relative to the aquifer water table (Figure 8). Solubility relations also depend on the temperature, meaning the magnitude of temperature alteration during operation must be considered in relation to the corresponding pressures needed to avoid gas exsolution.

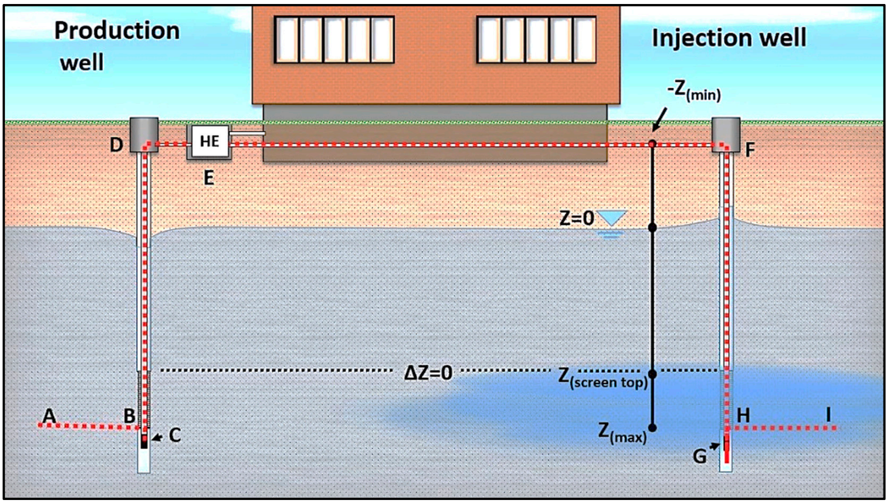

Figure 8. GWHP design concept. The heat exchanger is located outside the building in separate housing close to the production well. The slightly longer indirect loop of secondary fluid connects the heat pump to the groundwater. The depths of both well screens are equal.

The location and length of the production well screen enables extraction of groundwater with a fixed pressure range relative to the groundwater table (20–25 m). The highest pressures are found in the deepest part of the well, at the lower end of the screen. The installed depth of the screen bottom thus forms the baseline for the design (B = 25 m). The location of the pump below the screen bottom ensures that the pressure level is preserved until the water has entered the pump impellers

(C > 25 m). Similarly, the re-injection pipe in the injection well must be installed beneath the injection well screen to ensure over-pressure upon re-entry to the well (G > H). Without considering alterations to the groundwater temperature yet, it is evident that the injection well screen (H) must be installed at minimum the same depth as the production well screen to avoid a permanent loss of pressure after the groundwater has left the GWHP system.

The GPHGL analysis shows that these minor design adjustments ensure a pressure level that reduces the risk of gas exsolution in the production well and the injection well (Figure 9). The pressure drop in the aquifer around the production well (A–B) cannot be avoided, but the magnitude of drawdown can be controlled by adjusting the pumping rate through the system.

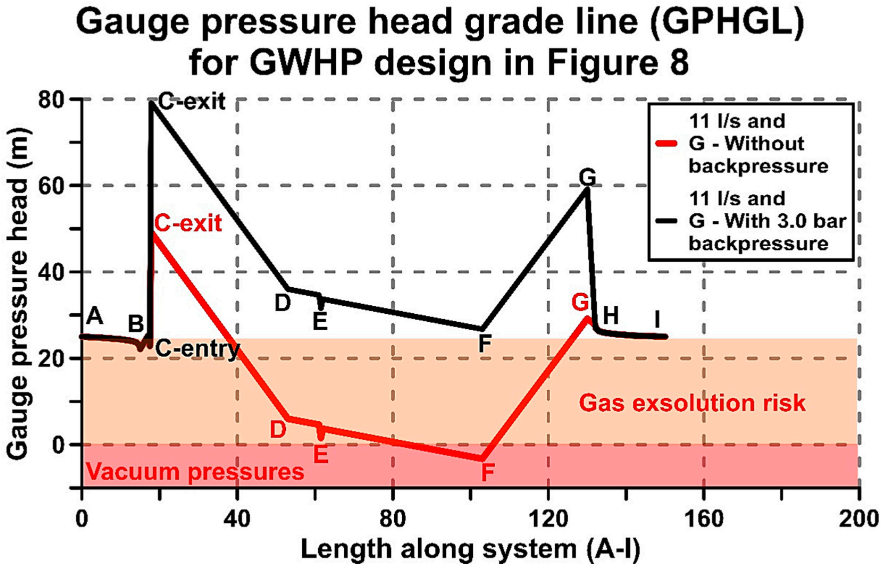

Figure 9. Pressure grade line (GPHGL) for the groundwater flow line A–I in Figure 8. Groundwater flow rate is 11 l/s for both cases. Backpressure valve is 3.0 bar (30 m) and is installed at the injection pipe exit (G).

The pressure within the groundwater pipeline (C–G) is still not sufficiently controlled. Sufficient over-pressure is only achieved by installing a backpressure devise (G). The magnitude of backpressure required is a function of the reference pressure in the production well (2.5 bar), the required elevation lift above the water table (1.0 bar), and the groundwater flow rate in the system. For instance, for the pressure to be 2.5 bar at F at zero flow, the additional backpressure at G must be 3.5 bar to simulate a 25-m-high "water column" above F. During groundwater circulation, the friction in the injection pipe and the water level increase in the injection well provide some of this backpressure. The additional backpressure needed is correspondingly less. If the flow rate is set to, e.g., 11 l/s, the GPHGL analysis of this system shows that the pipeline pressure is sufficient if the backpressure valve is 3.0 bar (Figure 9). The main drawback with the backpressure technique is the substantial amount of additional pumping power required for groundwater circulation. This is seen in the 30-m-higher C–exit point for the black GPHGL (Figure 9).

The precise location of the injection well screen and the magnitude of backpressure required is a function of the mode of system operation. The system is typically operated in heating mode or cooling mode, or a combination of these two modes, depending on the demand in the building. Since the solubility of the dissolved gases is affected by temperature, the risk of gas exsolution is affected by the mode of operation. The SGL of the black GPHGL (Figure 9) is shown in Figure 10. The SGL shows that the GWHP system in heating mode reduces the risks of gas exsolution after heat extraction. Operating the system in cooling mode forces the solubility line bellow the initial solubility limit and CO_2 exsolution occur (Figure 10). The backpressure valve of 3.0 bar is not sufficient to prevent CO_2 exsolution during cooling mode. Furthermore, the installed injection screen depth needs to be deeper in cooling mode to avoid gas exsolution in the injection well and aquifer formation. This is not necessary in heating mode, where a shallower depth would suffice for the colder water.

The location of the heat exchanger in the new design is moved to separate housing close to the production well (Figure 8). The distance D–F is reduced to 50 m in this case. This is done to exemplify the strategic benefit of controlling where in the system the temperature change should occur (Figure 10). Early heat exchange provides additional gas solubility in heating mode, and vice versa in cooling mode. The optimum location of the heat exchanger is not necessarily at the same location for both modes and installing the heat exchanger close to the production well helps to avoid vacuum pressures in the heat exchanger.

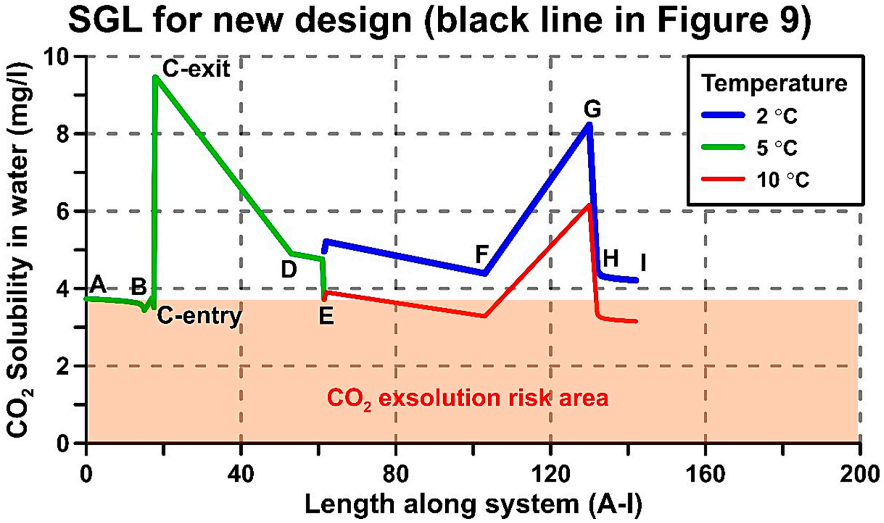

Figure 10. Solubility grade line (SGL) for the groundwater flow line A–I in Figure 8. The SGL is calculated from the black GPHGL (Figure 9) and the solubility of CO_2 in water (Figure 4). The backpressure valve is set to 3.0 bar. Return temperature after heat exchange is 2 °C for heating mode (blue) and 10 °C for cooling mode (red).

4. Discussion and Comparison of Design and Design Tools

Two different GWHP system designs have been presented in an attempt to highlight the risks of gas exsolution in such systems. GPHGL analysis is a useful tool for system analysis because it can display the effect of each system component on the hydrostatic pressure. The analysis presented in this paper only shows a simplified representation of actual systems, but demonstrates how the GPHGL can be applied for dimensioning of GWHP systems. For dimensioning of actual systems, a detailed description that includes all relevant components should be analyzed. Alternatively, an existing GWHP system can be installed with pressure sensors and the values from these sensors can be plotted in a similar fashion. This would represent the actual GPHGL of the system. It is recommended to install pressure sensors in both well water tables (B and H), on both well housings (D and F), and on both sides of the groundwater heat exchanger (E) to ensure the proper visualization of the most basic GPHGL. Some systems might require more sensors depending on the complexity of the design.

The GPHGL analysis of the traditional Norwegian GWHP system configuration shows that the system configurations are predisposed to gas exsolution risks. To some degree, these risks are unavoidable, particularly in view of the production well and its influence on the aquifer. Extraction of groundwater from an aquifer always induces loss of pressure around the well, and these losses can presumably be enough to trigger exsolution of dissolved gases if the groundwater is saturated with gas. Pre-investigation of the aquifer formation with appropriate techniques is necessary for establishing the limits of the system. The current state-of-the-art techniques applied in Norway do not consider levels of dissolved gas in the pre-investigation phase of projects [2], but this should be included in the portfolio of water quality sampling. These limits can function as the baseline for the dimensioning GPHGL analysis.

The only design parameters that can influence aquifer pressure loss are the rate of groundwater extraction or the size and length of the well screen. In this regard, it is recommended that due consideration is given to reducing the required flow rate, rather than increasing the well screen length. The length of the well screen essentially limits the range of pressures that can be extracted from the aquifer; longer screens enable groundwater with larger pressure variability and, thereby, gas solubility to enter the well bore. The screen length thus determines the risk of "groundwater quality mixing" and "pressure mixing" before groundwater extraction, as exemplified in Figure 7. Reducing the extraction rate would limit the pressure loss, but also reduce the required screen length of the well, which seems doubly beneficial if chemical stability is a concern for the system.

The GPHGL analysis shows that the installation depth of the submersible pump is a key feature in the system design. The location of the pump high above the production well screen is a possible gas exsolution trigger. The current well design is not able to prevent gas bubbles from escaping the well bore [4]. If these gases are pH-regulating, e.g., CO_2, the design might facilitate alterations of the groundwater chemistry and trigger precipitation reactions. Installing the pump below the screen bottom helps negate the risks of gas exsolution in the production well but triggers a range of other operational consequences that increase the investment cost of the production well. For instance, a flow sleeve that forces water past the motor is necessary to ensure appropriate cooling of the pump. The flow sleeve increases the width of pump and the size of the well must increase slightly to meet the space requirements. The well must also be slightly deeper to account for the installation space needed by the pump. Furthermore, a sensor that regulates the speed of the pump motor is necessary to ensure and control that excessive drawdown is prevented. The risk of sediments entering the pump is higher when the pump is installed below the screen, and appropriate screen design should be given high priority.

The highest risks are linked to the onset of the vacuum in the system, and the GPHGL analysis identifies the injection well configuration as a particularly high-risk vacuum area in the system. If the vacuum region in the system is left unchecked, it might extend backwards to the groundwater heat exchanger. Observed vacuum conditions in some of the injection wells and systems in Melhus confirm this effect. The vacuum poses a problem even if the groundwater is not fully saturated with gas, because the vacuum causes severe flashing conditions for dissolved gases and might cause the water to boil. Alternatively, if the groundwater piping system is insufficiently sealed, the vacuum can also cause invasion of air into the system through leaky components. These leakages would not be visible on the outside of, e.g., a pipe, which makes these types of faults particularly difficult to discover. This means that the traditional system design is also predisposed to air-mixing risks if components are not airtight. The onset of the vacuum can be prevented by installing a backpressure devise at the injection pipeline exit, but the magnitude of backpressure required is dependent on several factors. These factors will be highlighted in the subsequent discussion.

The GPHGL analysis shows similar results to that of the installation depth of the pump in the production well for the installation depth of the pipeline in the injection well. The location of the pipeline exit at a shallow depth, high above the injection well screen, is a possible gas exsolution trigger. A sudden drop in flow speed after the pipeline exit aids the escape of gas bubbles up the well bore, possibly triggering precipitation reactions. Installing the pipe exit below the injection well screen can negate the risks of gas exsolution in the injection well, but only if the injection well screen is installed at a depth that yields satisfactory solubility conditions. This depth is not directly revealed by the GPHGL analysis. As a general rule of thumb, this would be the same depth as the production well screen, but might be deeper or shallower depending on the mode of GSHP operation and the initial level of dissolved gas in the groundwater. There would be considerable risks associated with installing the injection pipeline below the screen if the screen is not installed sufficiently deep in the aquifer. Gas bubbles can then enter the well screen with ease and clog the well and aquifer formation.

The new design concept incorporates the solubility grade line (SGL) analysis as a tool for deciding on the specific location of the injection well screen depth. The added benefit of the SGL compared to the GPHGL is the possibility to analyze the system for groundwater qualities that are under-saturated with respect to gas. The actual gas solubility in an aquifer, discovered through pre-investigative measures, can function as a limit in the SGL (Figure 10), and the injection depth and the operational temperatures must be selected according to the limit. In the presented case (Figure 10), the groundwater is saturated with CO_2 and the injection depth should be deeper than the extraction depth if the water is used for the cooling of the building. If the water is utilized for heating purposes, the injection depth can be shallower than the extraction depth.

Operating the GSHP system in heating mode provides additional gas solubility in the groundwater and reduces the risk of gas exsolution. The strategic benefit of achieving heat exchange early in the system is apparent. This means that the groundwater heat exchanger should be installed as close as possible to the production well in systems with a predominant annual heating demand (Figure 8), and not necessarily in the basement of the building (Figure 5). The SGL also shows that the magnitude of temperature alteration in the heat exchanger can be used strategically, depending on the mode of operation. For instance, if the groundwater quality is sensitive to increased temperatures, the increase should be kept small, i.e., $\Delta T = 2–3\ ^\circ C$. Thus, most of the thermal energy could be supplied by circulating larger quantities of groundwater. Alternatively, the groundwater flow rate can be kept low and most of the thermal energy extracted by means of a larger temperature alteration, e.g., $\Delta T = 5–6\ ^\circ C$, increasing gas solubility before re-injection. Before determining the optimal mode of operation, these alternatives should be reviewed in light of their influence on the heat pump system's seasonal coefficient of performance (SCOP). Increasing the ΔT means that a heat pump would receive lower suction pressures to the compressor, which reduces the SCOP and the heating capacity of the system [33].

A major disadvantage of the alternative design strategy (Figure 8) is the large increase of work required for the groundwater circulation. A backpressure devise (G) supplies additional losses. Assuming the efficiency of a submersible pump in Figure 9 is 0.6, the added power consumption for a 3.0 bar backpressure valve is approximately 5.4 kW if the circulation rate is maintained at 11 l/s (Equation (4)). Assuming that reducing the flow rate by half would reduce the efficiency of the pump to 0.5 and the required backpressure would increase to 3.25 bar, the additional pumping power required would reduce to 3.2 kW. If this backpressure is supplied by a passive flow valve devise, e.g., a ball valve, spring valve, or a constriction at the pipe ending, this added loss leads to large amounts of "wasted" energy in the process of water circulation. These losses can presumably be too high in some cases, especially for small installations where even a slight alteration of system SCOP can disturb the financial benefit of the GWHP installation.

Passive backpressure devises also provide pressures that are flow rate-dependent, and the required backpressures could be difficult to achieve for a range of flow rates with a single devise. For instance, avoiding gas exsolution when the system is shut-off would be difficult if the backpressure is supplied by a constriction of the injection pipe. Minimizing the total amount of frictional losses, and thereby the required pumping power, is a possible solution to the problem. This could be done by increasing the pipe diameter and reducing the length of the pipeline and number of fittings, bends, valves, etc.

(D–F), or by selecting a mode of operation that requires a low rate of flow, e.g., higher ΔT through the heat exchanger.

An alternative and favorable approach would be to supply the necessary backpressure by installing a turbine that can regenerate the losses into electrical energy. A turbine can essentially be a pump working in reverse and can be preprogrammed to follow a predefined algorithm that accounts for flow rate variations in the system and only provides the backpressure needed. The turbine would also be able to retain the backpressure when the system is shut-off. Installing a turbine in GWHP systems also provides a range of benefits in regard to simplifying certain maintenance routines of the system. For instance, it enables the operator to alter the flow direction through the loop, which is useful when cleaning the system. The turbine can also function as a backup solution if the production well pump suffers unforeseen problems and must be taken out of service. A turbine seems beneficial for ATES systems in particular. ATES systems have well doublets with submersible pumps in both the production well and the injection well, irrespective of the groundwater quality. Utilizing these pumps as turbines seems beneficial, regardless of gas-related groundwater quality issues.

Another problem with the alternative design can occur if groundwater is extracted from deep aquifers with high native pressure levels. A typical example can be the Challenge Stadium installation in Perth, Australia, where the production well is located at 750 m depth [11]. Maintaining the same pressure level throughout the loop would result in more than 75.0 bar over-pressure at the surface. Some system components, the plate heat exchanger in particular, have problems with operating at such high-pressure loads. Piping materials also have pressure limitation and it is reasonable to assume that avoiding gas exsolution in deep aquifers can lead to increased investment costs if "high-grade" materials are needed in the design. On the other hand, deep aquifers have higher gas solubility and can dissolve more gas than shallow aquifers, and the alternative design might be the best solution nonetheless.

The alternative design solution offers a range of design and control strategies that arguably benefit GWHP and ATES systems in gas-saturated aquifer conditions. Some of the solutions have both benefits and drawbacks, which proposes that deriving a single optimal solution for all aquifer conditions is difficult. The added effort of avoiding gas-related issues should outweigh the downside of allowing gas exsolution to occur. The additional investment and operational costs should be lower than the clogging maintenance cost of a system built in the traditional manner. Alternatively, the additional costs must provide a more stable system with less unforeseen faults. GWHP systems that function relatively well, even though they allow vacuum conditions in the loop exist. Aquifers with low concentrations of dissolved iron and manganese ions presumably pose less risk than aquifers with high dissolved ion concentrations. In Norway, aquifers utilized for domestic water purposes have to satisfy certain national guidelines to qualify as a source of potable water. Similar guidelines should be developed for GWHP systems, where risks associated with different levels of ion concentrations and gas concentrations are explained. The guideline should preferably relate levels of ion concentrations and gas concentrations to the risks of clogging in a fashion that allows designers to select the best system configurations for particular conditions. Applying the SGL methodology to the gas solubility data allows such water quality data and guidelines to be integrated in the monitoring scheme of the plant. The data can be presented as a figure in the control unit display that is easily understood by the operator, e.g., similar to that of Figure 10. The operator would then be able to see the situation live on a monitor and assess whether the current mode of operation is within the safety limits of the aquifer.

Often in groundwater quality studies, e.g., [21–23], the effects of a GWHP system on the groundwater quality is simplified to models that investigate the production wells, injection wells, or the aquifer conditions alone. The influence of the whole system design on the pressure, temperature, and quality alterations are not necessarily accounted for. The presented examples demonstrate that, e.g., the pressure conditions within the system piping layout can provide worse gas solubility conditions in the groundwater than can be identified in the wells or aquifer itself, particularly in view of vacuum conditions. At any given GWHP aquifer, it is thus relevant to incorporate the influence of the actual system design on the development of the local groundwater quality. It is often the intension of the system designer to not alter the groundwater chemistry, but the presented results show that a given system must be customized to the particular water quality situation in question for this to be a genuine objective. Both Bakema [7] and Banks [10] emphasize the lack of input from a hydrogeologist as one of the major shortcomings in the design of groundwater GSHP systems. By simplifying the design of the piping system, it would be easier for the hydrogeologist to customize the heat source system in agreement with the challenges given by the aquifer. The application of the GPHGL and the SGL would then be easy to construct in the planning and dimensioning phase of new projects.

5. Conclusions

Problems caused by dissolved gases are closely linked to that of chemical precipitation in GWHP and ATES systems. Exsolution of dissolved gases from groundwater can be induced by alterations of in-situ pressure, concentration, and temperature conditions, and exsolution of some gases, e.g., CO_2, can catalyze precipitation reactions of dissolved ions. The design and control strategy of GWHP systems must include considerations regarding pressure and temperature alterations to mediate these risks. The gauge pressure head grade line (GPHGL) is an adequate design tool for evaluating pressure-related risks, while the solubility grade line (SGL) is a new design tool that directly evaluates and identifies gas exsolution risk zones in the entire system configuration with respect to specific gases. For this reason, the SGL should be included in the design strategy of GWHP and ATES systems.

Avoiding gas exsolution is possible through correct system design. The conditions at the production well screen depth function as the baseline of the design, and the other components must be selected based on the in-situ gas solubility in the aquifer at this location. The findings from the SGL analysis presented in this paper can be summarized as follows:

- The traditional Norwegian GWHP design is predisposed to clogging risks in gas-saturated groundwater conditions. Installing the injection well at a shallow depth compared to the production well is unfavorable. The traditional injection well configuration is a particularly high-risk component in the design because it can trigger vacuum pressures in the piping system. The injection well must utilize a backpressure devise to avoid vacuum conditions if the elevation lift from the water table is too high.
- The new design methodology can prevent gas exsolution. The new design utilizes the depth of the production well as a baseline for the design of all other components. The analysis shows that installing the pump and injection pipe below the well screens and utilizing a turbine to supply parts of the necessary backpressure in the system are necessary to avoid gas exsolution.

The new system design configuration requires higher investment costs than the traditional solution. Optimizing the design through strategic heat exchange, reducing the groundwater pipeline length, and reducing the groundwater flow rate can help decrease the cost of the new system design. However, if viewed in a broader picture, the new design might allow utilization of challenging aquifers as heat sources that would otherwise be too risky for the traditional design configuration.

Further work is being conducted that investigates the correlation of vacuum, gas exsolution, and precipitation in the affected GWHP systems in Melhus. The solubility grade line method and the alternative design methodology can then be tested and verified when designing new systems and configurations. Similar investigations in a variety of groundwater conditions should be conducted to help develop and verify the methods.

Author Contributions: Conceptualization, S.G.; methodology, S.G., L.A.S., and P.-T.S.S.; formal analysis, S.G. and L.A.S.; field investigation, S.G., L.A.S., R.K.R., B.O.H., and B.S.F.; data curation, S.G. and L.A.S.; writing—original draft preparation, S.G., L.A.S., and P.-T.S.S.; writing—review and editing, S.G., L.A.S., P.-T.S.S., R.K.R., B.O.H., and B.S.F.; visualization, S.G. and L.A.S.; Supervision, R.K.R., B.O.H., and B.S.F.; Project administration, R.K.R. and B.S.F.; Funding acquisition, R.K.R. and B.S.F.

Funding: The Regional Research Funds in Mid-Norway (grant number 209074) funded this research. The Norwegian University of Science and Technology funded the APC.

Acknowledgments: This work was conducted as part of the research project "Optimal Utilization of Groundwater for Heating and Cooling in Melhus and Elverum (ORMEL)". The project is a cooperation between the municipalities of Melhus and Elverum, the Norwegian University of Science and Technology, Asplan Viak AS, and the Geological Survey of Norway. We would like to thank all the involved institutions and persons for cooperation and financial contributions.

Conflicts of Interest: The funders had no role in the design of the study; in the collection, analyses, or interpretation of data; in the writing of the manuscript; or in the decision to publish the results.

References

1. Bloemendal, M.; Olsthoorn, T.; van de Ven, F. Combining climatic and geo-hydrological preconditions as a method to determine world potential for aquifer thermal energy storage. *Sci. Total Environ.* **2015**, *538*, 621–633. [CrossRef] [PubMed]
2. RIISE, M.H. Praktisk Guide for Grunnvarmeanlegg Basert på Oppumpet Grunnvann—Hydrogeologiske Forundersøkelser, Etablering, Drift og Oppfølging med Utgangspunkt i Erfaringer fra Etablerte Anlegg i Melhus Sentrum [eng: Guide to the Open Loop GSHP Systems in Melhus]. Master's Thesis, NTNU, Trondheim, Norway, 2015.
3. Brøste, H.M. Vannkvalitet Knyttet til Grunnvannsbaserte Grunnvarmeanlegg i Melhus og Elverum [eng: Water Quality with Respect to Open Loop GSHP Systems in Melhus and Elverum. In Norwegian]. Master's Thesis, NTNU, Trondheim, Norway, 2017.
4. Gjengedal, S.; Ramstad, R.K.; Hilmo, B.O.; Frengstad, B.S. Video inspection of wells in open loop ground source heat pump systems in Norway. In Proceedings of the IGSHPA Conference, Stockholm, Sweden, 18–20 September 2018. [CrossRef]
5. Gjengedal, S.; Ramstad, R.K.; Hilmo, B.O.; Frengstad, B.S. Fouling and clogging surveillance in open loop GSHP systems. A systematic procedure for fouling and clogging detection in the whole groundwater circuit. *Bull. Eng. Geol. Environ.* **2019**. [CrossRef]
6. Jenne, E.A.; Andersson, O.; Willemsen, A. Well, hydrology, and geochemistry problems encountered in ATES systems and their solutions. In Proceedings of the Aquifer Thermal Energy Storage, San Diego, CA, USA, 2–7 August 1992. [CrossRef]
7. Bakema, G. *Well and Borehole Failures in UTESS: State of the Art 2000 (Second Draft)*; IF Technology Report 2/9805/GW; 2001; Unpublished work.
8. Banks, D.; Pumar, A.F.; Watson, I. The operational performance of Scottish minewater-based ground source heat pump systems. *Q. J. Eng. Geol. Hydrogeol.* **2009**, *42*, 347–357. [CrossRef]
9. Oldmeadow, E.; Marinova, D. Into Geothermal Solutions: The Sustainability Case for Challenge Stadium in Perth, Western Australia. *Environ. Prog. Sustain. Energy* **2010**, *30*, 476–485. [CrossRef]
10. Banks, D. *An Introduction to Thermogeology: Ground Source Heating and Cooling*, 2nd ed.; Wiley-Blackwell: Chichester, UK, 2012; pp. 1–526.
11. Pujol, M.; Richard, L.P.; Bolton, G. 20 years of exploitation of the Yarragadee aquifer in the Perth Basin of Western Australia for direct-use of geothermal heat. *Geothermics* **2015**, *57*, 39–55. [CrossRef]
12. Nordell, B.; Scorpo, A.L.; Andersson, O.; Rydell, L.; Carlsson, B. *Long-Term Evaluation of Operation and Design of Emmaboda BTES: Operation and Experiances 2010–2015*; Research Report; LTU: Luleå, Sweden, 2015; ISBN 978-91-7583-530-3.
13. Snijders, A.L.; Drijver, B.C. Open-loop heat pump and thermal energy storage systems. In *Advances in Ground-Source Heat Pump Systems*, 1st ed.; Rees, S., Ed.; Woodhead Publishing: Amsterdam, The Netherlands, 2016; pp. 247–268. [CrossRef]
14. Yon-Gyung, R.; Hyun-Kwon, D.; Kyoung-Ho, K.; Seong-Teak, Y. Vertical Hydrochemical Stratification of Groundwater in a Monitoring Well: Implications for Groundwater Monitoring on CO_2 Leakage in Geologic Storage Sites. *Energy Procedia* **2017**, *114*, 3863–3869. [CrossRef]
15. Houben, G.J. Iron oxide incrustations in wells. Part 1: Genesis, mineralogy, and geochemistry. *Appl. Geochem.* **2003**, *18*, 927–938. [CrossRef]
16. Stumm, W.; Morgan, J.J. *Aquatic Chemistry: Chemical Equilibria and Rates in Natural Waters*, 3rd ed.; Wiley: New York, NY, USA, 1996.
17. Garrels, R.M.; Christ, C.L. *Solutions, Minerals and Equilibria*, 2nd ed.; Harper & Row: New York, NY, USA, 1965.

18. Appelo, C.A.J.; Postma, D. *Geochemistry, Groundwater and Pollution*, 2nd ed.; CRC Press: Leiden, The Netherlands, 2005.
19. Krauskof, K.B. *Introduction to Geochemistry*, 2nd ed.; McGraw-Hill: New York, NY, USA, 1979.
20. Stumm, W.; Lee, G.F. Oxygenation of Ferrous Iron. *Ind. Eng. Chem.* **1961**, *53*, 143–146. [CrossRef]
21. Possemiers, M.; Huysmans, M.; Batelaan, O. Influence of Aquifer Thermal Energy Storage on groundwater quality: A review illustrated by seven case studies from Belgium. *J. Hydrol. Reg. Stud.* **2014**, *2*, 20–34. [CrossRef]
22. Larroque, F.; Franceschi, M. Impact of chemical clogging on de-watering well productivity: Numerical assessment. *Environ. Earth Sci.* **2011**, *64*, 119–131. [CrossRef]
23. García-Gil, A.; Epting, J.; Ayora, C.; Garrido, E.; Vázquez-Suñé, E.; Huggenberger, P.; Gimenez, A.C. A reactive transport model for the quantification of risks induced by groundwater heat pump systems in urban aquifers. *J. Hydrol.* **2016**, *542*, 719–730. [CrossRef]
24. Brown, K.A. Sulphur in the environment: A review. *Environ. Pollut. Ser. B Chem. Phys.* **1982**, *3*, 47–80. [CrossRef]
25. Brookins, D.G. *Eh-pH Diagrams for Geochemistry*, 1st ed.; Springer: Berlin, Germany, 1988; ISBN 3540184856.
26. Henry, W., III. Experiments on the quantities of gases absorbed by water, at different temperatures, and under different pressures. *Philos. Trans. R. Soc. Lond.* **1803**, *93*, 29–273.
27. Colt, J. *Dissolved Gas Concentration in Water: Computation as Functions of Temperature, Salinity and Pressure*, 2nd ed.; Elsevier: Amsterdam, The Netherlands, 2012.
28. Weiss, R.F. Carbon dioxide in water and seawater: The solubility of a non-ideal gas. *Mar. Chem.* **1974**, *2*, 203–215. [CrossRef]
29. Millero, F.J.; Poisson, A. International one-atmosphere equation of state of seawater. *Deep Sea Res. Part A Oceanogr. Res. Pap.* **1981**, *28*, 625–629. [CrossRef]
30. Çengel, Y.A.; Cimbala, J.M. *Fluid Mechanics: Fundamentals and Applications*, 2nd ed.; McGraw-Hill: Boston, MA, USA, 2014.
31. Kruseman, G.P.; Ridder, N.A.D.; Verweij, J.M. *Analysis and Evaluation of Pumping Test Data*, 2nd ed.; International Institute for Land Reclamation and Improvement: Wageningen, The Netherlands, 1990.
32. Grundfos A/S. Grundfos Data Booklet. SP A, SP Submersible Pumps, Motors and Accessories. ECM: 116286. Denmark. Grundfos a/s. 2017. Available online: http://www.grundfos.com (accessed on 9 April 2019).
33. Stene, J. *Varmepumper: Grunnleggende Varmepumpeteknikk [eng: Heat Pumps: Basics]*; SINTEF Energi, Klima-og Kuldeteknikk: Trondheim, Norway, 2001.

Paper IV

Fouling and clogging surveillance in open loop GSHP systems

Sondre Gjengedal, Randi K. Ramstad, Bernt O. Hilmo & Bjørn S. Frengstad

Bulletin of Engineering Geology and the Environment
The official journal of the IAEG

ISSN 1435-9529

Bull Eng Geol Environ
DOI 10.1007/s10064-019-01556-5

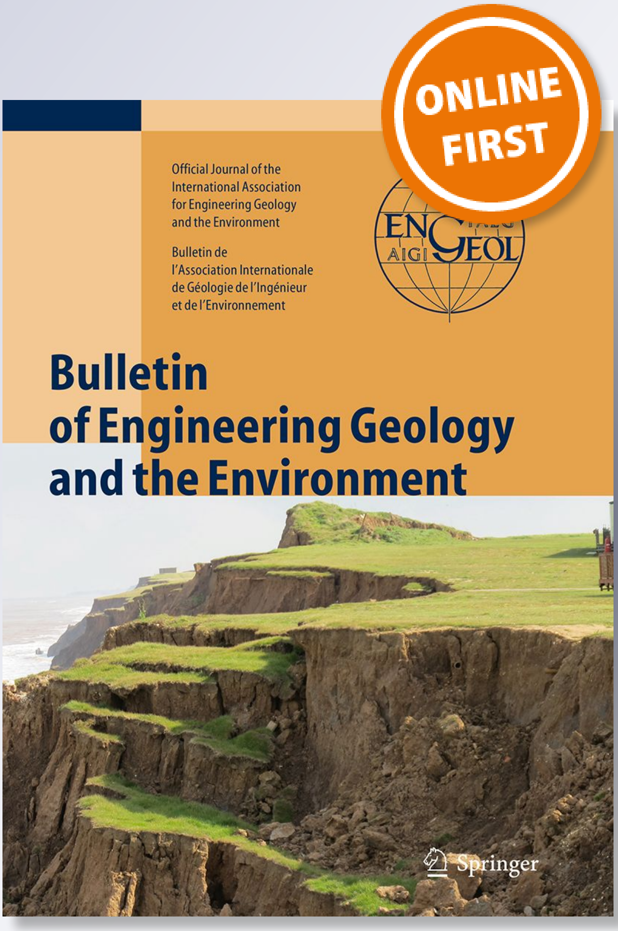

Springer

Bulletin of Engineering Geology and the Environment
https://doi.org/10.1007/s10064-019-01556-5

ORIGINAL PAPER

Fouling and clogging surveillance in open loop GSHP systems

A systematic procedure for fouling and clogging detection in the whole groundwater circuit

Sondre Gjengedal[1] · Randi K. Ramstad[1] · Bernt O. Hilmo[2] · Bjørn S. Frengstad[1]

Received: 29 August 2018 / Accepted: 28 May 2019

Abstract

Fouling and clogging are some of the major water quality problems encountered in open loop ground source heat pump (GSHP) systems and aquifer thermal energy storage (ATES) systems. Here we present a surveillance strategy that can detect if and identify where in the system fouling and clogging might be developing without having to shut off the heat pump. In the presented system design, the test requires a minimum of four temperature sensors and two pressure sensors to describe the performance of the four major heat source system components, namely, the production well, the injection well, the submersible pump and the groundwater heat exchanger. The surveillance procedure involves conducting a step-test with incremental increases in the groundwater flow rate while measuring the pressure and temperature responses in the system components. The performance of the newly constructed installation functions as a baseline for future tests. By conducting the test systematically during operation an altered performance of the system can indicate clogging or fouling issues. Even though the cause of the problem must be identified through other means, the surveillance procedure presented here allows the operator to plan necessary maintenance and avoid critical damage to the heat source system.

Keywords Open loop GSHP systems · Aquifer · Fouling · Clogging · System performance surveillance · Step-test

Introduction

Groundwater quality is an important factor in open loop ground source heat pump (GSHP) installations (Bakema 2001; Banks 2012; Rees 2016). Chemical reactions, suspended soil particles and/or microbial growth in the water can cause a wide range of problems for the system. These problems can involve corrosion, clogging and increased fatigue and erosion of the submersible pump, groundwater heat exchanger, well screen and pipeline as well as clogging of the aquifer formation. Usually the performance of the heat pumps and overall cost of the operation is affected by reduced heat production. However, in severe cases, the complications can lead to complete system failure.

In this paper we present experiences with fouling and clogging of open loop GSHP systems in Melhus, Norway. We first describe the effects of fouling and clogging on the four major affected components in the system, i.e. the production well, the injection well, the submersible pump and the groundwater heat exchanger. We then present a surveillance procedure for fault detection. The described surveillance procedure measures the system performance and, when applied systematically during operation, it can identify potential clogging or fouling issues in each of the four major components. The surveillance procedure is also valid for aquifer thermal energy storage (ATES) systems as well as relevant for groundwater wells for drinking water and industrial purposes.

Clogging and fouling of system components of GSHP systems is a commonly encountered problem in Melhus (Riise 2015; Brøste 2017). The main concerns are the chemical reactions that result in the precipitation of particles that subsequently accumulate on surfaces inside pumps, pipes, heat

✉ Sondre Gjengedal
sondre.gjengedal@ntnu.no

Randi K. Ramstad
randi.kalskin.ramstad@ntnu.no

Bernt O. Hilmo
BerntOlav.Hilmo@Asplanviak.no

Bjørn S. Frengstad
bjorn.frengstad@ntnu.no

[1] Department of Geoscience and Petroleum, Norwegian University of Science and Technology, Trondheim, Norway

[2] Asplan Viak AS, Trondheim, Norway

exchangers and other components in contact with the circulating groundwater. Since the buildup of particles occurs on surfaces that are not visible to the operator, the problems are often not predictable during normal system operation and undetected until a critical failure is imminent. The examples presented in this paper were discovered during maintenance checks when components such as pipes, well screens, submersible pumps or heat exchangers had failed and had to be repaired or cleaned. This approach is costly, not only because of the maintenance cost and downtime of the heat pump, but also because the heat pump operates at a lower coefficient of performance (COP) prior to failure.

The current GSHP systems in Melhus are not sufficiently equipped with sensors to detect the development of fouling and clogging problems. While some installations are now endeavoring to do so, there still exists a need for a procedure that can help the operator to distinguish normal system performance from the effects caused by fouling and clogging. If clogging and fouling can be detected at an early stage, the operator would be able to plan necessary maintenance and avoid critical damage to the heat source system.

Background

Within the concept of ground source heat, the open loop system differs from the more common closed loop system. The open loop system utilizes groundwater as a source of thermal energy by employing a heat pump coupled with a heat distribution system in the building. Groundwater wells in Norway are typically established in aquifers of unconsolidated sand and gravel deposit. This is also the case for the town center of Melhus in Norway. The Melhus aquifer has been utilized for heating and cooling purposes since 1999, which makes Melhus a pioneering municipality in Norway in terms of open loop systems (Riise 2015). At the present time, the aquifer supplies nine building complexes with heat, and three of them with cooling as well.

There are two typical open loop GSHP system schemes in Melhus (Fig. 1). The heat pump system connects to the aquifer through a production well with slotted screens. The submersible pump is installed above the top of the well screen to minimize the risk of air entering the aquifer, which potentially could allow air bubbles to clog the well screen and the aquifer formation. Groundwater is pumped from the production well through a heat exchanger, where heat energy is extracted from the water by reducing its temperature. A temperature reduction of 3–4 °C is typical, but this depends on the heat demand in the building and often varies throughout the heating season. The two oldest GSHP systems dispose of the heat-exchanged groundwater to a nearby river through the local drainage system (Fig. 1a). The newer and more common systems re-inject the exchanged groundwater back into the aquifer through an injection well (Fig. 1b). Re-injection is deemed favorable because it helps maintain the water level in the aquifer.

Similar to other water heat sources, such as seawater or lakes, open loop GSHP systems are disposed to complications arising from water quality problems (Bakema 2001; Stene 2001). Typical problems can involve corrosion of components or different types of biological, chemical or mechanical clogging and fouling. The severity of the problems often depend on the on-site water quality, and a tap is often installed in the systems for groundwater quality sampling (Fig. 1). The groundwater in the Melhus aquifer has a brackish quality and contains more dissolved ions than does freshwater (Riise 2015; Brøste 2017). Thus, the open loop system design follows the same principles of some seawater heat pump systems in which an indirect system with an additional

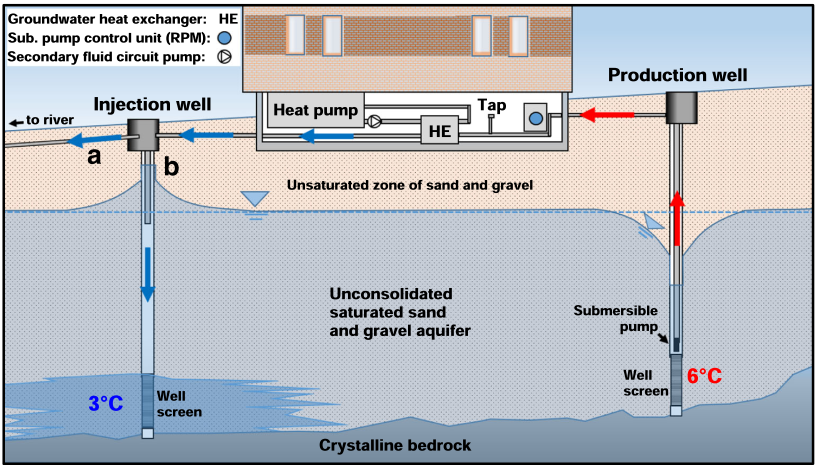

Fig. 1 Two types of open loop ground source heat pump (GSHP) systems in Melhus. **a** Design solution with run-off to nearby river through the local drainage system, **b** most common design with re-injection of groundwater

groundwater heat exchanger separates the heat pump unit from the groundwater (Fig. 1). The groundwater heat exchanger is customized to the particular water quality condition. This customization protects the evaporator from corrosion, fouling and freezing risks and will often be the most economical capital cost solution for the system. However, the additional heat exchanger has the disadvantages of lowering the COP of the system and increasing the operational costs (Stene 2001).

Precipitated hydroxide particles are present in all of the nine heat pump installations in Melhus. Water quality investigations have shown that high concentrations of dissolved iron and manganese occur naturally in the groundwater at levels of up to 5.78 and 0.68 mg/l, respectively (Riise 2015; Brøste 2017). When exposed to an oxidizing agent, such as, oxygen in the air, dissolved iron and manganese ions readily precipitate as hydroxide particles. Thus, some of the fouling and clogging problems are deemed to be related to leakages of air into the heat source systems. Other possible causes might be related to alterations in groundwater pH through a loss of pressure and subsequent degassing of dissolved carbon dioxide, as discussed by Banks (2012) and Bakema (2001).

Fouling and clogging problems can be categorized into five major problem types in GSHP systems. Depending on the system design and water quality, one or more of the following problems might develop:

Problem (1): **Clogging of the production well screen** leads to reduced groundwater flow rate and a loss of well production capacity. Clogging of the screen causes the water level in the well to drop further than intended during pumping. If the water level in the well drops down to the pump, mixing of air into the system will become a major problem. Two such events have occurred in Melhus (Fig. 2a, b).

Problem (2): **Clogging of the injection well screen** leads to reduced groundwater flow rate and insufficient injection capacity. This development is the most commonly encountered problem, and all of the seven injection wells in Melhus have had clogging problems. The clogging material is often found to be a mixture of sand, silt and clays along with iron and/or manganese hydroxides. Microbial growth has been discovered in one injection well. Flooding on the surface has occurred where the clogging issue was severe.

Problem (3): **Clogging in the aquifer.** It is possible for particles to deposit in the aquifer formation itself. This is a problem discussed by Andersson et al. (1984) and Bakema (2001). The problem might develop if particles infiltrate through the injection well screen, allowing the particles to re-enter the aquifer and clog the pore-space in the sediments. The problem might also develop because of chemical reactions between the native groundwater and the injected groundwater with a different chemical composition. The clogging reduces the hydraulic conductivity of the aquifer locally and can affect the performance of the production well or injection well. There are registered two cases of aquifer clogging in Melhus.

Problem (4): **Precipitation within pipes and other components** of the GSHP systems narrows the cross-sectional flow area and induces increased friction to groundwater flow through the system. The increased friction ultimately renders the submersible pump unable to supply enough water to the groundwater heat exchanger. Five of the open loop GSHP systems in Melhus have experienced such problems. On one occasion, a 1-cm-thick film of iron hydroxide coating was found during a maintenance check (Fig. 2c). If the friction losses become

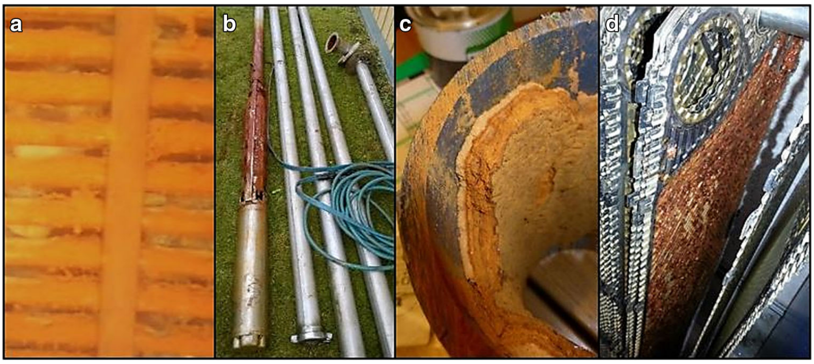

Fig. 2 Iron hydroxide problems encountered in the open loop GSHP systems in Melhus. **a** Clogging of a production well screen, **b** damaged submersible pump, **c** old pipe section with 1-cm-thick film of iron hydroxide (photograph courtesy of Rolf Aune, Trondheim), **d** fouling in a plate heat exchanger

too high, the submersible pump will not operate reliably and can fail. This has occurred once in Melhus.

Problem (5): **Particles deposit in the heat exchanger.** The deposits not only cause increased friction to flow, but also function as insulation that reduces the heat transfer efficiency of the heat exchanger (Fig. 2d). Plate heat exchangers (PHE) are the preferred heat exchanger type in the GSHP systems in Melhus. Gasket PHE types can be opened for inspection and are often preferred over the brazed PHE types, but both types are used. Compared to other heat exchanger types PHEs are deemed to be reliable with respect to fouling because they are designed to operate within turbulent flow conditions (Melo et al. 1988; Stene 2001). Nevertheless, seven of the open loop GSHP system in Melhus have experienced heat exchanger fouling and clogging issues, typically caused by iron and/or manganese hydroxides.

Common system control and surveillance strategies

The heat pump units in open loop GSHP systems are controlled in order to produce enough heat to meet the heat demand in the building being serviced by the system. The demand varies throughout the year, with peak demands during the winter months and minimum demands during the summer months. The heat demand is transferred to the heat pump by controlling the heat extraction process from the groundwater heat exchanger. Typical control and instrumentation schemes are illustrated in Fig. 3. The secondary fluid pump is usually equipped with an on/off control and a constant flow rate. A variable speed drive (VSD) control unit typically controls the submersible pump in the open loop GSHP systems. This VSD control unit allows the system to adjust the rotational speed of the submersible pump motor (RPM), specifically in terms of its frequency (Hz), which in turn adjusts the flow rate. Seven of the nine systems in Melhus operate the VSD at constant speeds. Consequently, these systems control the heat production rate through temperature variations in the groundwater heat exchanger. The remaining two systems operate the VSD according to the temperature of the heat-exchanged and injected groundwater. These latter two systems control the groundwater flow rate to maintain a fixed temperature in the temperature sensor denoted T3, typically 2–3 °C (Fig. 3). To minimize the risk of excessive pumping, one of the two systems simultaneously controls the flow rate according to the water level in the production well. The flow rate is reduced if the pressure level in the well drops below a predefined level in sensor p1 (Fig. 3).

As shown in Fig. 3, pressure (p1–p3) and temperature (T1–T4) sensors are the main sensor types applied for system surveillance in Melhus because these are low cost and easy to fit. Some of the larger installations monitor the volume flow rate, but the overall cost of the sensors is probably the main reason why volume flowmeters (FL in Fig. 3) are absent in the small-capacity (≤ 100 kW) open loop GSHP systems. These sensor types are common in many heat pump applications (Stene 2001; Rees 2016) and also commonly used for system surveillance in other industries and industrial applications, such as, for example, district heating applications, oil and gas industries (Melo et al. 1988; Müller-Steinhagen 2000) and food processing industries (Nema and Datta 2005).

None of the installations in Melhus follows a defined surveillance procedure with systematic data logging. Furthermore, the data provided by the sensors and instruments shown in Fig. 3 are inadequate because they fail to incorporate all of the relevant components in the system. Common to all the systems is a lack of pressure monitoring of the production well and the injection well. Only one system monitors the pressure in the production well, while none of the systems monitor the pressure in the injection well. Only four of nine installations monitor the volume flow rate, which is considered to be a vital parameter in open loop systems surveillance (Banks 2012; Rees 2016). The most common approach focuses on detecting fouling of the groundwater heat exchanger

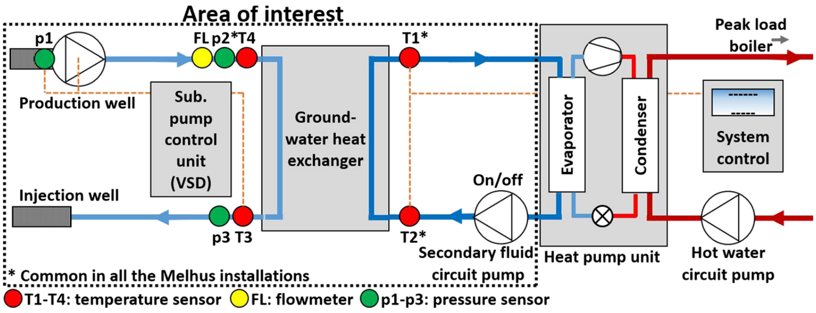

Fig. 3 Schematic diagram of the principle components of the typical open loop GSHP system in Melhus with temperature sensors, pressure sensors and flowmeter. *VSD* Variable speed drive

with pressure sensors p2 and p3. An increase in the differential pressure between pressure sensors p2 and p3 can indicate a potential fouling problem in the groundwater heat exchanger. However, pressure is dependent on the flow rate, and such data are often difficult to interpret without information from a flowmeter. This is particularly the case when the flow rate is highly variable, which can occur when the VSD controls the flow rate according to the return temperature of the heat-exchanged groundwater (T3). Furthermore, only two of the nine installations in Melhus have included temperature sensors T3 and T4 into their system surveillance scheme.

System performance

Each of the five problems described in the Background section affect the performance of the open loop GSHP system in a distinctive way, and the respective effects are detectable if the system is equipped with the appropriate sensors and control equipment. The initial system performance must be understood, and there must also be an understanding of how fouling and clogging can change the initial performance. In this section we focus on explaining these changes and provide the necessary analytical tools for detecting fouling and clogging.

In the specific open loop GSHP system shown in Fig. 1, the design of the system limits the potential problems to an area of interest, as shown in Fig. 3. Within this area, the submersible pump and the secondary fluid circulation pump are active components that provide fluid flow through the groundwater heat exchanger. The heat exchanger can be termed an active component in terms of the flow of heat from one fluid to the other. The wells and the pipes can be termed passive components. Understanding the behavior of the pumps and the heat exchanger is important because they are affected regardless of where in the system fouling or clogging develops.

Groundwater heat exchanger performance and fouling effects

There are a large variety of different heat exchangers, and their respective performance is dependent on both design and materials. The overall performance of any heat exchanger can be described by heat rate Eqs 1–3 (Stene 2001; von Böckh and Wetzel 2012).

$$Q_w \cdot \Delta T_w \cdot \rho C_{Pw} = P \tag{1}$$

$$Q_{sf} \cdot \Delta T_{sf} \cdot \rho C_{Psf} = P \tag{2}$$

$$U \cdot A \cdot LMTD = P \tag{3}$$

These equations are relevant for both heating and cooling operations. In heating mode, Eqs. (1) and (2) state that heat extracted from the groundwater, P (kW), is proportional to the groundwater flow rate, Q_w (l/s), the volumetric heat capacity of water, ρC_{Pw} (kJ/l·K) and the temperature reduction of the groundwater, ΔT_w (K). The secondary fluid absorbs this heat, P (kW), and undergoes a corresponding increase in temperature, ΔT_{sf} (K), depending on the flow rate, Q_{sf} (l/s) and the volumetric heat capacity of the secondary fluid, ρC_{Psf} (kJ/l·K). The heat is transmitted through the steel plates in the heat exchanger, and the amount of heat in Eq. (3), P (kW), is equal to the heat extracted from the groundwater and absorbed by the secondary fluid in Eqs. (1) and (2), respectively. U (W/m^2·K) denotes the overall heat transfer coefficient of the heat exchanger, and A (m^2) denotes the total heat transfer area in the heat exchanger. LMTD is the logarithmic mean temperature difference between the groundwater and the secondary fluid (Fig. 4). The LMTD is calculated from Eqs. (4) or (5) where ΔT_a denotes the temperature difference at the groundwater inlet of the heat exchanger and ΔT_b denotes the temperature difference at the groundwater outlet (von Böckh and Wetzel 2012).

$$LMTD = \frac{\Delta T_a - \Delta T_b}{\ln\left(\Delta T_a / \Delta T_b\right)} \quad if \quad \Delta T_a - \Delta T_b \neq 0 \tag{4}$$

$$LMTD = \frac{\Delta T_a + \Delta T_b}{2} \qquad if \quad \Delta T_a - \Delta T_b = 0 \tag{5}$$

The overall heat transfer coefficient is a parameter that describes the rate at which heat flows from the groundwater to the secondary fluid. The rate depends on the individual heat transfer properties of the two fluids, as well as on the properties of the steel plate that separates them. During normal heat pump operation with constant groundwater

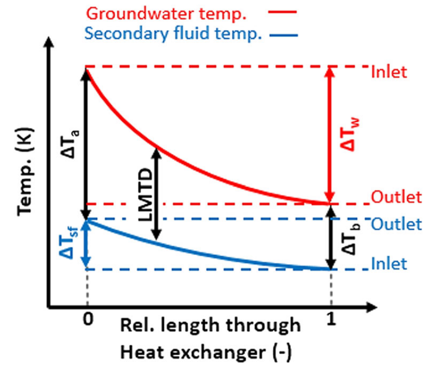

Fig. 4 Principle sketch of temperature development in the groundwater and the secondary fluid through a cross flow heat exchanger. *LMTD* Logarithmic mean temperature difference between the groundwater and the secondary fluid, ΔT_{sf} increase in termperature of the secondary fluid, ΔT_w temperature reduction of the groundwater, ΔT_a temperature difference at the groundwater inlet of the heat exchanger, ΔT_b temperature difference at the groundwater outlet

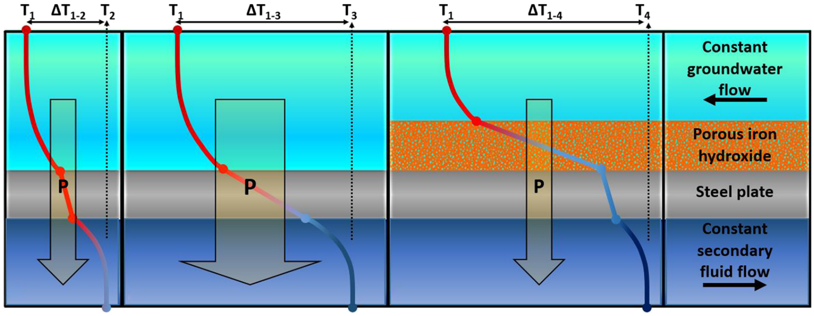

a Small heat flux, P(kW), with small $\Delta T_{1\text{-}2}$ (°K)

b Large heat flux, P(kW), with large $\Delta T_{1\text{-}3}$ (°K)

c Small heat flux, P(kW), with large $\Delta T_{1\text{-}4}$ (°K) due to Increased thermal resistance caused by fouling

Fig. 5 Change of temperature profile and heat rate (*P*, in kW), at a fixed location in a heat exchanger at constant groundwater flow rate and secondary fluid flow rate. **a** Small heat rate with small temperature difference (ΔT_{1-2}), **b** large heat rate with large temperature difference (ΔT_{1-3}), **c** iron hydroxide precipitation on the steel effectively reduced the heat rate and an increased temperature difference (ΔT_{1-4}) is needed to maintain the same heat production from the heat exchanger

flow rate and secondary fluid flow rate through the heat exchanger, the U·A value is constant, and the magnitude of the LMTD controls the heat flux. An increased temperature difference would result in an increase in the heat flux from the groundwater and an increase in heat production from the heat exchanger (Fig. 5a vs. b).

Fouling of the heat exchanger affects the overall heat transfer coefficient by adding an additional layer of material on the steel plate. The heat must travel through the deposited material; consequently, the thickness of the deposit and the thermal conductivity of the material determine its overall influence on the U·A value. Some deposits are porous and a certain amount of the fluid in which they deposited often fill the pore space. In such cases, the thermal properties of the fluid will affect the thermal properties of the deposit, and the fouling deposits will often have poor thermal conductivity (λ; W/m·K). According to Atlas (2010), porous iron hydroxides ($\lambda = 0.6$ W/m·K) have a low conductivity compared to that of most metals, such as steel alloys ($\lambda = 15$–58 W/m·K). Fouling effectively reduces the U·A value of the heat exchanger. To maintain the same heat flux the temperature difference increases and compensates for the loss of the heat transfer coefficient in Eq. (3) (Fig. 5a vs. c). This means that a heat pump receives lower secondary fluid temperature at the evaporator inlet, which results in lower evaporation temperature and pressure. Depending on the type of heat pump working fluid, the lower suction pressure will reduce the COP of the heat pump by 2–3% and the heating capacity by 3–4% for each 1 K increase in the LMTD (Stene 2001).

In many laboratory studies, such as that of Hasan et al. (2017), fouling is detected by monitoring the development of the U·A value over time by rearranging Eqs. (1) and (3) into Eq. (6). This approach is also common in industrial applications (Kerner 2011). A reduction of the U·A value could mean that fouling is developing in the heat exchanger. Figure 6 illustrates a typical example of such a behavioral change where crystallization fouling reduces the heat transfer coefficient in a double pipe heat exchanger over a range of different flow rates.

$$U \cdot A = \frac{P}{LMTD} = \frac{Q_w \cdot \Delta T_w \cdot \rho C_{Pw}}{LMTD} \tag{6}$$

Note the flow rate dependency of the U_0 value, depicted in Fig. 6 with respect to Reynolds number, which is proportional to flow rate. The flow rate dependency of the heat transfer coefficient has practical implications for the heat exchanger in situations where clogging occurs outside of the heat exchanger, such as in the injection well only. In that case, the U·A value is reduced, and fouling or clogging

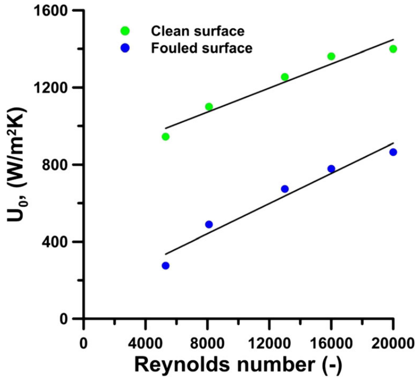

Fig. 6 Reduced heat transfer coefficient of a double pipe heat exchanger (U_0) due to fouling (crystallization fouling effects). Modified after Hasan et al. (2017)

of the passive components in the open loop system affects the groundwater heat exchanger indirectly through reduced flow rates.

Pump performance and clogging effects on the groundwater flow rate

Pump performance curves are specified by pump manufacturers, and these curves specify the range of operations suitable for the pump. The submersible pump should ideally be selected so that it operates at or close to the Best Efficiency Point (BEP) (Mackay 2004; Gülich 2014). This is achieved by selecting a submersible pump whose pumping curve intersects the system characteristics curve at the designed flow rate (Fig. 7). The system characteristics curve represents the energy needed to move groundwater through the system. The friction induced to the groundwater flow by the system components are flow dependent, and the required energy to move the fluid increases with increasing flow rate. Thus, a pump is selected to fit a specific system design. If the system characteristics change with time, the pump performance is affected. Generally, the manufacturers recommend operating the pump within the range of 70 to 120% of the BEP; outside this range the pump will not operate reliably (Mackay 2004).

In the case of fouling or clogging, the system characteristics change with time and induce increased friction to flow, for example, by reducing the internal diameter of a pipe (Fig. 2c). The system curve moves to the left of the BEP and the system characteristics curve will intersect the pumping curve progressively further away from the initial design point, which results in reduced flow rates (Fig. 7). There are increased risks associated with minimum flows, such as suction recirculation or discharge recirculation, two phenomena with similar symptoms to cavitation. These risks involve damage to the seals and bearings as well as increased fatigue and erosion on the impeller and shaft. At very low flow rates the risks associated with high temperatures and insufficient cooling of the pump motor also come into effect (Mackay 2004).

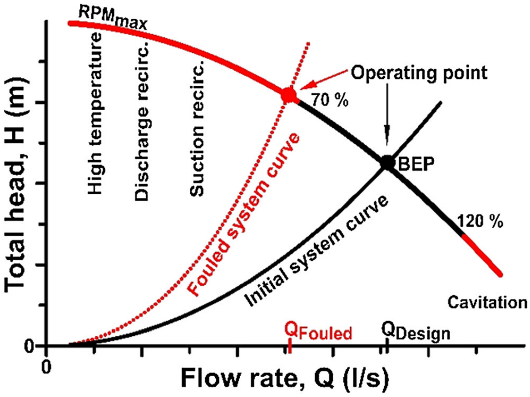

Fig. 7 Single pump performance curve (*RPM*$_{max}$) with risk areas highlighted in red along the curve. Fouling and clogging of system components increase the hydraulic friction, which results in lower flow rates and less reliable operating conditions. *BEP* Best Efficiency Point. Modified after Mackay (2004)

The system characteristics curve incorporates a combination of hydrostatic and hydrodynamic losses, often referred to as head losses. The hydrostatic head, H_{stat} (m), represents the pressure and elevation difference through the system, while the dynamic head, H_{dyn} (m), represents losses that are dependent on the flow rate. Equation 7 states that the pump's point of operation occurs where the total head available from the pump, $H_{available}$ (m), is equal to the total head required by the system, $H_{required}$ (m). The required head is a sum of the static head and the dynamic head losses (Çengel and Cimbala 2014).

$$H_{available} = H_{required} = H_{stat} + H_{dyn} \tag{7}$$

$$H_{required} = H_p + H_I + kQ_w^{\ 2} \tag{8}$$

In GSHP systems, where groundwater is extracted and injected at equal depth the equation can be simplified to Eq. 8. H_p (m) and H_I (m) imply the pressure drop in the production well and the pressure increase in the injection well, respectively, and k is a combined friction coefficient for the other components in the system, such as the pipes, valves and the groundwater heat exchanger. If fouling develops in the system the friction coefficient k will increase and the groundwater flow rate, Q_w, must decrease to maintain the balance of Eq. 7. H_P and H_I are flow dependent, implying that fouling in the system leads to a change in the water level in the wells. Alternatively, if fouling occurs in the wells, the flow rate from the submersible pump will decrease. Thus, the performance of the submersible pump is a good indication of the overall performance of the system.

Well performance and the effects of clogging and fouling

The wells are the connection between the GSHP systems and the aquifer. A well's behavior is unique and controlled by the overall behavior of the aquifer and the submersible pump. Acknowledging that a description of many possible scenarios may be relevant, here we show only some generalized examples; for more examples, the reader is referred to Kruseman et al. (1990) and Banks (2012).

Most crucial is the distinction between a production well and an injection well and, because neighboring wells might influence each other, whether only a single well is active or whether multiple wells are active simultaneously. The typical behavior of a single production well is illustrated in Fig. 8. During pumping, the water level in the production well will suffer a drawdown caused by the loss of pressure inside the well. The surrounding groundwater flows in through the screen in response to this pressure drop. With time, a cone of depression develops around the well. The magnitude of the drawdown is a function of the pumping rate and of the hydraulic properties of both the soil and the well screen. During production, the pumping rate controls the drawdown by adjusting the speed of the pump motor, as shown for three different speeds in Fig. 8a. The maximum allowed drawdown is limited by the placement of the pump with respect to the water table. The limit is not stationary, but can fluctuate or change. A typical example is seasonal variations in the water table caused by variations in groundwater recharge throughout the year. Figure 8b illustrates a difference in an aquifer's natural water table between the summer and the winter months (Norwegian climate); this difference in turn affects the maximum available drawdown in the well. Consequently, the maximum production capacity of the well might have seasonal limitations.

The drawdown in the production well, H_P, as a function of the pumping rate, Q_w, can be described by Eq. 9, where B, C and P are site-specific parameters for the well (Rorabaugh 1953). The parameters are identified by conducting a "step-drawdown" test in the production well, by example, through the methods developed by Jacob (1947) and Rorabaugh (1953) (described in Kruseman et al. 1990). The step-drawdown test involves pumping the well with a series of steps of increasing flow rates. Each flow rate induces a different magnitude of water level drawdown (Fig. 8a). The resulting drawdown of each step needs time to develop, and a minimum of 0.5–2 h is recommended for each step. Reliable interpretation of the test data often requires each step to be of equal duration, and a minimum of three steps are needed to identify the three unknown parameters in Eq. 9.

$$H_P = BQ_w + CQ_w{}^{P} \tag{9}$$

Experiences from Norwegian domestic waterworks have shown that the results from step drawdown tests can give a good indication of the performance of the production well (Banks 1992). Assuming that the sediment and screen properties remain the same throughout the lifetime of the well, a second test of the well after some time should ideally yield equal parameters to those of the first test. However, if the parameters change with time, the test can indicate changes in the hydraulic properties of the well or changes in the hydraulic properties of the aquifer. In the case of mechanical, chemical or microbial fouling of the well, particles clog the well screen and pores in the soil that in turn induce increased friction to the groundwater flow. As a result, the B, C and P parameters increase, with a corresponding increase of drawdown in the production well. A subsequent reduction of the flow rate follows as the submersible pump must maintain the balance of Eq. 7. A distinction between fouling of the screen and fouling of the aquifer is often relevant because each requires a different cleaning approach. Since both scenarios would result in increased drawdown in the production well, additional information from a nearby observation well is necessary to distinguish between the two. If the fouling is limited to the screen alone, the cone of depression surrounding the well will diminish due to the reduced flow rate through the sediments (Fig. 8c). However, if the sediments are affected, the cone of depression, in terms of pressure loss, should also increase around the well (Fig. 8d).

The typical behavior of a single injection well is similar to that of a single production well, but instead of a drawdown both the water level in the well and the sediments increase. The rise of the water level in the injection well, H_I, as a function of the injection rate, Q_w, can be described by Eq. 10, where D, E and I are site-specific parameters for the well. The parameters are identified by conducting the same step test

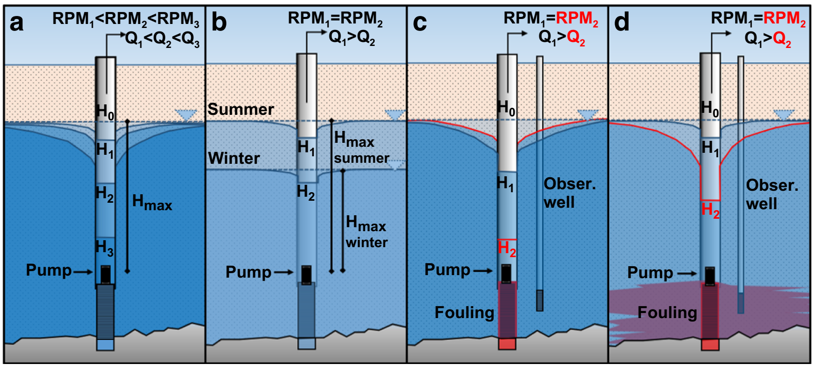

Fig. 8 Production well behavior with different pump speeds (RPM_x). **a** Increased pumping rates (Q_1–Q_3) induce increased drawdown in the well (H_1–H_3) and in the aquifer . **b** Different maximum available drawdown in the summer (H_1) and winter months (H_2). **c** Local clogging or fouling of the well screen leads to increased drawdown in the well (H_1–H_2), but reduced drawdown in the aquifer formation. **d** Clogging of the screen and deposition of the sediments lead to increased drawdown (pressure loss) in the well (H_1–H_2) and the aquifer formation

as for the production well, but with the injection rate rather than the pumping rate.

$$H_I = DQ_w + EQ_w{}^I \tag{10}$$

In an open loop GSHP system a minimum of two wells are often active at any given time: one production well and one injection well. In large installations, there might even be several production wells and injection wells in the same system; these are the so-called well fields (Banks 2012). Depending on the hydraulic properties of the sediments and the general behavior of the aquifer, these wells might influence each other in distinct ways. Figure 9 shows a typical example of where a well field of two production wells and two injection wells influence each other. In the production well field, both production wells induced additional drawdown in each other because they extract water from the same aquifer. A similar effect can be observed in the injection well field, but with an additional increase in water level. Additionally, the two well fields might interact across the aquifer. For example, the production wells could induce a drawdown in the injection wells and limit the increase in water level by a small amount and vice versa (Fig. 9). All of these influences affect the maximum production capacity of a well during operation.

The complexity of each individual well's behavior increases as more wells operate in the same aquifer. The overall well behavior of each individual well could include the well interaction effects by adding a series of sums into each individual equation. Banks (2012) suggested an approach that incorporates the Theis or Cooper–Jacob approximations for this purpose. As an alternative to this approach, the step test analysis described earlier can be applied to drawdown data of neighboring wells and added in Eqs. 9 and 10 for each well, for example as in Eqs. 11 and 12.

$$H_P = BQ_w + CQ_w{}^P + \sum_{i=1}^{n} (\pm) A_n Q_n \tag{11}$$

$$H_I = DQ_w + EQ_w{}^I + \sum_{i=1}^{n} (\pm) F_n Q_n \tag{12}$$

Where A_n and F_n are site-specific and well-specific drawdown parameters, respectively, induced by each neighboring well. Thus, if the flow rate in a neighboring well is known, Q_n (l/s), the additional drawdown in the well or increase in water level in the well can be estimated and accounted for in the overall well behaviors.

Proposed surveillance sensors and surveillance procedure

The main goal of the surveillance procedure is to discover if and identify where fouling or clogging is developing, without having to stop the heat pump or any of the other system components. Considering the system described in the previous sections, the main concern for the open loop system is to ensure adequate heat flow to the heat pump evaporator. This is ensured by maintaining a sufficiently high groundwater flow rate through the groundwater heat exchanger with a sufficiently high groundwater temperature that meets the heat demand in the building. Consequently, the main parameters that should be monitored are the groundwater flow rate, the secondary fluid flow rate and the temperature variations of the groundwater and the secondary fluid.

Figure 10 illustrates the minimum number of sensors required to describe the performance of the production well, the injection well, the aquifer locally, the submersible pump and the groundwater heat exchanger. With the correct pre-investigative procedure, it is possible to monitor the system behavior with four temperature sensors, T1, T2, T3 and T4, and two pressure sensors, p1 and p2. The temperature sensors identify the heat

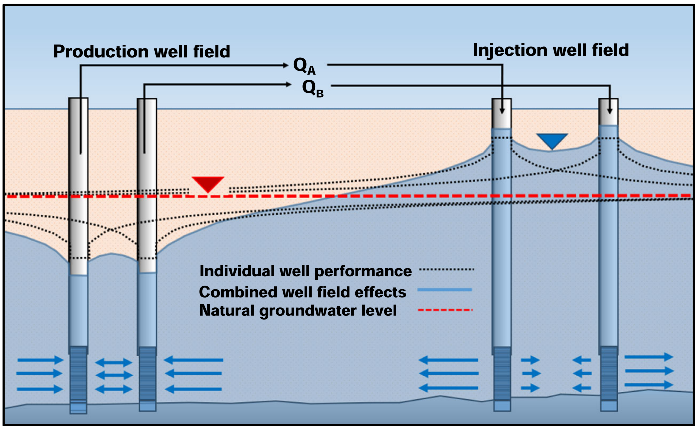

Fig. 9 Individual wells can influence neighboring wells. This becomes an issue in large well fields, where multiple wells operate simultaneously. Production wells induce increased water level or pressure drawdown, while injection wells induce an increase in the water level or pressure in nearby wells

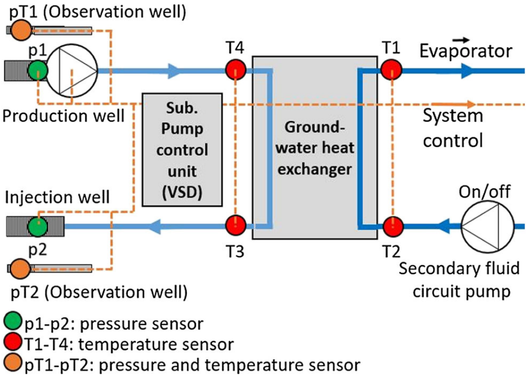

Fig. 10 Proposed surveillance sensors. The temperature sensors (*T1–T4*) combined with pressure sensors (*p1–p2*) in the wells allow detection of fouling and clogging in the groundwater circuit. The pressure and temperature sensors in the observation wells (*pT1* and *pT2*) supply additional information on the local aquifer conditions in near proximity to the respective wells

exchanger performance. The pressure sensors are required to identify the well performance with respect to the groundwater flow rate. Additionally, the pT1 and pT2 sensors (pressure and temperature) are necessary to distinguish variations in the the system from those in the local aquifer. All sensors are connected to the overall system control unit. The function and purpose of each sensor are described in Table 1.

Figure 10 does not include volume flowmeters. The proposed sensors (T1–T4) can estimate the groundwater flow rate by rearranging Eqs. 1 and 2 to Eq. 13. In the presented system design, the secondary fluid flow rate, Q_{sf}, is constant, and if ΔT_w and ΔT_f are sufficiently small to ensure limited variations in the volumetric heat capacities (ρC_{Psf} and ρC_{Pw}), the only variables on the right hand side are the fluid temperatures.

$$Q_w = \frac{\Delta T_{sf}}{\Delta T_w} \cdot \frac{Q_{sf} \cdot \rho C_{Psf}}{\rho C_{Pw}} \tag{13}$$

Through Eqs. 6 and 13, the proposed temperature sensors allow surveillance of the groundwater flow rate and heat extraction rate from the groundwater. In open loop systems without VSD control the heat flow rates and volume flow rates are determined by the system characteristics only, and continuous surveillance of p1, p2, Q_w and U·A should be sufficient for the detection of fouling. However, with VSD control these rates are often highly variable because of the applied control strategy. To distinguish any performance changes in a given component from one time to another it is necessary to follow a distinct procedure that describes the system performance from a known point of reference. One point of reference is the speed (RPM) of the submersible pump motor.

A testing procedure, similar to the well capacity test of Jacob (1947) and Rorabaugh (1953), can be conducted during normal system operation. During the test, the performance of the submersible pump, the groundwater heat exchanger, the production well and the injection well are identified at different groundwater flow rates. A minimum of three different speeds are necessary to estimate the unknown parameters in Eqs. 6, 8, 9 and 10. More steps will provide a higher accuracy in the estimates. Typically, the minimum RPM (or Hz) will function as the first step and the maximum RPM (or Hz) will function as the last step. Any number of additional steps should be selected between these two speeds at regular intervals (Fig. 11). Each step must be of equal duration and last between 0.5 and 2 h.

A test conducted when the open loop GSHP system is new will provide data describing the initial system performance and function as a baseline for the initial capacity of the open loop GSHP system (Figs. 6, 11). Later, a second test with the same RPM settings might show a change in the system performance from the initial test and possibly a reduction of the system capacity, such as the red curves in Fig. 11. Eventually, the system characteristics might change so much that the original control strategy or open loop system design is predisposed to failure. Figure 11 illustrates some suggestions of failure modes, such as the reliable operation range for the submersible pump, possible flooding risks around the injection well or air mixing risk in the production well.

The test should also take into account the seasonal water level and temperature variations in the aquifer. Nearby observation wells can supply this information, which is useful when determining the maximum limits for both the production well and the injection well at different seasons. One example might be the summer and the winter limits shown in Fig. 11.

Discussion

System performance analysis through pressure, flow rate, and temperature parameters is a classical detection method in a wide range of different heat exchanger applications. There are alternative methods for the detection of heat exchanger fouling, but these generally involve the use of specialized fouling equipment, such as ultrasonic acoustics or electrical probes (Wallhäußer et al. 2013). Such methods have been developed for heat exchangers and pipes and are not necessarily applicable for use in groundwater wells. Therefore, the open loop GSHP wells would have to be subjected to individual tests. From an operator's point of view, it is beneficial to have a surveillance procedure that can detect faults in the whole heat source system. In this framework, the step-test performance analysis method is a good approach because it combines the well performance tests and heat exchanger performance test into a single test.

The system performance will show similarly symptoms regardless of the cause of the clogging. Thus, system

Table 1 Description of the surveillance sensors

Sensor	Monitoring function	Main purpose	Additional purpose
T1	Secondary fluid return temperature to the evaporator.	- Input to Eq. 13, these sensors allow continuous estimation of Q_w. - Input to Eq. 6, these sensors allow continuous monitoring of U·A-value. - Allow calculation of energy output from the aquifer. - Calculation of COP if additional information from the heat pump is available.	-supply information about the working conditions for the evaporator.
T2	Secondary fluid temperature from the evaporator.		
T3	Return temperature of the groundwater before injection.		-Indicates risk of groundwater freezing in the heat exchanger. -system control
T4	Groundwater temperature from the production well.		Indicates risk of thermal short-circuiting in the aquifer
p1	Water level in the production well.	Input to Eq. 9 this sensor allow operator to test well performance and discover well clogging.	-Indicates risk of air mixing into the system. -system control.
p2	Water level in the injection well.	Input to Eq. 10 this sensor allow operator to test well performance and discover well clogging.	-Indicates risk of surface flooding. -system control.
pT1	Water level and temperature in the aquifer close to the production well.	-Distinguish seasonal changes in the aquifer from changes in the production well water level. -Discover clogging in the aquifer.	- Indicates influence of other nearby wells. - Indicates risk of thermal short-circuiting in the aquifer.
pT2	Water level and temperature in the aquifer close to the injection well.	-Distinguish seasonal changes in the aquifer from changes in the injection well water level. -Discover clogging in the aquifer.	Indicates influence of other nearby wells.

Q^{w}, groundwater flow rate; U·A value, overall heat transfer coefficient of the heat exchanger (U) · total heat transfer area in the heat exchanger (A); COP, coefficient of performance

[a] T1–T4, Temperature sensors; p1, p2, pressure sensors; pT1, pT2 pressure and temperature sensors

performance analysis allows for a general approach to system surveillance and is a suitable tool for all clogging problems. This flexibility in applicability is an advantage for open loop GSHP systems because of the considerable challenge of eliminating all of the potential problems in the design phase of new projects. The method can function as a standardized procedure for system surveillance before an initial fault has taken place. If better methods exist for monitoring particular faults, these can replace the step-test for that particular situation from then on. Specialized fouling equipment can then be installed because it is actually needed—rather than as a precaution.

The proposed procedure and sensors do not identify the cause of the clogging problem. However, by identifying which of the four major components that are affected, the test results enable the operator to plan necessary maintenance to the affected components without having to spend time on unaffected parts of the system. The cause of the problem can then be identified through other means, such as by video inspection of the affected wells or pipes (Gjengedal et al. 2018). Furthermore, the operator is able to investigate how effective the maintenance has been by conducting the same test procedure after the maintenance and comparing the results.

The procedure does not necessarily rely on an initial investigation of the system to work, but the behavior of the initial system provides a point of reference for future tests. The initial investigation would essentially confirm if the open loop GSHP system performs as well as the required specifications agreed upon in the tender document. Thus, the initial test should be part of the overall commissioning test of the system before the heat pump system is deemed finalized and handed over to the building owner.

The procedure in itself only involves incremental adjustments of the speed of the submersible pump motor. While these adjustments should be easy to conduct, data interpretation may be a challenge for the system operator. A key success factor in the surveillance procedure will be the pre-processing of the data in the system control unit. The data from the sensors shown in Fig. 10, the groundwater flowmeter measurements (FL in Fig. 3) or flow rate estimates (Q_w in Eq. 13) and the estimated U·A value should be presented on a control display in the machinery room as numbers and with the system limits visible as guidance.

Supervision and input from a specialist is probably necessary in most cases. Hydrogeological expertise is essential for

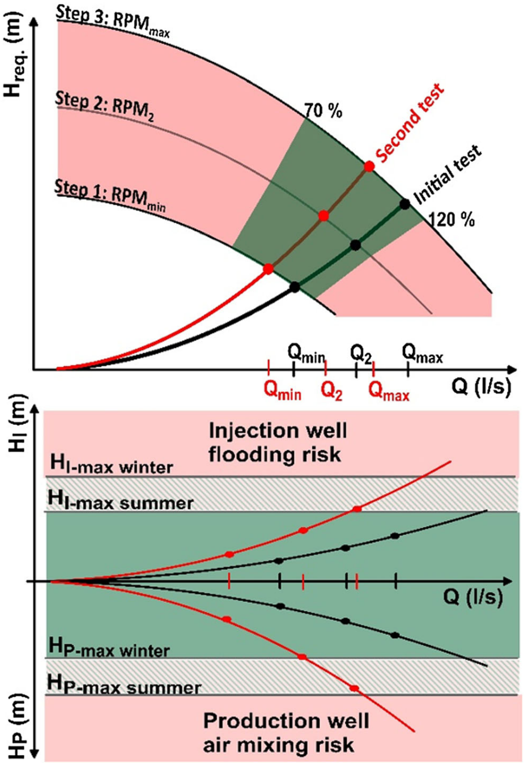

Fig. 11 Systemized "step-test" data with initial test shown as the black curve. A second test might detect fouling effects, which could result in the red curves. Green zones indicate areas of safe operation, while red zones indicate areas of unreliable operation where the system is predisposed to failure. *RPM* Rotational speed of the submersible pump motor (in Hz)

the interpretation of aquifer data and production well and injection well data and for the establishment of limitations to the aquifer system as a whole. Such expertise is especially essential in complex open loop GSHP systems, such as installations with multiple wells in multiple well fields, where the individual well performances might be difficult to identify due to well interaction effects. For small installations, such as those of ≤ 100 kW, the cost of hiring a specialist on a regular basis might be an issue. However, the time needed to conduct the step-test will be within a single workday, on the scale of 3–8 h (per well doublet), and the test can be conducted during normal system operation without switching off the heat pump unit; both factors will limit the cost of the test. By allowing integrated remote control and monitoring of the GSHP system through an Internet Cloud solution, a specialist would be able to follow the test on-line without having to visit the installation. This might help minimize the cost of routine surveillance over longer periods.

The cost and stability of the sensors are important concerns to consider, as well as their degree of sensitivity and reliability. The proposed number of pressure and temperature sensors in Fig. 10 is the minimum that enables full system surveillance of the system components highlighted in the figure and illustrates the least expensive solution. Additional sensors can and sometimes should be included, for example, a volume flowmeter or additional pressure sensors along the groundwater pipeline; however, these will increase the overall cost of the surveillance system and might not be deemed necessary in small-capacity installations (e.g. ≤ 100 kW). In large-capacity installations the number of sensors needed increase proportionally with the number of wells and heat exchangers, respectively. However, temperature and pressure sensors have multiple purposes in open loop GSHP systems (Table 1), and some sensors are also likely to be included in the system design and control strategy. By utilizing the same sensors for fouling and clogging detection, the initial investment cost for the procedure is reduced.

The key parameter in the surveillance strategy is the groundwater flow rate through the system (Q_w). A direct measurement of the flow is favorable. However, a potential problem offered by water quality issues can complicate the matter if fouling affects the flow-measuring devices and leads to incorrect flow rate measurements. This could for example, occur when fouling forms on a pipe section where the flow-measuring device is installed. In the surveillance procedure described herein, this potential problem is avoided by estimating the groundwater flow rate indirectly (Eq. 13). The accuracy of the estimate then relies on the accuracy of the temperature measurements. Proper mounting of the temperature sensors in probes inside the pipes, close to the heat exchanger entrances, in addition to proper calibration of the temperature sensors and the recording instruments are vitally important to ensure maximum accuracy (McMillan and Toarmina 2011). The temperature-estimated flow should be compared to a direct flow measurement by a portable flowmeter during the initial test to ensure accurate documentation of the sensor calibrations and flow rate estimate.

The accuracy of the estimate might still be insufficient for flow rate estimation if, for example, the ΔT_w and ΔT_{sf} are within the error range of the temperature sensors. For this reason, the recommended sensor types should have a small as possible error range (e.g. high-quality resistance thermometers [Pt100 A] with an error range ± 0.1–0.3 °C). The ΔT_w and ΔT_{sf} can become an issue, for example, when the flow rates are high relative to the heat demand in the building. A possible solution for the problem would then be to control (VSD) the submersible pump to ensure a ΔT_w of at least 3 °C, which would limit the error in the estimated flow rate.

The indirect flow rate estimate depends on a temperature difference through the heat exchanger and works for both heating and cooling modes. However, even though the submersible pump and the secondary fluid circulation pump operate at constant flow rates during each step of the test, the heat rate through the groundwater heat exchanger might not have a constant rate and consequently might not operate at steady state. This can pose a problem for both the groundwater flow rate estimation and the U·A value estimation. This issue is discussed by Jonsson et al. (2007) and solved by introducing a physical state space model for on-line fouling detection in heat exchangers during normal system operations (transient time states). The implementation of an extended Kalman filter algorithm by these authors shows promising results. Combining their method with the step-test procedure might solve the parameter estimation issues.

Finally, the groundwater flow rate cannot be estimated via the temperature sensors if there is no heating or cooling demand in the building. In a typical Norwegian open loop GSHP system there is only a heating demand during the early spring, the late autumn and through the winter months. If there is no cooling demand in the building during the summer, a flowmeter is essential and must be installed for testing of the system in the summer. Open loop GSHP systems that have heating and/or cooling needs all year round can manage with the sensors in Fig. 10.

The main purpose of the proposed surveillance scheme is to monitor the system performance in relation to clogging issues. However, if the data from the sensors are recorded and stored, they also supply important information and documentation that describe hydraulic and thermal development in the aquifer over time. For example, it should be possible to draw conclusions regarding excessive heat extraction from the aquifer by assessing conditions detectable by the temperature sensors T4, pT1 and pT2 in relation to the injection temperature T3. The pT1 and pT2 sensors in particular are useful for evaluating the local aquifer conditions at the installed location, while sensor T4 only describes an average temperature of the entire screened section of the well in the aquifer. If governmental agencies require such documentation, the surveillance scheme thus provides the GSHP plant owner with the most basic documentation regarding environmental impact issues, such as aquifer water level data, heat extraction/injection data or groundwater extraction data (in cases with no re-injection; Fig. 1a).

Conclusions

There is a need for fouling and clogging surveillance in open loop GSHP systems. Given that there is a heat flux through the groundwater heat exchanger, four temperature sensors, two pressure sensors and a specified "step-test" surveillance procedure allow monitoring of the system performance. The main benefits and drawbacks of the test procedure can be summarized as follows. The test:

- describes actual system performance and identifies if clogging has occurred in the production well, the injection well, the aquifer and the groundwater heat exchanger;
- measures if the system performs in accordance with the specifications agreed upon in the tender document and should be included as a standard commissioning procedure for groundwater heat pump systems;
- can be conducted within a single workday (3–8 h per well doublet) and without disrupting the heat production in the heat pump;
- can investigate the effectiveness of normal maintenance procedures;
- requires low-cost sensors, but relies on accurate temperature and pressure measurements;
- does not identify the clogging type or clogging cause.

Data interpretation might be a challenge due to system and aquifer complexity. The pre-processing of data in the system control unit might ease the data interpretation process, but supervision and input from a specialist will normally be necessary.

Further work will be to test the procedure on an active open loop GSHP installation with clogging or fouling issues. The possibility of implementing a Kalman filter algorithm in the data pre-processing procedure to improve the estimates of both groundwater flow rate and the U·A-value should also be investigated.

Acknowledgments This work was conducted as a part of the research project Optimal Utilization of Groundwater for Heating and Cooling in Melhus and Elverum (ORMEL). The project is a cooperation between the municipalities of Melhus and Elverum, the Norwegian University of Science and Technology, Asplan Viak AS and the Geological Survey of Norway, and receives funding from the Regional Research Funds in Mid-Norway. We would like to thank all of the involved institutions and persons for cooperation and financial contributions. Special thanks to open loop GSHP operator Rolf Aune for all of the information and discussions about the installations in Melhus and to Associate Professor Jørn Stene at the Department of Energy and Process Engineering (NTNU) for pre-submission review and constructive comments.

References

Andersson A-C, Andersson O, Gustafson G (1984) Brunnar: undersökning, dimensionering, borrning, drift [in English: Wells: investigation, dimensioning, drilling, operation]. Statens råd för byggnadsforskning, Stockholm (in Swedish)

Atlas VH (2010) VDI heat atlas. Springer, Berlin Heidelberg

Bakema G (2001) Well and borehole failures in UTESS. State of the art 2000, 2nd edn. IF Technology BV, Arnhem

Banks D (1992) Grunnvannsbrønner: kontroll, vedlikehold, rehabilitering [in English: Groundwater wells: control, maintenance, rehabilitation]. Norges Geologiske Undersøkelse, Trondheim (in Norwegian)

Banks D (2012) An introduction to thermogeology: ground source heating and cooling. Wiley-Blackwell, Chichester

Brøste HM (2017) Vannkvalitet knyttet til grunnvannsbaserte grunnvarmeanlegg i Melhus og Elverum [in English: Water quality with respect to open loop GSHP systems in Melhus and Elverum]. Norwegian University of Science and Technology (NTNU), Trondheim, Gjøvik, Ålesund (in Norwegian)

Çengel YA, Cimbala JM (2014) Fluid mechanics: fundamentals and applications. McGraw-Hill, Boston

Gjengedal S, Ramstad RK, Hilmo BO, Frengstad BS (2018) Video inspection of wells in open loop ground source heat pump systems in Norway. Editor: Prof. Jeffrey D. Spitler. International Ground Source Heat Pump Association, Oklahoma. In IGSHPA conferense proceedings 2018. https://doi.org/10.22488/okstate.18.000025

Gülich JF (2014) Centrifugal pumps, 3rd edn. Springer, Berlin Heidelberg

Hasan B, Jwair E, Craig R (2017) The effect of heat transfer enhancement on the crystallization fouling in a double pipe heat exchanger. Exp Thermal Fluid Sci 86:272–280

Jacob CE (1947) Drawdown test to determine effective radius of artesian well. Trans Am Soc Civ Eng 112(1):1047–1064

Jonsson GR, Lalot S, Palsson OP, Desmet B (2007) Use of extended Kalman filtering in detecting fouling in heat exchangers. Int J Heat Mass Transf 50:2643–2655

Kerner J (2011) Feature report compact, high-efficiency heat exchangers: understanding fouling. Chem Eng 118:35–41

Kruseman GP, Ridder NAD, Verweij JM (1990) Analysis and evaluation of pumping test data. International Institute for Land Reclamation and Improvement, Wageningen

Mackay R (2004) The practical pumping handbook. Elsevier, Oxford

McMillan GK, Toarmina CM (2011) Advanced temperature measurement and control. International Society of Automation

Melo LF, Bernardo CA, Bott TR (1988) Fouling science and technology. Kluwer, Dordrecht

Müller-Steinhagen H (2000) Heat exchanger fouling: mitigation and cleaning technologies : handbook. Publico Publications, Essen

Nema PK, Datta AK (2005) A computer based solution to check the drop in milk outlet temperature due to fouling in a tubular heat exchanger. J Food Eng 71:133–142

Rees S (2016) Advances in ground-source heat pump systems. Woodhead Publishing, Amsterdam

Riise MH (2015) Praktisk guide for grunnvarmeanlegg basert på oppumpet grunnvann—Hydrogeologiske forundersøkelser, etablering, drift og oppfølging med utgangspunkt i erfaringer fra etablerte anlegg i Melhus sentrum [in English: Guide to the open loop GSHP systems in Melhus]. Norwegian University of Science and Technology (NTNU), Trondheim, Gjøvik, Ålesund (in Norwegian)

Rorabaugh MJ (1953) Graphical and theoretical analysis of step-drawdown test of artesian well. Proc Am Soc Civ Eng 79(12):1–23

Stene J (2001) Varmepumper: grunnleggende varmepumpeteknikk [in English: Heat pumps: basics] Trondheim, SINTEF Energi

von Böckh P, Wetzel T (2012) Heat transfer: basics and practice. Springer, Berlin Heidelberg

Wallhäusser E, Hussein MA, Becker T (2013) Clean or not clean – detecting fouling in heat exchangers, Editor, Professor Dr. Gerald Gerlach, AMA Association, Dresden, pp. 121–125. AMA Conferences 2013 – Proceeding of Sensor 2013, ISBN 978-3-9813484-3-9

Paper V

Bulletin of Engineering Geology and the Environment
https://doi.org/10.1007/s10064-020-01963-z

ORIGINAL PAPER

Online remote-controlled and cost-effective fouling and clogging surveillance of a groundwater heat pump system

A case study from Lena Terrace in Melhus, Norway.

Sondre Gjengedal[1] · **Lars A. Stenvik**[1] · **Randi K. Ramstad**[1] · **Jan I. Ulfsnes**[2] · **Bernt O. Hilmo**[3] · **Bjørn S. Frengstad**[1]

Received: 4 December 2019 / Accepted: 25 August 2020

Abstract
Fouling and clogging of groundwater wells and heat exchangers are among the major operational challenges for groundwater heat pump (GWHP) and aquifer thermal energy storage (ATES) systems. This article presents the application of a step-test surveillance procedure developed for early detection of clogging in distinct parts of the GWHP system, tested at Lena Terrace in Melhus Norway. Three versions of the test procedure are presented and demonstrate that the test can be performed with a minimum of four steps, each of 15-min duration, while the GWHP system is actively producing heat. The results prove that the surveillance test can detect changes in the hydraulic resistance of the groundwater circuit and locate clogging problems within all of the relevant system components in the groundwater circuit simultaneously. At the Lena Terrace GWHP system, these tests indicate a gradual increase of hydraulic resistance with time, which verify that clogging issues are continuously developing in the injection well, in the production well, and in the groundwater heat exchanger. Cleaning of the heat exchanger was then performed. This increased the pumping capacity by 8.3% points, but continuous clogging of the injection well and the production well necessitates further maintenance to ensure a reliable operation. It is demonstrated that multidisciplinary competence and experience with GWHP-systems, aquifers, and groundwater wells are needed for the evaluation of the results. These results can therefore serve as a reference for other GWHP systems with similar design configurations.

Keywords Groundwater · Step-test · Clogging · Surveillance · Hydrogeology · Heat pumps

Introduction

Ground water heat pump (GWHP) systems have become increasingly popular in Norway during the latest decades. Recent studies indicate a large potential for this technology, and similar trends are also seen worldwide (Bloemendal et al. 2015). One of the largest consumers of GWHP heating and cooling in Norway is the municipality of Melhus. An aquifer beneath the town center of Melhus is currently utilized as a heat source by ten individual GWHP systems. The first installation started production already in 1999 and is still in operation today. All of these GWHP systems use a Quaternary deposit of saturated sand and gravel material as their heat source.

Many aspects of the system performance are governed by the local and the overall hydrogeological conditions within this deposit. The groundwater quality is an important factor in all types of GWHP installations (Bakema 2001; Banks 2012; Snijders and Drijver 2016). Problems caused by chemical reactions, suspended soil particles, or microbial growth in the water are a well-known and widespread issues for these systems, and clogging and fouling of system components is a common problem in Melhus (Riise 2015; Brøste 2017; Gjengedal et al. 2018; Gjengedal et al. 2019a; Gjengedal et al. 2019b). These problems typically involve clogging of the groundwater heat exchanger, the well screens, the pipeline, and the aquifer formation, also causing increased fatigue and erosion of the submersible pump. Usually, the heat pump performance and overall cost of the operation are affected by reduced heat production capacities and efficiencies. In severe

✉ Sondre Gjengedal
sondre.gjengedal@ntnu.no

[1] Norwegian University of Science and Technology, Trondheim, Norway
[2] Optiview AS, Vihals, Norway
[3] Asplan Viak AS, Trondheim, Norway

cases, the complications can lead to complete system failure. Fouling and clogging of groundwater wells and heat exchangers therefor put the long-term reliability and sustainability of GWHP and, similarly, aquifer thermal energy storage (ATES) systems at risk. Consequently, groundwater source systems require a higher level of surveillance and maintenance than other ground source heat pump systems (Banks 2012; Snijders and Drijver 2016; Gehlin and Andersson 2019).

Monitoring and surveillance of GWHP systems is typically carried out by recording and analyzing pressure, temperature, and volume flow rate data (Gjengedal et al. 2019a). This type of monitoring is common in many heat pump applications (Stene 2001; Rees 2016) and is also standard for many industrial heating and cooling applications. District heating applications and the oil & gas industries are some examples (Müller-Steinhagen 2000; Melo et al. 1988). However, a variety of clogging and fouling issues in GWHP systems can cause similar symptoms and data responses, hence making it challenging to evaluate the data correctly.

A surveillance procedure for early detection of clogging and fouling in GWHP systems has previously been developed for GWHP systems in particular (Gjengedal et al. 2019a). Gjengedal et al. (2019a) demonstrate that the dynamic behavior of GWHP systems requires the pressure, temperature, and volume flow rate data to be evaluated with a specific procedure to enable proper interpretation of the data. The suggested procedure allows for testing and evaluation of all of the individual system components in the GWHP system simultaneously. The procedure has now been applied regularly in one of the installations in Melhus during routine maintenance of the system. This paper presents the experiences with the surveillance method and demonstrates the usefulness of the method for performance monitoring.

Site description and system specification

The town of Melhus is located in the Gauldal valley in Mid-Norway, approximately 20 km south of the city of Trondheim (Fig. 1). The town is located on a floodplain next to the river Gaula. Immediately to the north of the populated area, the landscape is dominated by Melhusryggen, a forested terminal moraine that stretches halfway across the valley, from the mountain of Vassfjellet in the east to the eastern embankment of the river Gaula. This glaciofluvial ridge marks the upper part of the Quaternary sand and gravel deposit known as the Melhus aquifer, an aquifer that in part extends beneath the town center south of the ridge. The river Gaula intersects the town center and separates both the town center and the aquifer into a western and eastern part.

Today, this aquifer supplies ten individual building complexes with heat and three building complexes with both heating and cooling. The Lena Terrace apartment complex was built in 2003. It is located at the foot of the Melhusryggen ridge and is highlighted as the case study site in Fig. 1. The apartment complex' GWHP system is designed as a reinjection type system (Fig. 2). The local sediments are dominated by unconsolidated sand and gravel of glaciofluvial origin, and the groundwater water table is located approximately 20–21 m below the terrain level. At this depth and location within the aquifer, the groundwater temperature is found to be stable all year round at ~7 °C. The "natural" groundwater level, which imply the water level unaffected by the local GWHP activity, fluctuates approximately ± 1.0 m throughout the year (Hellestveit 2018). The aquifer is accessed by the GWHP system through two groundwater wells, one production well, and the other an injection well. The permeability of the aquifer formation is high, and this is reflected in the design of the wells.

The production well design is customized to the local soil conditions. The original design was a larger 219 mm OD well size, but due to drilling problems, the well size was reduced during construction. The finalized well design is 36.4-m deep and has a steel casing width of 168–158 mm (ODxID). The water is extracted from the well by a 10.8 kW Grundfos SP 60-5-MS6000 (50 Hz) submersible pump, which is installed at 28 m depth, immediately above the well screen. The well screen is the perforated section of the well and is installed from 29.4 to 35.4 m depth, providing 6 m of screened well length. The screen is a 161–150 mm ODxID con-slot screen, with 1.0 mm slot openings and a 31.3% perforation ratio. This screen design was selected based on grain size analysis of the soil, which are dominated by medium to coarse sand and gravel particles.

This production well design was originally selected to ensure proper operating conditions for the submersible pump. The Grundfos SP 60-5 pump generally requires 4–5 m of net pressure suction head (NPSH) during production (NPSH required depends on the motor speed). When the pump is inactive, the water table in the well is typically 6.0–7.0 m above the submersible pump. The available drawdown is thus limited to 2–3 m, leaving limited margin for potential clogging issues. There is however a 0.5-m sump pipe installed beneath the screen to accommodate potential sediment suffusion during operation.

The injection well is 36.5-m deep and has an identical design, but the screened segment of the well is installed from 23.5 to 33.5 m depth, which provide 10 m of screened well length. The return pipe is installed at 27.5 m depth, in the middle of the screened section of the well. There is a 3-m-long sump pipe beneath the screen to accommodate potential sediment suffusion during operation. The natural water table is typically 18.0–19.0 m below the well top during the heating season. This large elevation drop towards the well water level generates a suction in the groundwater piping system during production, causing vacuum pressures to develop in the pipe and in parts of the surface installation.

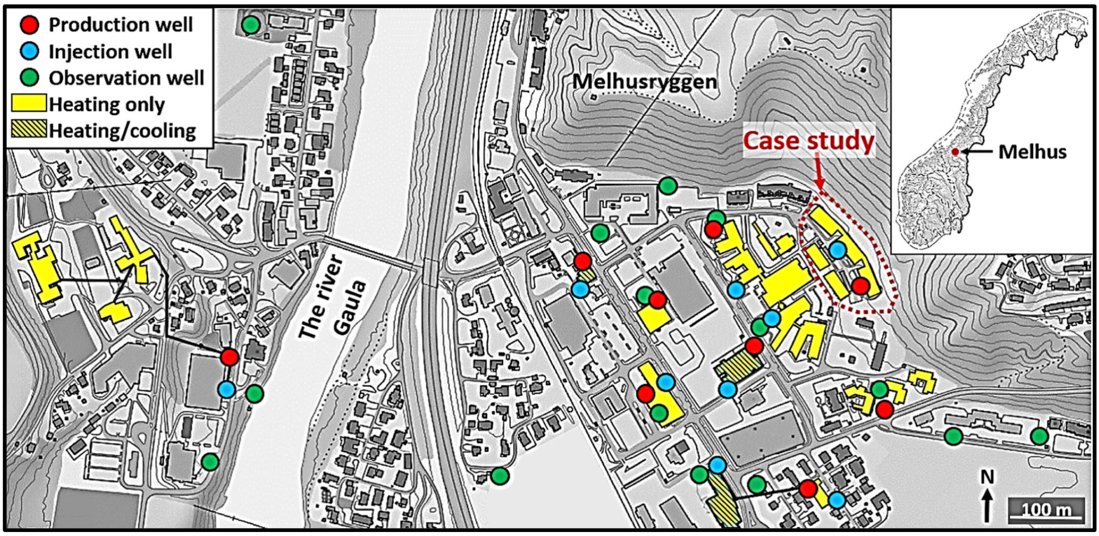

Fig. 1 Overview of the town center of Melhus with the ten GWHP installations (yellow buildings) and the corresponding groundwater wells indicated. There are 34 groundwater wells in the area, of which 18 are used for heating and cooling purposes. The location of the Lena Terrace building complex is highlighted as the case study site. Details of the Lena Terrace GWHP system are provided in Fig. 2 and Fig. 3

The groundwater circuit part of the surface installation is visualized in Fig. 3. The system consists of approximately 100 m of 160 mm ID HDPE pipes that connect the two wells to the groundwater heat exchanger situated in the basement of the building. The groundwater heat exchanger is a 260-kW gasket plate heat exchanger with a total of 72 m^2 plate surface area (1.3 fouling factor). The total peak heating demand of 350 kW is provided by two custom Chiller Oy heat pump units (R134a). The heat pumps are coupled in parallel to a secondary loop circuit with 20% ethylene glycol antifreeze fluid. The secondary loop is connected to a plate heat exchanger for heat transfer with the groundwater loop.

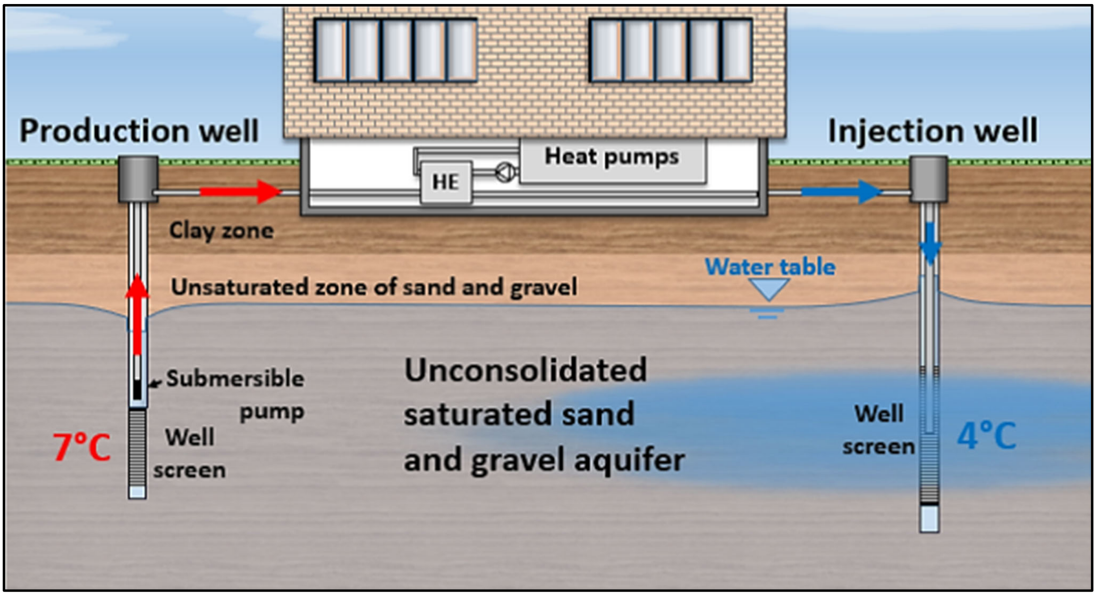

Fig. 2 Schematic sketch of the soil conditions and the reinjection type GWHP system employed at Lena Terrace in Melhus, Norway (the sketch is not to scale)

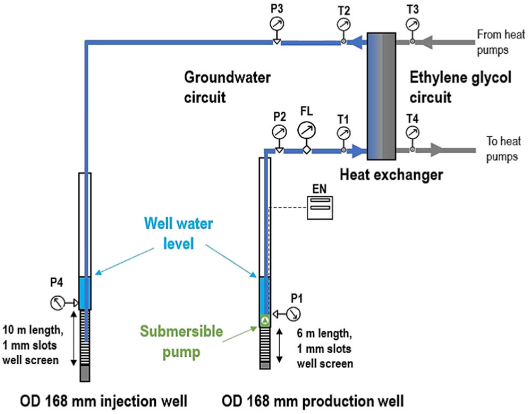

Fig. 3 Schematic sketch of the GWHP system at Lena Terrace, including real time monitoring of operational parameters. The groundwater pipe segment is approximately 100 m long. The relative location of the pressure transducer (P1–4), the flow meter (FL), the energy meter (and frequency converter) of the submersible pump (EN), and the temperature sensors (T1–4) are shown. The sketch is based on the online OPTIVIEW® interface

The designed efficiency point for the whole system is a coefficient of performance of 3 at maximum heating capacity (COP = 3). The groundwater system is designed to supply approximately 18 l/s of groundwater to accommodate the thermal demand during peak load conditions in the winter months. It assumed a groundwater temperature reduction from 7 °C to 4 °C (ΔT = 3 K) at these conditions. During part load conditions, in the autumn and spring, the amount of groundwater circulation is reduced. This is controlled by adjusting the operating point of the submersible pump, between 60 and 100% of the maximum pump motor frequency (30–50 Hz).

Since its construction in 2003 the Lena Terrace GWHP plant has been affected by a variety of clogging and fouling issues. These are recurring problems, where fouling of iron precipitates affects the heat exchanger, while soil particles clog the injection well. The heat exchanger was most recently replaced in 2018 because of insufficient heat transfer capacity. The injection well is cleaned annually, most recently in 2018 and 2019, in an effort to maintain the reinjection capacity. Following the latest rehabilitation measures in 2018, the installation was re-equipped with new sensory equipment to improve the monitoring. These sensors are visualized in Fig. 3. The implementation of an automated control system now allows for remote control of the installation through an online TOSIBOX® system.

It is planned to clean the heat exchanger annually with an organic acid treatment before each heating season to mediate the iron precipitation fouling problem. The step-test method data presented here was applied in a period before and after the cleaning treatment on the 8th–9th of October 2019, to evaluate the need and the effect of the acid treatment. Three of these step-tests are presented in this paper. The two first tests were conducted before the fouling treatment of the heat exchanger, while the third test was performed after the treatment.

Methodology

The surveillance procedure employed in this study involves conducting a series of incremental adjustments to the motor speed of the submersible pump, a so-called step-test. This is done by remote control through the online TOSIBOX® system, where the motor speed is controlled between 60 and 100% of its pumping capacity. The hydraulic and thermal performance of the system is then simultaneously measured at each speed, and the data is evaluated with least square regression analysis. The data response is evaluated with regard to potential clogging and fouling issues that affect the performance of the system in distinct ways, depending on their location within the system, as described in Gjengedal et al. (2019a).

The control system's integrated monitoring and control instrumentation are used for the data acquisition. The instrumentation and their relative location in the relevant part of the system control interface are shown in Fig. 3. The sensors used in the instrumentation are further described in Table 1. The temperature (T1–T4), pressure (P1–4), flow rate (FL), and the pumping power (EN) at the various speeds were recorded at each step of the test. All sensory data was automatically recorded by the monitoring system each minute and stored. The input data for the least square regression analysis and calculations are average values of the last eight measurements of each step of the tests, where steady-state conditions were assured.

The step-test procedure follows the methodology described in detail in Gjengedal et al. (2019a). Three variants of the procedure were tested to evaluate the applicability of the method (Table 2). The first test was performed with the minimum three steps required for the method, each of the steps having a duration of 1 h. Traditionally, each step of the tests is recommended to be between 0.5 and 2 h (Kruseman and de Ridder 1994), but the time can be reduced if the pressure response reaches steady state earlier. The purpose of test 1 was to evaluate the timeframe needed to achieve steady-state flow and pressure responses in the wells and the piping system. The pressures response stabilized within the first 1–3 min for each step, indicating a highly permeable aquifer formation. The duration of each step could therefore be reduced to 15 min for the two consecutive tests to investigate the possibility of reducing the timeframe of future tests.

The second test was performed with 19 individual steps to see if more steps would provide higher accuracy and possibly improve the usefulness of the surveillance data. The third test was an intermediate version with six steps. For tests 1 and 2,

Table 1 Instrumentation relevant for the step-test surveillance procedure

Location in Fig. 3	Instrument type	Accuracy
P1	Pressure transducer, Siemens SITRANS LH100	± 0.0015 bar
P2, P3	Pressure transducer, Danfoss MBS 4010 0–6 BAR ABS	± 0.03 bar
P4	Pressure transducer, Kacise GXPS430	± 0.015 bar
FL	Flow meter, Badger ModMAG M1000	± 0.04 l/s
EN	Energy meter, Grundfos CUE 3X380-500 V IP55 15KW 32A/2	–
T1–T4	Temperature probes, PT1000	± 0.3 °C

See Fig.3 for the relative location of the instruments in the GWHP system

the system was shut off before the tests to measure the unaffected pressure responses. Test 3 was performed without a shutoff period before the test, due to the continuous heat demand in the building. The unaffected groundwater level was then estimated via inverse calculation, using tests 1 and 2 as a reference for the expected water level draw-down at 60% pump capacity.

The procedure for test 2 is demonstrated in Fig. 4 and visualizes the progression of the test procedure. The test is performed with a pyramid-shaped speed increment adjustment. The first and the last step have the same speed (60%), while incremental adjustments were distributed evenly and mirrored around the 100% speed, producing the pyramid-shaped power curve. This mirroring of the test provided a mean of control during the test and confirmed that the behavior of the system is unchanged throughout the test procedure. Similar performance "pyramids" were observed in the data response in the control instrumentation.

Results

The four temperature sensors (T1–T4 in Fig.3) are installed on the four heat exchanger pipe segments to measure the temperature development of both fluids through the heat exchanger. In ideal conditions, the temperature data should be included in the analysis, but these temperature sensors were found to be incorrectly calibrated and could not be used to determine the efficiency of the heat exchanger. Thus, primarily the hydraulic performance of the system, with the pressure, energy meter, and flow meter data, is used in the performance analysis.

The pyramid shape of the test 2 procedure (Fig. 4) is reflected in the pressure response that is presented in Fig. 5 for the heat exchanger. The differential pressure between the two sensors describes the hydraulic losses through the heat exchanger, which is used in the regression analysis. The data also demonstrate that the groundwater heat exchanger is subjected to vacuum pressures if the groundwater flow rate is reduced below a given threshold value (red shaded area in Fig. 5). This is observed in the P3 sensor when the groundwater flow rate is lower than 10.0 l/s, which corresponds to the 80% step in Fig. 4. At the lowest step (the 60% step), a − 7 kPa gauge pressure is observed in the P3 sensor. When the pump is turned off, the vacuum extends to the whole surface installation and stabilizes at approximately − 70 kPa gauge pressure in both P2 and P3.

The results of the regression analyses of the three step-tests are presented in Table 3 and visualized in Fig. 6. The test results show that the electrical power consumption of the groundwater pump is equal for each corresponding step for each test, but the corresponding flow rates vary. A reduction in the pumping capacity signifies that the pump produces less water at a given motor speed. This can be observed by comparing the 100% speed flow rate of each test in Fig. 6d. In test 1, the flow rate is 16.2 l/s, which is 10% reduction from the initial 18.0 l/s capacity of the system. For test 2, the maximum capacity has reduced to 15.7 l/s, corresponding to a further 3.0% point reduction in pumping capacity over a 41-day

Table 2 The step-test specification for each of the three tests

Test no.	Date	Test time [h]	No. steps	Time per step [min]	Start point [% of 50 Hz]	Increment [% points]	Shutoff
1	28.08.2019 (Reference test)	4	3	60	0%	20	Yes
2	08.10.2019 (41 days later)	5.5	19	15	0%	2–3	Yes
3	16.10.2019 (55 days later)	1.5	6	15	60%	10	No

The various steps were distributed evenly through the 60–100% speed intervals, 60% (30 Hz) is the minimum speed and 100% (50 Hz) is the maximum speed of the pump. All measurements were automatically recorded each 1 min by the monitoring system

Fig. 4 Step-test procedure of test 2 at Lena Terrace GWHP system. The test involves 19 steps of incremental pumping speed adjustments between 60 and 100% of the pump power capacity. The first and final step are at the 60% speed. Each step lasts for 15 min. The test is completed with a shutoff sequence at the end

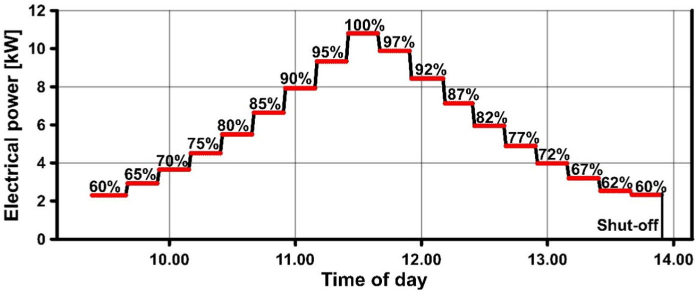

period. After the cleaning treatment, Test 3 shows a consistent increase in pumping capacity at all speeds and the pump provides 17.2 l/s with the same power consumption of 10.8 kW, a recovery of 8,3%-point compared with the initial 18.0 l/s capacity.

The variable pump performance implies that the hydraulic resistance of the system is different for each of the three tests. This is confirmed in the three differential pressure responses, which show both vertical and horizontal shifts of the pressure graphs in the data of the injection well, the production well, and of the groundwater heat exchanger (Fig. 6A-C). However, different types of performance changes are observed in these three components, which implies that the hydraulic resistance might have been altered differently in different parts of the system.

Since the sensors and the instrumentation were installed after the heat exchanger was replaced in the autumn of 2018 there are no initial on-site measurements of the heat exchangers hydraulic performance. However, the manufacturer provides a differential pressure of 2.64 m at 20.6 l/s pumping rate, which can serve as a reference for the tests. Plate heat exchangers are typically designed to operate within turbulent flow conditions, and this is observed for this installation as well where the groundwater heat exchanger pressure response is non-linear with respect to the flow rate (Fig. 6C). During Test 1 the pressure builds up to a maximum of 6.9 m of hydraulic head at 16.2 l/s flow rate, which is a substantial increase of hydraulic resistance compared with the data specified by the manufacturer. This has further increased in Test 2 to a maximum pressure head of 8.0 m, even with a 0.5 l/s lower flow rate, indicative of clogging development. After the cleaning treatment, test 3 shows a consistent decrease in pressure head for all pumping speeds. By comparing the regression results in Table 3, it is seen that both the linear and the non-linear data response have changed after the cleaning. The acid cleaning treatment has reduced the hydraulic resistance of the heat exchanger significantly.

Unlike the heat exchanger, a properly designed groundwater well should ideally have a fully linear pressure relation with respect to the pumping rate. This occurs in the injection well where the pressure increases linearly with the flow rate for all three tests. However, a consistent increase of magnitude of overpressure is observed between tests 1, 2, and 3, respectively. The linear regression results indicate that the hydraulic resistance in the injection well has increased by 65% from test 1 in August to test 3 in October. This is indicative of clogging development. Approximately half of the increased hydraulic resistance occurs after test 2, which indicates that the rate of clogging deposition is accelerating.

For the production well, the drawdown increases non-linearly with respect to the flow rate and the non-linear component dominates the pressure response (Fig. 6b). A consistent increase of water level drawdown is also observed between test 1 and 2, while the data points of test 3 plots almost equal to those of test 2. The peak drawdown was 0.3 m larger for test 3 at the 100% speed, but this corresponds to the

Fig. 5 Test 2 performance pyramid for the P2 and P3 pressure sensor. See Fig. 4 for test increments. At the 60% pumping speed, the pressures correspond to − 7 kPa pressure in the P3 sensor. After the pump is shut off, the vacuum extends to the P2 sensor, and a − 70 kPa vacuum is observed in the whole groundwater pipeline (outside the *y*-axis)

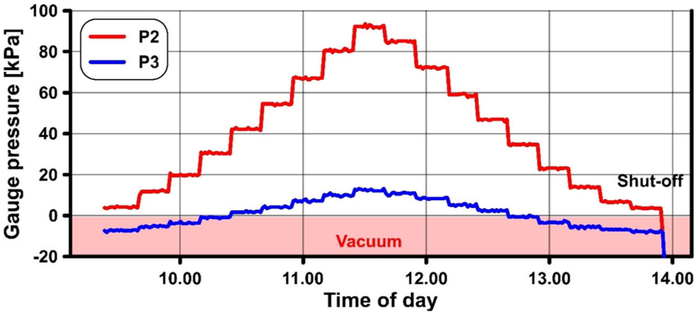

Table 3 The step-test regression results. ΔP [m] denotes the pressure differential and Q [l/s] denotes the variable flow rate. All regression curve fits are within $R^2 > 0.99$. The curves are visualized in Fig. 6

Test no.	Date	Injection well	Production well	Heat exchanger
1	28.08.2019 (Reference test)	$\Delta P = 0.068 \cdot Q$	$\Delta P = 0.018 \cdot Q + 0.010 \cdot Q^2$	$\Delta P = 0.064 \cdot Q + 0.022 \cdot Q^2$
2	08.10.2019 (41 days later)	$\Delta P = 0.094 \cdot Q$	$\Delta P = 0.030 \cdot Q + 0.011 \cdot Q^2$	$\Delta P = 0.056 \cdot Q + 0.029 \cdot Q^2$
3	16.10.2019 (55 days later)	$\Delta P = 0.112 \cdot Q$	$\Delta P = 0.039 \cdot Q + 0.010 \cdot Q^2$	$\Delta P = 0.016 \cdot Q + 0.011 \cdot Q^2$

increased pumping rate capacity of the submersible pump after the cleaning treatment. By comparing the regression results in Table 3, it is seen that it is primarily the linear data response that have changed, while the non-linear data response is virtually unchanged. The linear part of the regression results have increased by 116% from test 1 in August to test 3 in October. Approximately half of the increased hydraulic resistance occurs after test 2, similar to that of the injection well.

Discussion

The presented step-test data demonstrate how the performance of the heat source system at Lena Terrace can be monitored with the applied surveillance procedure. The integrated sensory equipment is able to detect changes in the hydraulic performance of the submersible pump, the groundwater heat exchanger, the production well, and the injection well. The results from the three different step-test procedures show that a variety of test configurations can be applied, but a minimum number of steps are preferable when the test is applied in practice. It is shown that test 1, with only three steps, describes the trends of the wells and the heat exchanger performances properly. The potential benefit of including more steps is not reflected in the added detail of the data of test 2 as it is possible to describe the same trend with only three of the data points. The surveillance procedure therefore only needs three steps to work in practice. This does however require a shutoff period before the test, which might not be acceptable if the building needs heating, e.g., during the winter months. As described in Gjengedal et al. (2019a), the benefit of the test 3 procedure is the possibility to perform the test without disrupting the heat production of the heating system. A step-test with four steps is thus recommended.

The step-test must be able to locate problems in the system in order to work as a surveillance tool. It is here demonstrated that the tests detect variability in the pump performance, which indicates that the hydraulic resistance of the system

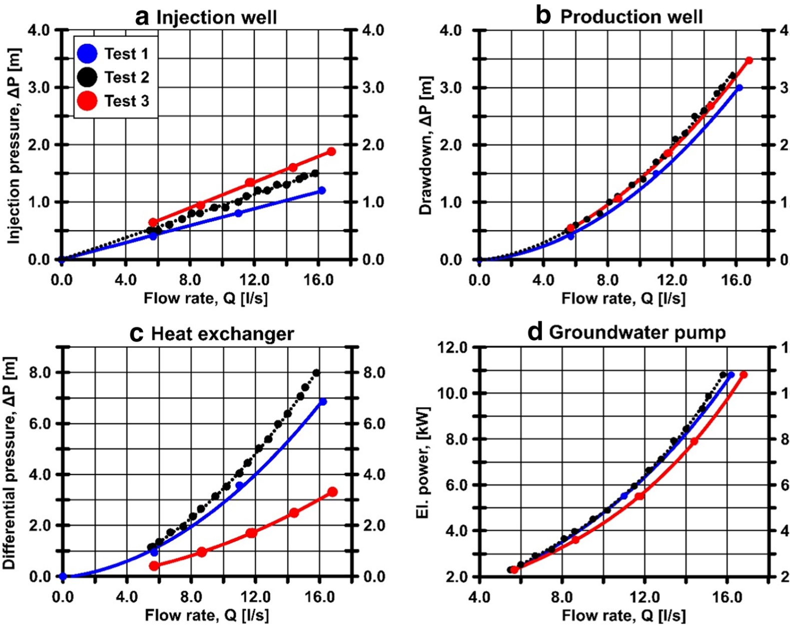

Fig. 6 The injection pressure (ΔP) responses for the injection well (**a**), the drawdown (ΔP) of the production well (**b**), the differential pressure response (ΔP) of the heat exchanger (**c**), and the electrical power supplied to the pump (**d**) as a function of the flow rate (Q) for the three step-test in the Lena Terrace GWHP system. Tests 1 and 2 are performed before the maintenance of the groundwater heat exchanger in October. Test 3 is performed after the cleaning

has changed. The first two tests show a reduction of production capacity for the whole groundwater system prior to the treatment of the groundwater heat exchanger. This increased hydraulic resistance indicates that clogging problems are developing in the entire system, especially in the production well, the injection well, and in the groundwater heat exchanger. Multidisciplinary competence and experience with GWHP-systems, aquifers, and groundwater wells are therefore needed to properly evaluate and interpret the results. The tests do not reveal what type of clogging material that impedes the system, but Bakema (2001) and Olsthoorn (1982) argue that monitoring over a longer timeframe can reveal different trends that are associated with various types of clogging, e.g., gas intrusion, chemical incrustations, or sediment suffusion. In this case, the test results can be interpreted and evaluated based on the system design and previous experience with faults found in the system. The tests can thus serve as a reference for other similar GWHP systems.

It was known beforehand that the groundwater heat exchanger is affected by fouling issues, typically by iron precipitates and fine soil particles clogging the heat exchanger plates. In these three tests, it is shown how this affects the hydraulic resistance of the heat exchanger. An increase in differential pressure, which is observed in tests 1 and 2, indicates that clogging and fouling development is in progress. The cleaning treatment reduced the hydraulic resistance, and test 3 demonstrates how the effects of the cleaning treatment yields a significant reduction in hydraulic resistance. The main benefit of the cleaning was presumably the improved heat transfer properties of the heat exchanger, but this could not be estimated accurately with the uncalibrated temperature sensors. The actual improvement to the thermal performance can therefore not be evaluated. However, the test shows that an increase in pumping capacity, by 1.5 l/s at maximum motor speed, is achieved after the cleaning. The test thus reveals how the lower hydraulic losses through the groundwater heat exchanger also affect the other parts of the system, e.g., through increasing the maximum drawdown in the production well at 100% pumping rate. Cleaning of the heat exchanger thus affects all parts of the system in the hydraulic sense, because the overall pumping capacity is affected.

An important benefit of the cleaning is that the pump is able to supply the necessary amount of groundwater at lower motor speeds. This reduces the electrical power consumption of the pump and the pumping cost for the installation. Some of the costs of annual cleaning of the heat exchanger are thus saved through improving the performance of the groundwater system. In the future, the performance of the heat exchanger should be monitored with calibrated temperature sensors. The heat-conducting properties of the heat exchanger are more sensitive to fouling than the hydraulic resistance. Monitoring the heat flux is thus expected to provide a more sensitive tool for fault detection in the heat exchanger (Gjengedal et al. 2019a).

The clogging material that was removed during the injection well cleaning operations and rehabilitations in 2018 and 2019 showed that the injection well was filled with a mixture of soil sediments and particles. These sediments were found to have been derived from suffusion through the production well screen. This has likely occurred this time as well. The increased hydraulic resistance observed in the injection well pressure response is a clear indication that clogging development is in progress. Similar pressure responses are described by Olsthoorn (1982) for injection well clogging in general. The data display a gradual buildup of the pressure response over the 55-day period, and the regression results (Table 3) show that the rate of clogging deposition is accelerating. In order to ensure continuous and reliable operation of the GWHP system, it is therefore necessary to perform additional maintenance on the injection well screen but also the production well to stop the suffusion of particles.

Suffusion of soil particles through the production well screen is known to affect the production well performance in a distinct manner (Olsthoorn 1982; Van Beek 2007). The presented tests demonstrate that the drawdown in the production well react non-linearly to the flow rate (Fig. 6b), deviating from the anticipated fully linear drawdown curve expected from a properly design groundwater well. The question is whether this excessive drawdown is a sign of clogging of the production well screen or not. By comparing the pressure response of tests 2 and 3, relative to test 1, it is observed that there is an increased hydraulic resistance in the well. However, the relative increase in drawdown originates from an increase of the linear pressure responses, while the non-linear pressure response is virtually unaffected. The majority of linear head losses originate from aquifer losses and/or well screen losses (Houben 2015a). This increase of linear head losses is therefore a likely sign of clogging of the well screen and/or the aquifer.

The lack of change in the non-linear component indicates that the cause of these losses has not been altered throughout the test period. Non-linear drawdown losses are associated with inertial losses that occur at high velocities (e.g., convective acceleration or turbulence). The fully linear response of the injection well reveals that the local soil conditions do not induce non-linear losses in the flow for the pumping rates tested. The production well has similar soil conditions, but compared with the injection well, it has slightly higher flow velocities through the well screen because of the shorter screen length. Assuming an even distribution of the flow along the entire well screen, the average maximum flow velocity (17.2 l/s flow rate at 100% Hz) through the production well screen is 1.81 cm/s, while it is 1.09 cm/s through the injection well screen. The 1.81 cm/s velocity is perhaps high enough to induce some non-linear losses in the aquifer

(Houben 2015a), but not to the degree that is measured here. The difference in screen flow velocity does therefore not explain the dominant non-linear component of the production well pressure response.

The most likely cause to these non-linear losses is the relatively large contraction and expansion of the flow channel in the well-bore segment around the submersible pump motor. Houben (2015b) states that the upwards flow velocity in a well should be kept below 1.5 m/s to maintain well losses at an acceptable level. This is ensured in the well-bore itself, but not in the section around the pump. The SP60-5-MS6000 submersible pump (Grundfos 2019) has a motor diameter of 139.5 mm. The internal well diameter of 158.0 mm then provides a 9.25-mm annular channel opening past the pump motor, which is very narrow for the 17.2 l/s flow rate. The average flow velocity past the 0.6 m long motor will then be approximately 3.9 m/s, indicating highly turbulent flow conditions. This channel opening is unchanged from test 1–test 3, and it is therefore reasonable that the non-linear component is unchanged as well. The non-linear behavior is thus not likely caused by clogging, but by a faulty well design with a too narrow well diameter.

Apart from the clogging issues that are detected, the tests reveal that the production well water level drawdown is too large to ensure that the pump operates reliably. The submersible pump requires 5 m of overpressure (NPSH) to operate reliably at 100% Hz motor speed (Grundfos 2019). With 3.5 m of drawdown, the pump operates with 2.9 m of overpressure, and the pump is thus subjected to increased risks of, e.g., flow separation and vacuum pressures at the suction inlet and internal cavitation at the pump impellers (Mackay 2004). To ensure continuous and reliable operation of the GWHP system, it is necessary to perform additional maintenance on the production well screen or to limit the pumping rate to 80% of the maximum capacity where 4 m of NPSH is sufficient.

The tests also reveal that parts of the groundwater pipeline operate with vacuum pressures. Vacuum pressure can potentially trigger exsolution of gases that are dissolved in the groundwater (Banks 2012; Snijders and Drijver 2016; Gjengedal et al. 2019b). The tests thus indicate that the system has an unfavorable design configuration with respect to the local groundwater conditions, which can potentially be the underlying reason for the clogging issues that has troubled this installation since 2003.

Conclusions

The performance of the Lena Terrace groundwater heat pump system has been monitored with a step-test surveillance procedure. Results from three versions of the test demonstrate that the test can be performed with a minimum of four steps, each of 15-min duration, while the GWHP system is active and producing heat. The results demonstrate that the surveillance test can detect changes in the hydraulic resistance of the groundwater circuit and locate clogging problems within all of the relevant system components in the groundwater circuit simultaneously. At the Lena Terrace GWHP system, these tests indicate a gradual increase of hydraulic resistance with time, which verify that clogging issues are continuously developing in the injection well, the production well, and in the groundwater heat exchanger. Cleaning of the heat exchanger has increased the pumping capacity by 8.3% points, but continuous clogging of the injection well and the production well necessitates further maintenance to ensure a reliable operation. These results can function as a reference for other GWHP systems with similar design configurations.

Acknowledgments Open Access funding provided by Norwegian University of Science and Technology (incl St. Olavs Hospital - Trondheim University Hospital). This work was conducted as a part of the research project Optimal Resource Utilization of Groundwater for Heating and Cooling in Melhus and Elverum (ORMEL). The project is a cooperation between the municipalities of Melhus and Elverum, the Norwegian University of Science and Technology, Asplan Viak AS, and the Geological Survey of Norway. We would like to thank all the involved institutions and persons for cooperation and financial contributions.

Funding The Regional Research Funds in Mid-Norway (grant number 209074) funded this research.

Compliance with ethical standards

Conflict of interest The authors declare that they have no conflict of interest.

References

Bakema G (2001) Well and borehole failures in UTESS. State of the art 2000, 2nd edn. IF Technology BV, Arnhem

Banks D (2012) An introduction to Thermogeology: ground source heating and cooling, 2nd edn. Wiley-Blackwell, Chichester

Bloemendal M, Olsthoorn T, van de Ven F (2015) Combining climatic and geo-hydrological preconditions as a method to determine world potential for aquifer thermal energy storage. Sci Total Environ 538: 621–633. https://doi.org/10.1016/j.scitotenv.2015.07.084

Brøste HM (2017) Vannkvalitet knyttet til grunnvannsbaserte grunnvarmeanlegg i Melhus og Elverum [eng: Water quality with respect to open loop GSHP systems in Melhus and Elverum]. Master thesis, Norwegian University of Science and Technology Trondheim (NTNU Trondheim) (in Norwegian)

Gehlin S, Andersson O (2019) Geothermal energy use, country update for Sweden. Proceedings of the European Geothermal Congress, Den Haag, The Netherlands, 11–14 June

Gjengedal S, Ramstad RK, Hilmo BO, Frengstad BS (2018) Video inspection of wells in open loop ground source heat pump systems in Norway. Editor: prof. Jeffrey D. Spitler. International ground source heat pump association, Oklahoma. In IGSHPA conference proceedings 2018. https://doi.org/10.22488/okstate.18.000025

Gjengedal S, Ramstad RK, Hilmo BO, Frengstad BS (2019a) Fouling and clogging surveillance in open loop GSHP systems. A systematic procedure for fouling and clogging detection in the whole groundwater circuit. Bull Eng Geol Environ. https://doi.org/10.1007/s10064-019-01556-5

Gjengedal S, Stenvik LA, Storli PT, Ramstad RK, Hilmo BO, Frengstad BS (2019b) Design of groundwater heat pump systems. Principles, tools and strategies for controlling gas and precipitation problems. Energies 12:3657. https://doi.org/10.3390/en12193657

Grundfos (2019) Grundfos data booklet. SP engineering manual https://nogrundfoscom/campaigns/download-sp-engineering-manualhtml Accesses on: 29 November 2019

Hellestveit MS (2018) 3D-modellering av grunnvannstrømning og varmetransport i akviferen i Melhus sentrum - en kvartær- og hydrogeologisk tolkning, med vurdering av uttakskapasitet. [eng: 3D modeling of groundwater flow and thermal development in the Melhus aquifer – an evaluation of quaternary and hydrogeological conditions and exploitation limitations] master thesis. Trondhiem. NTNU. (in Norwegian)

Houben GJ (2015a) Review: hydraulics of wells – the flow laws and influence of geometry. Hydrogeol J 23:1633–1657. https://doi.org/10.1007/s10040-015-1312-8

Houben GJ (2015b) Review: hydraulics of water wells—head losses of individual components. Hydrogeol J 23:1659–1675. https://doi.org/10.1007/s10040-015-1313-7

Kruseman GP, de Ridder NA (1994) Analysis and evaluation of pumping test data, 2nd edn. Wageningen, International Institute for Land Reclamation and Improvement

Mackay R (2004) The practical pumping handbook. Elsevier, Oxford

Melo LF, Bernardo CA, Bott TR (1988) Fouling science and technology. Kluwer, Dordrecht

Müller-Steinhagen H (2000) Heat exchanger fouling: mitigation and cleaning technologies: handbook. Publico Publications, Essen

Olsthoorn TN (1982) The clogging of recharge wells, technical report. The Netherlands Waterworks' testing and research institute KIWA, Rijswijk

Rees S (2016) Advances in ground-source heat pump systems. Woodhead Publishing, Amsterdam

Riise MH (2015) Praktisk guide for grunnvarmeanlegg basert på oppumpet grunnvann - Hydrogeologiske forundersøkelser, etablering, drift og oppfølging med utgangspunkt i erfaringer fra etablerte anlegg i Melhus sentrum [eng: Guide to a better design and operation of groundwater heat pump systems – with examples from Melhus]. Master thesis, NTNU Trondheim (in Norwegian)

Snijders AL, Drijver BC (2016) Open-loop heat pump and thermal energy storage systems. In: Rees S (ed) Advances in ground-source heat pump systems, 1st edn. Woodhead Publishing, Amsterdam, pp 247–268

Stene J (2001) Varmepumper: grunnleggende varmepumpeteknikk [in English: Heat pumps: basics] Trondheim, SINTEF Energi

Van Beek C (2007) Cause and prevention of clogging of wells. Abstracting groundwater from unconsolitaed aquifers. PhD Thesis, Vrije University, Amsterdam

Paper VI

Transport in Porous Media (2020) 134:1–40
https://doi.org/10.1007/s11242-020-01432-x

Fluid flow through 3D-printed particle beds: a new technique for understanding, validating, and improving predictability of permeability from empirical equations

Sondre Gjengedal, et al. ***[full author details at the end of the article]***

Received: 6 September 2019 / Accepted: 29 May 2020 / Published online: 6 July 2020

Abstract

The application of 3D technology for fabrication of artificial porous media samples improves porous media flow studies. The geometrical characteristics of a porous media pore channel: the channel shape, size, porosity, specific surface, expansion ratio, contraction ratio, and the tortuous pathway of the channel can be controlled through advanced additive manufacturing techniques (3D printing), computed tomography imagery (CT imaging) and image analysis methods. These 3D technologies have here been applied to construct and analyze four homogeneous porous media samples with predefined geometrical properties that are otherwise impossible to construct with conventional methods. Uncertainties regarding the geometrical properties are minimized because the 3D-printed porous media samples can be evaluated with CT imaging after fabrication. It is this combination of 3D technology that improves the data acquisition and data interpretation and contributes to new insight into the phenomenon of fluid flow through porous media. The effects of the individual geometrical properties on the fluid flow are then accounted for in permeability experiments in a Hassler flow cell. The results of the experimental work are used to test the theoretical foundation of the Kozeny–Carman equation and the extended version known as the Ergun equation. These equations are developed from analogies to the Hagen–Poiseuille flow equation. Based on the results from the laboratory experiments in this study, an analytical equation based on the analytical Navier–Stokes equations is presented as an alternative to the Hagen–Poiseuille analogy for porous media channels with non-uniform channel geometries. The agreement between experiment and the new equation reveals that the dissipating losses of mechanical energy in porous media flows are not a result of frictional shear alone. The mechanical losses are also a result of pressure dissipation that arise due to the non-uniformity of the channel geometry, which induced spatial variations to the strain rate field and induce acceleration of the velocity field in the flow through the porous medium. It is this acceleration that causes a divergence from linear flow conditions as the Stokes flow criterion ($\boldsymbol{Re} \ll 1$) is breached and causes the convective acceleration term to affect the flow behavior. The suggested modifications of theory and the presented experiments prove that the effects of surface roughness (1) do not alter the flow behavior in the Darcy flow regime or (2) in the Forchheimer flow regime. This implies that the flow is still laminar for the Forchheimer flow velocities tested.

Keywords Permeability · Particle size & shape · Porosity · Tortuosity · Empirical validation · Darcy · Forchheimer · Kozeny–Carman · Ergun · 3D fabrication · CT imaging

1 Introduction

Fluid flow through a porous media is a subject of global interest and a topic of extensive research within fields of scientific and industrial nature alike. Within the field of civil engineering, e.g., drinking water supply, water resource management, groundwater heat pump systems, coastal erosion, and water contamination there frequently exists a need to determine the rate of groundwater flow through soil formations. The groundwater flow is assumed to follow the relations given by Darcy's law (1856) and is governed by the hydraulic conductivity, **K** (m/s), of the soil. Naturally occurring soil formations have a potential for large spatial variation, and this often requires the determination of a large number of local hydraulic conductivities to adequately describe the over-all field **K** for an aquifer. Many engineering projects do not have the budget to perform time-consuming and costly field or laboratory permeability tests. Thus, simple predictive methods that estimate the hydraulic conductivity from individual soil samples are still a common and valued approach in the industry.

A range of predictive equations has been developed theoretically or empirically from laboratory tests. Chapuis (2012) has reviewed 45 of the most commonly used predictive methods in engineering and have recommended four of them, one of which is the Kozeny–Carman equation. Common for all the 45 methods is that they relate the hydraulic conductivity or permeability of a soil formation to properties of the solid soil matrix rather than to the pore-space matrix properties directly. This is done because soil samples are often routinely available in many projects. Properties of the soil solids, e.g., the grain size distribution curve, sediment bulk density, soil texture, and form, are properties that are relatively easy to measure compared to in situ pore-space properties. However, the four methods recommended by Chapuis (2012) incorporate simple dimensionless pore-space properties, e.g., the porosity (**n**) of the bed and the pore channel tortuosity ($\boldsymbol{\tau}$). These pore properties are vital for the accuracy of the methods, but are rarely measured or estimated in practice, at least in Norway. Continuous use of the predictive methods argues that further development and confirmation of their accuracy and applicability are useful for the industry.

The aim of this study is to further investigate how various geometrical properties of a porous media affect its permeability, and thereby improve the empirical equations further. As demonstrated by Chapuis (2012), the in situ pore properties can be difficult to quantify accurately in conventional permeability experiments on natural soils. Natural soils typically consist of a variety of soil particles, with different sizes and shapes, which makes it difficult to evaluate the significance of individual geometrical properties alone. Therefore, the relation between permeability and different geometrical properties of porous media is investigated in detail by applying an additive manufacturing (AM) technique, 3D printing, as a means of fabricating artificial soil samples. Geometries that previously were impossible to construct are now available through AM. AM has recently shown its usefulness in porous media studies (Osei-Bonzu et al. 2018; Gelhausen et al. 2018). In this study, the applied AM technique allows to determine the precise location, shape, and size of all individual particles in a porous media, thus minimizing uncertainties related to the pore-matrix configurations and geometry. The influence of the various pore geometrical properties can then be investigated in a controlled manner. Four different 3D-fabricated homogeneous porous media geometries have been tested in a Hassler flow cell and the results have been used to test the state-of-the-art analytical flow equations of Kozeny–Carman (1937) and Ergun–Orning (1949). These equations are developed based on analogies to the

Hagen–Poiseuille equation. As an alternative, a new analytical solution has been developed and is here presented, tested, and compared. The new equation is based on analogies to the analytical solutions of the Navier–Stokes equation and is proposed to be a better explanation for the porous media flow behavior observed in the presented experiments.

2 Theory

The dissipation of mechanical energy that arise as fluids flow through a porous media display a velocity-dependent behavior. At low flow velocities the relation is linear, while at high velocities the flow displays a non-linear behavior. The fundamental equation of fluid flow through a porous media is that of Darcy (1856). Darcy's law governs the phenomenon in flow conditions where viscous shear forces dominate the dissipating losses of fluid flow through a porous medium. For horizontally directed one-phase flow, the Darcy equation can be stated as Eq. (1) (Hubbert 1940).

$$\frac{\boldsymbol{\Delta P}}{\boldsymbol{L}} = \frac{\boldsymbol{\mu}}{\boldsymbol{k}} \cdot \boldsymbol{u}_s \tag{1}$$

where the pressure loss, $\boldsymbol{\Delta P}$ (Pa), across the superficial length unit of the porous medium, $\boldsymbol{L}$ (m), is proportional to the superficial velocity of the flow, $\boldsymbol{u}_s$ (m/s), the viscosity of the fluid, $\boldsymbol{\mu}$ (Pa·s), and is inversely proportional to the permeability of the porous medium, $\boldsymbol{k}$ (m^2). The superficial fluid velocity is defined as the bulk fluid flow rate, $\boldsymbol{Q}$ (m^3/s), divided by the bulk cross-sectional area perpendicular to the flow direction, $\boldsymbol{A}$ (m^2). Beyond a certain critical velocity limit the pressure loss diverges from the linear response and must typically be described by a polynomial equation of the second order, of which the Forchheimer equation (Eq. 2) is best known. The second-order term accounts for inertial losses that gradually dominate at progressively higher rates of flow. These losses are proportional to the inertial resistance factor, $\boldsymbol{\beta}$ (m^{-1}), and the density ($\boldsymbol{\rho}$ kg/m^3) of the fluid.

$$\frac{\boldsymbol{\Delta P}}{\boldsymbol{L}} = \frac{\boldsymbol{\mu}}{\boldsymbol{k_F}} \cdot \boldsymbol{u}_s + \boldsymbol{\beta\rho} \cdot \boldsymbol{u}_s^2 \tag{2}$$

In this paper, the empirical equations of Darcy (1856) and Forchheimer (1930) are linked with that of two analytical solutions of the Navier–Stokes equation. This is done by applying some alternative solutions commonly found in other fields of fluid mechanics. Similar solutions have been attempted by e.g., Brinkman (1947), Hasimoto (1959), Barnea and Mednick (1978), Collins (1976), Sangani and Acrivos (1981), and Happel and Brenner (1983), Wilkinson (1985), and Allen (1985); among others. In this paper, the analytical solution of choice corresponds to that of a horizontally directed, one-phase, incompressible fluid flow in channels, shown in Eq. 3.

$$\boldsymbol{F} = \left(\boldsymbol{C} + \boldsymbol{C_d} \cdot \boldsymbol{Re}\right) \cdot \boldsymbol{\mu} \cdot \boldsymbol{V} \cdot \boldsymbol{L} \tag{3}$$

where the dissipating forces, $\boldsymbol{F}$ (N), that resist the fluid motion within the flow channel, is a sum of two different force components. The first term on the right-hand side, represented by the dissipation factor $\boldsymbol{C}$ (-), is a linear term and signifies a force dominated by viscous shear stress and pressure dissipation. The dissipating forces that originate from the linear term are proportional to the dynamic viscosity of the fluid, $\boldsymbol{\mu}$ (Pa·s), the fluid velocity, $\boldsymbol{V}$

(m/s), and a characteristic length unit, $\boldsymbol{L}$ (m), that describes the channel. For internal flows, such as pipe flows, this is typically the length of the channel.

The second term, represented by the dissipation factor $\boldsymbol{C_d}$ (-), is a non-linear term and signifies the force of convective acceleration. When Eq. 3 is arranged as shown here, the dissipating forces that originate from the non-linear term are dependent on the Reynolds number of the flow ($\boldsymbol{Re}$). Note that this is not the conventional manner to describe the relation in pipe flows, but it is rendered here in this way because the Reynolds numbers in porous media are small and the main contributor to dissipation originates from the linear term. At high Reynolds numbers the non-linear term dominates, and the equation is typically rearranged in favor of the second-order term (White, 2006). In Eq. 3 the Reynolds number is defined by Eq. 4 where $\boldsymbol{Re}$ (−) signifies a dimensionless number that relates the ratio of inertial forces to viscous forces. The number depends on the velocity, $\boldsymbol{V}$ (m/s), the density, $\boldsymbol{\rho}$ (kg/m^3), and the viscosity of the fluid and the characteristic length unit, $\boldsymbol{m}$ (m), of the flow channel geometry.

$$\text{Reynolds number} = \boldsymbol{Re} = \frac{\boldsymbol{\rho} \cdot \boldsymbol{V} \cdot \boldsymbol{m}}{\boldsymbol{\mu}} \tag{4}$$

The linear ($\boldsymbol{C}$) term and the non-linear ($\boldsymbol{C}_\mathrm{d}$) term of Eq. 3 represent approximate solutions to the incompressible Navier–Stokes equation. The solutions are only valid if the following two assumptions are in force: (1) the effects of gravity affect the hydrostatic pressure component only and does not affect the dynamics of the flow; (2) the flow is *steady* or *quasi-steady*. These assumptions imply that the time-dependent term and the Froude number term of the Navier–Stokes equation are negligible small and can be ignored, and that the flow channel exhibits no free-surface effects.

For Eq. 3 to be relevant for porous media it is necessary to define what the various parameters signify and how they are described in relation to each other. In pipe flows and in porous media studies the dissipating force is measured as a loss of pressure across the superficial length of a pipe section or a porous media sample. The force is thus best described as a pressure loss-type equation. The equation should therefore be rearranged to describe a pressure relation, as in Eq. 5, where the loss of pressure, $\boldsymbol{\Delta P}$ (Pa), is associated with some characteristic length unit, $\boldsymbol{m}$ (m), that describes how the pressure forces and the friction forces of the fluid motion interact with the channel geometry.

$$\boldsymbol{m}^2 \cdot \boldsymbol{\Delta P} = \left(\boldsymbol{C} + \boldsymbol{C_d} \cdot \boldsymbol{Re}\right) \cdot \boldsymbol{\mu} \cdot \boldsymbol{V} \cdot \boldsymbol{L} \tag{5}$$

It is clear that both the characteristic length unit, $\boldsymbol{m}$, and the velocity, $\boldsymbol{V}$, of both Eqs. 4 and 5 must be defined identically for the equation to be further modified. The manner that these two parameters are defined are often determined according to the problem at hand, and there are certain conventions in different scientific fields (White 2006). In the study of suspended solids, both $\boldsymbol{m}$ and $\boldsymbol{L}$ are typically described as the size or diameter of the solid object, and the velocity is often described by the mean "free stream" velocity. For internal flows, however, such as for pipes, the velocity is typically described by the maximum velocity component within the flow, while $\boldsymbol{m}$ is typically described by Eq. 6. For a uniform circular pipe, the characteristic length unit $\boldsymbol{m}$ simplifies to an expression of the pipe internal radius, $\boldsymbol{r_i}$ (m), or diameter, $\boldsymbol{d_i}$ (m). It should therefore be noted that in Eq. 5, $\boldsymbol{L}$ describes the length of the channel, while $\boldsymbol{m}$ describes the shape of the channel along the channel length $\boldsymbol{L}$ (Schiller 1923).

$$\boldsymbol{m} = \frac{\textit{volume of fluid in pipe}}{\textit{pipe internal surface area}} = \frac{\boldsymbol{\pi} \cdot \boldsymbol{r}_i^2 \cdot \boldsymbol{L}}{2 \cdot \boldsymbol{\pi} \cdot \boldsymbol{r}_i \cdot \boldsymbol{L}} = \frac{\boldsymbol{d}_i}{4} \tag{6}$$

In the following subsections, a new theoretical method for defining these parameters for a single pore is presented. This expression is then tested if it applies to porous media that consist of numerous pores of equal shape.

2.1 The Stokes flow approximation

Equation 3 shows that if the flow velocity is sufficiently small ($\boldsymbol{Re} << 1$), the dissipation caused by convective acceleration of the fluid velocity is orders of magnitude smaller than the effects of the linear term ($\boldsymbol{C}$). The second-order term can then be ignored and Eq. 3 corresponds to the Stokes flow approximation with the general form of Eq. 7 (White, 2006).

$$\boldsymbol{F}_C = \boldsymbol{C} \cdot \boldsymbol{\mu} \cdot \boldsymbol{V} \cdot \boldsymbol{L} \quad \text{where} \quad \boldsymbol{C} = \boldsymbol{C}_f + \boldsymbol{C}_p \tag{7}$$

Equation 7 states that the dissipating forces, $\boldsymbol{F}_C$, within the flow must balance the dissipating frictional forces, $\boldsymbol{C}_f$ (−), and the dissipating pressure forces, $\boldsymbol{C}_p$ (−), enforced by the motion of a fluid past an object surface. The typical scenario would be a fluid flowing with a mean velocity, $\boldsymbol{V}_{avg}$ (m/s), past a three-dimensional object of characteristic length, $\boldsymbol{L}$ (m). The balance of dissipating forces is proportional to an unknown dissipation constant ($\boldsymbol{C}$), which depends on the objects shape and orientation in the flow field. The classical example of this dissipation constant is seen in Eq. 8 for a smooth sphere, e.g., falling in a stagnant fluid or suspended in a uniform velocity field with characteristic length equal to the sphere diameter, $\boldsymbol{d}$ (m), (Fig. 1a).

$$\boldsymbol{F}_C = 3 \cdot \boldsymbol{\pi} \cdot \boldsymbol{\mu} \cdot \boldsymbol{V}_{avg} \cdot \boldsymbol{d} \tag{8}$$

For a single sphere the dissipating frictional forces are found to be $\boldsymbol{C}_f = 2\pi$, and the dissipating pressure forces are found to be $\boldsymbol{C}_p = \pi$. The sum of these two coefficients is the Stokes sphere constant shown in Eq. 8. Equation 8 is frequently applied in the field of physical sedimentology and settling of particles (Allen 1985; Raudkivik 1990; Van

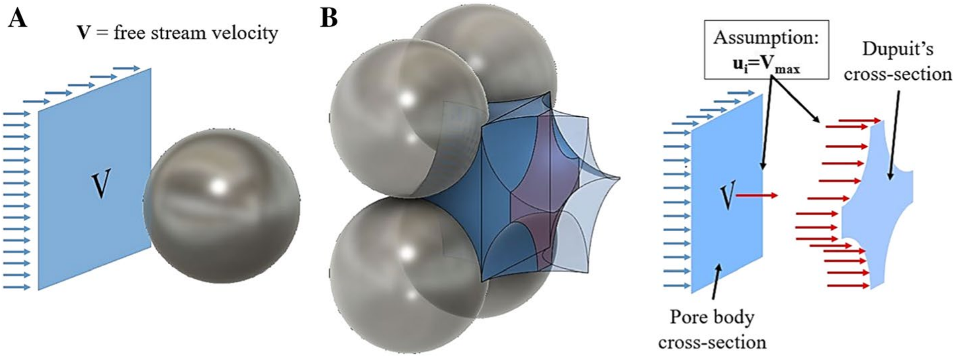

Fig. 1 Principle sketch of the Stokes creeping flow approximation. **a** A single sphere suspended in a uniform fluid flow field (V) is the classical example. **b** The velocity field in a pore is spatially bound by the geometry of the pore. The assumption of Dupuit is not correct for the whole pore but should be correct for a section of the pore where the volume ratio equals the area ratio. Equation 13 assumes that the average velocity in Dupuit's cross-section is equal to the maximum velocity in the pore body cross-section

Rijn 1993). $\boldsymbol{C}$ is found to be similar to 3π for a wide range of geometrical shapes. The $\boldsymbol{C}$ of, e.g., a thin flat circular disk of equal diameter to that of the sphere, but oriented perpendicular to the flow direction, is approximately 15% smaller than the sphere constant. If this disk is oriented parallel to the flow direction the constant is approximately 56% smaller than the 3π sphere constant (White 2006; Çengel and Cimbala 2010). Regarding settling of particles in a fluid, Eq. 8 is considered suitable for a variety of particle shapes provided that the particle sizes are sufficiently small to satisfy the criterion $\boldsymbol{Re} < \approx 1$ (Allen 1985, White 2006) (here the Reynolds number is defined with the particle diameter as the characteristic length unit L and with the mean fluid "free stream "velocity as the velocity component).

Alternatively, Eq. 7 should be valid for a range of particle sizes provided that the velocity is sufficiently small to ensure $\boldsymbol{Re} \ll 1$. This is the relevant situation for porous media, where the particles of the media can constitute a range of particle sizes. The corresponding Stokes flow approximation for fluid flow through a single pore is suggested to be Eq. 9, where the characteristic length of the pore channel is defined as the interstitial length, $\boldsymbol{L_e}$ (m), of the pore channel (which might be longer than the superficial flow axis).

$$\frac{\boldsymbol{\Delta P}}{\boldsymbol{L_e}} = \boldsymbol{C} \cdot \frac{\boldsymbol{\mu} \cdot \boldsymbol{V}}{\boldsymbol{m}^2} \tag{9}$$

The shape of the pore geometry along the L is assumed to be described according to the assumptions of Kozeny (1927), which is expressed as Eq. 10 for a single pore. This is the same expression as for Eq. 6, but since a pore channel is not uniform or consistently shaped, the expression does not simplify to an expression related to a diameter of the pore channel.

$$\boldsymbol{m} = \frac{porosity}{specific\ surface} = \frac{\boldsymbol{n}}{\boldsymbol{S}} \tag{10}$$

The corresponding Stokes flow equation for a pore then becomes Eq. 11, where the geometry of the pore is expressed as a ratio of the void volume per unit volume, $\boldsymbol{n}$ ($\mathrm{m}^3 \cdot \mathrm{m}^{-3}$), over the surface area per unit volume, $\boldsymbol{S}$ ($\mathrm{m}^2 \cdot \mathrm{m}^{-3}$).

$$\frac{\boldsymbol{\Delta P}}{\boldsymbol{L_e}} = \boldsymbol{C} \cdot \frac{\boldsymbol{\mu} \cdot \boldsymbol{S}^2 \cdot \boldsymbol{V}}{\boldsymbol{n}^2} \tag{11}$$

However, the interstitial velocity within a pore is difficult to quantify in practical experiments and a modification to an average superficial fluid velocity is performed in porous media studies. This is typically done through the application of Dupuit's assumption (1863, described in Carman (1937)) in Eq. 12.

$$\boldsymbol{u_i} = \frac{\boldsymbol{u_s}}{\boldsymbol{n}} \tag{12}$$

where the interstitial velocity of the fluid within the porous media, $\boldsymbol{u_i}$ (m/s), must be higher than the superficial velocity (Ref. Eq. 1). Dupuit assumed the interstitial velocity to be a function of the porosity ($\boldsymbol{n}$) of the bed. However, the assumption is assumed valid on the notion that for a randomly packed porous media the voids within a porous media are so *"evenly distributed throughout the bed that the fractional free area at any cross-section is constant and equal to the porosity…"* (Carman, 1937). Nevertheless, if Dupuit's assumption is applied to a single pore, this notion is incorrect, and the assumption is not valid. For the flow behavior to satisfy the conservation of mass, the flow velocity must be ever-changing through a pore in response to the contracting and expanding pore channel geometry.

As an alternative, the assumption of Dupuit can be presumed to be correct for a specific slice of pore cross-section within the pore where the slice of pore channel cross-sectional area equals that of the porosity of the whole pore (Fig. 1b). For any pore geometry, this cross-section, hereby termed Dupuit's cross-section, must be found somewhere in-between the pore body center cross-section and the pore throat center cross-section. If Dupuit's assumption represent the average interstitial fluid velocity in this cross-section, it is evident that the maximum velocity of the cross-section must be bound by the geometry of the cross-section. The conservation of mass then requires the velocity to be faster anywhere closer to the pore throat region, and slower anywhere closer to the pore body region of the pore. In the case of a uniform channel, e.g., a pipe of uniform cross-section, the relation of the maximum fluid velocity, $\boldsymbol{U_{max}}$, and channel geometry is seen in Eq. 13 (Çengel & Cimbala, 2010), where $\boldsymbol{k_0}$ is the channel geometry factor and $\boldsymbol{U_i}$ is the average velocity of the channel.

$$\boldsymbol{U_{max}} = \boldsymbol{k_0} \cdot \boldsymbol{U_i} \tag{13}$$

It is suggested here that if the velocity, $\boldsymbol{V}$, in Eq. 11 is described similarly to that of the "free stream" velocity in Eq. 8, the same dissipating constant of 3π should result (Fig. 1). This implies that the velocity must be described as the interstitial mean velocity in the pore body. The average pore body cross-section velocity is less than the average velocity in Dupuit's cross-section. It is therefore assumed that the average velocity in Dupuit's cross-section is approximately equivalent to the maximum velocity of the pore body cross-section. (Figure 1b). this assumption corresponds to the relation of Eq. 14, where the interstitial velocity of Eq. 12, $\boldsymbol{u_i}$, is thought to resemble the $\boldsymbol{U_{max}}$ of Eq. 13, and the velocity $\boldsymbol{V}$ of Eq. 11 resembles the average velocity of the channel, $\boldsymbol{U_i}$.

$$\frac{\boldsymbol{u_i}}{\boldsymbol{k_0}} = \boldsymbol{V} \tag{14}$$

Combining Eqs. 11, 12, and 14, results in Eq. 15 for the Stokes flow approximation for fluid flow through a pore. The $\boldsymbol{k_0}$ value will here be related to the shape of the pore body region of the pore.

$$\frac{\boldsymbol{\Delta P}}{\boldsymbol{L_e}} = \frac{\boldsymbol{C}}{\boldsymbol{k_0}} \cdot \frac{\boldsymbol{\mu} \cdot \boldsymbol{S}^2 \cdot \boldsymbol{u_s}}{\boldsymbol{n}^3} \tag{15}$$

The final corrections needed in the equation are to account for the tortuous pathway of the flow channel. The pore channel might not be oriented parallel to the measuring axis. This causes the actual travel path of the fluid to be longer than the superficial length of the pore. Kozeny (1927) proposed that the longer, tortuous pathway, $\boldsymbol{\tau}$ (−), can be expressed by Eq. 16.

$$\boldsymbol{\tau} = \frac{\boldsymbol{L_e}}{\boldsymbol{L}} \tag{16}$$

Carman (1937) stated that the same correction must be applied to the velocity field. As the point of reference is chosen to be the superficial velocity component, $\boldsymbol{u_s}$, it is necessary to account for the flow directions of the interstitial velocity components. Carman (1937) suggested that this should be done according to Eq. 17.

$$\boldsymbol{u_i} = \frac{\boldsymbol{u_s}}{\boldsymbol{n}} \cdot \boldsymbol{\tau} \tag{17}$$

Accounting for the additional distance of travel and the additional velocity with which the fluid progress through the pore, the final form of the Stokes flow approximation becomes Eq. 18. This theoretical approach provides an equation that describes the flow through a pore in relation to the average velocity of the pore body.

$$\textit{The Stokes–flow approximation}: \frac{\boldsymbol{\Delta P}}{\boldsymbol{L}} = \frac{\boldsymbol{C}}{\boldsymbol{k_0}} \cdot \frac{\boldsymbol{\tau}^2 \cdot \boldsymbol{\mu} \cdot \boldsymbol{S}^2 \cdot \boldsymbol{u_s}}{\boldsymbol{n}^3} \tag{18}$$

In practical experiments, the dissipating constant $\boldsymbol{C}$ will only be revealed if all other parameters are measured and quantified. Among the variables in Eq. 18, the $\boldsymbol{k_0}$ value is the most difficult parameter to determine. It is therefore suitable to define a new coefficient that account for both the $\boldsymbol{C}$ and $\boldsymbol{k_0}$ values in practice. The new coefficient, $\boldsymbol{k_S}$ (−), is suggested in Eq. 19 where it is expected that the 3π should be an approximate value for a pore with a non-uniform pore channel.

$$\boldsymbol{k_S} = \frac{\boldsymbol{C}}{\boldsymbol{k_0}} \approx \frac{3 \cdot \boldsymbol{\pi}}{\boldsymbol{k_0}} \tag{19}$$

A well-known alternative to Eq. 18 is the Kozeny–Carman equation (Carman 1937). In this equation, the velocity $\boldsymbol{V}$ component is identified differently and is related to the maximum velocity component within the channel ($\boldsymbol{V}$ is interpreted to resemble $\boldsymbol{U_{max}}$ of Eq. 13 and not the $\boldsymbol{U_i}$), as is convention for pipe flow equations where the pipes have uniform cross-sectional shapes (Carman 1937). Their approach corresponds to Eq. 20.

$$\textit{The Kozeny-Carman equation}: \frac{\boldsymbol{\Delta P}}{L} = \frac{\boldsymbol{k_C} \cdot \boldsymbol{\mu} \cdot \boldsymbol{S}^2 \cdot \boldsymbol{u_s}}{\boldsymbol{n}^3} \tag{20}$$

Much of the work of Carman (1937) was founded on the notion that the product of the $\boldsymbol{k_0}$ factor and the tortuosity factor, $\boldsymbol{\tau^2}$, is equal to the constant, $\boldsymbol{k_C}$ (−). Through his work, Carman (1937) concluded that $\boldsymbol{k_C}$ only ranges from 4.84 to 6.13 for porous media with a wide range of particle shapes and sizes, and that an approximate solution for $\boldsymbol{k_C}$ for any channel shape or form should be given by Eq. 21. The $\boldsymbol{k_C}$ factor is therefore perceived to be a factor that depends on the shape of the flow channel in similar fashion to that of Hagen–Poiseuille flow in pipes.

$$\boldsymbol{k_C} = \boldsymbol{k_0} \cdot \boldsymbol{\tau}^2 \approx 5 \tag{21}$$

Table 1 shows a selection of the different $\boldsymbol{k_0}$ values for Eqs. 18, 19, and 21. These values are originally calculated for different cross-section geometries in pipes (Çengel & Cimbala, 2010). The table also presents a range of $\boldsymbol{k_S}$ values that would result from Eq. 19, which are limited to 3.67–5.93 for the most relevant channel geometries. The lower limit of 3.14 (π) is obtained for the special case of a rectangular cross-section with infinite axis ratio, which would resemble fluid flow between two plates.

Table 1 k_0 values for streamline flow in different pipe cross-sections

Flow channel geometry	a/b or θ°	Darcy–Weisbach friction factor, f	k_0 geometry factor	k_S [Eq. 19]
Elliptical 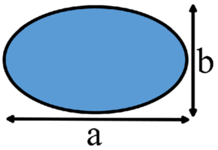	**a/b**			
	1–circle	$64.00/Re$	2.00	4.71
	2	$67.28/Re$	2.10	4.49
	4	$72.96/Re$	2.28	4.13
	8	$76.60/Re$	2.39	3.94
	16	$78.16/Re$	2.44	3.86
Rectangular 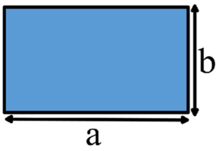	**a/b**			
	1–square	$56.92/Re$	1.78	5.29
	2	$62.20/Re$	1.94	4.86
	3	$68.36/Re$	2.14	4.40
	4	$72.92/Re$	2.28	4.13
	8	$78.80/Re$	2.46	3.83
	16	$82.32/Re$	2.57	3.67
	∞	$96.00/Re$	3.00	3.14
Triangular 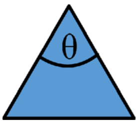	**θ°**			
	10°	$50.80/Re$	1.59	5.93
	30°	$52.28/Re$	1.63	5.78
	60°–equilateral	$53.32/Re$	1.67	5.64
	90°	$52.60/Re$	1.64	5.75
	120°	$50.96/Re$	1.59	5.93

The $\boldsymbol{k_0}$ values are reversed calculated from Reynolds number based on the definition of the *hydraulic diameter* of the pipe cross-section (modified and extended after Çengel & Cimbala (2010)). The $\boldsymbol{k_S}$ values are calculated from Eq. 19

2.2 Including the convective acceleration term

As the fluid flows through the pore, the channel geometry contracts and expands causing convective acceleration to occur. If the Reynolds number is sufficiently large, the non-linear term in Eq. 3 cannot be ignored, meaning that at a particular critical velocity threshold, the acceleration force can no longer be ignored. The characteristic parameters are defined in chapter 2.1, and the non-linear term (Eq. 22) must be arranged accordingly through combination with Eqs. 10, 12, 14, 16, and 17. This provides Eq. 23.

$$F_{C_d} = C_d \cdot \rho \cdot m \cdot V^2 \cdot L_e \tag{22}$$

$$\frac{\Delta P_{C_d}}{L} = \frac{C_d \cdot \tau^3 \cdot S \cdot \rho \cdot u_S^2}{k_0^2 \cdot n^3} \tag{23}$$

The C_d (−) is a dissipating coefficient that presumably depends on the channel shape, and degree of expansion and contraction along the length axis. A relevant approach for dealing with these effects can be found in fluid mechanics of pipes. A short description is presented here, but the reader is referred, e.g., Çengel & Cimbala (2010) and Idelchik (1994) for further details. The concept of minor losses due to pipe expansion or contraction is developed from the fundamental conservation laws for mass, momentum and energy. The general form of Eq. (24) relates to pipes of uniform internal diameter, d_i (m) (Eqs. 8–59 in Çengel and Cimbala 2010).

$$h_{L,total} = \left(f\frac{L}{d_i} + \sum K_L \right) \cdot \frac{V^2}{2 \cdot g}, \tag{24}$$

where the total losses of hydraulic head through a pipe, $h_{L,total}$ (m), of length L (m) is due to friction in the pipe, represented by, e.g., the Darcy–Weisbach friction factor in laminar flow, f (−), and due to additional losses caused by an contraction of the flow channel, e.g., a constricting pipe segment like that of Fig. 2a. A constricting segment enforces two losses, both the contraction and the expansion of the segment, and the sum of these losses constitutes the minor loss of the obstruction, K_L (−).

The loss coefficients, K_L, are highly dependent of the pipe geometry, diameter, surface roughness, and the Reynolds number of the flow and are generally larger for expansion segments than for contraction segments. Sharp angles and abrupt changes can cause considerable losses as the fluid is unable to make sharp turns at high velocities, e.g., causing flow separation at the rear of corners or edges (Çengel and Cimbala 2010). Flow separation can occur in areas where the channel size increases and causes the fluid velocity to decrease. According to the Bernoulli equation, the flow develops an adverse pressure gradient along the walls due to the decrease in velocity and this causes the boundary layer to separate from the channel walls (Idelchik 1994).

Semi-empirical equations for pipes exist (Çengel and Cimbala 2010; Crane 1957; Idelchik 1994). For uniform expansion, the loss coefficient, $K_{L\text{-}ex}$ (−), can be estimated from Eqs. 25 or 26, with reference to Fig. 2a. The coefficients are based on the velocity of the smallest channel as the reference velocity. The α (-) is a kinetic energy correction factor that depends on the flow characteristics. In fully developed turbulent flow the factor is close to 1.05, while in fully developed laminar flow the factor is 2.0. The losses are thus velocity dependent and depend on the Reynolds number of the flow and are relatively greater in laminar flow. In laminar conditions, the range is $K_{L\text{-}ex} \approx 0.0\text{-}2.0$,

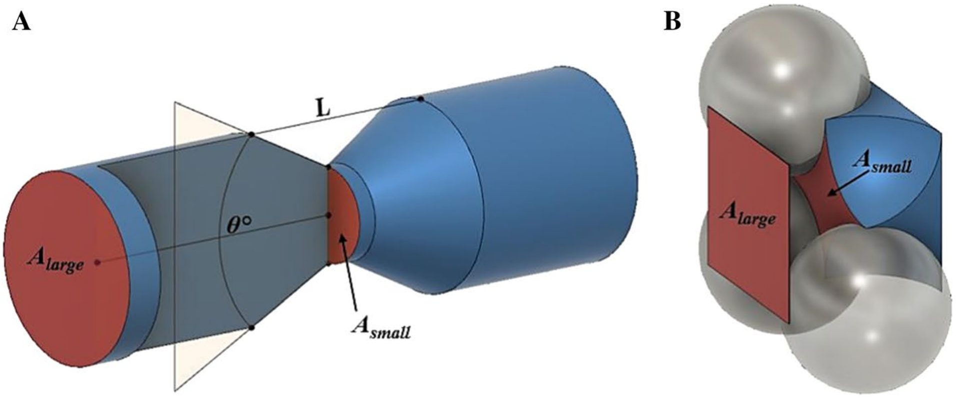

Fig. 2 Principal sketch of minor losses due to contraction and expansion of the flow channel. **a** A constricting obstruction in a pipe section of length L causes acceleration of the fluid to occur when the fluid flows through the smaller cross-section. The ratio of the smaller area, A_{small}, to the larger area, A_{large}, determines the magnitude of minor losses. A smooth angle, θ, of approach dampens the losses. **b** An equivalent phenomenon occurs in porous media when the fluid flows from one pore to another. The ratio of pore throat area, A_{small}, to the pore body area, A_{large}, is believed to determine these losses

while in turbulent conditions the expansion losses are typically bound by the range $K_{L\text{-}ex} \approx 0.0–1.05$.

$$K_{L\text{-}ex} = \alpha \cdot \left(1 - \frac{A_{small}}{A_{large}}\right)^2 \quad for \quad 45^\circ < \theta < 180^\circ \tag{25}$$

$$K_{L\text{-}ex} = \alpha \cdot \left(1 - \frac{A_{small}}{A_{large}}\right)^2 \cdot 2.6 \cdot \sin(\theta/2) \quad for \quad 0^\circ < \theta \leq 45^\circ \tag{26}$$

It is believed that C_d should depend on the constriction ratio similarly to that of K_L in pipes. The argument for this is that they both deal with the same geometrical aspects, namely the expansion and contraction of a channel. For these two to be comparable it is vital that both C_d and K_L describe the velocity from the same point of reference within the channel. Since the pipe coefficients K_L are based on the velocity of the smallest pipe as the reference velocity, a correction of the C_d constant is needed, since the C_d is expressed by the velocity of the larger flow channel. Rearranging the fundamental conservation laws provides the correction $1/a^2$ where a is defined according to Eq. 27 (Idelchik 1994; Crane 1957).

$$a = \frac{A_{small}}{A_{large}} = \frac{A_{pore\,throath}}{A_{pore\,body\,center}}. \tag{27}$$

The modified form of convective acceleration term is then given by Eq. 28, where the dissipation coefficient (C_{KL}) is a coefficient that corresponds to the average velocity of the pore throat region of the pore. In this form, the C_{KL} should therefore be dependent on both the constriction ratio of the channel and the streamlining of the pore channel geometry through the pore throat, similar to that of the K_L of pipes.

$$\frac{\Delta P_{C_d}}{L} = \frac{C_{K_L}}{a^2} \cdot \frac{\tau^3 \cdot S \cdot \rho \cdot u_s^2}{k_0^2 \cdot n^3}. \tag{28}$$

The final version of Eq. 3 then becomes Eq. 29 including the convective acceleration term.

$$\frac{\Delta P}{L} = \frac{3 \cdot \pi}{k_0} \cdot \frac{\tau^2 \cdot S^2}{n^3} \cdot \mu \cdot u_s + \frac{C_{K_L}}{a^2} \cdot \frac{\tau^3 \cdot S}{k_0^2 \cdot n^3} \cdot \rho \cdot u_s^2 \tag{29}$$

This equation represents a single pore. For a porous media that consists of numerous pores, these various geometrical factors of Eq. 29 are unique for each pore within the pore matrix. However, if all pores are equal within a homogenous pore matrix, the factors of each pore will be equal to every other pore and Eq. 29 will be able to describe the dissipation of mechanical energy through the whole porous media with a single set of geometrical factors.

A well-known alternative to Eq. 29 is the Ergun equation (Ergun and Orning 1949). The Ergun equation corresponds to Eq. 30. The Ergun equation assumes that the channel geometry of each pore in a porous media is similar to cylindrical channels, as is evident by the $k_0 = 2$ in the linear term and the number 4 in the polynomial term.

$$\textit{The Ergun equation}: \frac{\boldsymbol{\Delta P}}{L} = \frac{2 \cdot \boldsymbol{\alpha_0} \cdot \boldsymbol{S}^2}{\boldsymbol{n}^3} \cdot \boldsymbol{\mu} \cdot \boldsymbol{u_s} + \frac{\boldsymbol{\beta_0}}{4 \cdot 2} \cdot \frac{\boldsymbol{S}}{\boldsymbol{n}^3} \cdot \boldsymbol{\rho} \cdot \boldsymbol{u_s^2} \tag{30}$$

The first-order term of the equation is equivalent to that of the Kozeny–Carman equation, but with a fixed $\boldsymbol{k_0}$ factor of 2 (Table 1). The $\boldsymbol{\beta_0}$ is a factor of geometrical relation and Ergun and Orning (1949) do not explain the $\boldsymbol{\beta_0}$ factor in relation to pipes of various shapes, as Carman attempts to do for the $\boldsymbol{k_0}$ factor. They do, however, provide the range $1.1 < \boldsymbol{\beta_0} < 5.6$, with most values occurring in the range 2.0–3.3 for randomly packed columns of smooth spheres. Note that the velocity component is represented differently and is only altered according to Eq. 12, which states that the Ergun equation does not directly account for the tortuosity, $\boldsymbol{\tau}$ (−), of the porous media.

3 Experimental work and methods

3.1 Sample design

The four particle designs (Fig. 3) were selected to compare various aspects of geometrical relations and their effects on permeability; particle shape (A vs B), size (B vs C), and their packing configuration (B vs D). The geometrical configurations of all the designs result in homogeneous porous medias that should satisfy the assumptions of Kozeny (1927), that the granular beds are equivalent to a "…*group of parallel, similar channels…*". All the pores in the samples are thus created equal. The geometries are difficult to achieve in traditional experiments, especially in view of the high porosity medias.

The design properties of the four porous media are summarized in Tables 2 and 3. The spherical design (A) comprises 3500 individual 1.0 mm spheres of equal sizes arranged in cubical packing arrangement. This configuration results in a pore shape that corresponds to 47.6% porosity (Fig. 3a). The configuration has traditionally been the subject of fundamental research of fluid flow through porous media, especially in the late nineteenth and early twentieth century (Kozeny 1927; Schriever 1930; Muskat and Botset 1931; Carman 1937) and more recently by Rumpf and Gupte (1971) and Fand et al. (1987). In many of these studies the degree of packing was determined by the porosity of the samples and the exact

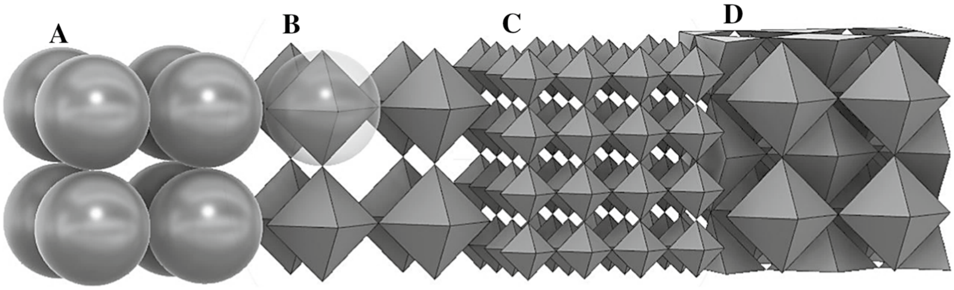

Fig. 3 The principal particle design and packing arrangements of the four sample types. **a** Sample A with 1.0 mm spheres stacked in the cubical arrangement. Pore corresponds to 47.6% porosity. **b** Sample B with 1.0 mm octahedrons stacked in cubical arrangement. Pore corresponds to 83.3% porosity. **c** Sample C with 0.50 mm octahedrons stacked in cubical arrangement. Pore corresponds to 83.3% porosity. **d** Sample D with 1.0 mm octahedrons stacked in two sets of equal cubical arrangements, where the one set is fixed in-between the other without touching the other set. Pore corresponds to 66.6% porosity

Table 2 Properties of the four 3D-printed porous media samples seen in Fig. 3

ID	Particle shape	Particle diameter, ***d*** [mm]	Smooth particle surface area [mm^2]	Porosity of bed n [%]	Tortuosity of bed τ [–]	Pore throat area ratio a (–)
A	Spherical	1.00	3.142	47.6	1.00	0.215
B	Octahedron	1.00	1.732	83.3	1.00	0.500
C	Octahedron	0.50	0.433	83.3	1.00	0.500
D	Octahedron	1.00	1.732	66.6	1.2247	0.666

The porosity ($\boldsymbol{n}$) and surface area properties corresponds to smooth particles (i.e., no surface roughness). The tortuosity ($\boldsymbol{\tau}$) is estimated according to the definition of Epstein (1988). The pore throat area ratio, **a** (-), is calculated according to Eq. 27

Table 3 Design parameters for the four types of 3D-printed porous media, A-D

ID	Number of sample duplicates	Number of particle beds	Number of particles per bed	Number of pores per bed	Number of pores in sample	*Sample surface area (mm^2)	Void volume of sample [ml]
A1-5	5	35	100	100	3 500	11,298	1.666
B1-6	6	35	100	100	3 500	6752	2.915
C1-6	6	70	400	400	28 000	12,824	2.915
D1-6	6	70	200	400	28 000	12,474	2.331

The bulk cross-sectional area of the cubical container core is 100.0 mm^2 and the length of the cores are 35.0 mm. (*) Sample surface is based on smooth particles surfaces and the estimates include the surface area of the container wall (remaining wall surface area is A = 301 mm^2, B = 700 mm^2, C = 700 mm^2 and D = 350 mm^2)

particle arrangements were never truly clear. Newer studies have investigated this packing arrangement numerically by applying computational methods with the Navier–Stokes equations (Hill et al. 2001). Numerical studies of other geometrical configurations have more recently been carried out by Newman and Yin (2013), Turkuler et al., (2014), Schulz et al. (2019).

The effects of particle angularity on permeability are considered in the second sample design. The angular configuration (B) consists of octahedron particles that are packed identical to that of the spheres (A), where the diagonal length of the octahedron is 1.0 mm. The six points of contact between each octahedron particle and the size of the octahedron are such that it fits within a sphere of equal diameter (Fig. 3b). The number of individual particles and pores is still 3500 (Table 2), but the porosity increases to 83.3%. In sample C the length dimensions of the octahedron particles are reduced by a factor of two, to 0.50 mm, while all other parameters remain unchanged. This increases the number of particles and pores in the sample by a factor of eight and the sample consists of 28,000 individual 0.50 mm particles (Tables 2 and 3). The porosity remains the same as for B, but the flow channels through the sample are smaller and the surface area of the solid matrix is increased by a factor of two.

The final particle configuration, sample D, consists of the same 1.0 mm octahedron particles as sample B (Fig. 3d). The specific geometry created by the octahedron particle beds allow for a second set of equal octahedrons to be fixed in-between the first octahedron configuration of sample B, without the second set touching the first set. The second set introduces a denser form of packing and the configuration corresponds to 66.6% porosity. The inter-fixed particle bed induces a tortuous channel pathway and increases the surface area of the solid matrix by a factor of two. The number of particles in the design is doubled to 7000, but the number of representative pores is increased by a factor of eight, corresponding to 28,000 pores.

The relative size and shape of the individual pores found in the four samples are shown in Fig. 4. The pore shape of sample A is curved and has the smallest pore throat ratio $\boldsymbol{a} = 0.215$ by definition of Eq. 27. The pores of sample B & C are cubical and has a pore throat area ratio of $\boldsymbol{a} = 0.500$. The pore of sample D is subdivided into eight pores of equal shape and size to highlight the internal octahedron particle and the corresponding tortuous pathway of the pore. This helps to show that the pore body of sample D is rectangular (aspect ratio $\approx 2/1$). The pore shape is less diverging than the other samples with a pore throat area ratio of $\boldsymbol{a} = 0.666$.

The tortuosity listed in Table 2 applies the definition of $\boldsymbol{\tau} = \boldsymbol{L_e}/\boldsymbol{L}$, where the center axis of pore length, $\boldsymbol{L_e}$, is longer than the length of the superficial flow axis, $\boldsymbol{L}$ (Epstein, 1988). For samples A, B, and C the pores are inline with each other and the flow axis and the pores are not tortuous in terms of the definition. The sample D pores are offset by the interfixed particle and the octahedron shape dimensions which provide $\boldsymbol{\tau} = 1.2247$ according to the Pythagorean equation.

The main design parameters are listed in Table 3. The sample design focuses on preserving the integrity of the pore-space matrix throughout the samples. In classical permeability experiments, the sample material is inserted into a hollow cylinder. The cylinder must have a wide enough diameter to ensure minimum effects from the container wall on the packing arrangement of the material (Fig. 5a) (Carman, 1937; Fand et al. 1987). This issue is avoided in the presented design solution by building the wall and sample material together in parallel. A cylindrical wall will never yield a satisfactory pore-matrix configuration when the particle packing arrangement is cubical (Fig. 5b). A cubical container in which all pores are equal contains the samples in this experiment. This is achieved by cutting the particles along the wall at the interface of the pore boundary and fixing these particles to the container wall (Fig. 5c). This approach allows

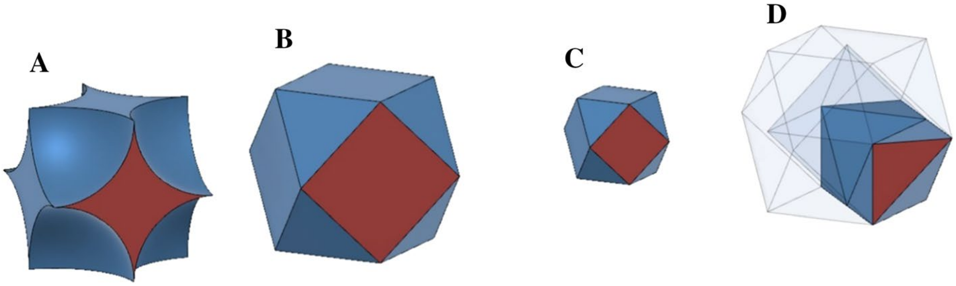

Fig. 4 The corresponding pore shapes and relative sizes of the pores in the porous medias in Fig. 3. The pore throat is red colored. **a** Sample A pore throat is 0.215 mm^2 and the area ratio a = 0.215. **b** Sample B pore throat is 0.500 mm^2 and the area ratio a = 0.500. **c** Sample C pore throat is 0.125 mm^2 and the area ratio a = 0.500. **d** Sample D pore throat is 0.125 mm^2 and the area ratio a = 0.666. The pore is sliced into eight parts to reveal the location of the internal particle and the corresponding tortuous pathway. Two of the pores are shown here

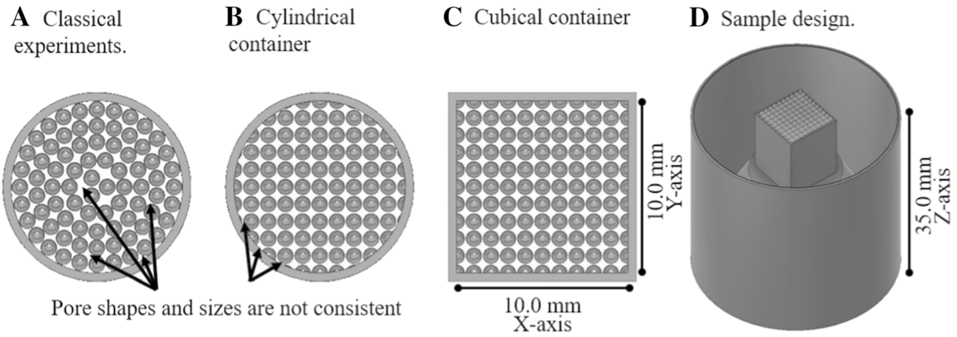

Fig. 5 The sample design avoids unwanted effects caused by container wall geometry. **a** The cylinder container in classical experiments affected the packing arrangement of spheres. **b** A cylindrical container will affect the pore shape and size in the adjoining layer when the packing arrangement is cubical. **c** The cubical container in this experiment provides consistent pore shapes and sizes throughout the sample. The cube has an internal dimension of 10.0 mm·10.0 mm in the X-axis and Y-axis. **d** The complete sample design with sample length of 35.0 mm in the Z-axis. To ensure a good fit for the samples in the Hassler cell, the samples are fabricated with an integrated impermeable cylindrical shell fitting

for the exact calculation of the remaining surface area provided by the container wall and this is included in the over-all sample evaluation in Table 3.

Six duplicates of each sample were fabricated to show the statistical discrepancies in the final product and to provide a means of control and reference in the permeability testing procedure. To ensure a good fit for the samples in the Hassler cell, the samples were fabricated with an integrated impermeable cylindrical shell fitting (Fig. 5d).

3.2 Sample fabrication

Additive manufacturing (AM), 3D printing, refers to a group of production methods where material is added and constructed successively, often layer by layer. AM is normally divided into seven categories (ISO/ATSM, 2015). The Powder Bed Fusion (PBF) category, with the specific PBF-LB subcategory utilizing laser beam, is the method applied in this study. PBF-LB describes a process where a layer of powder is spread on top of a substrate, thereby selectively being melted into a solid with a laser. These melted stacks will grow into the predefined shape that was described by the computer-aided design model. Building a part layer by layer has the advantage of turning difficult 3D shapes into simple 2D-layer projections that are easier to handle and produce. Each sample was designed and sketched in the *Autodesk® Fusion 360™ CAD* program. The CAD models were converted to stereolithographic (STL) format and were manufactured in a *Concept Laser M2*, PBF-LB machine with maraging steel *Marlok C1650* powder. The machine is equipped with a 200 W diode pumped Yb:YAG fiber laser with continuous wave mode and a laser beam diameter of 0.150 mm and a wavelength of 1050 nm. The spherical gas-atomized powdered material (Marloc C6150) has a size distributed of 5–22 μm. This size distribution is relatively small compared to standard powder batches and is ideal for geometries that require fine details in the finished product (Vock et al. 2019).

The key to producing fine particle structures is in applying the correct sample design, building sequence, and production parameters in the PBF-LB process. The production parameters have the governing role in the manufacturing. The samples were designed to build 2D projections of the X-axis and Y-axis layer by layer along the Z-axis of the machine

(Fig. 5c). It is not trivial to achieve good surface and tolerances in a shape that grows along this Z-axis, as this causes an overhang (Akram et al. 2018; King et al. 2015; Malekipour and El-Mounayri 2018). This mean that the laser beam will inevitably penetrate deeper than intended in the Z-direction, especially if standard production parameters are utilized (Trapp et al. 2017). The result is a surface that is larger than the specified dimensions and the surface has a rougher finish.

It is crucial that the laser beam does not burn through many powder layers but is melting just enough to get an impermeable outer particle shell with an acceptable surface roughness and pore-matrix configuration. The standard PBF-LB production parameters were not appropriate for this study and the customized parameters utilized were provided from an independent, unpublished study where fine geometries were much more important than mechanical strength of the sample. The Marloc C6150 steel has extraordinarily good mechanical properties (Brøtan et al. 2016), which make it unnecessary to discuss the strength of the sample parts for the applied pressures (eight bar) and stresses in the permeability tests. The specimens were built with one contour at 500 mm/s laser speed at 50 W with a layer thickness of 0.03 mm. The inner section had similar parameters with parallel scanlines 45 degrees on to the machine X-axis (Fig. 5c). For each layer the scan lines were rotated 90 degrees. The hatch spacing, which is the distance between the laser scan lines, was set to 0.105 mm. The customized parameters contributed to minimum Z-axis penetration.

3.3 Sample inspection, CT imaging, and image analysis procedures

Due to the specific design of the samples, traditional measuring and control equipment could not be used without destroying the samples. Porosity measuring devices, e.g., Helium or Nitrogen porosity meters, or surface area measurement techniques, e.g., gas adsorption methods (BET), were unsuccessful. To determine the internal properties of the samples, the samples were examined externally in a microscope and inspected internally in a *Nikon XT H 225 ST* industrial CT scanner.

The CT images and image analysis techniques were utilized for the estimation of sample porosity, internal surface area, and for calculation of the area ratio component, $\boldsymbol{a}$, that is needed for the empirical correlations. Due to time and funding limitations only the samples A3, B3, B6, C1, and D3 samples could be sufficiently analyzed. These samples were selected randomly from the different duplicates. The large density contrast of the steel particles to the air-filled voids in the samples contribute to high-quality images. The voxel size in the CT images was 22.297 µm in all three dimensions (X, Y, Z) for the image analysis of samples A3, B3, B6, and D3 (similar size as the *Marlok C1650* powder). The resolution was improved to 8.466 µm for all three dimensions (X, Y, Z) for sample C1. The CT images were filtered and analyzed with the VGSTUDIO MAX 3.1 software package. A greyscale threshold algorithm was applied to reduce noise and structural artifacts in the CT images and to determine the particle shape, size, and form in the different samples (Fig. 6). The sample porosity and sample surface area of the particle matrix were determined through volume analysis on the voxel data with the marching cubes method. The porosity was measured as a volume ratio of the designated void voxels to the solid voxels. The surface area of the solid voxels provided the surface area data. The CT-image stacks of the various shape matrices were further subjected to image analysis using the ImageJ 1.52a software package on pixel data for comparison. The open space (porosity) was measured as an area measurement by using the "Intermodes" auto threshold method and calculated as

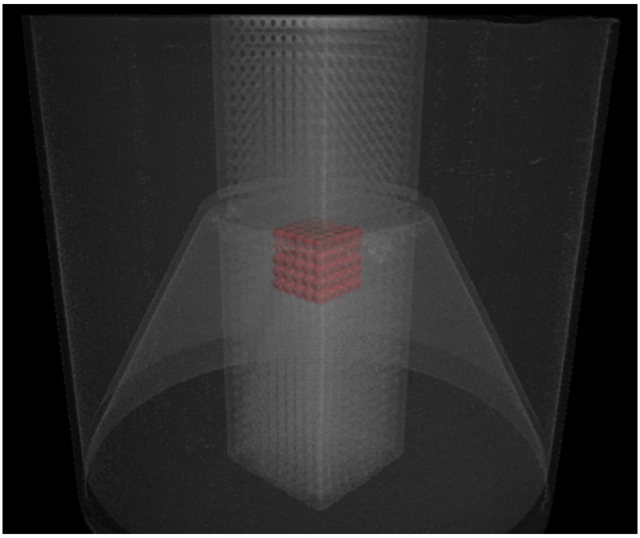

Fig. 6 Voxel data analysis on sample A3 with the VGSTUDIO MAX 3.1 software package. In this particular case, the sample A3 is ghosted (grey) and a section of the sample is isolated from the remaining sample to visualize the internal structure of the cubical sphere packing (red)

the ratio of the measured area to the total image area. This supplied the area ratio component, $\boldsymbol{a}$, measurements.

3.4 Permeability test procedure, calibration, and equipment

The permeability measurements were conducted with the constant flow rate methodology (McPhee et al., 2015). The absolute–permeability cell setup (Fig. 7) consists of a horizontal oriented, pressurized, 38.0-mm-diameter Hassler cell which is connected in parallel to three circulatory pumps and an outlet reservoir tank. The Hassler cell is customized with two enlarged feeding nodes that incorporate a fixture for the pressure transducers (P1 and P2 (type: *GE Druck PTX5072-TA-A3-CA-H1-PA-0-250mbara*) with 0.1 kPa accuracy) and

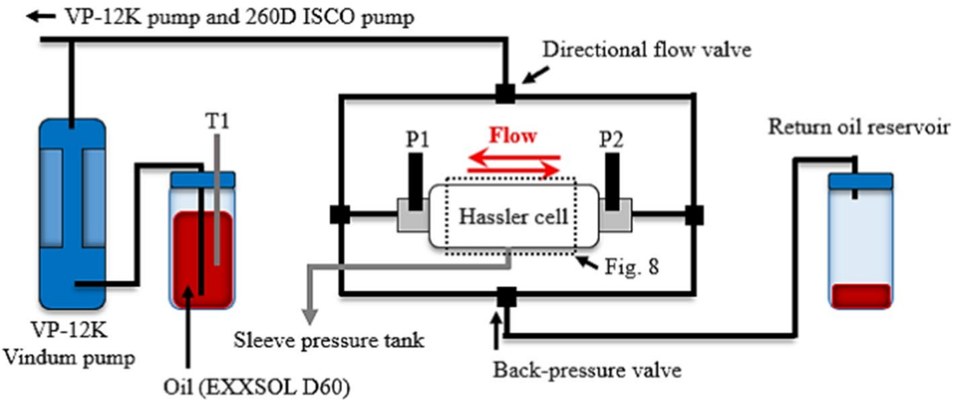

Fig. 7 Schematic sketch of the absolute-permeability cell setup. The T1-temperature sensor measured room and oil temperature during the test. The P1 and P2 pressure transducers are mounted in customized fixtures at the ends of the Hassler cell. The pumps are connected in series. The interior of the Hassler cell is shown in Fig. 8

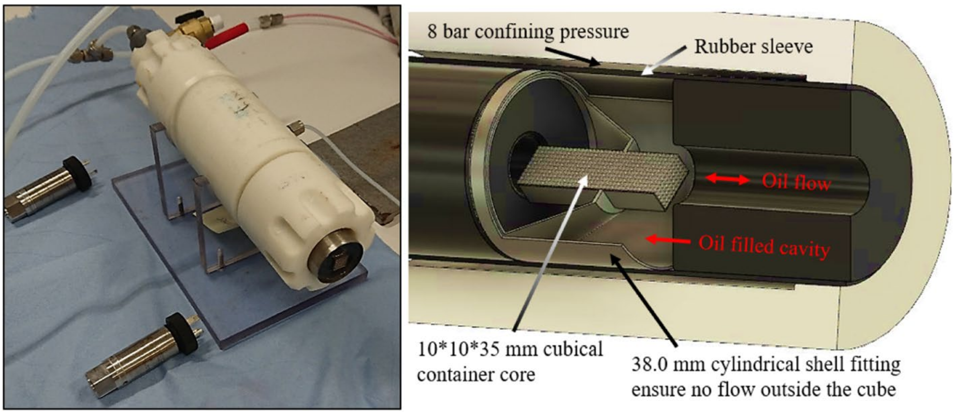

Fig. 8 Customized Hassler cell. Left: Picture of test preparations. Sample being inserted into the cell before mounting of the pressure sensors. Right: Schematic sketch of the interior of the cell with a 11-mm-internal diameter fixture for the pressure sensors. The cubical container core samples have a cylindrical shell that fits in the 38 mm diameter chamber and prevents flow outside of the cubical container core. The rubber sleeve is pressed around the fixtures and core sample with eight bar pressure

an enlarged 11-mm-internal diameter feeding pipe (Figs. 7 and 8). The enlarged feeding pipe ensures negligible parasitic pressure losses from the cell components between the P1 and P2 sensors within the flow rates provided by the pumps. The combination of two *VP-12 K Vindum Pumps* and one *260D Teledyne ISCO pump* provides a complete range of flow rates from 0.0001 to 165.0 ml/min with a pulse-free and continuous mode of rate delivery. The rates utilized in this study are 7.5–165.0 ml/min corresponding to superficial velocities from 0.0012 to –0.0275 m/s. The feeding nodes and the 3D core sample are fixed within the Hassler cell with an airtight rubber sleeve that is pressed around the core and feeding nodes with eight bar confining pressure. The cubical container samples are fabricated with a cylindrical shell fitting to ensure a tight sealing with the rubber sleeve and no leakages along the wall (Fig. 8).

The circulation fluid was *EXXSOL D60* oil at room temperatures (20.2–21.4 °C). The oil density of 790 kg/m^3 was measured by an *Anton Paar Density Meter, DMA 5000 M* at room temperature (21.0 °C). The dynamic viscosity was measured with a *SI Analytics KapillaryViscometer D50* to 0.001384 (Pa·s) at room temperature (21.0 °C) and 0.002543 (Pa·s) at (4.5 °C). The oil was dyed red to help locate leakages, from pipefittings etc., during the saturation procedure. The dye had no measurable influence on the density and viscosity measurements. During the saturation sequence, the Hassler cell was turned vertical and flooded from the bottom to help evacuate air from the cavities of the hollow cylindrical shell fittings (Fig. 8). A backpressure technique with an abrupt pressure drop (shocking) was applied to flush trapped air from the interior pore-space matrix. The backpressure was built up and released incrementally from 1–7 bar. The technique was then repeated with the opposite flow direction and vertical orientation. The samples were deemed fully saturated when the initial flow test revealed no zero-shift from the pressure transducer responses in both directions (Fig. 9).

The permeability test followed the multipoint flow rate technique (McPhee et al. 2015), equivalent to the step-test procedure in large-scale aquifer testing (Kruseman et al. 1990). The testing sequence from the C6 sample is presented in Fig. 9 as an example. Each sample test incorporates 24 individual measurements divided into four main sequences of

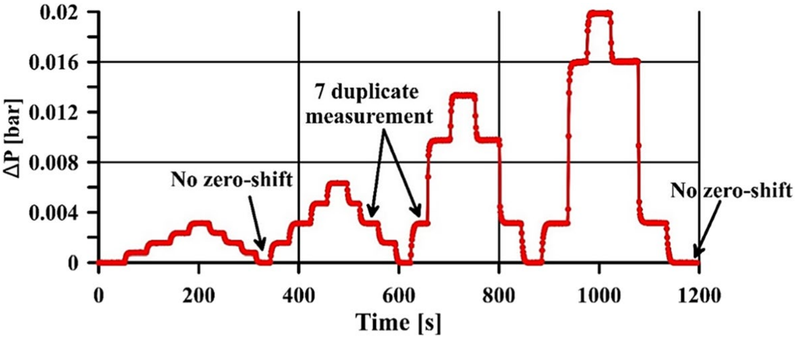

Fig. 9 Multipoint test sequence of sample C6 with 24 individual flow rates from 7.5 to 165.0 ml/min. The four main sequences include a "no zero-shift" pause between each sequence to ensure no pressure shift in the sensors. The procedure provides duplicate measurements that confirm each rate measurement and reduce uncertainties in the data analysis

incremental flow rate increases followed by a mirrored flow rate decrease. The mirroring of the sequences provides duplicate measurements that confirm each rate and reduce uncertainties in the regression. Each point of flow rate was run until steady state was reached. The speed of pressure stabilization is a function of the sample length and the permeability of the sample. The time needed for each test was different for each of the four sample types. All samples displayed steady state within 20–40 s. A sequence of zero flow was included between the four main sequences to ensure that no zero-shift of the pressure response had occurred during the test. Each main sequence includes the rate 29.0 ml/min which provides seven measurements of the same reference level to ensure that no pressure shift had occurred between the four sequences (Fig. 9).

To verify $\boldsymbol{k}$ (Eq. 1), $\boldsymbol{k_F}$, and $\boldsymbol{\beta}$ (Eq. 2) attained with the EXXCOL D60 oil experiments some samples were cleaned with toluene and further tested with distilled water. Most of these tests were not satisfactory because the steel samples showed signs of corrosion upon contact with water. Precipitated iron hydroxide powders (rust) were seen on the particles after the tests. However, some data from these tests are provided to show the general behavioral change observed and to allow for comparison with other published works.

4 Results

4.1 Fabrication results

Details of different A, B, C, and D samples are presented in Fig. 10. The pictures show that surface roughness is the limiting factor for retaining the designed particle shape and form. The powder that border the designed particle surface boundary is partly melted and remolded into the sample during the fabrication. The resulting particle surface is not smooth on the microscopic level but inhibit a certain fraction of the surrounding powder as a rough "coating". For instance, the fabricated contact point between two individual particles are slightly thicker than the designed specifications (Fig. 10b, c, e, and f), especially affecting the pore throat size of samples A and C more than the samples B and D.

The average estimated properties of porosity, area ratio, and surface area for A3, B3, B6, C1, and D3 are presented in Table 4. CT images of the samples show that the particle

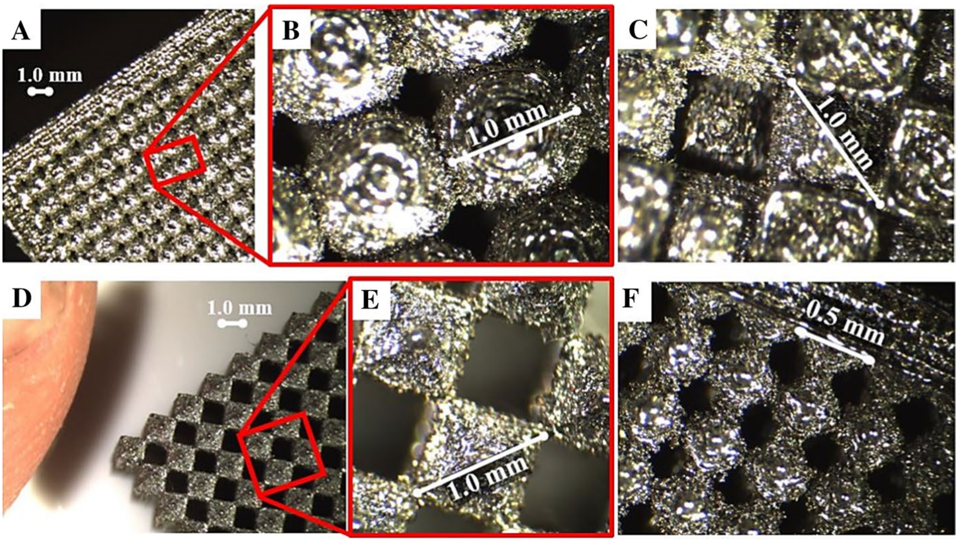

Fig. 10 Images of some of the 3D-printed test samples. **a** Sample A type with cubical container **b** Close-up of the 1.0 mm spheres. **c** Sample D type with free pore space between the two sets of octahedrons. **d** Sample B type without the cubical container. Notice the index finger for scale. **e** Close-up of the 1.0 mm octahedrons. **f** Sample C with cubical container

size, shape, and configuration were essentially maintained. However, the rough coating of powder along the particle surfaces altered the pore-shape matrix compared to that of the original smooth particle specifications. The particles are slightly larger than intended in the design, especially in regions where they were not bound by a neighboring particle. A selection of different CT images is given in Fig. 11 to show these effects for a single particle bed of each sample. The figure shows three images of each sample. Each image depicts the X-axis and Y-axis (Ref. Fig. 5) of the samples and shows a different cross-sections of a specific particle bed within each sample. The “pore body” image represents the section with the largest channel opening within the pore. The “Dupuit” image shows the section with a channel opening corresponding to the estimated porosity of the bed (Table 4). The “pore throat” image shows the narrowest channel section of the pores in the bed. The alterations are most easily observed for the spheres of A3 which have a thicker connection between neighboring particles of the next bed in the pore body image (Fig. 11). This image should ideally be similar to the B3 image if the spheres were smooth. The contact points between the octahedrons are also thicker than the intended design, but the images of B3 and C1 show that the pore body section of the samples is less affected than A3. This also applies to D3, but here the contact points are seen in the pore throat image. The pore throat images show that the channel openings are smaller than intended. Comparison between the properties of Table 4 to those of the intended design in Table 2 confirms the observed differences. The samples have lower porosities, larger contraction ratios, and rougher and larger surfaces than intended.

Figure 12 shows the void fraction of the combined CT-image stacks from the same section of the particle bed seen in Fig. 11. The images shown in Fig. 11 are highlighted in yellow markers. The black voids in the CT images are designated as the channel opening along the bed and calculated as a void fraction. The length through the bed is the Z-axis of the samples in Fig. 11. The void fraction data in Fig. 12 confirm that

Table 4 CT image estimated sample properties of porosity, area ratios, and surface area for the A3, B3, B6, C1, and D3 samples. Specific surface includes wall effects

ID	Number of measured particles	Average particle diameter (mm)	Average particle surface area (mm^2)	Porosity of sample n (%)	Average pore area ratio a (−)	Sample internal surface area (mm^2)	Specific surface of sample S (m^{-1})	Particle surface area vs. original design (%)
A3	900	1.00	3.767	34.96	0.128	13 545	3 869	119.9
B3	900	1.00	2.918	73.66	0.420	11 053	3 158	168.5
B6	900	1.00	2.646	75.40	0.427	10 101	2 886	152.8
C1	2000	0.50	1.032	68.72	0.292	29 736	8 496	238.3
D3	1800	1.00	2.635	51.16	0.643	18 795	5 370	152.1

The deviations from the original design are calculated as the ratios between the average particle surface area estimated from the CT images and from the ideal smooth design in Table 3

for each 1 mm length of sample, A3 and B3 have one bed of particles and one constriction segment of the channel. Samples C1 and D3 have two. The theoretical void fraction of the intended design is shown as full lines in the figure. Compared to these lines, the samples display smaller void fractions and greater constrictions. The particles are also not fully symmetrical in the Z-axis of the sample, as is indicated by the

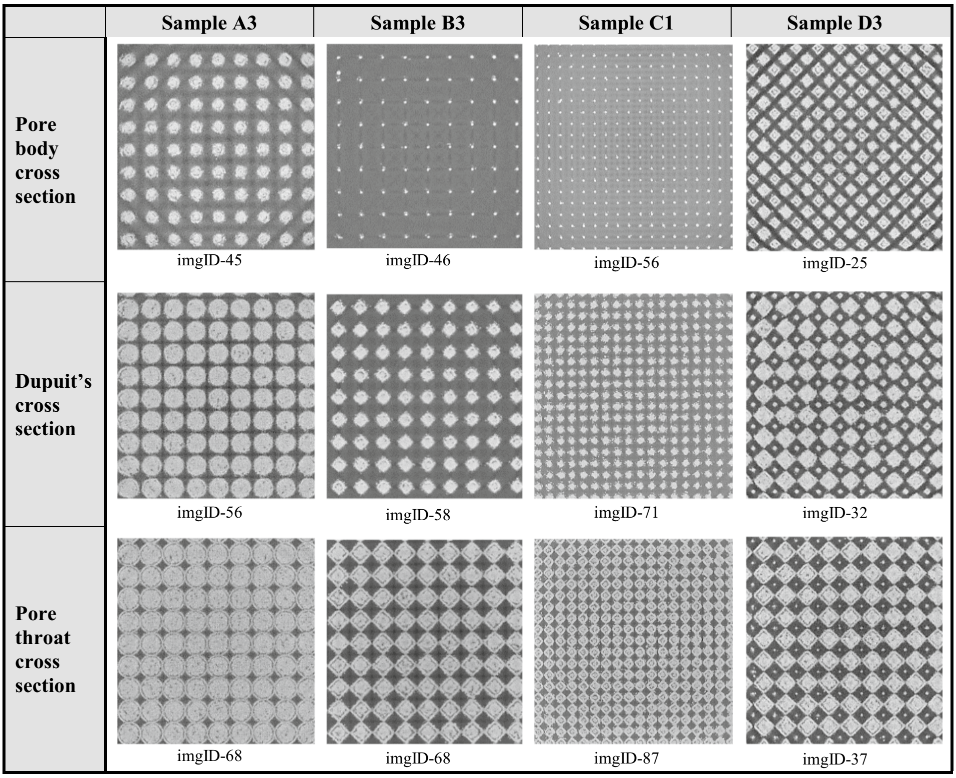

Fig. 11 Raw-data greyscale CT images. The images depict approximately 9 mm × 9 mm of the X-axis and Y-axis from a typical section of the particle beds of the cubical cores of A3, B3, C1, and D3. The "*pore body*" cross-section corresponds to the largest channel opening within the pores. The "*Dupuit's*" cross-section represents the area ratio corresponding to the porosity given in Table 4. The "*pore throat*" image shows the narrowest channel section of the pores in the bed. The estimated geometrical data are presented in Fig. 12 and Table 4. The images are yellow markers in Fig. 12

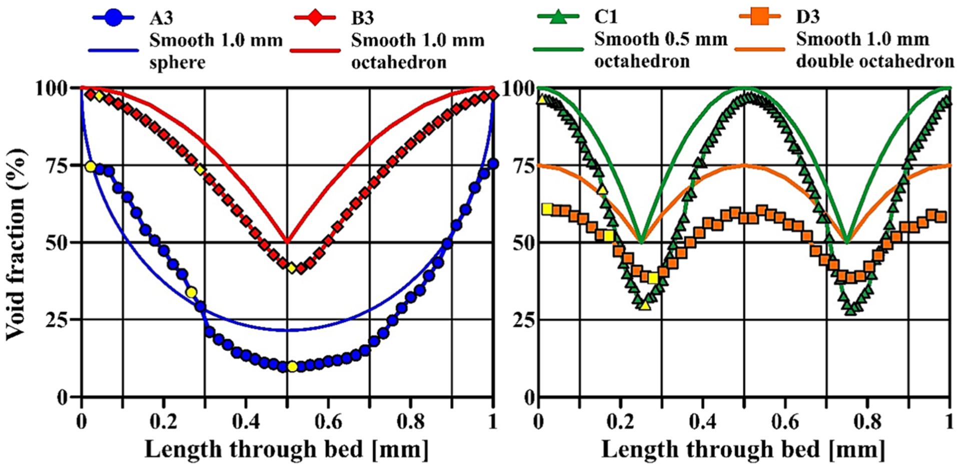

Fig. 12 Estimated void fraction (dotted lines) through a typical section of the particle beds in samples A3, B3, C1, and D3 with reference to Fig. 11. The data start at the pore body cross Sect. (0 mm) and transgress through the pore throat of the bed to the next pore body. The images of Fig. 11 are highlighted in yellow markers along the curves. For each 1 mm length of bed, A3 and B3 have one constriction segment, while C1 and D3 have two. The smooth lines illustrate the theoretical void fractions that would have been the result if the particles were smooth and symmetrical (Fig. 3). The geometrical properties are summarized in Table 4

non-symmetrical void ratios in Fig. 12. The lower half of the particles, e.g., from 0.5 to 1 mm of A3 and B3, are thicker due to the applied fabrication technique and the laser beam seems to have penetrated 2–3 layers beneath the particle boundary.

4.2 Hassler flow cell results

The results of the multipoint flow rate tests with EXXSOL D60 oil are presented in Table 5 and Fig. 13. The least square regression results of the pressure loss versus the flow rate data are obtained for both the linear fit (Darcy–Eq. 1) and the polynomial fit (Forchheimer–Eq. 2). The linear regressions only include the linear data of the test, which was done through iterative testing and comparison of the linear regressions (Fig. 13). The polynomial regression includes all the data points up to the maximum rate of 165 ml/min. All the samples show deviations from linearity after surpassing a threshold, termed critical velocity $\boldsymbol{u_c}$ [cm/s] in Table 5. The $\boldsymbol{u_c}$ is calculated as the rate of flow where the linear regression yields approximately 1% lower differential pressure loss than the polynomial regression. The $\boldsymbol{u_c}$ is calculated from superficial velocity because this velocity is used in the empirical correlations. The onset of $\boldsymbol{u_c}$ is observed at lower velocities for sample A and progressively increases in sample B–C–D, respectively. This affects the number of measurements ($\boldsymbol{i}$) included in the linear regression because the point of divergence is different for the four sample types, while the measurements are conducted on the same intervals. The accuracy of the pressure sensors is displayed in Fig. 13c as a reference and shows that some of the data points of sample B are close to the sensor limits. All other samples were within sensor accuracy range.

The permeability ($\boldsymbol{k}$) of samples A1–A5 range from 641 to 738 D (6.33×10^{-10} to 7.18×10^{-10} m^2) and samples C1–C6 display the range $\boldsymbol{k}$=756–920 D (7.46×10^{-10} to 9.07×10^{-10} m^2). The largest $\boldsymbol{k}$ is observed in samples B1–B6 with the range 7 796–9 988

Table 5 Least square regression results for EXXSOL D60 oil for the A, B, C, and D samples and for distilled water for sample A3

ID	T [°C]	Darcy regression: $\Delta P/L = (\mu/k) \cdot u_s$ kPa·m^{-1}=(kPa·s·m^{-2})·m·s^{-1}				Forchheimer regression: $\Delta P/L = (\beta\rho) \cdot u_s^2 + (\mu/k_F) \cdot u_s$ kPa·m^{-1}=(kPa·s^2·m^{-3})·m^2·s^{-2}+(kPa·s·m^{-2})·m·s^{-1}							u_c cm/s
		$\mu/k \cdot 10^3$ [Pa·s·m^{-2}]	k [D]	R^2	i	$\beta\rho \cdot 10^3$ [Pa·s^2·m^{-3}]	β [m^{-1}]	$\mu/k_F \cdot 10^3$ [Pa·s·m^{-2}]	k_F [D]	$\beta\rho/(\mu/k_F)$ [s/m]	R^2	i	
A1	20.4	2 150	651	>0.999	8	22,700	28,608	2 110	663	10.8	>0.999	24	0.27
A2	20.2	1910	733	>0,999	8	18,800	23,797	1 860	753	10.1	>0.999	24	0.36
A3	21.1	1900	738	>0.999	8	21,900	27,722	1810	775	12.1	>0.999	24	0.49
A4	21.3	1990	705	>0.999	6	19,300	24,430	1970	711	9.4	>0.999	22	0.21
A5	20.9	2180	641	>0.999	6	30,700	38,861	2060	679	14.9	>0.999	16	0.46
B1	21.3	140	9988	0.998	15	740	933	140	9988	5.3	>0.999	24	0.60
B2	21.1	140	9988	0.997	15	840	1070	140	9988	6.1	>0.999	24	0.41
B3	21.3	170	7796	0.998	15	860	1090	172	8255	5.0	>0.999	24	0.91
B4	21.1	150	9477	0.999	15	720	914	140	9741	5.0	>0.999	24	0.76
B5	21.3	150	9482	0.997	15	880	1110	150	9678	6.1	>0.999	24	0.52
B6	21.2	140	9988	0.999	15	710	903	130	9988	5.4	>0.999	24	0.90
C1	21.4	1 610	868	>0.999	17	7860	9949	1560	899	5.04	>0.999	24	0.84
C2	21.1	1550	902	0.999	17	7140	9038	1520	920	4.58	>0.999	24	0.64
C3	21.6	1 530	914	>0.999	17	7 260	9190	1480	945	4.90	>0.999	24	0.88
C4	21.3	1520	920	>0.999	17	6980	8835	1470	951	4.75	>0.999	24	0.93
C5	21.3	1750	799	0.999	17	12,600	15,570	1660	842	7.64	>0.999	24	0.87
C6	21.2	1850	756	>0.999	17	10,000	12,658	1790	781	5.59	>0.999	24	0.78
D1	21.0	2300	608	>0.999	20	5960	7544	2260	619	2.64	>0.999	24	1.07
D2	20.8	2410	580	>0.999	20	6280	7949	2370	590	2.65	>0.999	24	1.15
D3	21.1	2260	619	0.999	20	5090	6443	2240	624	2.27	>0.999	24	0.84
D4	20.2	3180	440	>0.999	20	8600	10, 886	3120	448	2.76	>0.999	24	1.11
D5	19.8	2520	555	>0.999	20	5780	7316	2480	564	2.33	>0.999	24	1.19
D6	20.2	2990	608	>0.999	20	5750	7278	2240	619	2.57	>0.999	24	1.24

Table 5 (continued)

ID	T [°C]	Darcy regression: $\Delta P/L=(\mu/k)\cdot u_s$ $\mathrm{kPa\cdot m^{-1}=(kPa\cdot s\cdot m^{-2})\cdot m\cdot s^{-1}}$				Forchheimer regression: $\Delta P/L=(\beta\rho)\cdot u_s^2+(\mu/k_F)\cdot u_s$ $\mathrm{kPa\cdot m^{-1}=(kPa\cdot s^2\cdot m^{-3})\cdot m^2\cdot s^{-2}+(kPa\cdot s\cdot m^{-2})\cdot m\cdot s^{-1}}$							u_c cm/s
		$\mu/k\cdot 10^3$ $[\mathrm{Pa\cdot s\cdot m^{-2}}]$	k [D]	R^2	i	$\beta\rho\cdot 10^3$ $[\mathrm{Pa\cdot s^2\cdot m^{-3}}]$	β $[\mathrm{m^{-1}}]$	$\mu/k_F\cdot 10^3$ $[\mathrm{Pa\cdot s\cdot m^{-2}}]$	k_F [D]	$\beta\rho/(\mu/k_F)$ [s/m]	R^2	i	
*Distilled water													
A3*	21.3	1630	618	0.999	6	29 100	29 158	1570	642	17.9	>0.999	11	0.27

i indicates the number of measurements included in the regression. The number of measurements in the linear regression only includes the linear data and varies depending of onset of the critical velocity, u_c. The permeabilities, k and k_F, are provided in units of Darcy, [**D**]. The transformation to SI units corresponds to 1 **D** = $0.9869233\cdot 10^{-12}$ m^2. Viscosity of oil and distilled water is 1.38 mPa·s and 0.994 mPa·s, respectively. Density of oil and distilled water is 790 kg/m^3 and 998 kg/m^3, respectively. The regression numbers are mean values within a 95% prediction interval

D (7.69×10^{-9} to 9.86×10^{-9} m^2), more than one order of magnitude larger than that of the other sample types. The lowest permeabilities are observed in samples D1–D6 with the range of 440–619 D (4.34×10^{-10} – 6.11×10^{-10} m^2). This indicates some slight differences in the pore-matrix geometry of the different samples in each sample group, even though the duplicate samples were fabricated in parallel with the same *Marlok C1650* powder batch, AM equipment, and laser beam specifications. This is most clear with samples B3 and D4 in Figs. 12g and 13c, which display markedly steeper tangent lines and lower permeability than the others in their respective group.

The permeability $\boldsymbol{k}$ of Eq. 1 is typically slightly less than $\boldsymbol{k_F}$ of Eq. 2, most clearly observed for samples A1-A5. The polynomial regression generally offers marginally better $\boldsymbol{R}^2$ than the linear regression, but the higher $\boldsymbol{k_F}$ tend to slightly under-estimate the pressure drop at the lowest rate of flow, 7.25 ml/min (0.00121 m/s). The linear regression slightly overestimates the pressure drop compared to the measurements at the lowest rates of 7.25 and 14.5 ml/min (0.00121 and 0.00242 m/s), which suggest that a small portion of non-linear losses are included in the regression. These variations are too small to be seen in Fig. 13, but they insinuate that the correct permeability is presumably found somewhere between the two regressions presented.

The inertial resistance factor ($\boldsymbol{\beta}$) of samples A range from 23,608 to 38,861 m^{-1}, which is considerably larger than that of the other sample types. However, the magnitude of the $\boldsymbol{\beta}$ is dependent of the permeability. For instance, the B1–B6 samples display the lowest $\boldsymbol{\beta}$ of 903–1 110 m^{-1}, which is more than one order of magnitude smaller than the A1–A5 samples. This is opposite to the observed permeability behavior. To compare the relative magnitude of the $\boldsymbol{\beta}$ one must evaluate the ratio of the inertial component to the viscous component, $\boldsymbol{\beta\rho/(\mu/k_F)}$ in Table 5. For A1–A5 the ratios are 9.4–14.9, which is twice as large as those of 5.0–6.1 and 4.58–7.64 for B1–B6 and C1–C6, respectively. The ratio for the B and C samples is twice as large as those of sample D of 2.33–2.76. This is reflected in the curvature of the data in Fig. 13 and corresponds to the same tendency in the observed onset of $\boldsymbol{u_c}$ occurring at lower superficial velocities for samples A than samples B–C–D, respectively. This is seen in Fig. 13b where the curvature of the data is more profound for A1–A5 than for other B–C–D samples in Fig. 13d, f, and h.

A multipoint test with distilled water for sample A3 is presented in Fig. 14 to demonstrate the general behavioral change for different fluids. The density of water (998 kg/m^3) is higher than the oil density (790 kg/m^3), while the viscosity of the oil (1.38 mPa·s) is higher than for water (0.994 mPa·s). The linear data in Fig. 14a for distilled water show lower pressure losses than oil, but the divergence from streamline flow is observed at a lower velocity. This agrees with oil having higher viscosity than water (Table 5). In Fig. 14b the pressure loss for distilled water is higher than for oil after the velocity exceeds approximately 2.3 cm/s. This agrees with water having a higher density than oil. The regression results in Table 5 show that the permeability attained with distilled water is not equal of the oil permeability. Some rust was identified on the steel spheres after the test and this might explain the differences.

4.3 Empirical correlations

The empirical correlations of the experimental data (Eqs. 1 and 2) to the Kozeny–Carman equation (Eq. 20) and the Ergun equation (Eq. 30) are presented in Table 6. It is convention for these equations to be described according to a representative particle

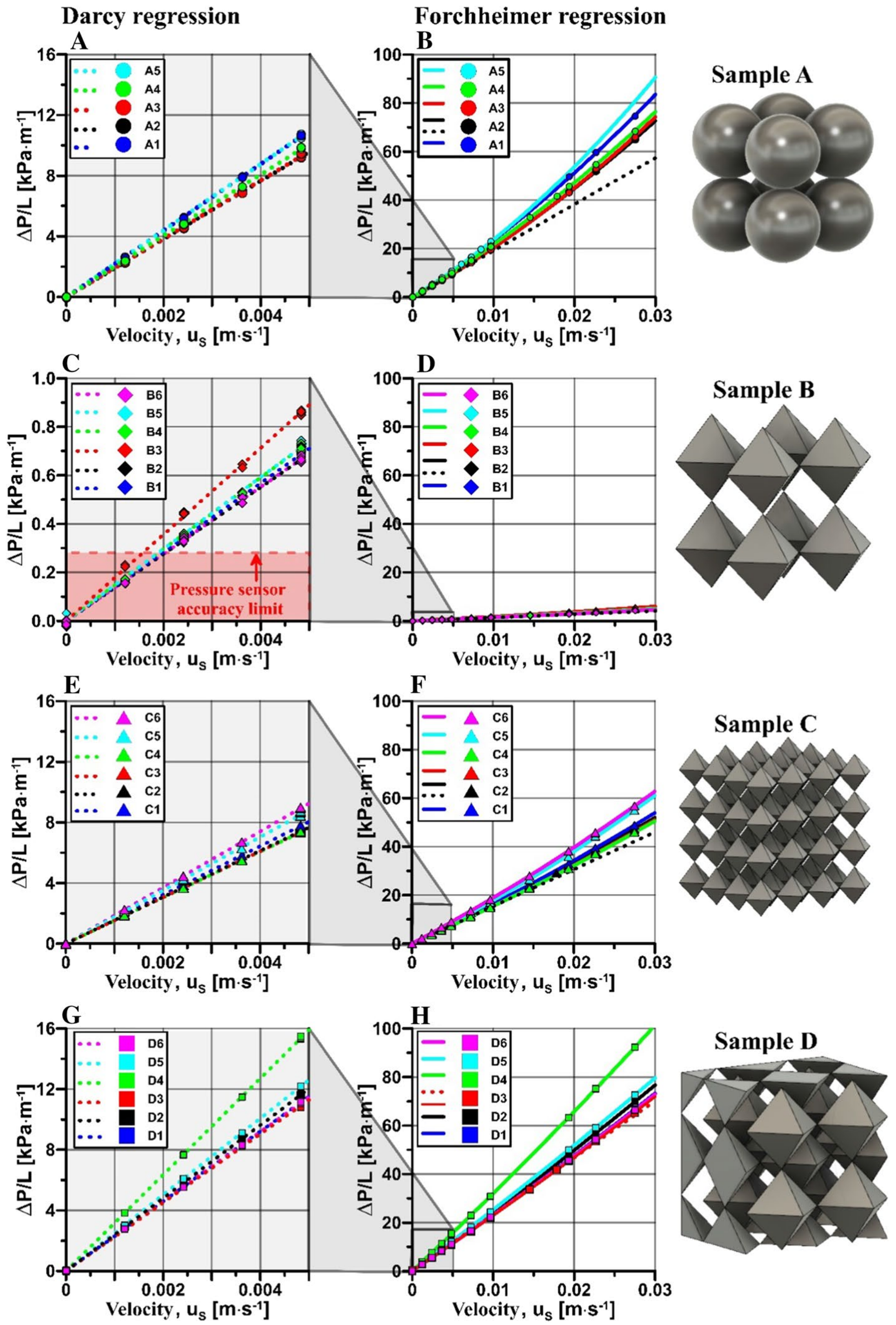

Fig. 13 Experimental results for the EXXSOL D60 oil multipoint Hassler flow cell tests for samples A, B, C, and D including all the 23 duplicates. The data are plotted as differential pressure loss per unit length versus the superficial velocity, **ΔP/L** vs. **u**$_s$. The velocity range of the tests is 0.00121–0.0275 m/s (7.25–165 ml/min). Linear least square regression fits are shown in dashed lines in figures **a**, **c**, **e**, and **g**, while polynomial least square regression fits are shown in full lines in figures **b**, **d**, **f**, and **h**. Regression results are presented in Table 5

diameter of the porous media (Carman, 1937; Ergun and Orning 1949; Fand et al. 1987; Macdonald et al., 1979). This is typically done through introducing the spherical relation of Eq. 31.

$$\boldsymbol{S} = \frac{\mathit{Area\ of\ sphere}}{\mathit{Volume\ of\ sphere}} \cdot \mathit{Volume\ ratio\ of\ solids\ in\ the\ porous\ media} = \frac{6 \cdot (1 - \boldsymbol{n})}{\boldsymbol{\varphi} \cdot \boldsymbol{d}} \tag{31}$$

where the particle diameter, $\boldsymbol{d}$ (m), the porosity of the bed ($\boldsymbol{n}$), and a surface factor that account for particle roughness and shape, $\boldsymbol{\varphi}$ (-), is defined to describe the specific surface area, $\boldsymbol{S}$. For a single particle the surface factor, $\boldsymbol{\varphi}$, is unity for smooth spheres and less than unity for all other shapes. The same convention is therefore presented as an additional equational form (Eqs. 33, 35 and 37) in Table 6, so that the results can be easily compared.

The Kozeny–Carman equations are correlated to the Darcy equation (Eq. 1), which corresponds to Eqs. 32 and 33. The only unknown parameters in Eqs. 32 and 33 are the constants $\boldsymbol{k_C}$ and $\boldsymbol{X_C}$, respectively, and these constants are adjusted to achieve a best fit with the regression data of Eq. 1.

$$\boldsymbol{k} = \frac{\boldsymbol{n}^3}{\boldsymbol{k_C} \cdot \boldsymbol{S}^2} \quad \text{where } \boldsymbol{k_C} = \boldsymbol{k_0} \cdot \boldsymbol{\tau}^2 \tag{32}$$

$$\boldsymbol{k} = \frac{\boldsymbol{\varphi}^2 \cdot \boldsymbol{d}^2 \cdot \boldsymbol{n}^3}{\boldsymbol{X_C} \cdot (1 - \boldsymbol{n})^2} \quad \text{where } \boldsymbol{X_C} = \boldsymbol{k_C} \cdot 6 \cdot 6 \tag{33}$$

Ergun equation is correlated to the Forchheimer equation (Eq. 2), which corresponds to Eqs. 34, 35, 36, and 37. The only unknown parameters in Eqs. 34, 35, 36, and 37 are $\boldsymbol{\alpha_0}$, $\boldsymbol{X_E}$, $\boldsymbol{\beta_0}$, and $\boldsymbol{Y_E}$, respectively, and these constants are adjusted to achieve a best fit with the regression data of the linear and polynomial term in Eq. 2, respectively.

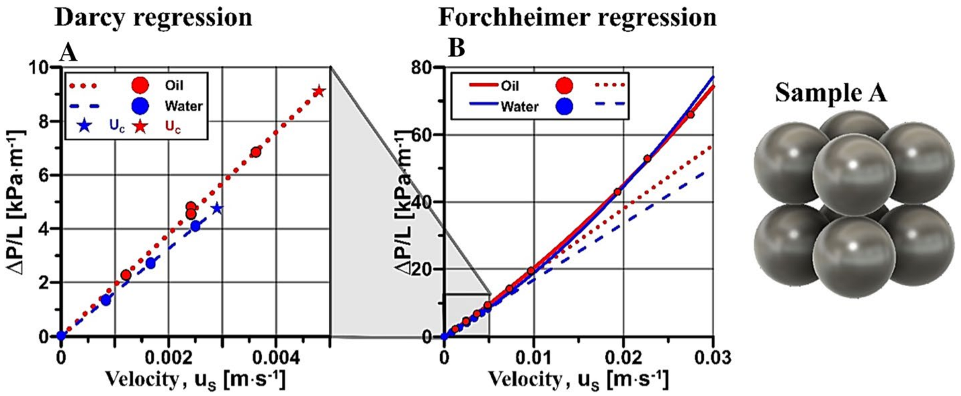

Fig. 14 Experimental results for the EXXSOL D60 oil and distilled water from the multipoint Hassler flow cell tests of sample A3. The data are plotted as differential pressure loss per unit length versus the superficial velocity. The velocity range of the tests is 0.00121–0.0275 m/s (7.25–165 ml/min). Linear least square regression fits are shown in dashed lines, while polynomial least square regression fits are shown in full lines. Regression results are presented in Table 5. **a** The pressure losses for distilled water are lower than for oil, but the divergence from linear flow occurs earlier. The stars indicate the onset of critical velocities, $\boldsymbol{u_c}$, of the two experiments. This is expected because of the higher viscosity of oil. **b** The pressure losses for water surpass that of oil at approximately 2.3 cm/s, due to the higher density of water

Table 6 Empirical correlation with parameters in Kozeny–Carman (Eqs. 32 and 33) and Ergun (Eqs. 34–37) for samples A3, B3, B6, C1, and D3

Input data	n [%]	S [m^{-1}]	φ [–]	d [mm]	τ [–]	a [–]	k [D]	k_F [D]	β [m^{-1}]
A3	34.96	3 869	1.0084	1.00	1.0	0.128	738	771	27 721
B3	73.66	3 158	0.5004	1.00	1.0	0.422	7 796	8 255	1 090
B6	75.47	2 886	0.5100	1.00	1.0	0.427	9 988	10 756	899
C1	68.72	8 496	0.4418	0.50	1.0	0.290	868	899	9 949
D3	51.16	5 370	0.5497	1.00	1.2247	0.640	619	624	6 443

Sample	Output data	k_c [Equation 32]	X_C [Equation 33]	Output data	α_0 [Equation 34]	β_0 [Equation 36]	X_E [Equation 35]	Y_E [Equation 37]
A3	Kozeny–Carman [eq. 20]	3.92	141	Ergun [Eq. 30]	1.87	2.45	135	1.84
B3		5.21	187		2.46	1.10	177	0.83
B6		5.23	188		2.43	1.06	175	0.80
C1		5.25	189		2.54	3.04	183	2.28
D3		7.60	274		3.77	1.29	271	0.97

The particle shape factor, φ, is calculated from Eq. 31. The permeabilities, k and k_F, are provided in units of Darcy, [**D**]. The transformation to SI units corresponds to 1 $\mathbf{D} = 0.9869233 \cdot 10^{-12}$ m^2

$$k_F = \frac{n^3}{2 \cdot \alpha_0 \cdot S^2} \tag{34}$$

$$k_F = \frac{\varphi^2 \cdot d^2 \cdot n^3}{X_E \cdot (1-n)^2} \quad \text{where} \quad X_E = 2 \cdot \alpha_0 \cdot 6 \cdot 6 \tag{35}$$

$$\beta = \frac{\beta_0 \cdot S}{8 \cdot n^3} \tag{36}$$

$$\beta = \frac{Y_E \cdot (1-n)}{\varphi \cdot d \cdot n^3} \quad \text{where} \quad Y_E = \frac{\beta_0 \cdot 6}{8} \tag{37}$$

The empirical correlations of the experimental data (Eqs. 1 and 2) to the new analytical Navier–Stokes approximations (Eqs. 18 and 29) are presented in Table 7, with the same input data of Table 6. The Stokes flow approximation are correlated to the Darcy equation (Eq. 1), which corresponds to Eq. 38. Equation 38 has two unknown coefficients, C and k_0, and these two parameters are treated as a single unknown coefficient, k_S (Eq. 19), which is adjusted to achieve a best fit with the regression data of Eq. 1. Equation 19 is then applied to see how the k_0 factor would result should the dissipation coefficient be defined $C = 3\pi$.

$$k = \frac{n^3}{k_S \cdot \tau^2 \cdot S^2} \quad \textit{where}\ k_S = \frac{3 \cdot \pi}{k_0} \tag{38}$$

Equation 29 is correlated to the Forchheimer equation (Eq. 2), which corresponds to Eq. 39 and 40. The unknown parameters in Eq. 39, are C, k_0, and these are treated equal to

Table 7 Empirical correlation with the parameters of the analytical Navier–Stokes approximations (Eqs. 38, 39 and 40) for samples A3, B3, B6, C1, and D3. Input data are found in Table 6

Sample	Output data	k_S [Equation 38]	k_0 [Equation 19]	Output data	k_{SF} [Equation 39]	k_{0F} [Equation 19]	C_{KL} [Equation 40]
A3	Darcy data [Equation 38]	3.92	2.40	Forch. data [Equation 39 and 40]	3.73	2.52	0.03
B3		5.21	1.81		4.92	1.92	0.09
B6		5.23	1.80		4.86	1.94	0.09
C1		5.25	1.80		5.08	1.85	0.11
D3		5.07	1.86		5.03	1.87	0.13

the coefficients in the Stokes flow approximation (Eq. 38) and are adjusted to achieve a best fit with the regression data of the linear term of Eq. 2. The C_{KL} are adjusted to achieve a best fit with the regression data of the polynomial term of Eq. 2.

$$k_F = \frac{n^3}{k_{SF} \cdot \tau^2 \cdot S^2} \quad \textit{where } k_{SF} = \frac{3 \cdot \pi}{k_{0F}} \tag{39}$$

$$\beta = \frac{C_{K_L}}{a^2} \cdot \frac{\tau^3 \cdot S}{k_{0F}^2 \cdot n^3}. \tag{40}$$

4.4 Critical Reynolds numbers

Three types of critical Reynolds numbers are presented in Table 8 to allow for comparison with values found in the literature. These numbers are typically utilized to describe when the flow characteristics deviate from linearity. The most common definition is that of Eq. 41, where the characteristic length is described by the diameter of the particle in the bed. Bear (2013) states that this definition provides Re_{C1} within the range 1–10 for porous media. Table 8 shows that all of the samples achieve numbers within this range. The definition of Re_{C2} follows the definition suggested by Blake (1922) and is the same definition used by Carman (1937) (Eq. 42). Carman (1937) concluded that Eq. 20 is valid for critical velocities corresponding to $Re_{C2} \approx 2.0$. Table 8 shows that the samples B3 and B6 achieve similar

Table 8 Critical Reynolds numbers for samples A3, B3, B6, C5, and D3. The Reynolds numbers are defined by Eqs. 41, 42, and 43

Sample		μ [mPa·s]	ρ [kg/m^3]	u_c [cm/s]	Re_{C1}	Re_{C2}	Re_{C3}	R_C
A3	Oil	1.38	790	0.49	2.81	0.73	0.28	0.06
	Water*	0.994	998	0.27	2.71	0.70	0.28	0.05
B3	Oil	1.38	790	0.91	5.20	1.64	0.85	0.05
B6	Oil	1.38	790	0.90	5.06	1.79	0.92	0.05
C1	Oil	1.38	790	0.84	4.81	0.57	0.31	0.04
D3	Oil	1.38	790	0.84	4.83	0.90	0.59	0.02

The ratio R_C of the non-linear to the linear dissipation component is represented by Eq. 44. The input values are provided in Tables 5, 6, and 7 values, while samples A3, C1, and D3 have values less than one. The Reynolds number definition utilized in this paper is presented in Eq. 4 and critical Reynolds numbers of this definition correspond to $\boldsymbol{Re}_{C3}$ in Eq. 43. Table 8 shows that all samples attain $\boldsymbol{Re}_{C3} < \approx 1$

$$\boldsymbol{Re}_{C1} = \frac{\boldsymbol{\rho} \cdot \boldsymbol{u}_c \cdot \boldsymbol{d}}{\boldsymbol{\mu}} \tag{41}$$

$$\boldsymbol{Re}_{C2} = \frac{\boldsymbol{\rho} \cdot \boldsymbol{u}_c}{\boldsymbol{\mu} \cdot \boldsymbol{S}} \tag{42}$$

$$\boldsymbol{Re}_{C3} = \frac{\boldsymbol{\rho} \cdot \boldsymbol{V}_c \cdot \boldsymbol{m}}{\boldsymbol{\mu}} = \frac{\boldsymbol{\rho} \cdot \boldsymbol{u}_c \cdot \boldsymbol{\tau}}{\boldsymbol{\mu} \cdot \boldsymbol{S} \cdot \boldsymbol{k}_{0F}} \tag{43}$$

An alternative definition is presented in Eq. 44 where the divergence from linearity is described as a ratio of non-linear over linear dissipation.

$$\boldsymbol{R}_C = \frac{\textit{non-linear dissipation}}{\textit{linear dissipation}} = \frac{\boldsymbol{C}_d \cdot \boldsymbol{Re}}{\boldsymbol{C}} = \frac{\boldsymbol{C}_d \cdot \boldsymbol{\rho} \cdot \boldsymbol{V}_c \cdot \boldsymbol{m}}{\boldsymbol{C} \cdot \boldsymbol{\mu}} = \frac{\boldsymbol{C}_{K_L} \cdot \boldsymbol{\rho} \cdot \boldsymbol{u}_c \cdot \boldsymbol{\tau}}{3 \cdot \boldsymbol{\pi} \cdot \boldsymbol{a}^2 \cdot \boldsymbol{\mu} \cdot \boldsymbol{S} \cdot \boldsymbol{k}_{0F}} \tag{44}$$

5 Discussion

The presented experiments show that AM in combination with high-resolution CT imaging technology and image analysis software enables the construction and detailed inspection of complex porous media. In this paper it was found that it is the combination of these three different 3D technologies that provide the full benefit of each individual technique. The technologies complement each other because they limit uncertainties in the interpretation of the pore-matrix configuration, especially if compared to conventional porous media studies, e.g., where particles are poured into a cylindrical container. In the presented work, the problem of the container wall affecting the particle arrangement of unconsolidated material is avoided. The exact placement of each particle can be controlled through the design and fabrication of the 3D samples. Since the properties of the design are known they can serve as a reference upon comparison with the final product. After fabrication, the CT imaging and image analysis software can provide a complete and highly accurate rendering of the samples which allows for comparison with the design properties. This allows for testing of geometries that previously would have been impossible to achieve. This demonstrates the potential benefit of combining these 3D technologies in porous media studies.

An issue for metal-based AM fabrication powder materials is the possibility that the material reacts with the fluid. This is observed in the presented experiments for oil and distilled water. The regression results in Table 5 show that the permeability attained with distilled water is not equal to the permeability attained with oil. This suggests that the difference in fluid properties do not fully explain the behavior of the data shown in Fig. 14. Corrosion products (rust) were identified in the samples after the test with distilled water and this is a probable explanation to the different permeabilities of the A3 sample. Other fabrication powder materials that would eliminate the corrosion problem, e.g., Aluminum, Titanium, or other stainless-steel blends or even plastic resins are readily available on the global market. Investigating how these powders react with the testing fluid is therefore recommended before performing the permeability tests.

5.1 Fluid flow through porous media

The Hassler flow cell test results demonstrate that the permeabilities ($4.34 \cdot 10^{-10}$ – $9.98 \cdot 10^{-9}$ m^2) of the four sample types (which have sand sized particles; $\boldsymbol{d}=1.0$ mm and $\boldsymbol{d}=0.5$ mm) are within the range of permeabilities associated with unconsolidated sandy soils (Bear, 2013). Medium to coarse sand have permeabilities between 10^{-11} and 10^{-9} m^2 (Bear 2013; Freeze and Cherry, 1979). The permeabilities of the four sample types (A, B, C, and D) are different and they are also slightly different for each sample within each sample group. The CT images of the five selected samples confirmed that the particle shapes, sizes, and configurations are preserved in the samples (Fig. 11). This argues that the variations of permeability within each group are caused by slight variations in porosity, surface area, and surface roughness of the individual samples in each sample group. Comparison of B3 vs. B6 data in Tables 5, 6, and 7 supports this statement.

For the packing arrangement with the cubical particle bed configuration, the alteration of particle shape from samples A to B displays a large influence on the permeability, from 641–738 D ($6.33 \cdot 10^{-10}$ – $7.18 \cdot 10^{-10}$ m^2) to 7796–9988 D (7.69×10^{-9} to 9.86×10^{-9} m^2), respectively (Darcy regression). While this is expected, it is surprising to see that the lowest permeability is observed in samples D with the range of 441–619 D (4.34×10^{-10} – 6.11×10^{-10} m^2). Both the sample B and D configurations consist of particles with the same size and shape, but the inter-fixed octahedron bed of sample D evidently alters the pore-matrix geometry drastically. The same trend is observed when the size of the particles is reduced from samples B to C. This demonstrates that it is not the particle shape or size that determines the permeability, but the corresponding pore shape and pore size that results from the packing of particles. These observations have good agreement with the literature (e.g., Bear 2013).

The empirical correlations on the linear flow data (Darcy regression in Table 5) show that the Kozeny–Carman equation attains coefficients of similar magnitude to those published by others, $\boldsymbol{k_C}=3.92$–7.60 (Eq. 32) and $\boldsymbol{X_C}=141$-274 (Eq. 33). Carman (1937) reports $\boldsymbol{k_C}$ values ranging from 4.84 to 6.13 from testing on randomly packed beds of smooth glass spheres. Fand et al. (1987) report $\boldsymbol{X_C}$ values ranging from 174 to 184, also from testing on randomly packed beds of smooth glass spheres. Even though the particle shapes, sizes, and packing arrangements of these various sample groups are different, it is interesting to note that the coefficients provided by the Kozeny–Carman equation are very similar. However, the presented experiments demonstrate that the analogy to the pipe geometry factors suggested in Eq. 21 by Carman (1937) is not correct for porous media. The tortuosity ($\boldsymbol{\tau}$) of samples A3, B3 B6, and C1 is unity, while it is 1.2247 for sample D3. The upper limit for the pipe geometry factors is 3.0 (Table 1). Consequently, there are no pipe geometry factors that can describe any of the datasets. The $\boldsymbol{k_C}$ coefficient is therefore not a function of the tortuosity factor ($\boldsymbol{\tau^2}$) and the pipe geometry factors ($\boldsymbol{k_0}$) in the form of Eq. 21 (corresponding to Eq. 45) for non-uniform pore channels.

$$\boldsymbol{k_C} \neq \boldsymbol{k_0} \cdot \boldsymbol{\tau}^2 \tag{45}$$

In the Darcy flow region, the Stokes flow approximation coefficient $\boldsymbol{k_S}$ derived from correlations with the linear regression is identical to the $\boldsymbol{k_C}$ of Kozeny–Carman for A3, B3, B6, and C1, where the tortuosity is unity. The main difference is seen in the sample D3 results where the $\boldsymbol{k_S}$ coefficient now resembles the other octahedron samples. The resulting geometry factors, $\boldsymbol{k_0}$, for the octahedron particle beds B3 ($\boldsymbol{k_0}=1.81$), B6 ($\boldsymbol{k_0}=1.80$), and C1 ($\boldsymbol{k_0}=1.80$) closely resemble the factor of a square ($\boldsymbol{k_0}=1.78$), or closer to a 2×1 rectangle ($\boldsymbol{k_0}=1.94$) for sample D3 ($\boldsymbol{k_0}=1.86$). These coefficients have good agreement with the actual shape of the pore body geometries of the sample configurations (Fig. 3, Fig. 4, and Fig. 11), where the pore bodies of samples B and C are squares, and sample D is rectangular. The geometry factor for sample A3 ($\boldsymbol{k_0}=2.40$) does not resemble that of a circle ($\boldsymbol{k_0}=2.0$). The geometry factors closest to the $\boldsymbol{k_0}$ value of sample A3 are elliptical or rectangular shapes (Table 1). All the five samples A-D achieve geometry factors within the range of possible values and samples B, C, and D show good agreement with the observed shape of the pore channel. These results argue in favor of the assumption that Eq. 19 can be approximated by the 3π constant (Eq. 46) for non-uniform pore channels.

$$\boldsymbol{k_S} \cong \frac{3\cdot\boldsymbol{\pi}}{\boldsymbol{k_0}} \tag{46}$$

Mao et al. (2016) note that the "Forchheimer" permeability ($\boldsymbol{k_F}$) is not always equal to the Darcy permeability ($\boldsymbol{k}$). This is also observed in this study and this affects the empirical correlations. The empirical correlations between the non-linear flow data (Forchheimer regression in Table 5) show that the Ergun equation attains linear coefficients, $\boldsymbol{\alpha_0}=1.87$-$3.77$ (Eq. 34) and $\boldsymbol{X_E}=135$-271 (Eq. 35), similar to those published by others. The sample A3 value (1.87) agrees with several of the experiments of Ergun & Orning (1949) who report a factor of $\boldsymbol{\alpha_0}=1.8$–$1.9$ for tests with beds of spheres with 30.3–37.2% porosity. The $\boldsymbol{X_E}=135$ of sample A3 agrees with the data of Rumpf and Gupte (1971) who report $\boldsymbol{X_E}$ values from 124-162 on beds of glass spheres with 43.6–64.0% porosity. The non-spherical particles (B, C, and D) attain values of $\boldsymbol{\alpha_0}=2.43$-$3.77$ and $\boldsymbol{X_E}=171$–271. Dudgeon (1966) report tests on angular sand and gravel particles, where most of the data range approximately from $\boldsymbol{X_E}=159$ to $\boldsymbol{X_E}=546$. Similar ranges are also reported by McDonald et al. (1978) and Olatunde and Fasina (2018). The coefficients provided by the Ergun equation are relatively similar for a wide range of particle sizes and shapes. Since the analogy to the pipe geometry factor (circular pipe $\boldsymbol{k_0}=2$) is not correct for porous media in this equational form, $\boldsymbol{\alpha_0}$ evidently adopts numerical values that have no logical meaning. Furthermore, the influence of the tortuosity factor ($\boldsymbol{\tau^2}$) is not accounted for in the Ergun equation. The $\boldsymbol{\alpha_0}$ will thus at best represent a clustered parameter that account for several erroneously defined geometrical variables.

The coefficient $\boldsymbol{k_{SF}}$ (Eq. 39) derived from correlations with Eq. 29 to the non-linear regression data is identical to twice the size of $\boldsymbol{\alpha_0}$ of the Ergun equation for A3, B3, B6, and C1, where the tortuosity is unity. The main difference is seen in the sample D3 results where the $\boldsymbol{k_{SF}}$ coefficient now resembles that of the other octahedron samples. The resulting geometry factors, $\boldsymbol{k_{0F}}$, for the octahedron particle beds B3 ($\boldsymbol{k_{0F}}=1.92$), B6 ($\boldsymbol{k_{0F}}=1.94$), and D3 ($\boldsymbol{k_{0F}}=1.87$) closely resemble a 2x1 rectangle ($\boldsymbol{k_0}=1.94$). These coefficients are still within the range of possible $\boldsymbol{k_0}$ values (Table 1), but only agree well with the pore body geometries of the samples with D3 configuration (Figs. 3, 4, and 11). Table 7 shows that the values of the $\boldsymbol{k_{SF}}$ coefficients are consistently less than the $\boldsymbol{k_S}$ coefficients. In the literature it is often suggested that the differences between Forchheimer permeability ($\boldsymbol{k_F}$) and the Darcy permeability ($\boldsymbol{k}$) are a result of different flow characteristics within the porous media consisting of a variety of pore sizes (Forchheimer 1930; Carman 1937; Fand et al. 1987; Newman and Yin 2013; Mao et al. 2016). Inertial effects might then occur in the larger pores, while the smaller pores are still in the fully linear region. However, in the presented experiments the pores within each porous media are virtually equal. This suggests that the differences between $\boldsymbol{k_F}$ and $\boldsymbol{k}$ might be an effect caused by the best-fit regression method applied to the experimental data.

Based on the results from the provided experiments it is shown that the assumption of Kozeny in Eq. 10 is proven suitable for porous media with homogenous pore matrixes. From a theoretical point of view the assumption is logical if viewed in relation to the assumptions enforced by the Navier–Stokes equation in Stokes flow conditions. In Stokes flow conditions the fluid wraps around the entire surface within the pore channels and the frictional shear forces act on all surface area available to the fluid (White 2006; Çengel and Cimbala, 2010). Applying Kozeny's assumption is then in accordance with the assumption of Stokes flow. A pore channel's specific surface area to volume ratio is thus the appropriate characteristic length unit ($\boldsymbol{m}$) for porous media flows. This is not a controversial conclusion because the expression is essentially the same definition applied in conventional fluid mechanics for pipe flow. For a uniform pipe this characteristic length unit simplifies to an expression in relation to the internal diameter of the pipe (Eq. 6). For a non-uniform pore channel, the expression does not simplify any further. A shape factor (φ in Eq. 31) does seemingly enable the application of the particle diameter as part of the expression, but the diameter of a particle is not the actual characteristic length unit of which the flow behavior relies, a fact that frequently seems to be forgotten.

The new porous media equation (Eq. 29) is based on analogies to the analytical Navier–Stokes equations for pipe flows. In the Darcy flow regime, the analogy of porous media flow to the Stokes flow around a single sphere is perhaps controversial, but the correlation of Eq. 18 to the experimental data shows coefficients ($\boldsymbol{k_S}$) that agree well with experiments (Table 7) and the theory (Table 1). The resulting geometry factor ($\boldsymbol{k_0}$ of Eq. 19) of the four sample types is indeed consistent with the observed shape of the channels in the pore body center region. The success of the analogy presumably relies on the fact that the dissipating forces of the flow are not just a result of frictional shear dissipation alone, as in the Hagen–Poiseuille equation, but also incorporates a significant portion of pressure dissipation. The application of the Stokes sphere constant, 3π, implies that a significant portion (1/3) of dissipation losses are due to pressure dissipation. The pressure dissipation arises due to the non-uniformity of the channel geometry, which induced spatial variations to the strain rate field and induces acceleration of the velocity field within the flow through the porous medium. In uniform straight pipes this type of dissipation does not occur as the cross-section is uniform and there is no change to the velocity field along the pipe in steady-state flows.

Based on the results from the provided experiments it is shown that the effects of particle roughness do not alter the flow behavior in Darcy/Stokes flow conditions. A particle with rough surfaces rather provides more surface area on which the dissipating frictional shear forces of the fluid flow can act. This is evident through comparison between samples B3, B6, and C1 which all yield matching $\boldsymbol{k_S}$ coefficients after accounting for surface area and porosity differences. This is also evident through comparison of the presented experiments with those of e.g., Carman (1937), Ergun and Orning (1949) and Fand et al. (1987) and others. The range of coefficients achieved for smooth particles, e.g., $\boldsymbol{k_C}=4.18$–6.13 for smooth spheres (Carman 1937), is similar to those achieved for the different rough particle arrangements presented here ($\boldsymbol{k_C}=3.92$–7.60). It is therefore important to describe the specific surface and the porosity of the porous media accurately when utilizing empirical equation for prediction purposes.

Macdonald et al. (1979) suggest that particle roughness should highly affect the flow dynamics in the "high" velocity flow region of the Forchheimer equation. This implies that the β_0 and Y_E of Eqs. 36 and 37 would be expected to be relatively larger if the particle roughness had significant influence on the convective acceleration term. The empirical correlation of sample A3 results in β_0 and Y_E equal to 2.45 and 1.84, respectively. These values are actually lower than the range $\beta_0 = 2.5\text{-}3.0$, reported by Ergun & Orning (1949) on experiments on randomly packed beds of smooth glass spheres and lead shots. The data of Fand et al. (1987) on experiments on randomly packed beds of smooth glass spheres provide Y_E range of 1.811-1.925. The surface area-to-volume ratio of sample A3 is comparable to what would be expected from a bed of smooth spheres of similar porosity, but the particles are indeed very rough. Much higher factors of β_0 and Y_E would therefore be expected if the particle roughness had significant influence on inertia at the velocities tested. The results thus prove contrary to the predictions of Macdonald et al. (1979).

The β_0 and Y_E of the orthorhombic samples B, C, and D show seemingly random variability in their behaviors (Table 6). The B3 and B6 show low β_0 values of 1.10 and 1.06, respectively, while sample C1 shows a high β_0 value of 3.04, even though the cubic packing arrangements of the samples are identical. The high β_0 of C1 agrees with the predictions of Macdonald et al. (1979) but the lower β_0 of B3 and B6 argues that there is some other cause than the surface roughness that affects the behavior. The β_0 and Y_E coefficients of sample D3 are also low and in a similar range to that of B3 and B6. Upon comparison, similar results are seen in, e.g., Dudgeon (1966) in his work on crushed marble and other granular material, or indeed, similar factors are achieved on the data of Becker (1947) on orthorhombic packings. Consequently, the application of the β_0 does not yield consistent or logical results and the outcome is therefore difficult to predict. Furthermore, the influence of the tortuosity (τ) is not accounted for in the Ergun equation. The β_0 will thus at best represent a clustered parameter that account for several undefined geometrical variables.

The convective acceleration dissipation coefficient C_{KL} (Eq. 40), derived from correlations with the non-linear data of the Forchheimer regression, are small and are similar for all four sample types A-D. These values cannot be easily compared to β_0 factors published in the porous media literature, but they are expected to be comparable to similar laminar pipe flows coefficients (K_L range between 0.0 and 2.0). The dissipation coefficient C_{KL} of all the samples, A3, B3, B6, C1, and D3, are within the range limits of K_L found in the literature of pipes (Çengel and Cimbala 2010; Idelchik 1994; White 2006; Crane 1957). Furthermore, they are very small. These results suggest a low degree of wake formation or flow separation within the pores, and that most of the non-linear pressure dissipation is due to the continuous acceleration and deacceleration of the fluid through the pores. This demonstrates that it is the magnitude of channel contraction (a) that governs the dissipation of mechanical energy in Forchheimer flow, in good agreement with the numerical studies of Newman and Yin (2013).

The spherical particles of sample A3 display the lowest $C_{KL} = 0.03$ which is probably due to the rounded particle shape and corresponding streamlining of the channel geometry through the pore throat. A specific value for $K_{L\text{-}co}$ of 0.03 (Eq. 25), similar to C_{KL} of sample A3, corresponds to, e.g., a well-rounded and smooth pipe contraction segment in turbulent flow conditions ($\alpha = 1.05$) (Tables 4–8 in Çengel & Cimbala, 2010). The marginally larger C_{KL} coefficients of the octahedron samples B3, B6, and C1 can be explained by a less-streamlined channel geometry through the pore throat with more rapid changes along the pore channel length. It is also interesting to note that sample D3 has the largest $C_{KL} = 0.13$ even though the β factor for samples D in Eq. 2 is the smallest of all the sample types. This can be explained by additional losses caused by the tortuosity of the channels. The alteration of the predominant flow direction from one pore to the next enforces a change in the velocity field not accounted for by the expansion of the channel alone (note that the modification leading to the $\boldsymbol{\tau}^3$ factor in Eq. 29 is not performed to account for this effect).

The $\boldsymbol{C_{KL}}$ coefficient should depend on the flow characteristics within the channel. This means that $\boldsymbol{C_{KL}}$ should include a kinetic energy correction factor (Ref. equation 25 with $\boldsymbol{\alpha}=2.0$), which infer that the flow is still fully laminar. This implies that the magnitude of the $\boldsymbol{C_{KL}}$ coefficient is expected to decrease as the flow characteristics turns turbulent and $\boldsymbol{\alpha}\approx 1.05$. A decrease of inertia is observed in several "high" velocity experiments, both analytically and numerically (Fand et al. 1987; Hill et al. 2010; Barree and Conway 2005), but this does not necessarily suggest a divergence from laminar flow condition. The divergence might be caused by separation of the laminar boundary layer, as presented and discussed in detail by Idelchik (1994) for conventional pipe flows. The limit of $\boldsymbol{Re} > 30$–50 for laminar flow separation in pipe diffusers shown by Idelchik (1994) suggests that the laminar boundary layer is still in force for flow conditions similar to those in this study. The application of the $\boldsymbol{C_{KL}}$ coefficient then offers an alternative explanation to the observed behavioral change of flow characteristics at higher Reynolds numbers, as opposed to the theories discussed by Barree and Conway (2005), on the existence of a "minimum permeability plateau" or the application of the cubic velocity term discussed by Firzoozabadi and Katz (1979) or Ezeudembah (1982).

5.2 Limitations of the equations

It is here shown that Eq. 29 works well for porous media consisting of multiple copies of equivalent pores. However, before applying the equation on different porous media, it is important to consider the limitations of the equation regarding the many assumptions underlying the applied modifications of the fundamental Eq. 3. The modifications are highlighted in Eq. 47 with different colors, signifying the modifications associated with the characteristic geometry of the porous media (green), the velocity field (red), the Stoke sphere approximation (blue—linear term), and the concept of minor losses in pipes (blue—non-linear term).

$$\frac{\Delta P}{L} = \mu \cdot 3 \cdot \pi \cdot \frac{\tau \cdot S^2}{n^2} \cdot \frac{\tau \cdot u_s}{n \cdot k_0} + \rho \cdot \frac{C_{K_L}}{a^2} \cdot \frac{\tau \cdot S}{n} \cdot \frac{\tau^2 \cdot {u_s}^2}{k_0^2 \cdot n^2} \tag{47}$$

A significant share of the modifications results from the endeavor to describe the interstitial fluid velocity field within the porous media from a measurable superficial fluid velocity component (red color). The velocity modifications are particularly profound in view of the velocity component of the convective acceleration term. The importance of Kozeny's assumption *"…that the granular bed is equivalent to a group of parallel, similar channels…"* has a major role in the limitations of the equation. If the channels of the porous media are a group of unparallel and dissimilar channels, as is often the case in natural soils, the modifications of the velocity field are unable to describe the flow relations by a single set of coefficients. A collection of different channel geometries would result in a collection of different velocity fields, each bound by the geometry of that particular pore channel within the porous media. The resulting "global" coefficients would then be an outcome of the average behavior of the sample.

The assumption of Kozeny does, however, not rely on the porous media to be homogeneous in terms of the size and shape distribution of the soil solids of the media. It is the pore-matrix configuration that determines whether the porous media is homogenous. As a consequence, Eq. 29 might function well as long as the mixture of soil particles and their arrangement result in a homogenous pore distribution. An inhomogeneous pore distribution would, however, complicate the matter because the divergence from linear flow occurs earlier for large pores. Additional non-linear dissipation will then occur in parts of the media while other parts will still be fully in the linear flow regime, as Forchheimer (1930) pointed out. It is therefore relevant to consider when the convective acceleration term must be accounted for.

The divergence from linearity is typically assessed through evaluation of the critical Reynolds number of the flow. A variety of critical Reynolds numbers have been presented in Table 8. The critical numbers of $\boldsymbol{Re_{C1}}$ and $\boldsymbol{Re_{C2}}$ are both within the expected range of each definition. The Reynolds number definition used in the Stokes approximation ($\boldsymbol{Re_{C3}}$) is less than one for all samples. This is consistent with the critical number criterion of $\boldsymbol{Re} < \approx 1$ for Stokes flow in general (White, 2006). The criteria of Stokes flow approximation require that the $\boldsymbol{Re} \ll 1$ when applying the linear term of Eq. 3 alone on fluid flow problems. Although the $\boldsymbol{Re_{C1}}$, $\boldsymbol{Re_{C2}}$, and $\boldsymbol{Re_{C3}}$ definitions fulfill this requirement experimentally, they do not provide information about the relative magnitude of the inertial versus the viscous component observed in the flow data (Figs. 13 and 14). This is only achieved with the ratio $\boldsymbol{R_C}$, where the samples have ratios between 0.02 and 0.06 (Table 8). This ratio essentially state that the non-linear term is 2–6% of the magnitude of the linear term for the critical velocity used in the equation. This might be a more useful definition for prediction purposes.

Unlike the conventional Reynolds number definitions, the ratio $\boldsymbol{R_C}$ incorporates the factors and coefficients ($\boldsymbol{C_{KL}}$ and $1/\boldsymbol{a}^2$) that account for the constriction and expansion of the pore channel. If a pore channel has a severe constriction, $1/\boldsymbol{a}^2$ will be a large number, which implies that the divergence from linearity has to occur at relatively lower flow velocities. Alternatively, if there is no contraction of the channel, the $\boldsymbol{C_{KL}}$ (Ref. equation 25) will approach zero, and there will be no divergence from linearity, even at very high flow velocities. Presumably this applies until the onset of turbulence, such as for conventional pipe flows ($\boldsymbol{Re}_{\mathrm{Pipe}} \approx 2300$).

6 Conclusion

The presented experiments demonstrate that the application of AM, CT imaging, and image analysis techniques represents an improvement in porous media studies. These 3D technologies enable the study of porous media in a controlled fashion and allow experimental testing on geometries that would otherwise be impossible to achieve with conventional study methods on natural soils or particle beds. Uncertainties regarding the geometrical properties are minimized because the 3D-printed porous media samples can be evaluated with CT imaging after fabrication. This combination of 3D technology improves the data acquisition and data interpretation and contributes to new insight into the phenomenon of fluid flow through porous media.

The presented experiments confirm that the equations of Kozeny–Carman (1937) and Ergun–Orning (1949) can be adjusted to fit the experimental data. However, their underlying fluid mechanical theory do not describe the variation in geometrical properties properly. This is due to the analogy of porous media flows to the Hagen–Poiseuille flow relation, which is seemingly inaccurate for non-uniform pore channels.

The empirical relations of the Darcy equation and the Forchheimer equation can be explained through the analogy to the analytical Stokes flow approximation and the analytical solution of the convective acceleration term of the Navier–Stokes equation. The success of applying the Stokes sphere constant implies that the dissipating forces of the flow are not just a result of frictional shear alone but that a significant portion of dissipation losses are due to pressure dissipation as well. The pressure dissipation arises due to the non-uniformity of the channel geometry, which induced spatial variations to the strain rate field and induced acceleration of the velocity field within the flow through the porous medium. The new analytical Navier–Stoke equation (Eq. 29) provides geometrical coefficients that agree with the observed geometries of the 3D samples. The new equation addresses and, to some extent, modifies some frequently applied assumptions of porous media flow. The conclusions regarding these assumptions are as follows:

- The assumption of Kozeny is applicable for porous media flow and Eq. 10 is the correct characteristic length unit for application in porous media flow equations.
- The assumption of Dupuit (1863) on interstitial flow velocity is not the appropriate average velocity found within a non-uniform pore channel. An extension to Dupuit's assumption is presented, where his assumption is viewed as an approximate value of the maximum velocity in the pore center. Correcting for the channel geometry provides a representative average velocity field of the pore body center. This velocity field is suggested as the analog to the "free stream velocity field" in Stokes flow, which allows for the 3π Stokes constant to apply to porous media flows.
- A new critical ratio number, $\boldsymbol{R_C}$, that predicts when the Darcy equation deviates from linearity has been suggested. This definition provides diverging limits to the Darcy equation that are in line with the assumptions required for the Stokes flow approximation ($\boldsymbol{Re} \ll 1$) and might be useful for prediction purposes.
- The tortuosity of a pore channel is an individual geometrical property of the porous media and functions as an input variable in Eq. 29.

These modifications of theory along with the experiments presented demonstrate that the effects of surface roughness do not affect the flow behavior in Darcy flow or in Forchheimer flow. The transition from Darcy flow to Forchheimer flow is largely governed by the ratio of constriction of the pore throat and the pore body. This constriction ratio governs the relative acceleration of the fluid and the corresponding inertia that are associated with higher flow velocities in porous media.

In order to evaluate the new theory and equations, there is a need to perform more permeability tests on porous media where the pore geometry is well defined and known. This will probably be achieved soon since the 3D printing and CT imaging technologies are mature enough to provide a means to do so already. Further work should also be focused on porous media with different pore size distributions and pore-shape variations. Combined with investigations of flow conditions into the region of higher Reynolds number flows, this will provide a better understanding of porous media flow and the transition from laminar to the turbulent flow regime in porous media.

Acknowledgements Open Access funding provided by NTNU Norwegian University of Science and Technology (incl St. Olavs Hospital - Trondheim University Hospital). This work was conducted as a part of the research project Optimal utilization of groundwater for heating and cooling in Melhus and Elverum (ORMEL). The project is a cooperation between the municipalities of Melhus and Elverum, the Norwegian University of Science and Technology, Asplan Viak AS, and the Geological Survey of Norway. We would like to thank all the involved institutions and persons for cooperation and financial contributions. The authors would like to direct special thanks to Steffen Wærnes Moen, Roger Overå, and Noralf Vedvik for help with customizing the Hassler flow cell and calibration of the measuring equipment. Special thanks to Autodesk® Fusion 360™ for providing the educational CAD license free of charge.

Author Contributions Conceptualization: SG; Theory: SG; Methodology: SG, VB, EL, OÅB & OTB; Formal analysis: SG; Data curation: SG, VB, EL, OÅB & OT.; Writing—original draft preparation: SG, VB & EL; Visualization: SG, EL, OTB; Writing—review and editing: SG, VB, EL, OTB, OT, RKR, BOH & BSF; Supervision: OT, RKR, BOH & BSF.

Funding The Norwegian University of Science and Technology, the Regional Research Funds in Mid-Norway (Grant Number 209074) and the PoreLab Center of Excellence funding scheme (no. 262644) funded this research.

Compliance with Ethical Standards

Conflict of interest The funders had no role in the design of the study; in the collection, analyses, or interpretation of data; in the writing of the manuscript, or in the decision to publish the results.

References

Akram, J., Chalavadi, P., Pal, D., Stucker, B.: Understanding grain evolution in additive manufacturing through modelling. Addit.Manuf. **21**, 255–268 (2018)
Allen, J.R.L.: Principles of physical sedimentology, Allen & Urnwin London, England (1985) ISBN 0045510954
Barnea, E., Mednik, R.L.: A generalized approach to the fluid dynamics of particulate systems part III: General correlation for the pressure drop through fixed beds of spherical particles. Chem. Eng. J. **15**(3), 215–227 (1978) ISSN: 0300-9467
Barree, R.D., Conway, M.W.: Beyond beta factors; a model for Darcy, Forchheimer, and trans-forchheimer in porous media. JPT **57**(3), 43–45 (2005) ISSN: 01492136
Bear, J.: Dynamics of Fluids in Porous Media., Dover Publications Newburyport, England (2013) ISBN 0-486-13180-7
Becker, J. C.: M.S. thesis, Carnegie Institute of Technology, **1947**
Blake, F.E.: The resistance of packing to fluid flow. Trans. Am. Inst. Chem. Eng. **14**, 415 (1922)
Brinkman, H.C.: On the permeability of media consisting of closely packed porous particles. Appl. Sci. Res. Amsterdam, **A1**, 81–86 (1947), ISSN: 0365-7132
Brinkman, H.C.: A calculation of the viscous forces exerted by a flowing fluid on a dense swarm of particles. Appl. Sci. Res. **A1**, 27–34 (1947) ISSN: 0365-7132
Brøtan, V., Åsebø Berg, O., Sørby, K.: Additive manufacturing for enhanced performance of molds, 6th Conference on Learning Factories. Procedia CIRP, **54**, 186–190 (2016)
Carman, P.C., Fluid flow through granular beds. Trans IChemE, 15, 150–166 (1937). ISSN: 0263-8762
Çengel, Y. A; Cimbala, J. M. Fluid Mechanics: Fundamentals and Applications, 2nd edn., McGraw-Hill Boston (2010). ISBN 9780071284219

Chapuis, R.P.: Predicting the saturated hydraulic conductivity of soil: a review. Bull. Eng. Geol. Environ. **71**, 401–434 (2012). ISSN: 1435-9529. https://doi.org/10.1007/s10064-012-0418-7

Collins, R.E.: Flow of Fluids through Porous Materials, *The petroleum publishing company*, Thulsa, **1976**, ISBN: 0-87814-072-7

Crane Company, Flow of fluids through valves, fittings, and pipe, Crane Company Chicago, **1957**

D'arcy, H.P.G., Les Fontaines Publiques de la Ville de Dijon, Victor Dalmont, Paris, (1856)

Dudgeon, C.R.: An experimental study of the flow of water through coarse granular material. La Houille Blanche No. 7, (1966). https://doi.org/10.1051/lhb/1966049

Dupuit, A.J.E.J.: Etudes Théorétiques et Pratiques sur le Mouvement des Eaux, (1863)

Epstein, N.: On tortuosity and the tortuosity factor in flow and diffusion through porous media. CES **44**, 777–779 (1989). ISSN: 0009-2509, https://doi.org/10.1016/0009-2509(89)85053-5

Ergun, S., Orning, A.A.: Fluid flow through randomly packed columns and fluidized beds. Ind. Eng. Chem. **41**(6), 1179–1184 (1949), ISSN: 0019-7866

Ezeudembah, A.S., Dranchuk, P.M., Flow mechanism of Forchheimer's cubic equation in high-velocity radial gas flow through porous media. In: Proceedings of SPE Technical Conference and Exhibition, New Orleans (1982)

Fand, R.M., Kim, B.Y.K., Lam, A.C.C., Phan, R.T.: Resistance to the flow of fluids through simple and complex porous media whose matrices are composed of randomly packed spheres. J. Fluids Eng. **109**, 268–273 (1987), ISSN: 00982202. https://doi.org/10.1115/1.3242658

Firzoozabadi, A.; Katz, D.: Analysis of high-velocity gas flow through porous media, JPT **31**(2), 211–216 (1979) ISSN: 01492136

Forchheimer, P.: Hydraulic, 3rd edn, p. 60. Teubner Verlagsgesellschaft, Berlin (1930)

Freeze, R.A., Cherry, J.A.: Groundwater. http://hydrogeologistswithoutborders.org/wordpress/1979-english/ (1979)

Gelhausen, M.G., Lenz, D., Krull, F., Korkmaz, V., Agar, D.W:; 3D printing for chemical process laboratories II: measuring liquid-solid mass transfer coefficients. Chem. Eng. Technol. **4**, 798–805 (2018), ISSN: 0930-7516, https://doi.org/10.1002/ceat.201700295

Happel, J.; Brenner, H.: Low Reynolds number hydrodynamics with special applications to particulate media. Martinus Nijhoff Publishers, The Hague., The Netherlands (1983) ISBN: 90-247-2877-0

Hasimoto, J.: On the periodic fundamental solutions of the Stokes equations and their application to viscous flow past a periodic array of spheres. Int. J. Multiphase Flow **5**, 317–328 (1959)

Hill, R.J., Koch, D.J., Ladd, A.J.C.: Moderate Reynold-number flows in ordered and random arrays of spheres. J. Fluid Mech. **448**, 243–278 (2001), ISSN: 0022-1120

Hubbert, M.K.: The theory of ground–water motion. J. Geol. **48**, 785–944 (1940), ISSN: 00221376. https://doi.org/10.1086/624930

Idelchik, I.E.: Handbook of Hydraulic Resistance, 3rd edn., CRC Press, Boca Raton (1994), ISBN: 0-8493-9908-4.

ISO/ASTM 52900:2015 Additive manufacturing—Part 1: Terminology

King, W., Anderson, A., Ferencz, R., Hodge, N., Kamath, C., Khairallah, S., Rubenchick, A.: Laser powder bed fusion additive manufacturing of metals; physics, computational, and materials challenges. Appl. Phys. Rev. (2015). https://doi.org/10.1063/1.4937809

Kozeny, J.: Über kapillare Leitung des Wassers im Boden. Wien Akad, Wiss **136**(2a), 271 (1927)

Kruseman, G.P., Ridder, N.A.D., Verweij, J.M.: Analysis and evaluation of pumping test data, *Wageningen*, International Institute for Land Reclamation and Improvement (1990), ISBN: 9070754207

Macdonald, I.F., El-Sayed, M.S., Mow, K., Dullien, F.A.L.: Flow through porous media—the Ergun equation revisited. Ind Eng Chem Fund, **18**(3), 199–208 (1979), ISSN: 01964313

Mao, D., Karanikas, J.M., Fair, P.S., Prodan, I.D., Wong, G.K.: A different perspective on the Forchheimer and Ergun equations. SPE *J* **21**(5), 1501–1507 (2016). ISSN 1086-055

Malekipour, E., El-Mounavri, H.: Common defects and contributing parameters in powder bed fusion AM process and their classification for online monitoring and control: a review. The International Journal of Advanced Manufacturing Technology **95**, 527–550 (2018)

Mcphee, C., Reed, J., Zubizarreta, I.: Core Analysis: A Best Practice Guide. Elsevier, (2015), ISBN: 0444635335

Muskat, M., Botset, H.: Physics **1**, 27 (1931)

Newman, M.S., Yin, X.: Lattice Boltzmann simulation of non-darcy flow in stochastically generated 2D porous media geometries. SPE J. **18**, 12–26 (2013). ISSN: 1086-055X. https://doi.org/10.2118/146689-PA

Olatunde, G., Fasina, O.: Modified Ergun equation for airflow through packed beds of Loblolly Pine Grinds. Kona **36**, 232–240 (2018). ISSN: 02884534, https://doi.org/10.14356/kona.2019003

Osei-Bonzu, K., Grassia, P., Shokri, N.: Effects of pore geometry on flowing flow dynamics in 3D-printed porous media. Transp. Porous Med. **128**, 903–917 (2018), ISSN: 0169-3913, https://doi.org/10.1007/s11242-018-1103-5

Raudkivik, A.J.: Loose Boundary Hydraulics, 3rd edn. Pergamon Press Oxford, (1990) ISBN 0-08-034074-1

Rumpf, H.C.H., Gupte, A.R.: Einflüsse der Porosität und Korngrößenverteilung im Widerstandsgesetz der Porenströmung. Chem. Ingenieur Technik, **43**, 367–375 (1971), ISSN: 0009-286X, https://doi.org/10.1002/cite.330430610

Sangani, A.S., Acrivos, A.: Slow Flow through a periodic array of spheres. Int. J. Multiphase Flow **8**, 343–360 (1981)

Schiller, L.: Über den Strömungwiderstand von Rohren verschiedenen Querschnitts und Rauhigkeitsgrades. Z. Angew. Math. Mech. **3**, 2 (1923)

Schulz, R., Ray, N., Zech, S., Rupp, A., Knaber, P.: Beyond Kozeny–Carman: predicting the permeability in Porous media. Transport Porous Media (2019). https://doi.org/10.1007/s11242-019-01321-y

Schriever, Trans. Amer. Inst. Min. Metall. Engrs. Pet. Div., Vol. 86, pp. 333, **1930**

Trapp, J., Rubenchik, A.M., Guss, G., Matthews, M.J.: In situ absorptivity measurements of metallic powders during laser powder-bed fusion additive manufacturing. Appl. Mater. Today **9**, 341–349 (2017)

Turkuler, O., Moghtada, M., Unver, O.: Determination of Kozeny constant based on porosity and pore to throat size ratio in porous medium with rectangular rods. Engineering Applications of Computational Fluid Mechanics **8**(2), 308–318 (2014). https://doi.org/10.1080/19942060.2014.11015516

Vock, S., Klöden, B., Kirchner, A., Weissgärber, T., Kieback, B.: Powders for powder bed fusion: a review. Progress in Additive Manufacturing **4**, 383–397 (2019)

White, F.M.: Viscous Fluid Flow, 3rd edn. McGraw-Hill Boston, USA (2006). ISBN 9780072402315

Affiliations

Sondre Gjengedal[1] · **Vegard Brøtan**[2] · **Ole T. Buset**[1] · **Erik Larsen**[1] · **Olav Å. Berg**[2] · **Ole Torsæter**[1] · **Randi K. Ramstad**[1] · **Bernt O. Hilmo**[3] · **Bjørn S. Frengstad**[1]

✉ Sondre Gjengedal
sondre.gjengedal@ntnu.no

[1] Norwegian University of Science and Technology, Trondheim, Norway

[2] SINTEF Manufacturing AS, Trondheim, Norway

[3] Asplan Viak AS, Trondheim, Norway

ISBN 978-82-326-5780-3 (printed ver.)
ISBN 978-82-326-5311-9 (electronic ver.)
ISSN 1503-8181 (printed ver.)
ISSN 2703-8084 (online ver.)

NTNU
Norwegian University of
Science and Technology